Photoactive Nanostructured Hybrid Materials for Optical and Biomedical Applications

Co-advised PhD

Nerea Epelde Elezcano

Under Supervision of

Dr. Virginia Martínez Martínez (UPV-EHU)

and

Dr. Sylvie Lacombe (UPPA)

Leioa, 2016

SUMMARY

Along this manuscript different hybrid materials are synthesized and extensively characterized for several uses: from optical to therapeutic applications.

First, by the intercalation of different dyes, styryl 722 and pyronine-Y into several smectite clay films, macroscopically ordered system are obtained. Clay films are elaborated by spin-coating technique and the dyes are intercalated by the immersion of clay thin films into dye solutions. The effect of clay on the dye properties is deeply analyzed and its preferential orientation in the interlayer space of the clay is studied by the anisotropic response of the films to the linear polarized light.

Second, large silica monoliths with embedded laser dyes with strong absorption and fluorescence bands in different region of the Visible spectrum are attained by sol-gel chemistry to obtain solid-state dye laser (SSDL) with good photo, thermal and chemical stabilities.

Third, silica nanoparticles (NP) with suitable size (50 nm) and functionalized external surface are also synthesised by sol-gel chemistry. Through the encapsulation of fluorescent dye molecules in their core and by the grafting of photosensitizers on their shell, biocompatible nanoparticles for bio-imaging and Photodynamic Therapy (PDT) applications are prepared. In order to optimize their properties, a careful investigation of the photophysical properties and mainly the singlet oxygen generation of a large range of new photosensitizers based on chromophores known as BODIPYs, is previously carried out. Based on these results, some efficient BODIPYs are selected for grafting on silica nanoparticles in order to use them for PDT.

The photophysical properties of all these hybrid materials are analyzed by absorption and fluorescence (steady-state and time correlated) spectroscopies, and the singlet oxygen measurements are monitored by direct method (recording the singlet oxygen luminescence at 1270 nm) and by indirect method (using selective chemical probe). Moreover, the hybrid materials are fully characterized by several techniques such as, SEM, TEM, XRD, XPS, IR, DLS, BET.

RESUMEN

En la presente tesis doctoral se sintetizan y caracterizan diferentes materiales híbridos para su uso en diversas aplicaciones en óptica y en terapia fotodinámica.

En primer lugar, se obtienen sistemas macroscópicamente ordenados mediante la intercalación en películas de arcillas tipo esmectita de distintos colorantes, Estirilo LDS 722 y Pironina-Y. Las películas de arcilla se elaboran mediante la técnica de *spin-coating* y la intercalación de los colorantes se lleva a cabo mediante inmersión de dichas películas en las disoluciones de los colorantes. Se estudia exhaustivamente el efecto del entorno arcilloso sobre las propiedades del colorante y se determina su orientación en el espacio interlaminar mediante la respuesta anisotrópica a la luz linealmente polarizada.

En segundo lugar, aplicando la química sol-gel se elaboran monolitos de sílice en los que se embeben diferentes colorantes láser, que absorben y emiten intensamente en diferentes regiones del espectro visible con el fin de obtener medios activos de láseres de colorante en estado sólido (SSDL) con buena estabilidad térmica y química y alta resistencia a la fotodegradación.

En tercer lugar, se sintetizan nanopartículas de sílice (NP) en torno a 50 nm y con una superficie externa funcionalizada. Mediante la encapsulación de colorantes fluorescentes en su interior y el anclaje de fotosensibilizadores en su exterior, se obtienen nanoparticulas biocompatibles para su uso en bioimagen y en terapia fotodinámica (TFD). Además, con el fin de optimizar la generación de oxígeno singlete, se ha llevado a cabo previamente el estudio de una amplia gama de nuevos fotosensibilizadores basados en los cromóforos conocidos como BODIPYs.

Las propiedades fotofisicas de todos los materiales híbridos sintetizados se han estudiado por espectroscopia de absorción y fluorescencia (en estado estacionario y resuelta en el tiempo), y el oxígeno singlete se ha determinado por método directo (luminiscencia a 1270 nm) e indirecto (sonda química selectiva). Por último, los materiales híbridos han sido íntegramente caracterizados por microscopias electrónicas, SEM, TEM, y otras técnicas tales como XRD, XPS, FTIR, DLS y BET.

LABURPENA

Doktorego tesi honetan material hibrido desberdinak sintetizatu eta karakterizatu dira hainbat erabilpen ezberdinetarako, hain zuzen aplikazio optiko eta terapeutikoetarako.

Lehenik eta behin, koloratzaile ezberdinak, LDS 722 Estiriloa eta PironinaY-a, bi esmektita buztin-motatan tartekatu dira, ordenamendu makroskopikoa duen material hibridoa lortzeko asmoz. Buztin-xaflak "spin-coating" teknika erabiliz lortzen dira eta koloratzaileen tratekatzea berriz, buztin-xaflak beraien disoluzioetan sartuz. Buztin xaflen arteko espazioan koloratzailearen goi-agregatuen orientazioa, linealki polarizatutako argiaren aurrean sistemak erakusten duen erantzunaz baliatuta determinatu da.

Bigarrenez, ikuskorrean absortzio eta fluoreszentzia intentsuak dituzten laser koloratzaile ezberdinak, silizezko monolitoetan xurgatu dira, egonkortasun foto- kimiko altuko material solidoak lortzeko asmoz.

Hirugarrenez, 50 nm-ko tamaina eta gainazala funtzionalizaturik duen silizezko nanopartikulak sintetizatu dira. Nanopartikularen "core"-an koloratzaile fluoreszentea kapsulatzerakoan eta nanopartikularen gainazalean fotosensibilizatzailea atxikituz gero, bioimaginerako eta terapia fotodinamikorako material biobateragarriak sintetizatu dira. Bestalde, oxigeno singletearen sorkuntza, BODIPY izenaz ezagunak diren hainbat fotosensibilizatzaile berri karakterizatu dira. Izan ere, lortutako emaitza fotofisikoak kontuan izanda, BODIPY berri batzuk aukeratu dira nanopartikulen gainazalean atxikituak izan daitezen.

Sintetizatutako material hibridoen propietate fotofisikoak, absortzio eta fluoreszentzia (egoera geldikorrean eta denboran korrelazionatuta) espektroskopiak erabiliz ebatzi dira. Oxigeno singletea berriz, bi metodo erabiliz determinatua da: metodo zuzena (oxigeno singletearen luminiszentzia 1270 nm-tan neurtuz) eta zeharkako metodoa (zunda kimiko selektiboa). Azkenik, sintetizatutako material hibrido guztiak zenbait karakterizazio teknika erabiliz analizatu dira, hots, SEM, TEM, XRD, XPS, IR, DLS, BET.

RÉSUMÉ

Dans ce manuscrit, la synthèse et la caractérisation complète de différents matériaux hybrides dédiés à des applications dans le domaine optique ou thérapeutique sont décrites.

Dans un premier temps, des systèmes macroscopiquement ordonnés sont obtenus par intercalation de colorants tels que le Styryl 722 ou la pyronine-Y dans plusieurs films à base d'argile de type smectite. Les films d'argile sont élaborés par spin-coating et les colorants intercalés par immersion des films dans les solutions de ces colorants. Les effets de l'argile sur les propriétés des colorants sont analysés en détail et leur orientation préférentielle dans l'espace inter-couches est étudié grâce à la réponse anisotropique des films en lumière linéairement polarisée.

Dans la deuxième partie, la synthèse par chimie sol-gel de monolithes de silice de grande dimension contenant des colorants laser présentant une forte absorption et une émission de fluorescence dans le visible est abordée. Des colorants laser à l'état solide (SSDL) avec de bonnes stabilités photochimique, thermique et chimique sont ainsi proposés.

Dans le troisième chapitre, la synthèse par voie sol-gel de nanoparticules de silice (NP) d'environ 50 nm de diamètre fonctionnalisées sur leur surface externe est ensuite décrite. Grâce à l'encapsulation de molécules de colorants fluorescents dans leur cœur et le greffage de photosensibilisateurs sur leur écorce, des nanoparticules biocompatibles adaptées à la bio-imagerie et la thérapie photodynamique (PDT) ont été préparées. Pour optimiser leurs performances, les propriétés photophysiques et plus particulièrement la production d'oxygène singulet d'une nouvelle série de photosensibilisateurs basés sur les chromophores de type PODIPY ont d'abord été étudiées en détail. A partir de ces résultats, des BODIPY particulièrement efficaces ont été greffés sur les nanoparticules de silice afin de les utiliser pour la PDT.
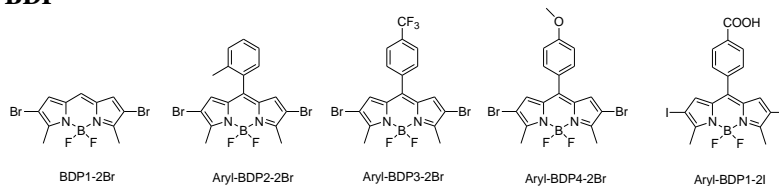
Les propriétés photophysiques de ces matériaux ont été analysées par spectroscopie d'absorption et de fluorescence (stationnaire ou résolue en temps) et les rendements quantiques de production d'oxygène singulet déterminés par des méthodes directe (émission de luminescence de l'oxygène singulet à 1270 nm) ou indirecte (utilisation de sondes chimiques spécifiques à l'oxygène singulet). Par ailleurs les matériaux hybrides ont été complètement caractérisés par plusieurs techniques (SEM, TEM, XRD, XPS, IR, DLS, BET).

8-Phenyl-BDP

BDP1-2Br   Aryl-BDP2-2Br   Aryl-BDP3-2Br   Aryl-BDP4-2Br   Aryl-BDP1-2I

8-Methylthio-BDP

methylthio-BDP2-2Br   methylthio-BDP3-Br   methylthio-BDP4-2I

8-Amino-BDP

amino-BDP1-2I   amino-BDP2-2I   amino-BDP3-2I

BDP DIM 546 as reference dimer   **Iodinated dimer as maximum reference**

BDP DIM 546   BDP DIM 546-3I

Donor/acceptor Dimers

BDP PNODIM   BDP PNHDIM   BDP P8ENDIM

Red shift BDP Dimers

BDP DIMTIO

BDP DIM 546-3Ph

BDP DIMKI

BDP PNOD3K
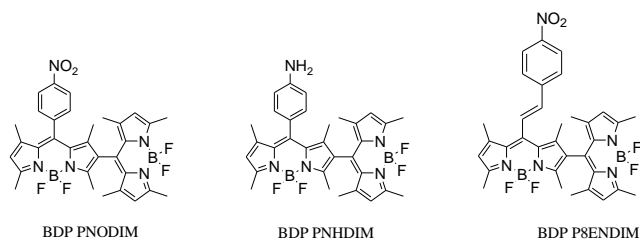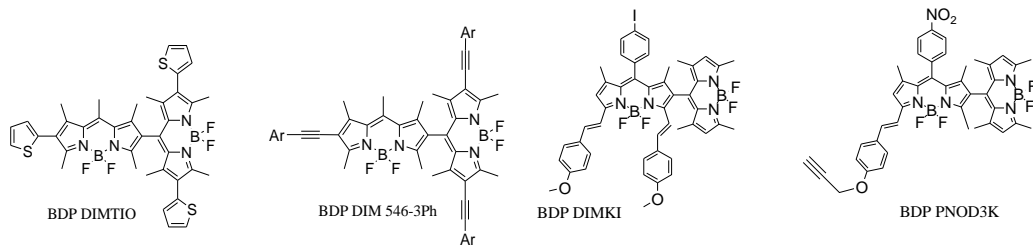
Multichromophoric BDP dimer with Pantachromic action
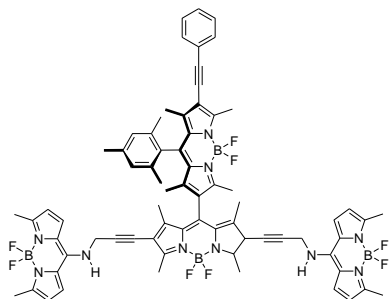
Halogenated Photosensitizers for Grafting

BODIPY-Si(OEt)$_3$ (BDP2)

Rose Bengal (RB)

BODIPY-Ph-COOH (BDP1)
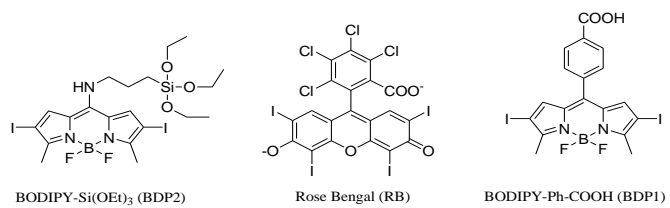
La presente memoria trata sobre el desarrollo de materiales híbridos (mediante la combinación de fluorofóros en diversos soportes inorgánicos) para su uso en diversas aplicaciones tales como ópticas o terapéuticas. El objetivo principal es diseñar diferentes materiales híbridos, por un lado altamente ordenados y fluorescentes, para posibles aplicaciones ópticas y por otro lado biocompatibles y con una alta producción de oxígenos singlete para su implementación en terapia fotodinámica. Por ello este trabajo se ha dividido en tres capítulos donde se detallan la síntesis y caracterización de diversos materiales híbridos los cuales tienen un objetivo diferente respecto a las aplicaciones. No obstante todos los sistemas híbridos sintetizados en este trabajo se basan en la encapsulación o el anclaje de un colorante orgánico en diversas matrices inorgánicas tales como arcillas, monolitos de sílice o nanopartículas de sílice. Todos estos materiales y colorantes se han estudiado en profundidad con técnicas espectroscópicas (absorción y emisión fluorescente de luz, tanto en estado estacionario como resuelta en el tiempo) y además la generación de oxigeno singlete se ha determinado mediante dos métodos, el método directo (mediante la luminiscencia del oxigeno singlete a 1270 nm) y mediante el método indirecto (mediante una sonda química selectiva).

- **Sistemas Arcillas/Colorantes**

La encapsulación de colorantes orgánicos en matrices rígidas inorgánicas da lugar a materiales híbridos donde en general, se produce un aumento importante de la fotoestabilidad del colorante, ya que la matriz inorgánica le protege de posibles degradaciones, aumentando así las propiedades fotofísicas del cromóforo.

Los materiales anfitriones nanoestructurados presentan una gran variedad de geometrías estructurales en 1D (nanotubos, sistemas con canales unidireccionales), 2D (materiales laminares) o de 3D (calanes interconectados en materiales zeoliticos…).

Los materiales huésped que se han elegido son dos arcillas de tipo esmectita, Laponita y Saponita. Estos sistemas bidiomensionales laminares, permiten acomodar de forma reversible una gran diversidad de moléculas, independientemente del tamaño molecular de las mismas, gracias a la hinchabilidad de sus espacios interlaminares manteniendo constantes el resto de sus características estructurales. Las arcillas son aluminosilicatos laminares dispuestas en estructuras TOT con una carga negativa neta en las laminas que es compensada por cationes inorgánicos intercambiables en la superficie de las arcillas, por lo que los colorantes orgánicos se incorporan por un proceso de intercambio catiónico.

La elaboración de las películas de arcillas, se lleva a cabo mediante la técnica "spin-coating" se les proporciona una distribución bidimensional ordenada de las láminas de arcilla. Dicho ordenamiento es ideal para la oclusión de colorantes catiónicos con una orientación preferencial respecto a la normal de la película dando lugar a un material híbrido macroscópicamente ordenado. Además, estos sistemas macroscópicamente ordenados, son susceptibles de generar propiedades de óptica no lineal (NLO) para el desarrollo de guías de onda, generadores de segundo armónico, cristales dicroicos, etc.

La topología y el espesor de las películas de arcillas se analizan mediante un perfilometro, mientras que la adsorción del colorante en el espacio interlaminar de las láminas de arcillas se comprueba por difracción de Rayos-X. Las propiedades fotofísicas del colorante se determinan mediante las espectroscopias de absorción y fluorescencia. La orientación preferencial se obtienen en base a la respuesta anisótropa del sistema a la luz linealmente polarizada. Finalmente debido a la agregación del colorante en un sistema constreñido, se analiza las propiedades fotofisicas de las moléculas de colorante desagregadas por la co-intercalación de moléculas de surfactante.

- ## <u>Colorantes en Estado Solido</u>

Los monolitos de sílice son elegidos como una matriz inorgánica adecuada para la encapsulación de colorantes láser en sus poros con el fin de obtener un material híbrido en estado sólido con buenas aplicaciones de láser y que presenten una buena estabilidad térmica y química y alta fotoestabilidad.

De hecho, la matriz de sílice es un buen material huésped debido a sus excelentes propiedades, tales como resistencia química y mecánica, su gran área superficial y transparencia óptica en la radiación Vis-NIR. Además, las suaves condiciones de síntesis sol-gel como la baja temperatura requerida permiten añadir las moléculas orgánicas de interés directamente en el gel de síntesis. Además, los precursores alcóxidos y los colorantes láser (cumarinas, xantenos, oxazinas,...) son solubles en los típicos disolventes alcohólicos utilizados en la síntesis.

En este trabajo se han sintetizado monolitos de sílice con forma de paralelepípedo de tamaño 0,5 cm x 0,5 cm x 1,5 cm con diferentes concentraciones de colorante ocluído. En primer lugar, se han encapsulado BODIPYs comerciales (BODIPY 597 y BODIPY 605) debido a su versatilidad y sus buenas propiedades fotofísicas y acción láser.

En segundo lugar, se han encapsulado varias Rodaminas con fuertes bandas de absorción y emisión en prácticamente todo el rango del espectro de luz Visible (Rodaminas 110, 123, 6G y 3B). Estos monolitos, especialmente con los colorantes Rh6G y Rh3B muestran altos rendimientos cuánticos de fluorescencia y aparecen estables después de 1 año. De hecho, la eficiencia de láser del monolito Rh6G es de un 31% (concentración de colorante 0,45 mM), que es notablemente más alta que las eficiencias laser ya probabas para este colorante en diferentes matrices inorgánicas tales como películas de alúmina (2%), xerogeles de sílice (16%) o xerogeles de aluminosilicato (25%). Por lo contrario, las irregularidades en estos monolitos (meniscos) inducen pérdidas importantes en la cavidad resonante y como alternativa y solución a este problema, se han sintetizado nuevo monolitos cilíndricos con el fin de eliminar la formación de meniscos y mejorar la eficiencia laser.

- **Nanoparticulas de Silice y Nuevos BODIPYs para Oxigeno singlete**

También se han sintetizado nanopartículas mesoporosas de SiO_2 esféricas, monodispersas, de 50 nm de diámetro y funcionalizadas en la superficie con grupos amino (*core-shell*). Con el fin de obtener nanopartículas fluorescentes se han encapsulado en su interior diversos colorantes de la familia de las rodaminas (con bandas de absorción y fluorescencia en distintas regiones del espectro Visible), mediante su adición directa en el gel de síntesis. Una vez optimizada la concentración de colorante en dicho gel para una de las rodaminas (R6G), de manera que se logre el mayor número de moléculas ocluidas manteniendo sus propiedades fotofísicas, se ha realizado la encapsulación de la Rodamina 640 con bandas de absorción y fluorescencia más al rojo del espectro Visible para su posible aplicación en bioimagen. Otro de los objetivos de este trabajo es conseguir nanoparticulas biocompatibles con una alta producción de oxígeno singlete, especie citotóxica, para su implementación en terapia fotodinámica contra el cáncer. Para ello, distintos fotosensibilizadores (moléculas orgánicas con alto producción de oxígeno singlete) se han anclado en la superficie externa de las nanoparticulas funcionalizada con grupos NH_2 y OH.

Además, mediante la combinación de la encapsulación de las rodaminas como moléculas fluorescentes en su interior junto con el anclaje de los fotosensibilizadores en su superficie exterior se obtienen nanopartículas para teragnosis, donde se combina la imagen con la terapia fotodinámica.

Por lo tanto, antes de la inmovilización en NPs, y con el fin de optimizar las propiedades fotofisicas principalmente la generación de oxígeno singlete de estas nanoparticulas para su aplicación en terapia fotodinámica, se ha llevado a cabo previamente el estudio en disolución de una amplia gama de nuevos fotosensibilizadores basados en los cromóforos conocidos como BODIPYs, tanto de tipo halogenado como díadas ortogonales de BODIPYs.

Probablemente la gran ventaja de los colorantes BODIPY es que su estructura básica es susceptible a un amplio abanico de reacciones orgánicas, lo cual se traduce en la posibilidad de sintetizar una amplia batería de derivados donde el patrón de sustitución condiciona las propiedades fotofísicas del colorante resultante y en este caso en particular la generación de oxígeno singlete. Por lo tanto el patrón de sustitución del BODIPY permite modular y optimizar sus propiedades espectroscópicas. Como ejemplo, la absorción y emisión de estos colorantes se puede desplazar hacía la región roja simplemente extendiendo su sistema π deslocalizado a través de grupos anclados al cromóforo. Por otro lado, tanto la posición en la que se incorporan las sustituciones como carácter dador/aceptor de electrones determina la producción de oxigeno singlete del colorante. Por lo tanto en este trabajo, se ha estudiado una batería de BODIPYs estructuralmente modificados, que nos ha permitido no solo optimizar la eficiencia de oxigeno singlete para la región visible si no que también extenderla a la región azul mediante la sustitución de heteroatomos en posición meso del BODIPY y también a la región roja mediante la extensión del sistema π deslocalizado. Además los sistemas multicromoforicos basados en estructuras BODIPYs unidos covalentemente en disposición ortogonal posibilita mejorar la absorción de luz y obtener emisión de oxigeno singlete tanto bajo la excitación visible, ultravioleta como luz blanca.

Por lo tanto después de analizar las propiedades fotofisicas de los BODIPYs en disolución se llevó a cabo la inmovilización de algunos BODIPYs en la superficie externa de nanopartículas de sílice, con el fin de usarlas en Terapia fotodinámica (TFD). En particular, los fotosensibilizadores utilizados son: un colorante comercial xanteno (Rosa de Bengala o RB) y dos derivados de BODIPY halogenados. Los BODIPYs anclados se diferencian porque uno de ellos lleva un grupo trietoxisilano y el otro lleva un grupo carboxilato, para su anclaje en la superficie de la nanoparticula. Por último, ambas aplicaciones se han combinado, bioimagen debido a la encapsulación de las moléculas fluorescentes y la terapia fotodinámica mediante el anclaje de los

fotosensibilizadores elegidos para un comportamiento dual y su futura aplicación en teragnosis.

Todos los sistemas se han caracterizado por diversas técnicas instrumentales como las microscopías electrónicas SEM y TEM, Dispersión de luz dinámica (DLS), espectroscopias de absorción y fluorescencia y la microscopia confocal de fluorescencia resuelta en el tiempo (técnica FLIM).

Como consecuencia del trabajo desarrollado se disponen de diversas alternativas para la obtención de sistemas híbridos y así poder elegir la más conveniente según la aplicación deseada.

Señalar por último que el desarrollo de esta tesis doctoral ha desarrollado en régimen de cotutela entre la UPV-EHU y la universidad de Pau (UPPA) lo que ha permitido una tarea multidisciplinar, por un lado la síntesis inorgánica de los materiales híbridos sintetizados y el estudio fotofísico de los materiales híbridos sintetizados entre ambos grupos, Espectroscopía Molecular de la Facultad de Ciencia y Tecnología de la UPV/EHU y el institut des sciences analytiques et physico-chimie pour l'environnement et les materiaux. Además, en la presente tesis doctoral se han llevado a cabo gracias a numerosas colaboraciones con grupos de síntesis orgánica (UCM en Madrid y Universidad de Guanajuato Méjico) y especialistas en laser (CSIC en Madrid).

INTRODUCTION

In recent decades, many efforts of the scientific community have been focused on the development of new multifunctional materials. These advances are consequences of the combination of chemists', biologists', physicists' and engineers' research in the nanoscience and material chemistry fields. Generally speaking, nanoscience is based on the design, study and manipulation of substances and devices smaller than one micrometer (10^{-6} m) and close to the nanometer (10^{-9} m) (Figure 1)[1].
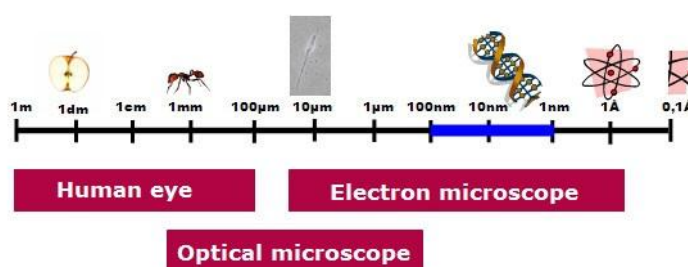
Figure1. Nanotechnology works between 1 and 100 nm

In this sense, hybrid organic–inorganic materials, defined as molecular or nano-composites with organic and inorganic components, intimately mixed where at least one of the component domains has a dimension ranging from a few Å to several nanometers, are recognized as one of the most promising systems for potential applications in many areas such as optics, electronics, mechanics, energy, environment, biology and medicine. The final properties of the hybrid materials are not the mere sum of the individual contributions of both moieties since new or enhanced properties can be found.

The nature of the interface of hybrid materials can be divided in two distinct classes[2]:

i) *Class I*, organic and inorganic components are embedded and they are connected though weak interactions such as van der Waals, hydrogen or ionic bonds

ii) *Class II*, organic and inorganic components are linked together through strong chemical covalent or ionic-covalent bonds.

In particular, the combination of photoactive molecules, such as fluorescent organic dyes, in solid inorganic matrices[3], e.g. silica xerogels, zeolitic materials[4], laminar oxides and clays[5–7], has raised an important interest, mainly in the development of new optical and photoelectronic devices[8] such as optical sensors, optical storage devices, solid-state dye laser[9,10], photovoltaic cells[11] as well as photocatalyzers[12,13], or even therapeutic vectors that combine targeting, imaging[14], therapy[15,16] and controlled release of active molecules[17]. Moreover, systems with 1D- and 2D-dimensionality of nanosized pores can afford a supramolecular organization for the embedded guest. Such ordered hybrid materials usually show a high anisotropic response to light, a vital property for their use in NLO (Non-Linear-Optics) applications such as second harmonic generation, dichroic filters and light waveguides[18–21].

Four important aspects can be covered by the design of these new materials:

➢ To improve the photo-, thermo- and chemical stability of the guest molecules. Indeed, chromophores embedded into different porous materials generally experience an important decrease in their photodegradation[22].

➢ To modify and to control the electrical, magnetic and optical properties of the guest molecules in constrained and rigid nanostructured environments in order to manufacture materials with very specific technological applications[18,23–25].

➢ To facilitate both integration and miniaturization.

➢ To induce a macroscopic order by the preferential orientation of the guests inside the 1D- or 2D-hosts[26–30].

This thesis is divided in three chapters, in which different photoactive hybrid materials are synthetized and characterized with the aim of potentially using them in different areas: from optical to therapeutic applications.

In chapter 1, the first hybrid system based on the encapsulation of organic dye molecules (guest) into inorganic Clay minerals (host) is studied. By elaborating supporting films, macroscopically ordered systems are achieved. The clay minerals used as host are Laponite and Saponite due to their excellent properties, such as high swellability of their 2D interlayer space, transparency and purity. Two different cationic laser dyes, Styryl 722 (LDS 722) and Pyronine Y (PY) are selected as organic guest.

In chapter 2, large monoliths are synthetized by the encapsulation of organic laser dyes (guest) within silica xerogels materials to attain solid-state dye laser (SSDL). These hybrid materials are based on the combination of the good laser action of the organic dyes together with a high photo- and thermo-stability provided by the silica glass network, which is highly porous and optically transparent in the Vis-NIR radiation.

The chapter 3 is divided in two parts. The first part is focused on the study of photophysical properties, modeling and singlet oxygen generation of a series of new photosensitizers based on the 4,4-difluoro-4-bora-3a,4a-diaza-s-indacene structure, also known as BODIPY, with the aim of developing alternatives to porphyrin compounds with better properties for photodynamic therapy (PDT) applications. In the second part, functionalized silica nanoparticles are used as non-toxic drug carriers where the Photodynamic therapy action arising from the grafting of different photosensitizers on the external surface is combined with the bioimaging application by the encapsulation of fluorescent dyes in their core for potential application in theranosis.

It has to be emphasized that this work benefitted from a co-advised grant between UPV-UHA and UPPA. This collaboration allowed taking advantage of the skills of both teams: combining the well-mastered photophysical studies in UPV-EHU with the synthesis experience (sol-gel chemistry, grafting reactions) in UPPA. Moreover, both teams benefitted from combining existing knowhow in UPPA on determination of singlet oxygen quantum yields and state-of-the-art detection newly acquired in UPV-EHU. The success of the synthesis and characterization of several systems summarized below is an example of the fruitful collaboration established between both Universities.

Bibliography

1.   http://ina.unizar.es/wp-content/uploads/2014/10/quees4.jpg.

2.   Clément Sanchez, G. State of the art developments in functional hybrid materials. *J. Mater. Chem.* **15,** 3557–3558 (2005).

3.   Nicole, L., Boissière, C., Grosso, D., Quach, A. & Sanchez, C. Mesostructured hybrid organic–inorganic thin films. *J. Mater. Chem.* **15,** 3598 (2005).

4.   Ivanova, I. I. & Knyazeva, E. E. Micro-mesoporous materials obtained by zeolite recrystallization: synthesis, characterization and catalytic applications. *Chem. Soc. Rev.* **42,** 3671–88 (2013).

5.   -   -   -Arbeloa, I. Preparation, Photophysical Characterization, and Modeling of LDS722/Laponite 2D-Ordered Hybrid Films. *Langmuir* **30,** 10112–10117 (2014).

6.   Bujdák, J., Iyi, N., Kaneko, Y., Czímerová, A. & Sasai, R. Molecular arrangement of rhodaine 6G cations in the films of layered silicates: the effect of layer charge. *Phys. Chem. Chem. Phys.* **5,** 4680 (2003).

7.   Bujdák, J. & Iyi, N. Optical properties of molecular aggregates of oxazine dyes in dispersions of clay minerals. *Colloid Polym. Sci.* **287,** 157–165 (2009).

8.   Garcia, O., Garrido, L., Sastre, R., Costela, A. & García-Moreno, I. Synthetic strategies for hybrid materials to improve properties for optoelectronic applications. *Adv. Funct. Mater.* **18,** 2017–2025 (2008).

9.   Costela, a. *et al.* Polymer-filled nanoporous silica aerogels as hosts for highly stable solid-state dye lasers. *J. Phys. Chem. B* **109,** 4475–4480 (2005).

10.   Mackey, M. S. & Sisk, W. N. Photostability of pyrromethene 567 laser dye solutions via photoluminescence measurements. *Dye. Pigment.* **51,** 79–85 (2001).

11.   Gong, J., Liang, J. & Sumathy, K. Review on dye-sensitized solar cells (DSSCs): Fundamental concepts and novel materials. *Renew. Sustain. Energy Rev.* **16,** 5848–5860 (2012).

12.   Ronzani, F. *et al.* Visible-light photosensitized oxidation of α-terpinene using novel silica-supported sensitizers: Photooxygenation vs. photodehydrogenation. *J. Catal.* **303,** 164–174 (2013).

13.   Saint-Cricq, P., Pigot, T., Nicole, L., Sanchez, C. & Lacombe, S. Hybrid functional mesostructured thin films with photo-oxidative properties in the visible range. *Chem. Commun.* 5281–5283 (2009). doi:10.1039/b911742c

14.   Yi, X., Wang, F., Qin, W., Yang, X. & Yuan, J. Near-infrared fluorescent probes in cancer imaging and therapy: an emerging field. *Int. J. Nanomedicine*

9, 1347–65 (2014).

15. Wang, Z. *et al.* BODIPY-doped silica nanoparticles with reduced dye leakage and enhanced singlet oxygen generation. *Sci. Rep.* **5,** 12602 (2015).

16. Gianotti, E. *et al.* An efficient rose bengal based nanoplatform for photodynamic therapy. *Chem. - A Eur. J.* 10921–10925 (2014). doi:10.1002/chem.201404296

17. Torchilin, V. P. Targeted pharmaceutical nanocarriers for cancer therapy and imaging. *AAPS J.* **9,** E128–E147 (2007).

18. Sanchez, C., Julián, B., Belleville, P. & Popall, M. Applications of hybrid organic–inorganic nanocomposites. *J. Mater. Chem.* **15,** 3559–3592 (2005).

19. Ogawa, M. & Kuroda, K. Photofunctions of Intercalation Compounds. *Chem. Rev.* **95,** 399–438 (1995).

20. Calzaferri, G., Huber, S., Maas, H. & Minkowski, C. Host-guest antenna materials. *Angew. Chemie - Int. Ed.* **42,** 3732–3758 (2003).

21. Takagi, S. *et al.* Size-matching effect on inorganic nanosheets: control of distance, alignment, and orientation of molecular adsorption as a bottom-up methodology for nanomaterials. *Langmuir* **29,** 2108–19 (2013).

22. López Arbeloa, F., Martínez Martínez, V., Arbeloa, T. & López Arbeloa, I. Photoresponse and anisotropy of rhodamine dye intercalated in ordered clay layered films. *J. Photochem. Photobiol. C Photochem. Rev.* **8,** 85–108 (2007).

23. Cao, G. *Nanostructures and Nanomaterials: Synthesis, Properties and Applications*. (World Scientific, 2004).

24. Ramamurthy, V. & Eaton, D. F. Perspectives on Solid-state Host-Guest Assemblies. *Chem Mater* **6,** 1128–1136 (1994).

25. Schulz-Ekloff, G., Wöhrle, D., van Duffel, B. & Schoonheydt, R. a. Chromophores in porous silicas and minerals: preparation and optical properties. *Microporous Mesoporous Mater.* **51,** 91–138 (2002).

26. Bujdák, J., Iyi, N., Kaneko, Y. & Sasai, R. Molecular orientation of methylene blue cations adsorbed on clay surfaces. *Clay Miner.* **38,** 561–572 (2003).

27. Kaneko, Y., Iyi, N., Bujdak, J., Sasai, R. & Fujita, T. Effect of layer charge density on orientation and aggregation of a cationic laser dye incorporated in the interlayer space of montmorillonites. *J. Colloid Interface Sci.* **269,** 22–25 (2004).

28. Iwasaki, M., Kita, M., Ito, K., Kohno, A. & Fukunishi, K. Intercalation characteristics of 1,1 '-diethyl-2,2 '-cyanine and other cationic dyes in synthetic saponite: Orientation in the interlayer. *Clays Clay Miner.* **48,** 392–399 (2000).

29.   Martínez-Martínez, V., García, R., Gõmez-Hortigüela, L., Pérez-Pariente, J. &
       Lõpez-Arbeloa, I. Modulating dye aggregation by incorporation into 1D-
       MgAPO nanochannels. *Chem. - A Eur. J.* **19,** 9859–9865 (2013).

30.   García, R., Martínez-Martínez, V., Sola Llano, R., López-Arbeloa, I. & Pérez-
       Pariente, J. One-dimensional antenna systems by crystallization inclusion of
       dyes (One-Pot Synthesis) within zeolitic MgAPO-36 nanochannels. *J. Phys.
       Chem. C* **117,** 24063–24070 (2013).

1

MACROSCOPICALLY ORDERED SYSTEMS

1.1. Introduction

Many benefits arise from the synergy between the inorganic host and organic guests[1–10]. On the one hand, the host matrix would provide thermal, chemical and photo-protection to the guest molecules and on the other hand, the photoactivity of the guest could be modulated by the host[11]. Furthermore, the matrix could also induce a preferential orientation to the guest molecules obtaining a macroscopic ordered system interesting for many optical devices such as frequency-doublers, dichroic filters and light waveguides. In this sense, layered structure materials are important inorganic matrices to design highly-ordered 2D films[5,12]. Particularly, clay minerals with expansible interlayer space can be appropriate hosts for many photoactive guest compounds such as laser dyes. Indeed, different dye/clay systems[13], previously studied, have showed anisotropic response to the linear polarized light as a consequence of the preferential orientation of the dye molecules respect to the normal to the clay film. Moreover, in the best of the cases, the dye had improved their chemical and photophysical properties[14].

In this work the incorporation of LDS 722 and PY dye molecules into Laponite and Saponite clay minerals is studied. The Laponite and Saponite clay minerals are chosen as a host because they offer films with high optical transparency (required for most of the optical applications) and a high capacity to absorb cationic dyes. On the other hand, these dyes are selected as guest because both are positively charged and they also have promising properties for potential applications in optoelectronic devices.

1.1.1. 2D-Clay hosts

In many cultures clay minerals were widely and daily used as porcelain. Nowadays the interests on those materials have increased in many other fields (i.e. science and industry) due to several advantages such as natural abundance, low cost and high adsorption capacities. In fact they are one of the most used systems as fillers, dressings in construction, purifying water waste, and in the paper, plastics, and rubber industries but also in the biomedicine field to treat acne, infections, indigestion, and other medical problems[15,16]

Clay minerals are laminar aluminosilicates formed by the condensation of tetrahedral SiO_2 (T) and octahedral Al_2O_3 or MgO (O) sheets. The layers usually presents a negative charge, due to the isomorphic substitution of some tetrahedral Si^{4+}

and/ or octahedral Al^{3+} or Mg^{2+} cations for other cations with lower valence, which is compensated by hydrated interchangeable inorganic cations[17]. The staking of clay layers usually formed the so-called tactoid structure (Figure 1.1) with two main adsorption surfaces: a) the external surface and b) the internal surface.
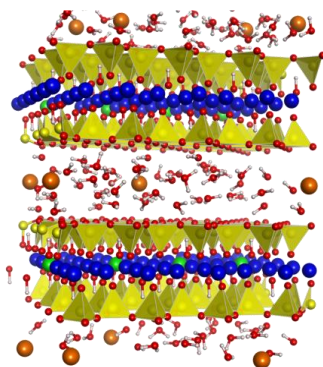
Figure 1.1. Schematic representation of Laponite clay. Si atoms are represented in yellow, Na in orange, Mg in blue, Li in green, O in red, and H in white.

The extent (charge density), the type (tetrahedral or octahedral) of the isomorphic substitution and the hydration degree of the inorganic cations are important factors which affect the adsorption capacity and the physicochemical properties (polarity, acidity, etc.) of the clay surfaces as well as the swelling characteristics of the interlayer space. A typical parameter that evaluates the absorption capacity in clays is the cationic exchangeable capacity or CEC (units of mequiv/100 g) that indicates the number of exchangeable cations per dry weight of clay.

Generally, the clay minerals are subdivided (Table 1.1) based on the clay layer structure and charge density[18,19].

➢ *Neutrals clay minerals*; are those which do not have isomorphic substitutions and, therefore, the clay minerals layers do not have a negative charge. This kind of clay minerals presents a hydrophobic surface and as a result the layers stick each other by van der Waals interactions and cannot be exfoliated (layers individually separated). Kaolinites, serpentinites, pyrophyllite and other talcs are included as neutral clay minerals.

> *Smectites-types*; these kinds of clay minerals have a moderate charge density, with a net charge per unit cell, x, between 0.2 and 0.7, which is compensated by hydrated cations (primarily K, Na, Ca, and Mg) in the interlayer space. These clays have an exchangeable capacity (CEC) between 50-100 mequiv/100, which is considered the best swelling capacity to accommodate a large amount of cationic or polar molecules in their interlayer space[20]. For these reasons, in this work, two smectite clays with similar charge density but different isomorphic substitution type (tetrahedral or octahedral) have been employed. They will be described in detail below.

> *Vermiculite*; these clay minerals are similar to smectites types but they have higher net negative charge, $0.7 \leq x \geq 1$ which mainly originates from the substitutions in T layer. Generally, vermiculites have Mg^{2+} as exchangeable cation. Water and polar organic molecules can be intercalated inside these clay mineral, but their layers swelling is more limited because the electrostatic interactions between layers are stronger than in smectites types clay minerals.

> *Mica-types*; these clay minerals groups present high net negative charge, $1 \leq x \geq 2$. This type of clay has a lot of isomorphic substitutions. In general, micas with x~1, denominated as *true micas*, have normally as exchangeable cations K^+ or Na^+, and for charges x~2, denominated *brittle micas*, the exchangeable cation is usually Ca^{2+}. Owing to their high charge density, the electrostatic interactions between layers are too strong and the swelling capacity is practically negligible.

Table 1.1. Classification of different clay minerals depending on their isomorphic substitution.

Layer type	x = net charge per unit cell	O sheets; Dioctahedral	O sheets; Trioctahedral	Adsorption capacity
TO	Null (x ≈ 0)	Kaolinite	Serpentine	no
TOT	Null (x ≈ 0)	Pirofilite	Talc	no
	Moderate (x ≈ 0.2-0.7)	Smectites (Montmorillonite)	(Hectorite, Laponite)	optimum
	High-moderate (x ≈ 0.7-1)	Verticulite		yes
	High (x ≈ 1-2)	Micas		no

Table 1.1 shows the different clay minerals classification depending on their isomorphic substitution.

For all these reasons, in this work, two different Smectites clay minerals with Na^+ exchangeable cation are chosen as the best host to lodge different photactive organic guest due to their good swelling capacity in water: Laponite (Lap) and Saponite (Sap)[18,19].

> Laponite (Lap) is a trioctahedral synthetic clay mineral with $[Si_8]^t$ $[Mg_{6-x}Li_x]^O$ $O_{20}(OH)_4$ structure and TOT network. The x charge of Laponite is between 0.6-0.7 valence per cell unit; the negative charge is attributed to the Mg^{2+} substitutions by Li^+ in the O layer. Laponite is a homoinic clay with sodium as exchangeable cation with a CEC of 73.3 mEq/100g. Besides, Laponite has small particle size, 0.03μm, which gives very stable aqueous suspension and high natural viscosity, important property to control the clay film thickness (discuss later in this chapter). Furthermore, Laponite does not have many impurities and its iron percentage is practically negligible (%0.06 in weight), which is an efficient fluorescent quencher.

> Saponite (Sap) is a trioctahedral natural clay mineral with $[Si_{8-x}]^t$ $[Mg_6]^O$ $O_{20}(OH)_4$ structure and TOT network. The cationic exchange capacity of Saponite is 56.8mEq/100g and most of the negative charge is due to the substitution of tetrahedral silicon by the aluminum in T layers. The sodium form and particle size lower than 0.2 μm was previously obtained as described elsewhere[20].

The main differences between Laponite and Saponite are: Lap is a synthetic clay with very low impurities and iron content which its charges is due to the more internal octahedral substitution while Sap is a natural clay with more iron content and higher particle size with a more external charge at the tetrahedral sheet[17,18,21]. In Figure 1.2 and Table 1.2 the Lap and the structural properties are described.

Table 1.2. Structural properties of different smectites types used in this work.

Clay mineral	CEC (mEq/100g)	Amount of Fe (in weight)	Particle size (nm)
Laponite	73.3	0.06	~30
Saponite	56.8	11.22	≤ 200
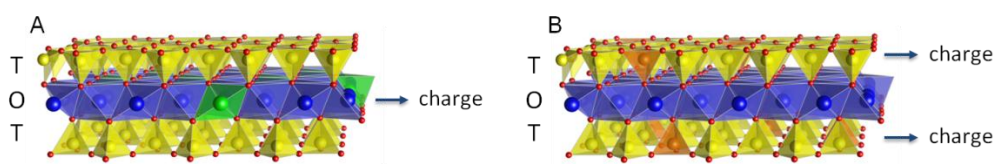
Figure 1.2. Schematic representation of a sheet of (a) Laponite and (b)

In this work, these two smectite clay minerals are used as attractive host materials with well-organized 2D multilayer structure to embed dyes of interest. Therefore, by elaborating supporting films and the adsorption of dyes with a preferential orientation, a macroscopically ordered system will be obtained[4,5].

1.1.2. Photoactive guests; Styryl 722 and Pyronine Y Dyes
1.1.2.1. LDS 722 dye

On the one hand, in this work, a hemicyanine dye, LDS 722, is selected as guest to be incorporated in the interlayer space of clay films. The molecular structure of LDS 722 presents an electron donor part (aniline) and one electron acceptor part (pyridine) separated by a conjugated chain (Figure 1.3).
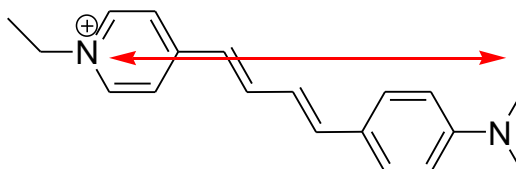
Figure 1.3. Molecular Structure of LDS 722

In general, styryls and particularly LDS 722, has high absorption capacities in the blue region (around 470nm) of the visible and a fluorescent emissions very red-shifted (around 600-700 nm). This large Stokes shift in such dyes, important for minimizing inner filters for laser applications, is a result of its push-pull nature, since the emission takes place from a intramolecular charge transfer state (ICT), which upon excitation the aniline electronic charge is transferred to the pyridine (Figure 1.4).

Figure 1.4. Electronic densities of the HOMO and LUMO states of LDS 722 dye. The intramolecular charge transfer mechanism. The Radiative and non-radiative transitions are represented by solid and dashed lines.

Usually, π-conjugated organic molecules with push-pull groups are interesting for NLO applications due to its high hiperpolarizability[22,23]. However, they usually crystallize in a centrosymetric fashion in an anti-parallel stacking. Besides, they are very flexible molecules and it presents very poor fluorescence quantum yield ($\Phi_{flu}<$ 0.1) in solution because the rotational motions around the different bonds are responsible for the non-radiative deactivation, such as trans-cis isomerization, but mainly the formation of twisted intra-molecular charge transfer (TICT) states, usually non-fluorescent [24–27]. In this sense, a tight confinement of these molecules into 2D-layered structure could restrict their molecular motions in order to achieve high fluorescence or lasing efficiency and on the other hand in a preferential orientation to get an acentric disposition will be of crucial interest. The inclusive approach to study the hybrid material provided us very valuable information, essential for future developing of dye/clay films with potential for NLO applications.

1.1.2.2. Pyronie Y dye

On the other hand, Pyronine Y (PY) dye (Figure 1.5), is also used as photoactive guest to be intercalated into clay minerals. PY is a xanthene derivate dye which is characterized for its bright pink colour and also for its high fluorescence quantum

yield (φ_{fl}= 0.66 in ethanol). However, a typical effect of xanthene-like dyes is that they usually have a great molecular aggregation tendency in concentrated solution or in adsorbed-state[28–39].
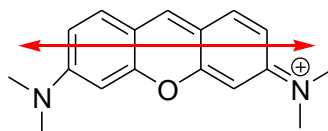
**Figure 1.5**. Molecular Structure of PY

Depending on the dye aggregation the photophysical properties can be drastically changed. Considering the first state of the molecular aggregation there are two main types of dimers: case A_1) perfect H-dimer (monomers disposed in parallel planes in a sandwich-like conformation) which is characterized by new absorption bands at lower wavelength respect to the monomer band and case A_2) perfect J-dimer (monomers in line in a head-to-tail disposition) with shows absorption bands at higher wavelength respect to monomer band. However, dimers can adopt structures with intermediate geometries to optimize the attractive permanent/induced/instantaneous dipole interactions and to minimize the repulsive interactions and steric hindrances between monomeric units. In those cases, dimer can show both absorption bands (blue- and red-shifted respect to the monomer band) being the H-band more intense for the twisted sandwich-type dimer (case B), whereas J-band is more intense in an oblique head-to-tail dimer (case C). Indeed, Fujii et al.[40] have proposed a ratio between the absorption intensities (obtained from the area under the curve) of both H- and J-bands as an indicative parameter for the type of dimer and A_H/A_J values of ≥ 1.3 and ≤ 0.7 are indicative of a sandwich and a head-to-tail geometry, respectively. In Figure 1.6 is depicted the absorption characteristic for dimers with different geometries proposed by the Exciton Theory[41] and their representative orientation with respect to the clay-layer.
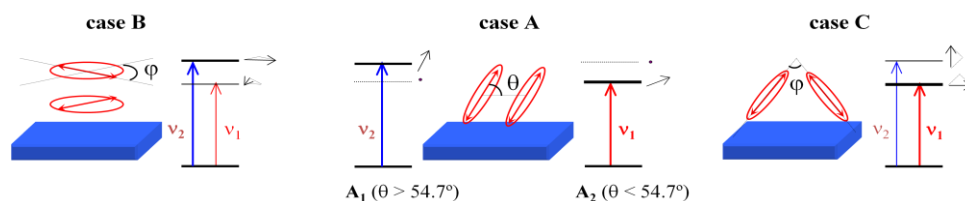
Figure 1.6. Characteristic electronic transitions of dimers with different geometries proposed by the Exciton Theory and representative orientations with respect to the clay-layer.

Regarding their fluorescence properties H-aggregates are not fluorescent and also dramatically quench the fluorescence of the monomer units, decreasing enormously the fluorescence lifetime and quantum yield of the system. However, J-aggregates can be potentially fluorescence although their relative quantum yield would be much smaller than that of the monomers[42]. Indeed, red-emission from J-aggregates of PY dye have already detected in different 1D- channelled systems [11,43–46].

In this chapter, the aggregation process of Pyronin Y (PY) laser dye intercalated into supported thin films of trioctahedral clays, Laponite (Lap) and Saponite (Sap), at different dye loadings is studied: i) experimentally by means of electronic absorption and fluorescence spectroscopies and ii) theoretically by modeling the distribution of the dye into the interlayer space of the clays. The type and extent of the aggregation of PY dye are mainly considered and their impact in the optical properties of the material. Moreover, the effect of the surface charge of the different smectites clays, particularly the charge localization on the TOT clay layer (i.e. net negative charge in octahedral sheets for Lap *vs* in tetrahedral sheets for Sap) on the aggregation state of PY dye is analyzed

1.2.   Results and Discussion

This section presents the main results obtained for the different dye/clay thin films. The general characterization of the dye/clay films was performed by different techniques such as profilometry (thin film thickness), elemental analysis (amount of absorbed dye), thermogravimetry (dye thermostability, and interstitial water of the clay) and X-ray diffraction (clay interlayer swelling). Afterwards, a detail photophysical characterization was performed at different dye loadings by absorption and fluorescence spectroscopies. Additionally, preferential orientation of the dye molecules respect to the normal to the thin film is determined by the anisotropic response of these systems to the linearly polarized light. Finally, with the aim of improving the photophysical properties of the dye/clay films, surfactant molecules are co-adsorbed into the clay interlayer space.

1.2.1. LDS 722 /Laponite Thin Films

Transparent films of clay, adequate for dye adsorption were made by spin coating and the thickness of the supported thin-films was checked by Laser profilometry. The thickness of Lap films was of around ~ 400 nm (Figure 1.7), which is easily reproducible from sample to sample under the conditions detailed in the methodology section.
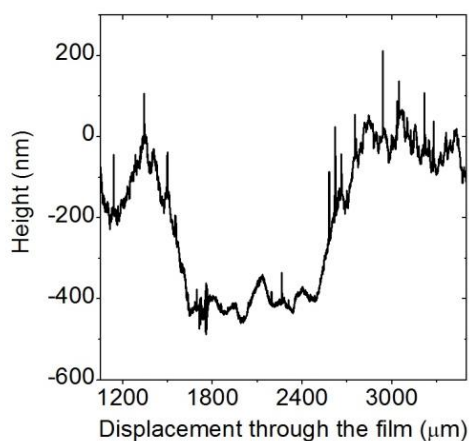

**Figure 1.7**. Thickness of Lap films measured by laser profilometry.

Taking into account that the adsorption procedure is from immersion of the Lap film into LDS 722 solutions, solvent-clay and solvent-dye can affect the extent of the adsorption [47]. To study the solvent effect on the adsorption of LDS 722 into Lap film, different H2O/EtOH mixture with volume fractions of 100/0, 80/20, 50/50, 20/80 and 0/100, were considered for the dye solutions. However, experimental observations show that the immersion of Lap films into LDS 722 solutions with a volume fraction higher than 50% in water leads to the unstuck of the Lap clay from the plate. This process is induced by the dye molecules in the medium, because solvents mixture (without dye) leads to a less appreciable flocculation of the clay particles of the film into the solution[13].

Figure 1.8 shows that maximum fluorescence efficiency of LDS 722/Lap films (determined from the ratio between the area under the emission band and the absorbance of the sample at the excitation wavelength, I_{flu}/A_{exc}) is obtained at a volume fraction of 0.5 in the mixture H_2O/EtOH (v/v %). The decrease of the water content in the mixture reduced the fluorescence efficiency of the dye for a common dye concentration and Lap film preparation. This result is likely attributed to a smaller swelling of the interlayer space for LDS 722 intercalation due to a less amount of water. Hence, for an optimal dye intercalation, the highest amount of water in the dye solution it is required in which the detachment of the clay layers do not take place. Thus, the best condition for LDS 722/Lap films is considered a H_2O/EtOH mixture of 50/50 % in volume.
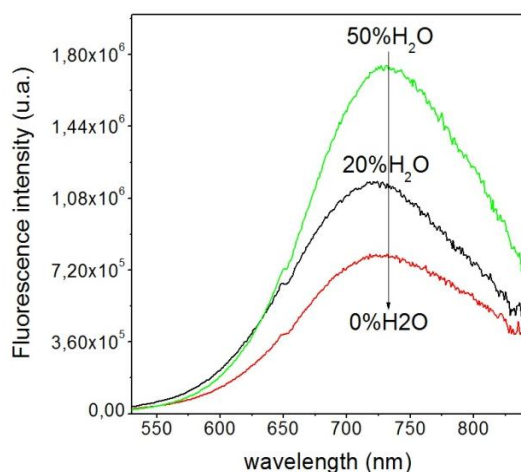

Figure 1.8. LDS 722/Lap Fluorescence efficiency at different water/ethanol fractions.

Then, different dye loadings were achieved by varying the immersion of the clay film into dye solutions of H_2O/EtOH mixture of 50/50 %. After the dye intercalation process, we considered the percentage of the cationic exchange capacity of the clay occupied by dye molecules (%CEC) as the most representative parameter. The final cationic exchange (%CEC) reached was characterized by elemental analysis in the films with high dye loading and for low -moderate loading samples, where the amount of the organic material is too low to be detected by elemental analysis, by photometrically reading, extrapolating a LDS 722/Lap sample with known loading of the dye. By increasing the immersion time of the clay film into a 10^{-5} M LDS 722 dye solution, a linear increase of the dye loading is observed. After 1 day, which corresponds to 23% CEC (Figure 1.9), the dye loading tends to asymptotic values due the chemical potential equilibration between the solution and the film. To achieve larger loadings, a greater concentration gradient was induced using more concentrated LDS 722 solution (10^{-4} M). The saturated state is reached for an immersion time of 5 h, with a maximum % CEC of 45 since longer immersion times and higher concentrated solutions did not increase the absorbance value.
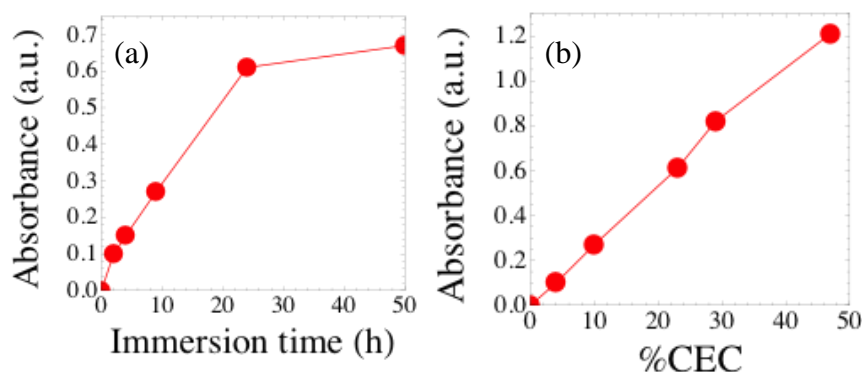
Figure 1.9. (a) Maximum absorbance of the material as a function of the immersion time in 10-5 M LDS 722 solution and (b) as a function of the cationic exchange percentage.

On the other hand, interactions between dye-clay and particularly with water molecules of the interlayer space of the clay (super acidic water) have also to be into account. In this sense, the interstitial water (super acidic water) can produce the LDS 722 protonation. For that, the interstitial water is quantified by the thermogravimetry technique.
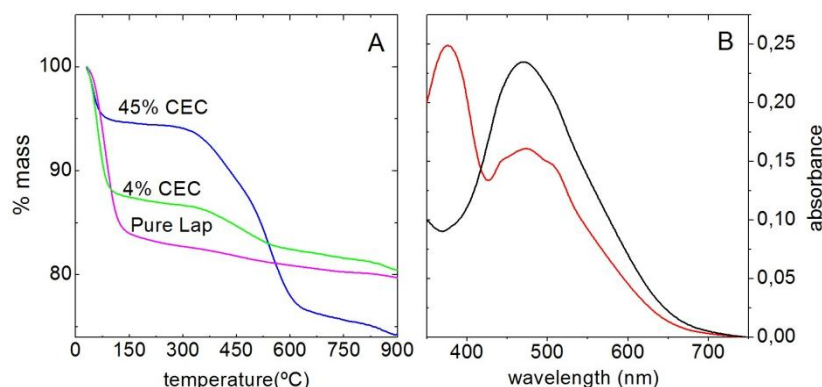
Figure 1.10. LDS 722/Lap films (A) TGA curves and (B) absorbance spectra

In Figure 1.10A, the mass decrease obtained between 30ºC and 140ºC is attributed to the interlaminar water desorption. The water amount in the interlayer space decreases as the LDS 722 dye loading increases, from 16% in the pure Lap film to a 12.5% for a dye content of 4 % CEC and up to 5% for a dye saturated dye film of 45% CEC. Note here that for this reason, the interlayer water effect is not very important for high dye loading but LDS 722/Lap films of ≤ 10% CEC has a great impact in the photophysical behaviour of the dye. Indeed, Figure 1.10 B shows the absorption spectrum of a LDS 722/Lap film of 4 %CEC before drying (red curve) and after drying (black curve). The well dried LDS/Lap thin film shows the typical absorption band of LDS 722 placed at 470 nm but for the wet film a new and more intense band centered at 375 nm in detriment of the main band is also obtained. This new blue-shifted band is a consequence of the protonation of the amine group of the dye reducing the delocalization of the lone par in the π-system. More importantly, the formation of the ICT state is hindered because of the decrease in donor character of the amine group once is protonated, reducing the emission efficiency of the dye. Indeed, the direct excitation of the protonated species gives rise to a new excited state that is not fluorescent. Thus, the LDS 722/Lap films is recommended to be previously dried (for 24h at 50ºC) to avoid as much as possible the protonation of the dye with worst optical properties respected to the un-protonated LDS 722 dye molecules.

One of the aims of the encapsulation into the 2D-space of the clays is the enhancement of the dye thermostability. In this sense TGA curves of pure LDS 722 dye and of a 722/Lap films 45 % CEC are compared.
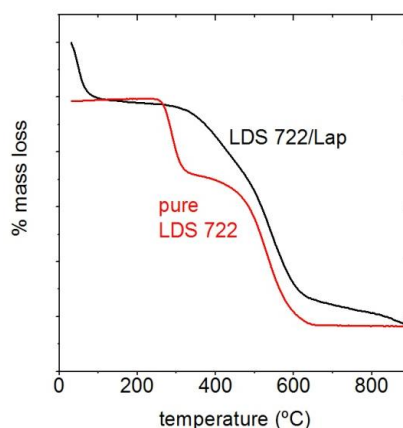
Figure 1.11. TGA curves of pure LDS 722 and 45 % CEC LDS 722/Lap films.

In Figure 1.11 shows the TGA curves were normalized at 140ºC (the temperature of the Lap films interlaminar water) for a better comparison. The TGA curves of the pure LDS 722 shows two clear degradation steps: 1) at 300ºC, attributed to the LDS 722 fragmentation and 2) at 530ºC assigned to the dye decomposition. However, in LDS 722/Lap film, the first weight loss up to 140 ºC, is due to the interlayer water loss (5%) as it was previously described, but more importantly the next loss registered is not as steep as for the pure dye and the degradation inside the clay take place in the range of 400-540ºC. Therefore, the thermostability of LDS 722 intercalated in the interlayer space of Lap films has increased up to 100ºC due to the clay protection.

On the other hand, the adsorption of LDS 722 dye in the interlayer space of the Lap films was characterized by XRD technique[13] and spectroscopically by absorption and fluorescence spectroscopies.

In XRD patters, the first peak in the diffractogram corresponds to d_{001}, which indicates the clay interlaminar space for different LDS 722 loadings. The 001 progressively shifts to lower 2θ values by increasing the dye loading, indicative of the swelling of the interlayer space of the clay by the presence of LDS molecules (Figure 1.12). At the same time, the peak becomes sharper and more intense with the dye loading indicating a more ordered arrangement of the films in the c-axis likely attributed to the greater packing of the dye molecules in the interlayer space improves the stacking of the clay layers.
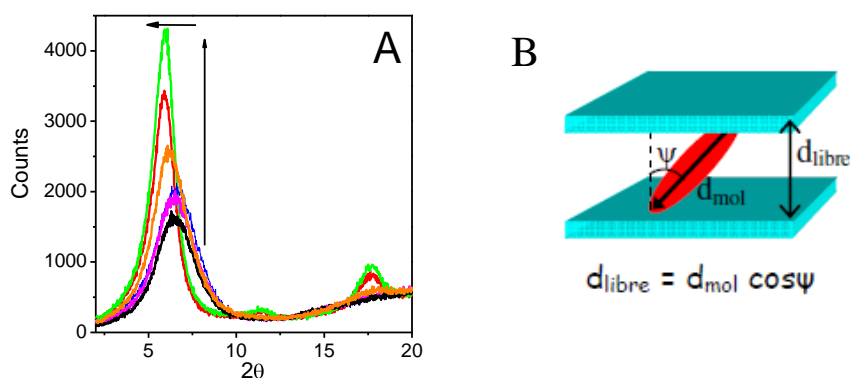
Figure 1.12. A) LDS 722/Lap films XRD spectra and B) scheme of the tilted angle of dye molecules.

Note here that the basal space obtained by XRD is an average value for all the interlayer distances, which is usually underestimated for films with low-moderate dye loadings because not all the interlayer spaces are equally swelled. However, for very high dye loading, the estimation of the orientation of dye molecules by the interlayer distance is usually more accurate. Indeed, at saturated dye conditions an increase of the interlayer space of 2.1 Å respect to the pure Lap, give rise a free distance between the clay layer of 5.4 Å (Table 1.3). Taking into account the dye dimension (4.9 x 18.6 x 2.5 Å) two different dye disposition can be supposed: a) with a angle respect to the normal to the clay that assuming that the interlayer space is given by the projection of the long-molecular axis of LDS 722 to the c-axis. In saturated film this tilted angle is estimated around 73º, denoting a relatively planar distribution of the LDS 722 molecules (see Figure 1.12B) a bilayer distribution of dye molecules with a totally planar disposition respect to the clay layers.

Indeed, the obtained theoretical calculations of different % CEC are completely in agreement with the experimental (Figure 1.13, Table 1.3) and predict the dye molecules distribution in a monolayer with a slight tilted angle respect to the normal to the clay film.

Nevertheless, a more detailed study on the orientation of dye molecules adsorbed in clay films at different loading will be described later by the anisotropic response to the linear polarized light.
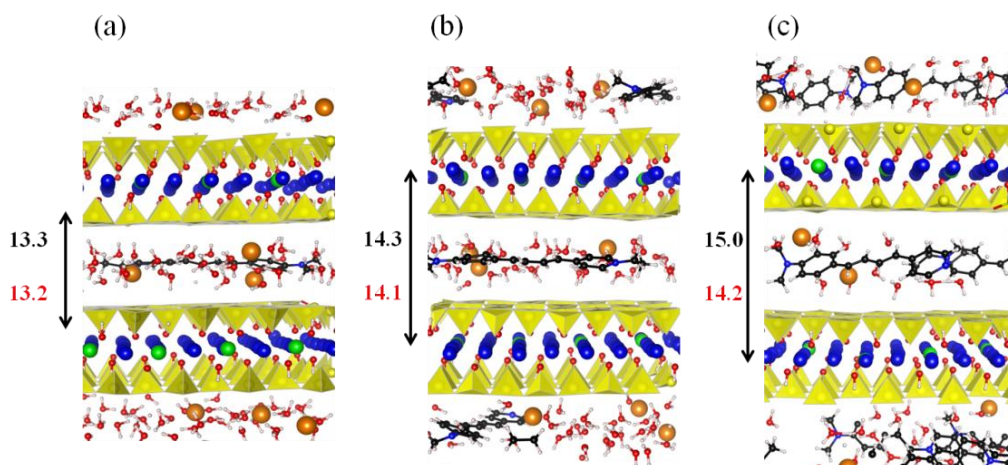
Figure 1.13. Snapshots from molecular dynamics simulation of LDS 722/Lap hybrid material at the simulated %CEC: (a) 4, (b) 23, and (c) 45%. The basal spaces (in angstroms) obtained from X-ray diffraction experiments and simulations are indicated in black and blue, respectively. The code color is the same as in Figure 1.1.

Table 1.3. Time: immersion time in hours ([1]into dye solution 10^{-5} M and [2]into dye solution 10^{-4} M), %CEC: reached cation exchange capacity; water content in % weight obtained by TG analysis; d001: interlayer distance in Å (exp: obtained by XRD and sim: by molecular dynamics simulations); ψ (º): theoretical tilted angle between the long molecular axis of the dye and the normal to the Lap Layer from XRD.

| time	%CEC	Water	d_{001} (Å)		
			exp	sim	ψ
0	0	16 %	12.9		
2h[1]	4	12.5 %	13.3	13.2	78.5
9h[1]	10	-	13.6	-	77.7
24h[1]	23	10 %	14.3	14.1	75.4
2h[2]	29	-	14.9	-	73.6
5h[2]	45	5 %	15.0	15.2	73.2

The LDS 722/Lap films photophysical properties are studied by absorption and fluorescence spectroscopies at different dye loadings. Indeed, optical applications usually require high dye density, conditions in which the dye properties usually become worse.

In this regard, the absorption spectra of the LDS 722/Lap films show a main band centred at 494 nm that is progressively more intense and blue shifted as the dye loading increases up to 475 nm for the saturated dye film of 45% CEC (Table 1.4 and Figure 1.14). The shift to higher energies could be originated by the torsion of the molecular structure due to the confinement, reducing the electronic delocalization of the system. However, molecular dynamics does not predict significant torsion of the dye, ruling it out as the origin of the emission shift. Another possible reason for the blue shift is the increasing of the hydrophobicity of the interlaminar space by the own presence of more dye molecules. In fact, previous studies for the dye LDS 722 in solvents of different polarities, showed a hypsochromic shift with decreasing polarity of the solvent (maximum at 499 nm in ethanol and at 493 nm in acetone and at 488 nm in dioxane)[48].

On the other hand, another possible reason for the blue shift is the interaction of the LDS 722 with water molecules confined in the interlayer space. In this sense, the interaction of water-dye is analyzed by the molecular dynamics trajectories (Figure 1.15).

Table 1.4. $\lambda ab(A)$: absorption wavelength (absorbance value); $\lambda fl(\%\phi)$: fluorescence wavelength (% fluorescence quantum yield); ψ (°): tilted angle between the long molecular axis of the dye and the normal to the Lap Layer. The photophysical data of LDS 722 in water/ethanol mixture is also included (%V/V).

| %CEC	λ_{ab} (A)	λ_{fl} (%ϕ)	Ψ (°)
4	494 (0.1)	685(6.4)	64
10	479 (0.27)	723 (1.3)	62
23	479 (0.61)	727(1.3)	61
29	479 (0.80)	733(0.5)	59
45	475 (1.23)	737 (0.3)	58
% V/V	λ_{ab}	λ_{fl} (%ϕ)	
0/100	446	711(1.2)	
50/50	487	713(8.0)	
100/0	499	714(14)	
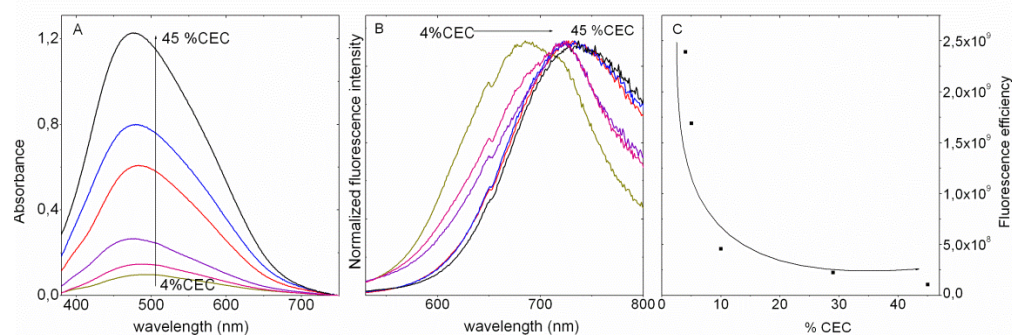
Figure 1.14. LDS 722/Lap (A) absorbance spectra, (B) Normalized fluorescence spectra under 470 nm excitation and (C) LDS 722/Lap films efficiency respect to the LDS 722 dye concentration.

In Figure 1.15 the radial distribution function of water molecules around nitrogen atoms of acceptor and donor positions are shown, taking into account the N-Ow and N-Hw distance or amine donor and pyridine acceptor groups, respectively. In that image, it can also see that the distance between water and nitrogen atoms decreases while the dye loading increases, namely when the water content is lower inside clay interlayer. Under these conditions, the probability of a water−dye interaction is higher because of the increasing difficulty of establishing water−water hydrogen bonds[49]. In Figure 1.15 can also help us to see better the water distribution around the nitrogen atoms. The blue isosurfaces represent the most probable process of water oxygen and hydrogen atoms around the amine and pyridine nitrogen atoms, respectively. At low dye concentration and at high water molecules in clay interlayer, the water molecules tend to self-associate because of the hydrophobic character of the organic dye molecules. As a result, the LDS 722 solvation increases especially on the donor groups when water content is limited producing the absorption band hysochromic shifted.

This results indicates that the donor amine group can establish hydrogen bonds with water molecules particularly at high dye loading, that on the one hand stabilizing the ground state and increasing the HOMO-LUMO energy gap[23] and on the other hand, this higher water−dye interaction can be partial protonation of the amine nitrogen, reducing the resonance with the π-system[50], responsible of the blue-shifted in the absorption spectra.
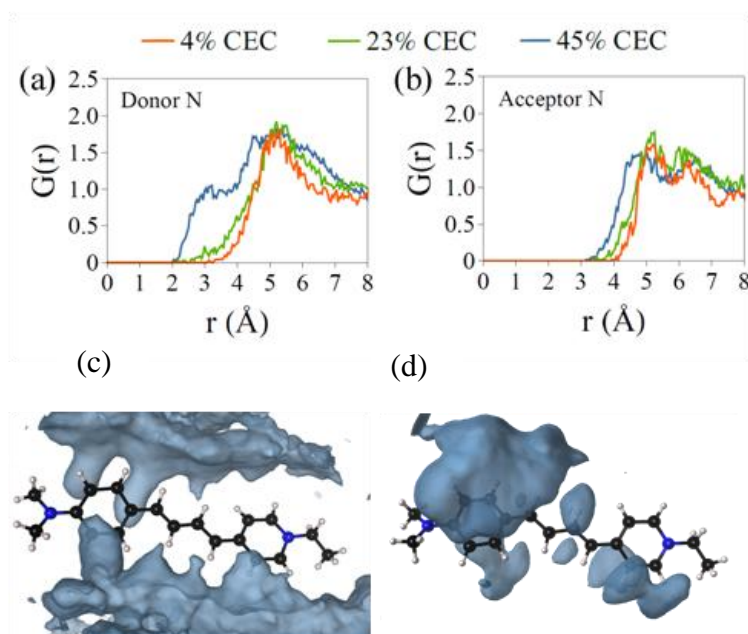
Figure 1.15. Radial distribution function of N-Ow and N-Hw distances for the (a) amine donor and (b) pyridine acceptor groups, respectively, at different dye loadings. Spatial distribution functions of the same atomic pairs (c) 4% CEC and (d) 45% CEC.

Conversely, a bathochromic shift is observed in the fluorescence band as dye loading increase together with a decrease on the, the fluorescence efficiency. One can think that a plausive cause could be the reabsorption and reemission phenomena. However, in this dye should be considered negligible due to the very large stokes shift ≤ 5000 cm^{-1} as consequences of the intramolecular charge-transfer mechanism from the donor (amine) to acceptor (pyridine) groups, responsible of the emission. Other alternative to explain this tendency with the dye loading could be that the emissive could be a switching from an intramolecular to intermolecular charge-transfer as responsible species of the emission owing to the proximity between two LDS 722 molecules when the dye concentration is high. In this sense, molecular dynamics simulations is applied in order to determinate the distance between two dye molecules, According to the LDS 722 molecular dimensions, the distance at which the intramolecular mechanism take place, that is between the amine (donor) and pyridine (acceptor) groups, is 14 Å which is constant at any loading while the dye maintains its planar structure. However, the distance between neighbour dye molecules decrease

from 18 Å to 5 Å as the dye %CEC is increased. Such small distances, considerably lower than the intramolecular one, can increase the probability of intermolecular charge transfer, originating the red-shift in the emission In addition, the decrease of the fluorescence quantum yield with the CEC is also a consequence to an intermolecular charge transfer, as these processes are usually less emissive than intramolecular ones[51].

Note here that the fluorescence efficiency of the LDS 722/Lap films at low dye loading is similar to fluorescence efficiency than LDS 722 in solution, which are quite poor (Table 1.4). Indeed, although an increase in the emission capacity of LDS 722 was expected by the rigidity impose by the clay to the dye[45,48,52], molecular similations indicated that the interlayer space of the clay is not such a rigid environment and does not restrict the dye internal motions.
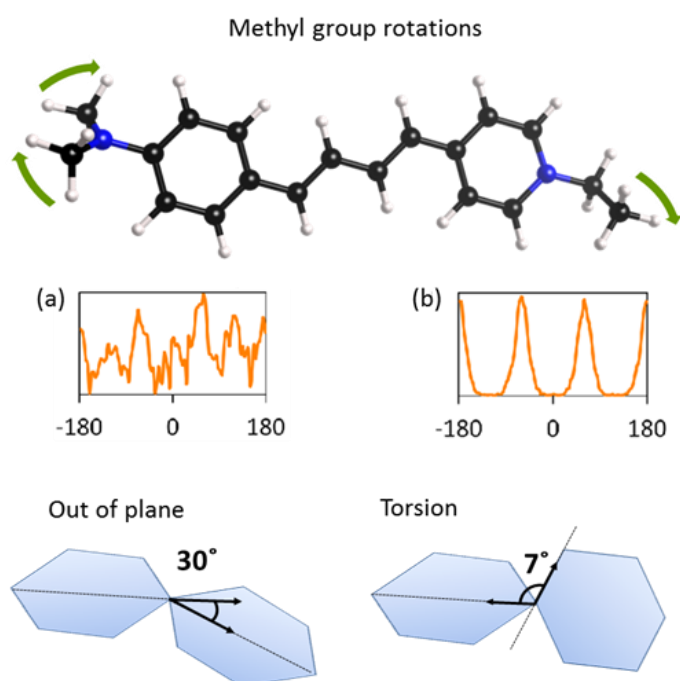
Figure 1.16. Molecular rotation and torsion in LDS 722 (A, B) Most probable angles of rotation around the amine methyl groups and pyridine ethyl group, respectively (indicated with green arrow in the molecular representation). Schematic representation of the dye out of the plane and torsion movements, with the maximum angle values at the 45% CEC. The hexagons represent the aromatic rings on each side of the LDS 722.

Thus, for more accurate information about the confinement of LDS 722 molecules, the molecular twisting and the methyl rotations were computed, see Figure 1.16. The rotation of the methyl groups in both extremes of the dye is not hindered by the confinement into the interlayer space of the clay film. As shown in Figure 1.16, the hydrogen atoms can complete full rotations around the carbon atoms. The hydrogen atoms in the ethyl group (right side, acceptor) have very well define positions in the staggered conformation, while the hydrogen atoms in the methyl groups (left side, donor) present less defined because their movement is coupled. In vacuum, the characteristic rotational times (τ), defined as the necessary time to achieve a full rotation, are 39.2 ps and 76.6 ps for the hydrogen atoms at the donor and acceptor extremes. While τ increases with the confinement up to 83.2 and 97 ps at the highest dye loading, the rotations are still considerably faster than the excited state lifetime and therefore can be responsible of non-radiant deactivation processes. The out of plane bending and the torsion angles deviate only +/- 30 degrees and +/- 7 degrees from planarity respectively, values similar under confinement and isolated in vacuum.

Finally, by the anisotropic response of the LDS 722/Lap supported films to the linear polarized light, the preferential orientation of the dye molecules is evaluated at different dye loadings. Figure 1.17 shows the evolution of the absorption band for X-polarized light at different twisting angles (δ), from 0 to 80°. From the linear correlation of the dichroic ratio, $D_{X,Y}$ against the $\sin^2 2\delta$ value at a certain wavelength, the tilted angle ψ (angle between the transition moment which is along the long-molecular axis of the dye molecule and the normal to the clay layers is analyzed. According to equation 1 of experimental section (chapter 4) ψ corresponds to an angle of around 60° in all samples, indicating a relatively planar distribution respect to the plane of the clay. This orientation is in concordance with the small increase registered in the interlayer space by XRD, and also obtained by the molecular dynamics.
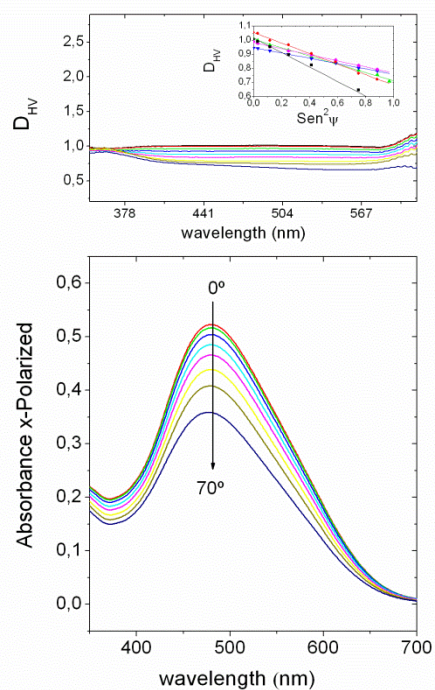
Figure 1.17. Evolution of X-polarized absorption spectra (bottom) and dichroic ratio (top) of 45%CEC LDS 722/lap film for different orientations of the sample with respect to the incident beam. The linear relation between the dichroic ratio with the twisted δ angle at the absorption maximum is inset.

1.2.1.1. Conclusion

The LDS 722 dye was successfully incorporated into the interlayer space of Lap at different loading by immersion of the pure clay films into adequate dye solutions varying the immersion time. In this regards, a novel hybrid dye-clay systems based on the intercalation of LDS 722 into the interlayer space of Laponite clay films is easily elaborated. Due to the synergy between the guest dye and the host clay, the thermostability of the dye inside the clay was improved around 100ºC respect to the pure dye. Secondly, a preferential orientation of the dye molecules respect to the normal to the clay films is achieved, which would be interesting for the development of films with non-linear optical properties. However, the fluorescence efficiency of the dye has not been improved respect to that in solution since the swelling capacity of the clay does not impose a rigid environment to restrict the molecular motions, responsible of the deactivation of the emissive ICT state. As far as we know, this is the first study performed by molecular simulations on the rigidity of the interlayer space of the clay environment. On the other hand, the water molecules present in the interlayer space play also an important role in the photophysics of the dye. In this sense, the films should be properly dried to avoid the protonation of the dye, which also reduce the emission capacity. On the other hand, the blue-shift of the absorption spectra with the dye loading was attributed to the stabilization of the ground state structure by hydrogen bonds between the donor aniline group of the dye and water molecules as the dye load increases. Conversely, the dye suffers a bathochromic shift in emission, which is assigned to a switch from an intramolecular to intermolecular charge transfer process as the dye load increases. As a result, the Stokes shift of the material can be easily tuned by adjusting the CEC during the preparation. Finally, by the anisotropic response of the dye/Lap films to the linear polarized light, the preferential orientation of the dye molecules is evaluated. They are disposed with a tilted angle of 60° between their transition dipole moment and the normal direction to the clay sheets. This angle is almost independent to the dye load.

1.2.2. Laponite/Py-Y and Saponite/Py/Y Thin Films

In this second dye/clay hybrid system, the dye used, Pyronine Y, is a rigid molecular structure but with a high tendency to self-aggregate, process which also considerably reduces the emission efficiency of the dye, as previously described. For this reason, in this section two different clays, Laponite and Saponite, are employed to study the effect of the different charge density and mainly charge distribution (tetrahedral or octahedral) on the aggregation process of Pyronin Y (PY) laser dye intercalated at different dye loadings[53,54]. Particularly, in this section, the type and extent of the aggregation of PY intercalated into two different smectite clay films is deeply analyzed. Thus, by means of evolution of the absorption spectra of PY/clay films with the dye loading, the association constant and the spectra of the dimer are calculated at moderate dye concentrations. The experimental results are confirmed theoretically by modelling the distribution of the dye into the interlayer space of the clays. On the other hand, the photoluminescence of the PY/clay films as the concentration increase is also studied by steady state fluorescent spectroscopy. With the aim of minimizing the molecular aggregation of PY dye into the interlayer space of the clay film and consequently increasing the fluorescence efficiency of the system, a surfactant, dodecyltrimethylammonium bromide (CTAB), is co-intercalated at an appropriate concentration together with the dye.

In the same way that the former hybrid system, the clay films were elaborated by spin-coating and the interaction of the dye was performed by immersion of the pure clay films into adequate dye solutions varying the immersion time. The thickness of the supported clay thin-films elaborated by spin-coating technique was checked by Laser profilometry.
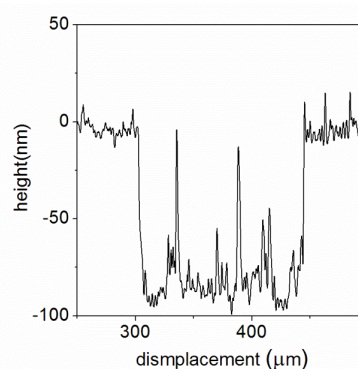
Figure 1.18. Thickness measured by laser profilometry of Sap (B) film.

For the case of Saponite films, the thickness of ~ 100 nm (Figure 1.18) was smaller than in Lap films of around ~ 400 nm, previously described (Figure 1.7). The reason is that Lap clay gives rise to a very stable and viscous aqueous suspensions as a consequence of its small particle size (~25 nm) respect to Saponite ($\leq$ 200 nm). Nevertheless, the thickness of the Sap films is thick enough to allow a proper photophysical characterization of the adsorbed dye into these films[13].

By increasing the immersion time of the pure clay films into PY dye solution of 10^{-5} M from few minutes to days, an increase in the % CEC from 0.5 % to 10 % is reached in Lap films (5 min - 8h) and from 0.9 to 20% in Sap films (15 min-49h) (Table 1.5). Longer immersion times into 10^{-5} M PY solution do not produce significant increase in the % CEC (Figure 1.19) due to the equilibrium concentration is established between the films and the dye solution. To reach further increase in the % CEC, the clay films were immersed in a more concentrated dye solution (10^{-4} M) varying the time from hours to days, up to reach dye saturated films with similar % CEC values of 27% and 32 % for Lap and Sap films, respectively (Table 1.5).
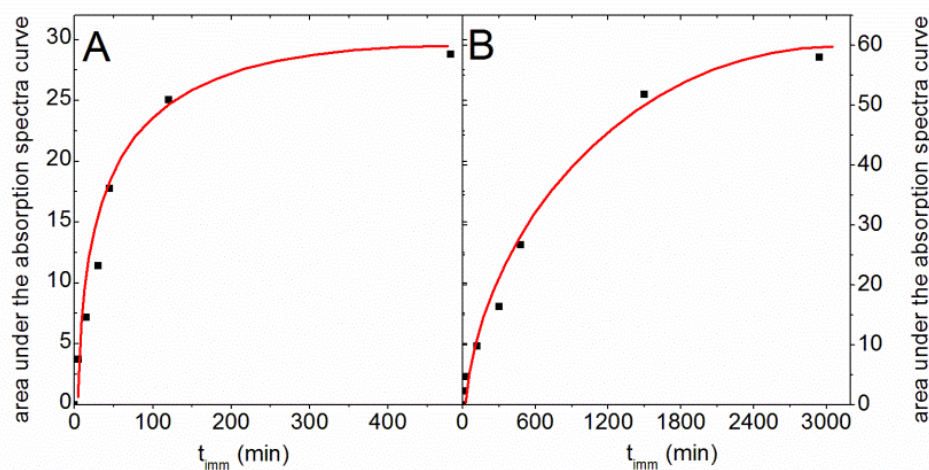

Figure 1.19. Dye loading in the interlayer space estimated by the area under the absorption spectra as a function of the immersion time into 10-5 M PY solution in Lap (A) and Sap (B) films.

Table 1.5. Data of PY/Sap and PY/Lap films with different dye loadings: time (inmmersion time of clay films into PY solution; λ_{abs} (absorption wavelength); λ_{flu} (fluorescence wavelength); E_{flu} fluorescence efficiency determined from the area under the emission curve and the absorbance of the sample at the excitation wavelength), ψ (tilted angle between the long molecular axis of PY dye and the normal to the clay layer obtained from absorption with polarized light), d_{001} (Interlayer space distances of PY clay films obtained by X-ray diffraction technique).

% CEC	Time	λ_{abs} (nm)	λ_{flu} (nm)	E_{flu}	ψ	d_{001} (DRX)
0.5 Lap	5min	547	563	1.05×10^9	-	12.90
1.1 Lap	15min	541	565	6.6×10^8	-	-
0.9 Sap	15min	554	563	1.7×10^9	-	12.50
1.8 Lap	30min	547/471	566	5.25×10^7	63	-
2.5 Lap	45min	544/473	566	2.6×10^7	62	13.40
1.7 Sap	30min	554	564	9.1×10^8	62	12.50
2.4Lap +Surfc	45min	553	568	9.98×10^8	62	13.81
3.8 Lap	2h	541/471	568	1.15×10^7	-	-
3.7 Sap		555	566	3.9×10^8	-	-
4.5 Lap	5h	536/468	566/672	3.8×10^6	61.5	14.80
6.6 Sap		557	570	1.8×10^8	61.5	12.50
10.2 Lap	8h	473	682	1.26×10^6	62	15.24
10.0 Sap	8h	557	572	1.2×10^8	61	12.50
9.3 Lap +Surfc	8h	541/474	572/665	3.8×10^8	61	15.51
20 Sap	16h	558	574/614/670	8.2×10^8	61	12.60
15 Lap	2h*	489	685	1.16×10^6	59	15.64
22 Sap	49h	560/516	574/616/675	1.8×10^7	60	13.0
27 Lap	24h*	492	687	19.5×10^5	58	15.78
31-32 Sap	2-24h*	508	575/628/678	2.4×10^6	58	13.4-15.8

According to the XRD patters, as the dye loading increase the 001 peak of the clay films shifts to shorter 2θ values (Figure 1.20), indicative of the swelling of the interlayer space of the clay by the presence of PY molecules. However, there are significant differences in the evolution of 001 peak with the dye loading between both clays. In the case of Lap, the interlayer space increase more gradually and is more pronounced at moderate dye loading (≤ 20% CEC) than in Sap films (Table 1.5). This result could be attributed: 1) to the localization of the net negative charge of the clays, i.e. the isomorphous substitution at external surface (Tetrahedral layer) in Sap clay can reduce its swelling capacity respect to the Lap sited at the internal octahedral sheets, as other authors has described[55,56]; but also 2) to the different molecular association (aggregates), distribution and orientation adopted by dye molecules in the interlayer space of each clay.
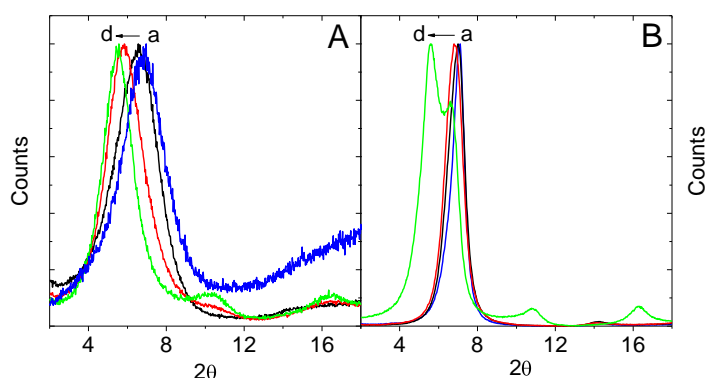
Figure 1.20. Normalized X-ray diffractions of PY at different dye loadings (in %CEC): (A) Laponite; pure Lap (a), 2.5 %CEC (b), 10.2 %CEC (c), 27 %CEC (d) and (B) Saponite; pure Sap (a), 1.8 %CEC (b), 20 %CEC (c), 32 %CEC (d)

According to previous studies [41], the progressive increase of the interlayer distance could denote a more perpendicular orientation of the PY molecules respect to the clay surface as the dye content increased. The estimation of the orientation of dye molecules by the interlayer distance is applied at dye saturated clay films. Indeed, both films show a similar increase of the interlayer spaces of around 15.8 Å (Table 1.5 and Figure 1.20) at that condition. Thus, assuming that this distance is given by the projection of the long-molecular axis of PY (13.2Å) to the c-axis, the tilted angle obtained between the long-molecular axis and the normal to the surface for dye

saturated films of both clays is around 62º, denoting a relatively planar distribution of the PY molecules. Nevertheless, a more detailed study on the orientation of dye molecules adsorbed in clay films at different loading will be described later in this work by means of UV-Vis absorption spectroscopy with linear polarized light.

On the other hand, it is important to note also here that in the difractogram of the saturated Sap film (32 % CEC) also show another overlapped peak placed at higher angles (Figure 1.20B), indicative of a inhomogeneous covering of the interlayer space by dye cations, likely assigned to the lower swellability and more restricted space in Sap clay, above mentioned.

Regarding the photophysical properties of the dye in both clay films, the increase of PY loading not only produces an intensification of the global colour of the films but also modifies the shape of the absorption spectra (Figure 1.22). These changes mainly consist in the replacement of the main absorption band by other absorption bands placed at lower wavelength, known as metachromatic effect and it is ascribed to the aggregation of the dye [32].

However, the changes in the absorption spectra with the PY dye loading are drastically different depending of the clay type. For instance, in PY/Lap films very abrupt changes are registered even at very low dye content (≤ 4.5 %CEC), Indeed, a narrow absorption band placed at 547 nm, similar to that recorded in diluted aqueous solution (Figure 1.21) and assigned to the monomer of PY into the interlayer space of Lap films, is only registered for most diluted PY/Lap films (0.5 % CEC).
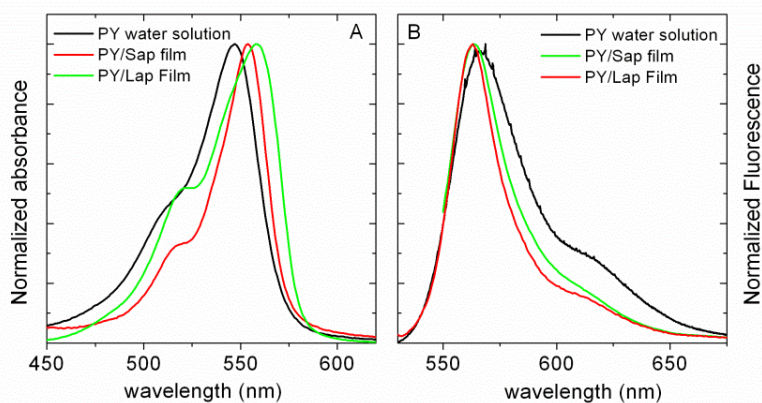
Figure 1.21. (A) Absorbance spectra and (B) Fluorescence spectra of PyY in different media PyY in water solution.

However, as the dye loading increase the relative intensity of the main absorbance band significantly decrease and new band centered at around 470 nm becomes already apparent at 1.1% CEC. The appearance of new absorption band at higher energies in detriment of the monomer band would correspond to the absorption of the H-band of a sandwich-like aggregate, likely a dimer at such low dye coverage. Actually, at 4.5 % CEC of PY into Lap films, the more energetic band is already more intense than the absorption band assigned to the PY monomer. These results obtained for quite low dye content in Lap films ($<$ 5%) indicates a very high molecular aggregation process of PY dye into Lap films. In fact, for dye loading % CEC $>$ 10 %, reached by the immersion of Lap film into more concentrated dye solution (10^{-4} M), the absorption band of the monomer practically disappears and only a band centered at around 470 nm is recorded.
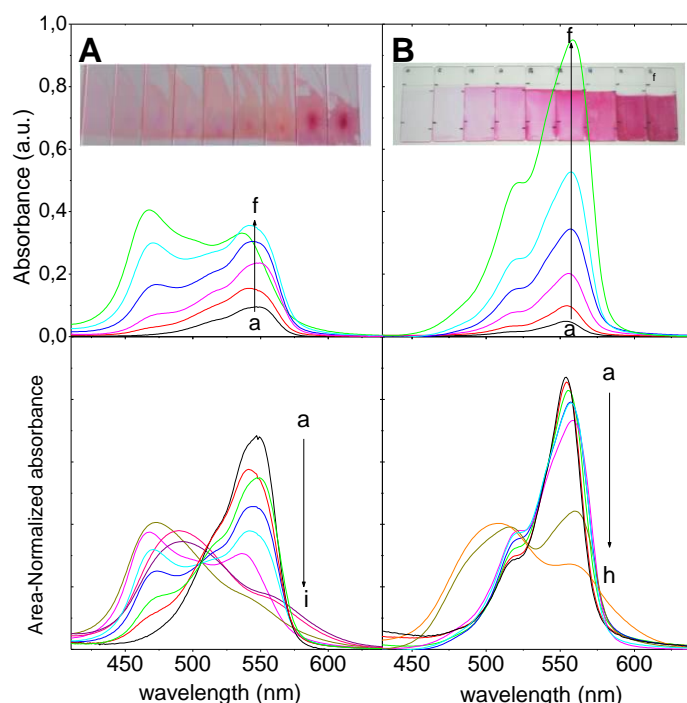
Figure 1.22. (top) Absorption spectra of PY (in %CEC) and (bottom) area-normalized absorption spectra of PY (in %CEC) into **A)** Laponite at: 0.5 %CEC (a), 1.1 %CEC (b), 1.8 %CEC (c), 2.5 %CEC (d), 3.8 %CEC (e), 4.5%CEC (f), 10.2 %CEC (g), 15 %CEC (h), 27 %CEC (i) and into **B)** Saponite at 0.9 %CEC (a), 1.7 %CEC (b), 3.7 %CEC (c), 6.6 %CEC (d), 10 %CEC (e), 20%CEC (f), 22 %CEC (g), 31 %CEC (h) (Inset picture of the respective dye/clay films)

Conversely, very slight changes are registered in the absorption spectra for PY into Sap films with the dye loading up to 20% CEC (Figure 1.22), indicating a much lower aggregation tendency of PY dye into Sap. First note that the absorption band registered in the most diluted PY/Sap film (0.9 % CEC), assigned to the PY monomer absorbed in the interlayer space of Sap films is even narrower than that obtained in aqueous solutions (Figure 1.21). In addition, the absorption band of de PY monomer into Sap, placed at 554 nm, is red-shifted respect to PY in solution (547 nm), possibly as a consequence of higher dye-clay interactions in the interlayer space of Sap respect to Lap. As the dye loading increase up to $\leq$ 20% CEC, the main absorption band slightly shifts to lower energies and the shoulder at higher energies at around 520 nm slightly increases with respect to the main absorption band (Figure 1.22). These slight changes indicate the formation of molecular aggregates, probably dimers, but in much less extent than in Lap films at similar dye concentrations. However, much evident changes are also registered for CEC > 20 % (Figure 1.22) in PY/Sap films, *i.e.* absorption spectra is much wider and the adsorption band at higher energies becomes more important than the monomer band, similar tendency to that recorded in PY/Lap films at % CEC $\geq$10 %, indicative of the formation of high-order aggregates.

To get further information about the extent and type of PY aggregates in the different clay films, the dimerization constant, K_D, and the dimer absorption spectrum, $\varepsilon_D(\lambda)$, is calculated from the evolution of the concentration-normalized absorption spectra at moderated PY/clay films ($\leq$ 20% CEC) with the concentration factor, by means of a non-linear least square fitting equation obtained from the mass-law, described elsewhere[57]. The fit proposes those K_D and $\varepsilon_D(\lambda)$, values that minimize the reduced chi-square between the experimental and the fitted data.

Figure 1.23 shows the fit curve obtained for the PY/Lap and PY/Sap films in moderate dye loadings at the two most representative wavelengths: the main absorption band of the monomer (545 nm and 555 nm for PY/Lap and PY/Sap films, respectively); and at the absorption wavelength of the new hypochromic band as the dye loading increase (470 nm and 522 nm for PY/Lap and PY/Sap films, respectively). The fit was realized as a global analysis at the two wavelengths where K_D is an adjustable parameter but linked to be a common value to the two analysis wavelengths. All fits supply analogous values with correlation coefficients (r) close to unity, suggesting the viability of the mathematical procedure.
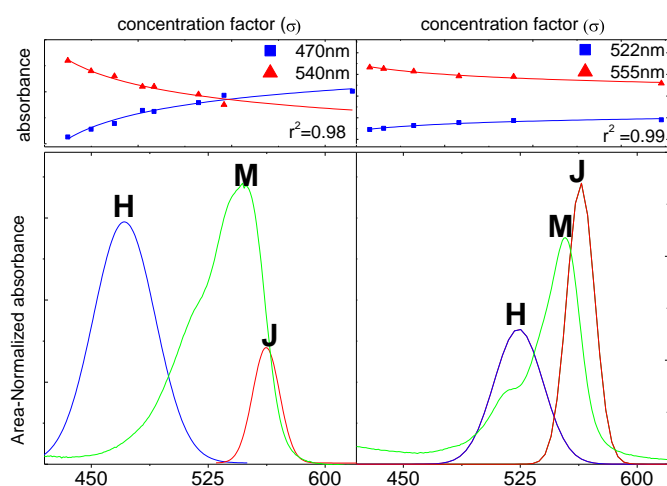
Figure 1.23. The monomer absorption spectra and the deconvoluted absorption bands of the dimer spectra calculated from the on-linear least square fitting process (the nonlinear curve fit in each clay system at the two representative wavelengths is included).

The global analysis provides a K_D value of 0.025 for PY/Lap film (standard concentration, $c^o \equiv 0.5\%$ CEC) and K_D value of 0.015 for PY/Sap films (standard concentration, $c^o \equiv 0.9\%$ CEC) for moderate PY loading samples ($\leq 10.2\%$ CEC for PY/Lap and $\leq 20\%$CEC for PY/Sap films). This result clearly confirms the higher aggregation tendency of the PY molecules absorbed into the Lap films respect to the Sap films.

Once determined the K_D, the dimer spectra can be calculated for each system. In both clays, these spectra consist of two absorption bands placed at both sides of the monomer absorption band (Figure 1.23). However, there are important differences in the dimer spectra of PY into both clays: the H-band in PY/Lap films, placed at 471 nm, is more intense with an area under the curve around 5 times higher than that obtained for the red shifted J-band, centered at 562 nm. In contrast, the J-band placed at 564 nm obtained in PY/Sap films is slightly more intense with an area under the curve around 1.2 times higher than the H-band centered at 522 nm. According to the Exciton Theory, the geometry of the PY dimer is consistent with the twisted sandwich type (case A in Figure 1.6) in PY/Lap films and with an oblique head-to-tail type (case B, in Figure 1.6) in PY/Sap films.
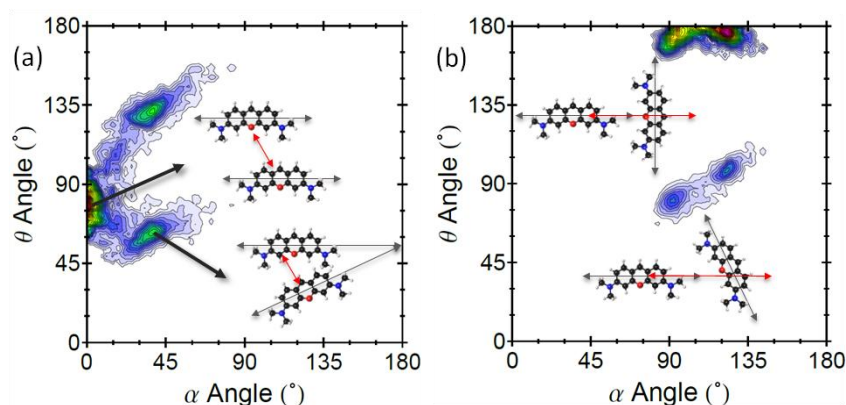
Figure 1.24. Angle α and θ combined distribution function of dimer species in (a) Laponite and (b) Saponite. The angles α and θ, defined by the Exciton theory[58] as: angle θ by the transition dipole moment vector of one PY molecule and a vector between the center of mass of two PY molecules; and the angle α was formed by the transition dipole moment vectors of two PY molecules.

Indeed, those evidences are supported by theoretical calculations. Molecular dynamics simulations have confirmed the existence of PY dimers in both clays by means of the study of the relative distribution of the dyes in their interlaminar spaces (Figure 1.24). Thereby, in PY/Sap films at high dye loading the highest probability of finding dimers is at $\theta = 0°$ and $\alpha \neq 0°$, corresponding to oblique head-to-tail dimers. On the other hand, the main geometry of dimers in PY/Lap is related to twisted sandwich type, with $\theta = 90°$ and $\alpha = 0°$.

The differences found in the extent and type of the aggregation of PY dye could be attributed to the negative charge location in the Lap vs Sap clay although other factors such the differences on their CEC and particle size cannot be discarded. The net negative charge at the external T-sheet in Sap films allows stronger electrostatic clay/dye interactions than in Lap clay with an internal distribution of the negative charge in its O layer. Accordingly, dye/dye interactions are more favored in Lap films promoting high extent in the molecular aggregation in sandwich like because since this configuration maximizes the surface contact area between the dye molecules which also counteract the intrinsic hydrophilic environment of the interlayer space of the clays. Another plausible explanation would be referred to the interlaminar water distribution which could influence dye aggregation. That is, the water bilayer distribution founded in the interlayer space of laponite clay (Figure 1.25) may lead to

dye aggregation to minimize the solvation due to the intrinsic hydrophobic character of the organic molecule avoiding to be surrounded by water molecules. Contrary, in a water monolayer distribution, as in saponite, the water-dye interactions are less important, and the chemical driving force for aggregation is lower.
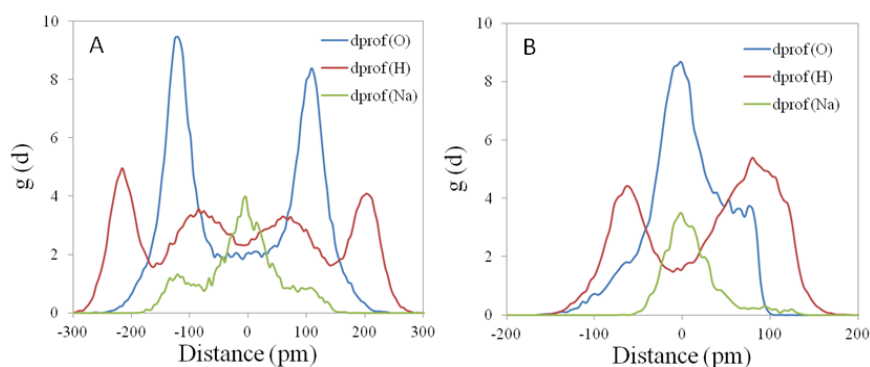
Figure 1.25. Density profile of O atoms (blue), H atoms (red) and Na cations (green) of (A) PY/Lap films and (B) PY/Sap films.

The dye aggregation tendency of PY in clay films was clearly confirmed by fluorescence spectra (steady-state). Since the fluorescence intensity of a sample depends on others factors, on the excited molecules, in order to compare the fluorescence efficiency of PY in each clay, is analysed the ratio between the fluorescence intensity (determined from the area under the curve) and the absorbance of the sample at the excitation wavelength, I_{flu}/A_{exc} (Figure 1.26). Note first the drastic drop of the fluorescent capacity observed in PY/Lap at even very low dye concentration (Figure 1.26A), *i.e.* the emission efficiency of a PY/Lap film of 3.8 % CEC decreases around 90 times respect to the most diluted PY/Lap film of 0.5 % CEC (Table 1.5). The loss is even more prominent at moderate dye loading with a decrease of 830 times for a PY/Lap film of 10% CEC, as a consequence of a mayor contribution of H-type aggregates. Indeed, the emission spectra of PY/Lap films recorded for low-moderate dye loading (< 10% CEC) do not show any new bands (Figure 1.26A) but the narrow emission bands similar to the spectra of the PY in diluted aqueous solution (Figure 1.21), assigned to the PY monomer emission band into Lap films. This band gradually shifts to the red as the dye loading increase (from 563 nm up to ~ 574 nm, Table 1.5) likely attributed to reabsorption-reemission phenomena, typical effect in optically dense materials.

Conversely, the loss in the fluorescence for PY/Sap films as the dye loading increase is much less prominent for such moderate dye loadings, *i.e.* a decrease of around 4 times for a PY/Sap film of 3.7 % CEC and around 14 times for a PY/Sap film of 10% CEC, with respect to the most diluted PY/Sap film of 0.9 % CEC (Table 1.5, Figure 1.26B). Note also here that in PY/Sap films at moderated concentration ($\leq$ 20% CEC) new fluorescence shoulders at around 620 and 675 nm (Figure 1.26B) are weakly manifested likely attributed to the fluorescence bands of J-aggregates. Those new red-shifted bands become evident at $\geq$ 22% CEC in Sap films (Figure 1.26B inset). In fact, PY show similar reminiscent red-shifted emission in both clays at such saturated dye conditions, *i.e.* centered at $\sim$ 675 nm in Sap for loading > 20% CEC and at ~685 nm in Lap for $\geq$ 10 % CEC, which could be attributed to the emission of J-bands of high-ordered aggregates.
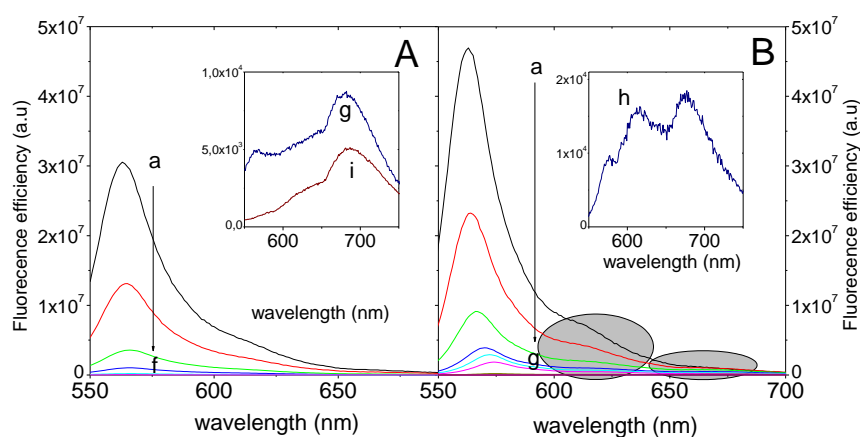
Figure 1.26. Fluorescence efficiency of PY films with different dye loadings (in %CEC): (A) PY/Lap films 0.5 %CEC (a), 1.1 %CEC (b), 1.8 %CEC (c), 2.5 %CEC (d), 3.8 %CEC (e), 4.5%CEC (f), 10.2 %CEC (g), 15 %CEC (h), 27 %CEC (i) and (**B**) PY/Sap films0.9 %CEC (a), 1.7 %CEC (b), 3.7 %CEC (c), 6.6 %CEC (d), 10 %CEC (e), 20%CEC (f), 22 %CEC (g), 31 %CEC (h).

Furthermore, it is also well documented that the co-intercalation of surfactant molecules in the interlayer space of the clays can reduce the dye molecular aggregation and/or change their state, *i.e.* from the undesirable H-aggregates to potential fluorescent J-aggregates [59–61] since the co-adsorption of surfactant can counteract the hydrophilic environment of the interlayer space of the clays [60,62]. With the aim of minimizing the molecular aggregation of PY dye into the interlayer space

of the clay film and consequently increasing the fluorescence efficiency of the system, alkylammonium ions (CTAB) are co-intercalated at an optimized concentration.

For that propose two representative PY/Lap films with a dye loading of 2.5 % and 10.2 % CEC are chosen to study the effect of the co-adsorption of surfactant molecules. Thus, the surfactant is intercalated by the immersion of Lap film into the CTAB solution previously to the dye intercalation process. Several experiments with different amounts of surfactant adsorbed (by varying the immersion time and concentration of CTAB solution) have been carried out with the aim of optimized the photophysical properties in such PY/Lap films. Then, the dried surfactant/Lap films were immersed into 10^{-5} M PY solution at the corresponding immersion times, 45 min and 8 h, for the Lap films with PY loading of 2.5 %CEC and 10.2 %CEC, respectively. The final amount of PY dye intercalated was estimated photometrically by the area under the resultant absorption curve.
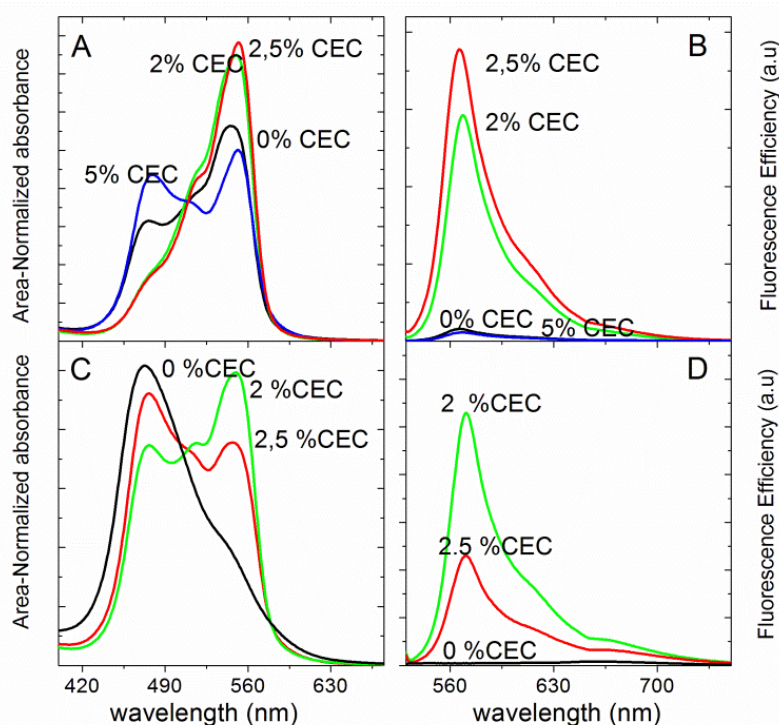
Figure 1.27. (A, C) Absorbance spectra and (B, D) fluorescence efficiency of PY/Lap films of (top) 2.5% and (bottom) 9.3% CEC dye loading with surfactant previously adsorbed in Lap thin film.

In fact, the presence of the surfactant in the interlayer space does not practically modify the total amount of the dye adsorbed with respect to the PY/Lap films without surfactant, reaching similar % CEC of 2.4 % and 9.3% for the same immersion times, respectively (Table 1.5). However, important changes in the shape absorption spectra are registered in both samples (Figure 1.27). In the PY/Lap film of 2.4 % CEC, the absorption band centered at higher energies, around 470 nm, previously assigned to H-band of aggregates, practically disappears and the monomer band is only recorded at around 550 nm for a surfactant concentration between 2-2.5 %CEC, previously intercalated. This fact indicates that an important dye disaggregation process take place in presence of an appropriate amount of surfactant. Note here that CEC > 2.5 % of surfactant incorporated into Lap films (*i.e.* 5 % CEC) leads to a higher molecular aggregation (Figure 1.27A) whereas CEC < 2 % does not practically modifies the aggregation state of PY into Lap films (data not-shown). Likewise, very significant disaggregation process can be also reached for the sample with 9.2% CEC of dye by the presence of the surfactant in the interlayer space. The only absorption band at around 470 nm previously recorded for 10.2 % CEC PY/Lap film without surfactant and ascribed to H-aggregates, is significantly decreased in detriment of the PY monomer band at 547 nm in the homologous PY/Lap film of 9.2% CEC with a surfactant loading between 2-2.5 CEC% (Figure 1.27B). Indeed, the monomer band is registered as the main absorption band at a surfactant concentration of 2% CEC, indicating that higher molecular disaggregation has been reached with respect to 2.5% CEC. Although seems that the optimized surfactant concentration is in a very narrow range (2-2.5 % CEC), it can be easily controlled by the immersion of pure Lap films into diluted CTAB solution of 10^{-6} M and varying the immersion times between 2h and 6h, for 2% and 2.5 % of CEC respectively.

Indeed, although results could be reached carrying out the intercalation of the surfactant and dye simultaneously, by immersion of pure Lap films into PY/CTAB solutions of different concentration ratio (Figure 1.28), it is very difficult the control of the optimal amount of surfactant with this methodology and is not recommended.
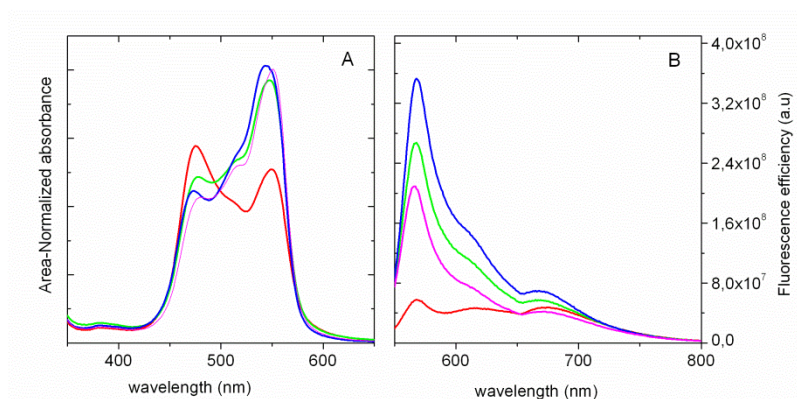
Figure 1.28. (A) Absorbance spectra (B) fluorescence efficiency spectra of Lap films with PY and surfactant intercalating simultaneously: varying the relative dye/surfactant concentration: 1:0 (blue), 1:1 (red), 5:1 (green) and 15:1 (pink).

The disaggregation tendency of PY dye molecules by the presence of surfactant molecules in the interlayer space of Lap at the optimized CTAB concentration is nicely confirmed by the fluorescence properties of the films (Figure 1.27C,D). Indeed, the fluorescence efficiency for a PY/Lap films of 2.4 % CEC in dye and 2.5% CEC in surfactant has increased at around 40 times respect to the equivalent PY/Lap sample without surfactant (Table 1.5), practically recovering the fluorescence capacity registered for the most-diluted PY/LAP films of 0.5 % CEC (Table 1.5). Moreover, much impressive improvement is reached in the fluorescence properties of the PY/Lap film with 9.3% CEC of dye intercalated and 2% CEC of surfactant co-absorbed with respect to homologous PY/Lap film of 10.2% CEC dye loading without surfactant. In this case, the reminiscent band centered at 682 nm recorded, previously assigned to the emission of J-band of high-order aggregates, revert to the monomer emission band at 570 nm with fluorescence efficiency of around 100 times greater.

To finish a complete characterization of the PY/ clay films, the orientation of dye molecules respect to the clay layer is evaluated by the UV-Vis absorption spectroscopy with linear polarized light for the most representative samples (Table 1.5, Figure 1.29). First note that all the dye/films analyzed showed anisotropic response to the vertical polarized light which indicates that the adsorbed dye molecules are disposed with a regular orientation towards the normal to the clay film. Secondly note that similar orientation angles are registered for all dye/clay films (with and without surfactant), (Table 1.5).

Generally, PY molecules adopt a relative parallel disposition to the clay layer with a tilted angle of around 63-62º with respect to the film normal for low and moderated dye loading that slightly varies up to 58º at saturated dye films. Note here that this tilted angle derived from the experiments with linear polarized light agrees well with the estimated previously by XRD at high dye loading (Table 1.5). More importantly, it is confirmed a macroscopic order even in the organo-clay films indicating that the presence of surfactant molecules in the interlayer space of the Lap films do not disrupt the orientation of the PY dye molecules (Figure 1.29).
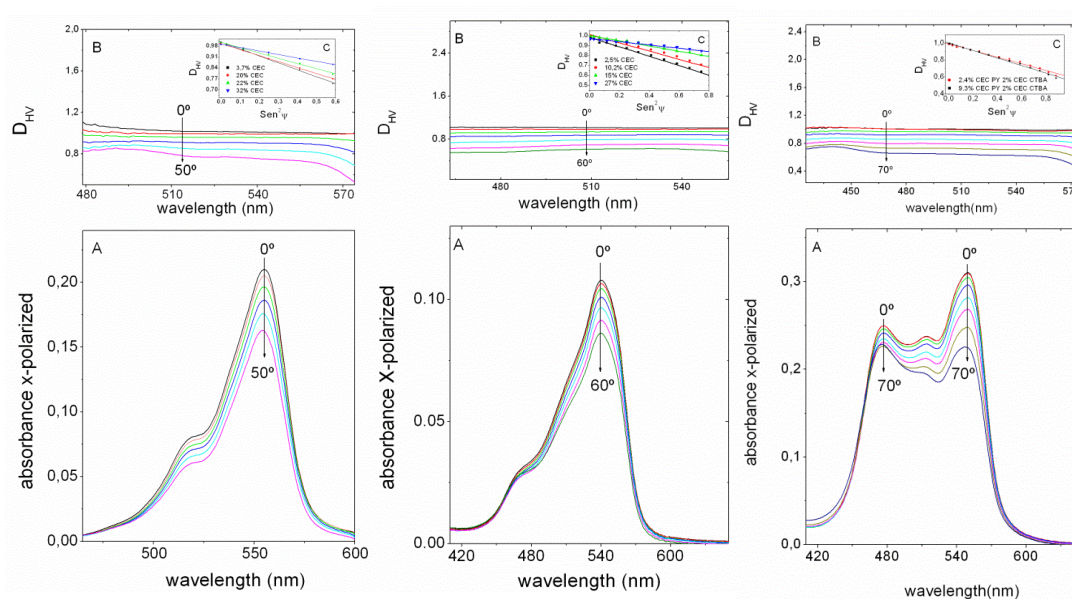
Figure 1.29. (A) X-Polarized absorption spectra of the PY/Clay hybrid materials recorded from 0º to 60º every 10º. (B) Evolution of the dichroic ration of PY/Clay thin film for different orientations of the sample with respect to the incident beam and (C) The linear relationship between the dichroic ratio with the twisted δ angle at the absorption maximum for different dye/clay loaded films: (Left) PY/Sap thin film 1.7% (middle) CEC PY/Lap thin film 1.8 %CEC and (right) Lap thin films of 9.3% CEC of PY and 2% CEC of CTBA.

1.2.2.1. Conclusion

According to the experimental and theoretical results different type and extent of the aggregation of PY dye molecules take place in Lap with respect Sap clay films. The reason is attributed to the different strength of electrostatic interactions between the dye and the clay and the different interlaminar water distribution in the interlayer space of both clays.

That is, the net negative charge at the external T-sheet in Sap films allows stronger electrostatic clay/dye interactions than in Lap clay with an internal distribution of the negative charge in its O layer. Accordingly, a better dye distribution is achieved in interlayer space of Sap reducing the molecular aggregation and favoring J-type aggregates, a more open geometry in which the dye molecules are in better contact with the clay surface.

On the contrary, the bilayer of water distribution founded in the interlayer space of laponite clay and the less effective dye-clay interactions lead to a higher dye aggregation in H-type geometry to maximize the surface contact area between the dye molecules counteracting in this way the hydrophilic environment of the interlayer space. In these Lap films, the dye aggregation process is ameliorated and the fluorescence properties have been significantly improved by the co-intercalation surfactant molecules in the interlayer space at an optimized concentration.

Finally, PY molecules in all the clay films show a preferential orientation respect to the normal to the surface. Indeed, the co-adsorption of the surfactant molecules does not disrupt the orientation of the dye molecules. Generally, the PY molecules adopt a relative parallel disposition to the clay layer with a tilted angle of around 63-62° with respect to the film normal for low and moderated dye loading that slightly vary to 58° at saturated dye clay films.

1.3. General conclusions of chapter 1

Cationic dyes of different nature were successfully incorporated into the interlayer space of smectite clay at different loading by immersion of the pure clay films into adequate dye solutions varying the immersion time. In this regards, novel hybrid dye-clay systems are easily elaborated. Due to the synergy between the guest dye and the host clay, the thermostability of the dye inside the clay has been was improved respect to the pure dye. Secondly, a preferential orientation of the dye molecules respect to the normal to the clay films is achieved, achieving a macroscopically ordered system which would be interesting for the development of films with non-linear optical properties.

Conversely, the interlayer space of the clay does not impose a rigid environment to restrict the dye motions, particularly in flexible molecular structures such as LDS 722 dye, and the fluorescence efficiency of the dye has not been improved respect to that in solution. Moreover, xanthenes-type dyes such as PY, show a high molecular aggregation one they are intercalated in the interlayer space of the clay resulting in the deactivation of fluorescence efficiency and limiting their used as optical devices. The dye aggregation highly depends on the smectite clay-type, particularly, the net negative charge location and the water molecules distribution on the interlayer space. Finally, this aggregation tendency can be reduced by co-intercalation of surfactant molecules in the interlayer space.

1.4.   Bibliography

1.   Hüsing, N. Ordered porous nanoarchitectures with specific functions. *Angew. Chem. Int. Ed. Engl.* **43,** 3216–3217 (2004).

2.   Simon, U. in *Host-Guest-Systems based on Nanoporous crystals* (eds. Laeri, F., Schüth, F., Simon, U. & Wark, M.) 621 (Wiley-VCH, 2003). doi:10.1016/0378-3774(83)90081-1

3.   Calzaferri, G. Nanochannels: Hosts for the supramolecular organization of molecules and complexes. *Langmuir* **28,** 6216–6231 (2012).

4.   Sanchez, C., Julián, B., Belleville, P. & Popall, M. Applications of hybrid organic–inorganic nanocomposites. *J. Mater. Chem.* **15,** 3559–3592 (2005).

5.   Ogawa, M. & Kuroda, K. Photofunctions of Intercalation Compounds. *Chem. Rev.* **95,** 399–438 (1995).

6.   Rao, C. N. R., Cheetham, a K. & Thirumurugan, a. Hybrid inorganic–organic materials: a new family in condensed matter physics. *J. Phys. Condens. Matter* **20,** 083202 (2008).

7.   Yu, J. *et al.* Second-Order nonlinear optical activity induced by ordered dipolar chromophores confined in the pores of an anionic metal-organic framework. *Angew. Chemie - Int. Ed.* **51,** 10542–10545 (2012).

8.   Brühwiler, D. & Calzaferri, G. Molecular sieves as host materials for supramolecular organization. *Microporous Mesoporous Mater.* **72,** 1–23 (2004).

9.   Brühwiler, D. *et al.* Nanochannels for supramolecular organization of luminescent guests. *J. Mater. Chem.* **19,** 8040 (2009).

10.   Davis, M. E. Ordered porous materials for emerging applications. *Nature* **417,** 813–821 (2002).

11.   Martínez-Martínez, V., García, R., Gõmez-Hortigüela, L., Pérez-Pariente, J. & Lõpez-Arbeloa, I. Modulating dye aggregation by incorporation into 1D-MgAPO nanochannels. *Chem. - A Eur. J.* **19,** 9859–9865 (2013).

12.   Schulz-Ekloff, G., Wöhrle, D., van Duffel, B. & Schoonheydt, R. a. Chromophores in porous silicas and minerals: preparation and optical properties. *Microporous Mesoporous Mater.* **51,** 91–138 (2002).

13.   Martínez, V. M., Arbeloa, F. L., Prieto, J. B., López, T. A. & Arbeloa, I. L. Characterization of supported solid thin films of Laponite clay. Intercalation of Rhodamine 6G laser dye. *Langmuir* **20,** 5709–5717 (2004).

14.   Shim, T., Lee, M. H., Kim, D., Kim, H. S. & Yoon, K. B. Fluorescence properties of hemicyanine in the nanoporous materials with varying pore sizes. *J. Phys. Chem. B* **113,** 966–969 (2009).

15. Zadaka, D., Rabinovitz, O. N. N., Serban, C., Groisman, L. & Rubin, B. Water Purification from Organic Pollutants by Optimized Micelle - Clay Systems. *Environ. Sci. Technol* **39,** 2343–2348 (2005).

16. Cheng, S.-H. *et al.* Mesoporous silica nanoparticles functionalized with an oxygen-sensing probe for cell photodynamic therapy: potential cancer theranostics. *J. Mater. Chem.* **19,** 1252 (2009).

17. López-Arbeloa, F., López Arbeloa, T. & López Arbeloa, I. in *Encyclopedia of Surface and Colloid Science 2nd Edition* (ed. Somasundaran, P.) 2325–2337 (2006).

18. Auerbach, S. M., Carrado, K. a. & Dutta, P. K. *Handbook of Layered Materials*. (2004). doi:ISBN: 0-8247-5349-6

19. López Arbeloa, F., Martínez Martínez, V., Arbeloa, T. & López Arbeloa, I. Photoresponse and anisotropy of rhodamine dye intercalated in ordered clay layered films. *J. Photochem. Photobiol. C Photochem. Rev.* **8,** 85–108 (2007).

20. Tapia Estevez, M. J., Lopez Arbeloa, F., Lopez Arbeloa, T. & Lopez Arbeloa, I. Absorption and fluorescence properties of Rhodamine 6G adsorbed on aqueous suspensions of Wyoming montmorillonite. *Langmuir* **9,** 3629–3634 (1993).

21. Martínez-Martínez, V. Intercalación de Rodamina 6G en Películas Ordenadas de Arcilla. (Universidad del Pais Vasco UPV-EHU, 2005).

22. Parrondo, J. M. R., Toral, R. & Kawai, R. Photophysical properties of styryl derivates of amoniobenzoxazinones. *Am. Chem. Soc.* **96,** 701–710 (1992).

23. Seth, D. *et al.* Photophysical studies of a hemicyanine dye (LDS-698) in dioxane - Water mixture, in different alcohols, and in a room temperature ionic liquid. *J. Phys. Chem. B* **113,** 6826–6833 (2009).

24. Strehmel, B., Seifert, H. & Rettig, W. Photophysical Properties of Fluorescence Probes. 2. A Model of Multiple Fluorescence for Stilbazolium Dyes Studied by Global Analysis and Quantum Chemical Calculations. *J. Phys. Chem. B* **101,** 2232–2243 (1997).

25. Huang, Y. *et al.* Photophysical studies on the mono- and dichromophoric hemicyanine dyes III. Ultrafast fluorescence up-conversion in methanol: Twisting intramolecular charge transfer and 'Two-State Three-Mode' Model. *J. Phys. Chem. B* **106,** 10041–10050 (2002).

26. Spatial, S., Second, T. S., Martin-gassin, G., Villamaina, D. & Vauthey, E. Nonradiative Deactivation of Excited Hemicyanines Studied with. *J. Am. Chem. Soc.* **133,** 2358–2361 (2011).

27. Kim, J. & Lee, M. Excited-State Photophysics and Dynamics of a Hemicyanine Dye in AOT Reverse Micelles. *J. Phys. Chem. A* **103,** 3378–3382

(1999).

28.   Sato, N., Fujimura, T., Shimada, T., Tani, T. & Takagi, S. J-aggregate formation behavior of a cationic cyanine dye on inorganic layered material. *Tetrahedron Lett.* **56,** 2902–2905 (2015).

29.   De, S., Das, S. & Girigoswami, A. Environmental effects on the aggregation of some xanthene dyes used in lasers. *Spectrochim. Acta - Part A* **61,** 1821–1833 (2005).

30.   Valdes-Aguiler, O., & Neckers, D. C. Aggregation Phenomena in Xanthene Dyes. *Accounts Chem. Res.* **22,** 171–177 (1989).

31.   Wang, H. *et al.* Aggregation states of rhodamine 6G in electrospun nanofibrous films. *J. Colloid Interface Sci.* **341,** 224–231 (2010).

32.   Meral, K., Ylmaz, N., Kaya, M., Tabak, A. & Onganer, Y. The molecular aggregation of pyronin y in natural bentonite clay suspension. *J. Lumin.* **131,** 2121–2127 (2011).

33.   Tabak, a. *et al.* Pyronin y (basic xanthene dye)-bentonite composite: A spectroscopic study. *J. Mol. Struct.* **1059,** 271–279 (2014).

34.   Czímerová, A., Bujdák, J. & Gáplovský, A. The aggregation of thionine and methylene blue dye in smectite dispersion. *Colloids Surfaces A Physicochem. Eng. Asp.* **243,** 89–96 (2004).

35.   Neumann, M. G. in *Encyclopedia of surface and colloidal science* (ed. somasundaran, P.) 389–410 (CRS Press, 2012).

36.   Epstein, M. & Yariv, S. Visible-spectroscopy study of the adsorption of alizarinate by Al-montmorillonite in aqueous suspensions and in solid state. *J. Colloid Interface Sci.* **263,** 377–385 (2003).

37.   Endo, T., Nakada, N., Sato, T. & Shimada, M. Fluorescence of clay-intercalated xanthene dyes. *J Phys Chem Solid* **49,** 1423–1428 (1988).

38.   Lopez Arbeloa, F., Lopez Arbeloa, T. & Lopez Arbeloa, I. Characterization of clay surfaces in aqueous suspensions by electronic spectroscopies of adsorbed organic dyes. *Trends Chem. Phys.* **4,** 191–213 (1996).

39.   Arik, M. & Onganer, Y. Molecular excitons of Pyronin B and Pyronin Y in colloidal silica suspension. *Chem. Phys. Lett.* **375,** 126–133 (2003).

40.   Fujii, T. Absorption spectra of rhodamine B dimers in dip-coated thin films prepared by the sol-gel method. *Chem. Phys. Lett.* **233,** 424–429 (1995).

41.   Martınez Martinez, V., López Arbeloa, F., Banuelos Prieto, J. & López Arbeloa, I. Orientation of Adsorbed Dyes in the Interlayer Space of Clays. 1. Anisotropy of Rhodamine 6G in Laponite Films by Vis-Absorption with Polarized Light. *Chem. Mater.* **17,** 4134–4141 (2005).

42. Arques, A. *et al.* Sepiolites as supporting material for organic sensitisers employed in heterogeneous solar photocatalysis. *J. Mol. Catal. A Chem.* **271,** 221–226 (2007).

43. Lemmetyinen, H. & Vuorimaa, E. Global Analysis of the Fluorescence Decays of N,N′-Dioctadecyl Rhodamine B in Langmuir-Blodgett Films of Diacylphosphatidic Acids. *J phys Chem* **100,** 13701–13715 (1996).

44. García, R., Martínez-Martínez, V., Sola Llano, R., López-Arbeloa, I. & Pérez-Pariente, J. One-dimensional antenna systems by crystallization inclusion of dyes (One-Pot Synthesis) within zeolitic MgAPO-36 nanochannels. *J. Phys. Chem. C* **117,** 24063–24070 (2013).

45. Martínez-Martínez, V. *et al.* Distribution and orientation study of dyes intercalated into single sepiolite fibers. A confocal fluorescence microscopy approach. *J. Mater. Chem.* **21,** 269 (2011).

46. Busby, M. *et al.* Time, space, and spectrally resolved studies on J-aggregate interactions in zeolite L nanochannels. *J. Am. Chem. Soc.* **130,** 10970–10976 (2008).

47. Schoonheydt, R. a. Smectite-type clay minerals as nanomaterials. *Clays Clay Miner.* **50,** 411–420 (2002).

48. Cerdán, L., Costela, a., García-Moreno, I., Bañuelos, J. & López-Arbeloa, I. Singular laser behavior of hemicyanine dyes: unsurpassed efficiency and finely structured spectrum in the near-IR region. *Laser Phys. Lett.* **433,** 426–433 (2012).

49. Bakker, H. J., Gilijamse, J. J. & Lock, A. J. Energy transfer in single hydrogen-bonded water molecules. *Chemphyschem* **6,** 1146–1156 (2005).

50. Krishnamoorthy, G. & Dogra, S. K. Dual fluorescence of 2-(4′-N,N-dimethylaminophenyl)benzoxazole: effect of solvents. *Spectrochim. Acta - Part A* **55,** 2647–2658 (1999).

51. Grabowski, Z. R., Rotkiewicz, K. & Rettig, W. Structural Changes Accompanying Intramolecular Electron Transfer: Focus on Twisted Intramolecular Charge-Transfer States and Structures. *Chem. Rev.* **103,** 3899–4031 (2003).

52. Kim, J., Lee, M., Yang, J.-H. & Choy, J.-H. Photophysical properties of hemicyanine dyes intercalated in Na-fluorine mica. *J. Phys. A* **104,** 1388–1392 (2000).

53. Bujdák, J., Martínez, V., Arbeloa, F. L. & Iyi, N. Spectral properties of rhodamine 3B adsorbed on the surface of montmorillonites with variable layer charge. *Langmuir* **23,** 1851–1859 (2007).

54. Bujdák, J., Iyi, N., Kaneko, Y., Czímerová, A. & Sasai, R. Molecular

arrangement of rhodaine 6G cations in the films of layered silicates: the effect of layer charge. *Phys. Chem. Chem. Phys.* **5,** 4680 (2003).

55.   Endo, T., Nakada, N., Sato, T. & Shimada, M. The Fluorescence properties of coumarine dye intercalated in a swelling clay. *J. Phys. Chem. Solids* **50,** 133–137 (1989).

56.   Bujdák, J. Effect of the layer charge of clay minerals on optical properties of organic dyes. A review. *Appl. Clay Sci.* **34,** 58–73 (2006).

57.   Martínez Martínez, V., López Arbeloa, F., Bañuelos Prieto, J. & López Arbeloa, I. Characterization of rhodamine 6G aggregates intercalated in solid thin films of laponite clay. 2 fluorescence spectroscopy. *J. Phys. Chem. B* **109,** 7443–7450 (2005).

58.   Kasha, M., Rawls, H. R. & Ashraf~El-Bayoumi, M. The Exciton Model in Molecular Spectroscopy. *Pure Appl. Chem.* **11,** 371–392 (1965).

59.   Salleres, S., López Arbeloa, F., Martínez, V., Arbeloa, T. & López Arbeloa, I. Photophysics of rhodamine 6G laser dye in ordered surfactant (C12TMA)/clay (Laponite) hybrid films. *J. Phys. Chem. C* **113,** 965–970 (2009).

60.   Salleres, S., López Arbeloa, F., Martínez, V., Corcóstegui, C. & López Arbeloa, I. Effect of surfactant C12TMA molecules on the self-association of R6G dye in thin films of laponite clay. *Mater. Chem. Phys.* **116,** 550–556 (2009).

61.   Sasai, R. *et al.* Luminescence Properties of Rhodamine 6G Intercalated in Surfactant / Clay Hybrid Thin Solid Films. *Thin Solid Films* **20,** 4715–4719 (2004).

62.   Bujdák, J. & Iyi, N. Spectral and Structural Characteristics of Oxazine 4/Hexadecyltrimethylammonium Montmorillonite Films. *Chem. Mater.* **18,** 2618–2624 (2006).

2

SOL-GEL MONOLITHS FOR SOLID-STATE LASER

2.1. Introduction

   "Laser", which is an acronym for Light Amplification by Stimulated Emission of Radiation, is an essential tool in many areas of science, engineering, industry or medicine. In short words, a laser consists in three main components: an excitation or pumping source, an active laser medium and an optical resonator (Figure 2.1). The pumping mechanism is necessary to excite the active media, which is disposed in the resonant cavity usually formed by two parallel mirrors. That configuration allows the amplification of emitted photons since the radiation beam is reflected by mirrors and passes successively through the active medium (feedback) increasing the stimulated photons emission. Once the amplification of radiation exceeds the losses of light in the resonant cavity, a monochromatic, coherent and amplified laser beam exits the cavity through the semi-reflective mirror[1,2].
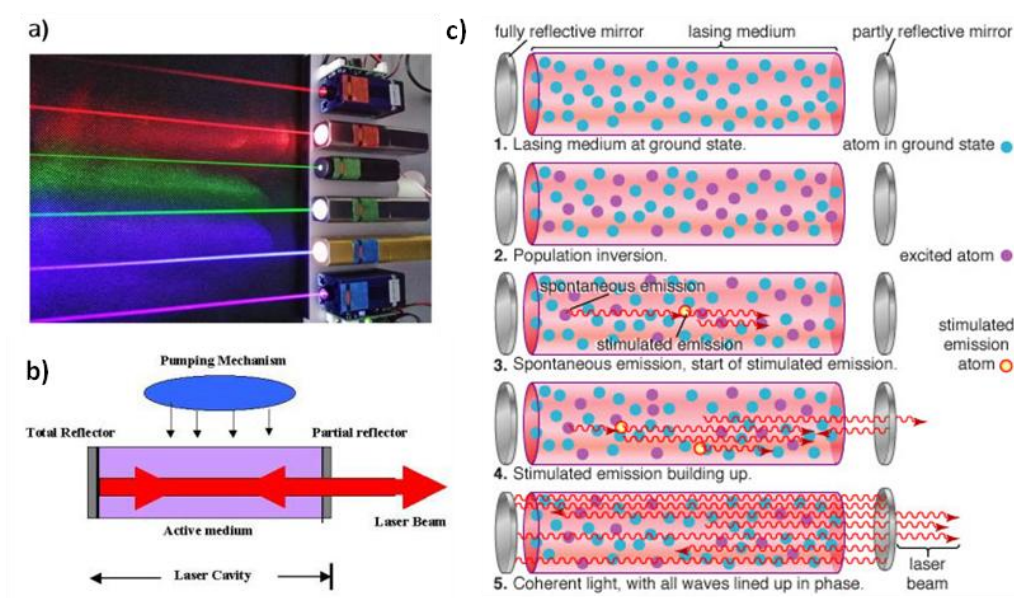
Figure 2.1. (A) Picture of different lasers; (B) general scheme of lasers (C) emission scheme: (1) lasing medium at ground state, (2) population inversion, (3) spontaneous emission, start of stimulated emission, (4) stimulated emission building up and (6) coherent light and laser emission[3].

   There are different types of lasers depending on their active medium: a) Gas lasers, which use gases such as helium and helium-neon for the most common gas lasers; b) Excimer lasers, based on the combination of a noble gas such as argon, krypton, or xenon and a reactive gas like fluorine or chlorine; c) Semiconductor lasers or diode

lasers, in which the optical gain is produced in a semiconductor material and the light is generated by radiative recombination of electrons and holes; d) Solid state lasers in which the active medium consists of a glass or crystalline host doped generally with rare earth elements such as neodymium, chromium, erbium, or ytterbium; and d) Dye lasers which use an organic dye usually as a liquid solution. In comparison with the other type of lasers, dye lasers offer wider bandwidth (Figure 2.1C) making them suitable for tunable and pulsed lasers up to femtoseconds.

The first organic laser dye in solution was developed in 1966, by Sorokin and Lankard[4] and at the same time by Schäfer, Schmidt and Volze[5] using phthalocyanine and various cyanine organic dyes, respectively. Generally, liquid state dye lasers require a high dye concentration in order to overcome degradation processes. Moreover, they also involve large volumes of solution and solvents which often are toxic and flammable[1]. As a consequence, there is a great interest in the development of solid state dye laser (SSDL), for example by embedding the dye into different hosts such as polymer matrices[6], inorganic sieves[7] or xerogel materials[8]. Solid state dye lasers (SSDL) exhibit well-recognized advantages over conventional liquid dye lasers as they avoid the problems of toxicity and flammability posed by the use of organic solvents, present a low-cost gain medium, and are compact and easy to operate and maintain. Moreover, the inorganic matrices generally offer mechanical, thermal, photo and chemical stabilities to the embedding organic compounds[9]. Thus, such SSDL lasers combine the convenience of solid-state lasers with the broad tuning range and high efficiency of organic laser dyes[10].

The requirements of a suitable solid matrix to be used as host for lasing dye molecules are:

> ➢ transparency to both pump and lasing wavelengths
> ➢ high optical quality with low level of scattering
> ➢ good thermal and photochemical stability.

On the other hand, the main requirements that a laser dye needs to fulfill are:

> ➢ Strong absorption and fluorescence bands that make easier the population inversion induced by pumping, increasing the probability of stimulated emission, and thus, more gains in the resonant cavity.

> ➢ Low non-radiant deactivation probability in the resonant cavity. Especially the intersystem crossing to the triplet state should be avoided because the triplet-triplet absorption band usually overlaps with the laser emission[11].

➢ Low aggregation tendency, since dye aggregates quench the radiative deactivation of the monomers[12].

➢ High Stokes shift, which means a low overlap between the absorption and fluorescence band to reduce reabsorption/reemission processes, typical in high optical density systems[13].

➢ High chemical, thermal and light stability to ensure active media with long operating time.
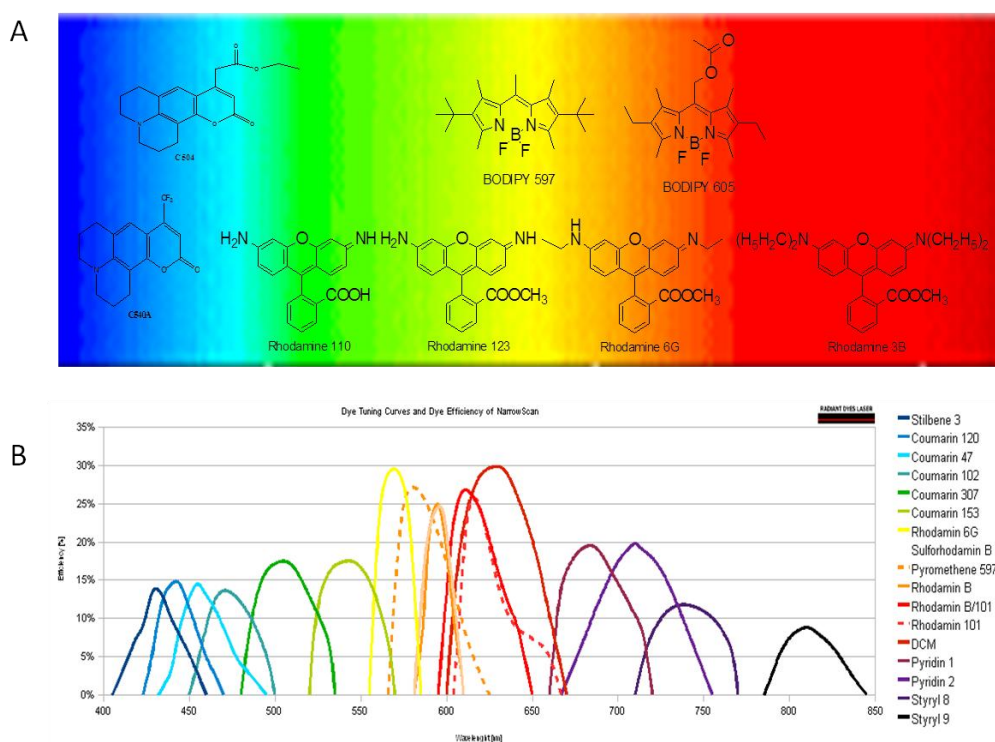
Figure 2.2. (A) Molecular structure of typical laser dyes (B) emission spectra of laser dyes.

Actually, there is a wide range of commercial laser dyes with absorption and emission bands in different region of the UV-Vis spectrum. Traditionally the most used commercial laser dyes are coumarins in the blue region, xanthenes derivatives (fluorescein and rhodamines) in the yellow and green region and oxazines in the red region (Figure 2.2) [14,15].
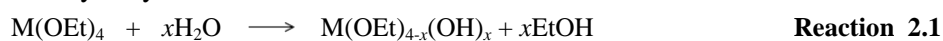
Regarding the previously described organic-inorganic hybrid dye-clay films (chapter 1, macroscopically ordered systems), owing to the clay minerals swelling capacity and to the low dye-clay interaction, a huge tendency to aggregation resulting in the deactivation of fluorescence efficiency and accordingly limitations as laser devices are expected. Among other hosts, inorganic glasses exhibit generally good thermal properties and a higher damage threshold than organic polymers. The low temperature sol-gel process allows the incorporation of organic dyes into silica xerogel inorganic glasses, and may result in relatively photostable materials with acceptable laser efficiencies. Thus, the main objective of this chapter is the elaboration of a solid-state laser medium based on the encapsulation of commercial laser dyes into silica monoliths suitable for laser application
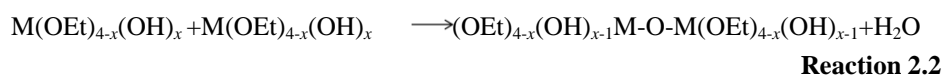
Silica-Monoliths: Sol-gel process

Sol–gel method is a mild chemical technique used to synthesize inorganic materials and organic–inorganic hybrids from liquid sources. Among the various compositions explored in sol–gel synthesis, silicate systems have been studied most extensively because molecular silicon sources with moderate reactivity (e.g., tetraalkoxysilanes) are readily available. The hydrolysis and polycondensation of tetraalkoxysilanes in liquid sols yield silica gels, which can be converted into silica xerogels (or dried gels) at relatively low temperatures without melting. This melt-free process is attractive for the development of glasses, because it has for instance the potential to increase the concentration of dopants. However, sol–gel-derived wet gels are easily fractured during drying, making it difficult to obtain monolithic dried xerogels. Although in the recent years the interest in fabrication of large monolithic materials increased, the sol–gel synthesis of monolithic silica glasses and silica-based functional glasses remains a major challenge.

The typical sol-gel process consists in the hydrolysis and condensation of precursors:

> Hydrolysis:

$M(OEt)_4 + xH_2O \longrightarrow M(OEt)_{4-x}(OH)_x + xEtOH$ **Reaction 2.1**

> Condensation:

$M(OEt)_{4-x}(OH)_x + M(OEt)_{4-x}(OH)_x \longrightarrow (OEt)_{4-x}(OH)_{x-1}M\text{-}O\text{-}M(OEt)_{4-x}(OH)_{x-1} + H_2O$

Reaction 2.2

Both the hydrolysis and condensation reactions steps occur in multiple-step, parallel and reversible reactions[16,17].

The advantages of the sol-gel process include chemical purity and homogeneity, reactions at relatively low temperatures, flexibility in the selection of composition and final shapes. In this sense, by controlling specific synthetic characteristics, the sol-gel process allows the synthesis of different kind of materials such as powders, fibers, thin films or monoliths, among others[18].

The typical sol composition for fabrication of gels with large physical dimensions consists in the mixture of the orthosilicate such as tetramethyl orthosilicate (TMOS) or tetraethyl orthosilicate (TEOS), ethanol, water and a catalyst. The proportion of these precursors plays an important role in the gel microstructure. Thus, by controlling the proportions of the precursors, the diameter of the monoliths pore can be modified. Importantly, the sol formulation and its ageing will also control the breakability of the final material, mainly due to the stress arising from the large degree of shrinkage, attributed to the small volume fraction of the silica component in the precursor solution. The term ageing is applied to the process of change in structure and properties after gelation. It involves further condensation (Equation 1), dissolution and reprecipitation of monomers and oligomers or phase transformations within the solid and liquid phases. Some gels exhibit spontaneous shrinkage; called syneresis as bond formation or attraction between particles includes contraction of the network and expulsion of liquids from the pores[18].

Monoliths are defined as bulk gels cast to shape and processed without cracking. The technical challenge is to avoid cracking and to reproducibly account for volume changes accompanying drying and sintering. In this chapter 2, silica monoliths were chosen as a suitable inorganic matrix for the encapsulation of laser dyes in their pores to obtain solid-state hybrid material with good laser applications and high photo- and thermo-stability. Indeed, the silica matrix is a good host material due to its excellent properties, such as chemical and mechanical resistance, large surface area and optical transparency in the Vis-NIR radiation. Moreover, the mild low-temperature conditions of the sol-gel synthesis allow the addition of organic molecules directly to the silica gel. Additionally, both alkoxide precursors and the common laser dyes (coumarins, xanthenes, oxazines, ...) are soluble in the typical alcoholic solvents used in the synthesis. However, one of the drawbacks of xerogels is their high ability to cracking triggered by the shrinkage that occurs when solvent is evaporated during the ageing process. The driving force for the shrinkage is the evaporation of solvent, leading to capillary pressure in the liquid–vapor interface and inducing meniscus at the liquid-vapor interface.

2.2 Results and discussion

In this section the synthesis of large (5 x 5 x 15 mm³) silica monoliths adapted from previous studies[19,20] with different encapsulated dyes in their pores is reported (synthesis details in the experimental section 4.1.2.). Particularly, two different commercial laser dye families are chosen to cover the visible region from green to yellow (Figure 2.3):

i)   BODIPYs dyes, abbreviation for boron-dipyrromethene, because of their very favorable chemico-physical features, including high extinction coefficients in the visible region and resistance to photobleaching[21,22] such as BODIPY597 and 605.

ii)   Rhodamines dyes, from the xanthene family, typically used as dye laser gain medium [23] such as Rhodamine 110, 123, 6G and 3B with different absorption and emission bands to cover the Vis range from green to red.
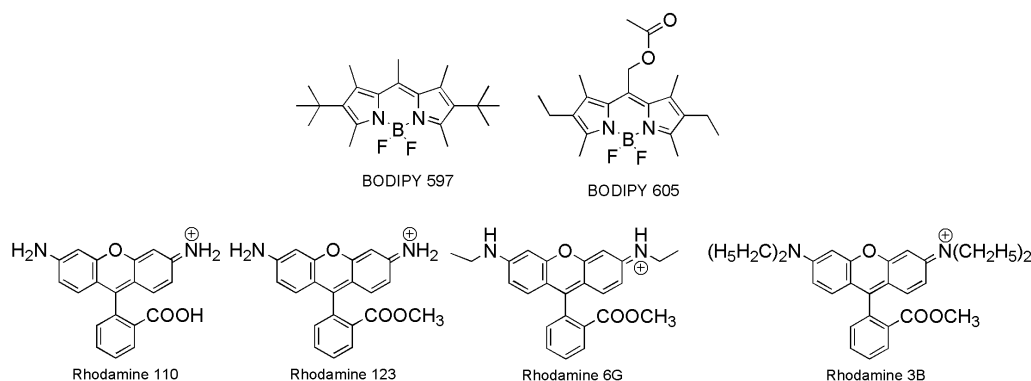

Figure 2.3. Molecular structure of embedded laser dyes, BODIPYs and Rhodamines.

Note here that one of the most important parameter that has to be taken into account for laser applications is the dye optical density. For that reason, the concentration of the embedded dyes has to be optimized. Hence, the concentration of dyes previously dissolved in methanol was varied from 10^{-5} to 10^{-3} M (experimental chapter 4.1.2, see monoliths synthesis section).

Therefore, taking into account the initial MeOH volume and the final monoliths dimensions, the final laser dye concentration in the monolith can be calculated[19,20]. In fact, after the drying process, the monoliths obtained are parallelepipeds of dimension 0.5 cm x 0.5 cm x 1.5 cm (Figure 2.4). Note here that as a consequence of the

significant shrinkage that occurs during the ageing process, the dye concentration is around 5 times higher than in the initial MeOH solution. Figure 2.4 shows the synthesized Rh6G monoliths at different dye concentrations, from 0.45 mM to 36 mM.
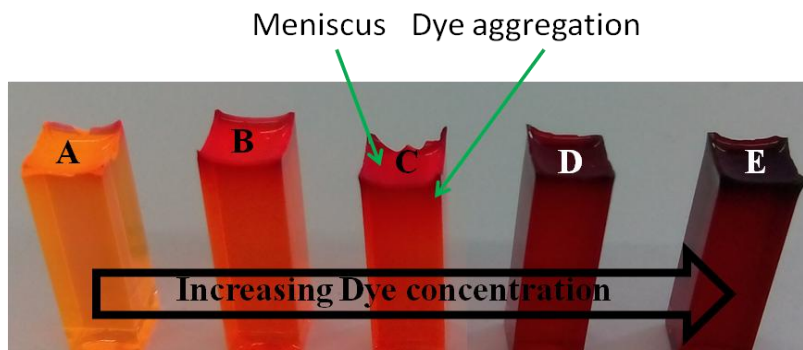
Figure 2.4. Pictures of synthesized Rhodamine 6G monoliths at different dye concentration (A) 0.45 mM, (B) 2.2 mM, (C) 3.6 mM, (D) 22 mM and (E) 36 mM.

Due to the inherent problems in the characterization of samples of high optical density, the photophysical analysis was carried out on the monoliths with the lowest dye concentration (of around 0.45 mM).

### 2.2.1. Photophyscal Characterization

First, the photophysical characterization of monoliths with BODIPY597 and BODIPY605 embedded in the silica network is addressed and compared with the laser dyes in methanol solution (Table 2.5).

Both BODIPYs, BDP597 and BDP605, embedded inside the silica network show absorption bands wider and blue-shifted by around 20 and 30 nm respectively, with respect to those recorded in methanol solution (Table 2.1 and Figure 2.5) [24]. Indeed, these effects are typical of dyes in adsorbed-state since their high confinement can distort the vibrational states of the dye. On the other hand, the blue shift can be attributed to the hydrophilic nature of the silica pores due to the silanols OH groups of the external surface together with the presence of remaining water molecules. Indeed, it has been already demonstrated that the spectral bands of BODIPY dyes in polar solutions are usually shifted to higher energies because the excited state is less polar

than the ground state. Consequently the ground state is more stabilized than the excited state in polar environments[25,26].

Table 2.1. BODIPY597 and 605 photophysical results: Absorption (λ_{ab}), fluorescence wavelength (λ_{fl}), fluorescence yield (ϕ_{fl}), average lifetime (τ_{ia}).

	λ_{abs}	λ_{fl}	ϕ_{fl}	$<\tau_{ia}>$
BDP597 monolith	505	518	-	3.69
BDP597 solution	523	567	0.42	4.21
BDP 605 monolith	511	552	-	4.14
BDP 605 solution	543	560	0.62	6.65
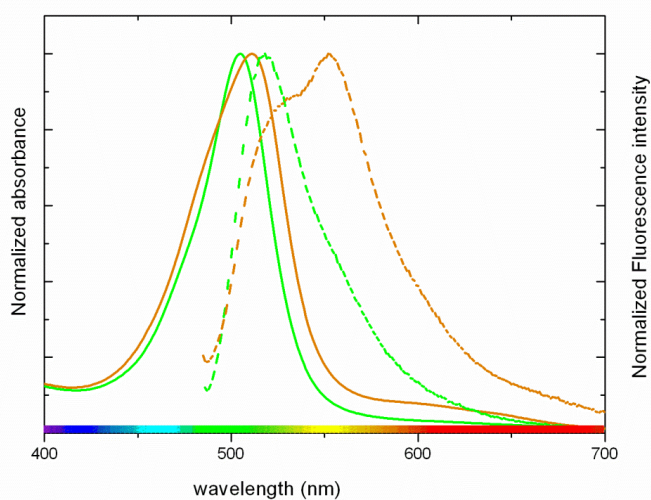
Figure 2.5. BODIPY597-monolith (green) and BODIPY 605-monolith (orange) absorbance and fluorescence bands.

The fluorescence properties of these monoliths with different embedded BODIPY dyes are analyzed in order to evaluate their possible use for laser applications. Although a typical wider and blue-shifted emission band with respect to solution is recorded for BDP597-monolith, the fluorescence spectrum of the BDP605-monolith shows two discernible bands, tentatively attributed to the formation of fluorescence

aggregates together with the monomeric units of BDP605. Regarding the fluorescence decay curves, a multiexponetial behavior is found and at least 3 or 4 exponentials are required in the fitting process. This result gives an idea of the complex environment that surrounds these BODIPY dyes once embedded in the silica matrix. Owing to the difficult proper interpretation of each derived lifetime, an average lifetime ($<\tau_{ia}>$) was estimated (Equation 2.1) [27].

$$\langle\tau\rangle_{ia} = \frac{\sum A_i\,\tau_i^2}{\sum A_i\,\tau_i} \qquad\qquad \textbf{Equation 2.1}$$

It is concluded that the average lifetime of the BODIPY dyes embedded inside the monoliths is shorter than that obtained in solution. This would suggest that the non-radiative deactivation process is more significant in the monoliths than in solution.

More importantly, although the emission spectra and the fluorescence decay curves of these monoliths could be recorded just after their synthesis (t = 1 week) after two months these monoliths became dark and non-fluorescent (Figure 2.6) and therefore the fluorescence quantum yield was not recorded.
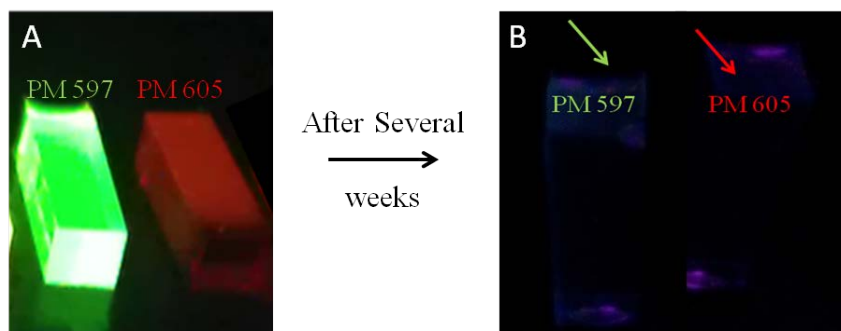
Figure 2.6. The fluorescence image of embedded BODIPYs monoliths under UV light (A) After their synthesis (t = 1 week) and (B) t = two months after their synthesis.

The reason of these changes in the fluorescence of BDP-597 and BDP-605-monoliths are still unknown, although several assumptions could be postulated: *i)* chemical reaction inside the pore that finally degrades the BODIPY dyes *ii)* migration of dye molecules to avoid the inherent polar environment of silica pores (with water

molecules and OH-groups). In this later case, dye agglomeration will induce the fluorescence quenching with the aging time.

Indeed, the same problem was also found for the several coumarins dyes encapsulated in the silica network (data non-shown). It is worth recalling that both types of dyes are neutral and are more soluble in less polar solvents than alcohols and water. Besides, the relatively small molecular structure could favor the dye migration through the silica pores. However, further experiments should be done to address these issues.

Therefore, another family of laser dyes, namely Rhodamines, was tested. Actually, Rhodamines are cationic dyes with good solubility in alcoholic solvents and also with larger molecular dimensions than BODIPYs or coumarins. In order to achieve lasing applications in different ranges of the visible spectra, several Rhodamines with various absorption and fluorescence bands were chosen for encapsulation in silica monoliths: Rhodamine 110, Rhodamine 123, Rhodamine 6G and Rhodamine 3B (Figure 2.3).

The dyes were directly introduced in the methanol solution of the initial sol, also containing alkoxide and water. Since the dye concentration varied significantly between 10^{-4} and 10^{-2} M in the monoliths, we controlled that the porosity of the silica matrix was not affected by these different concentrations. BET measurements (see experimental chapter 4) were thus carried out and the N_2 adsorption isotherms are presented Figure 2.7.

Table 2.2 BET results for Rhodamine6G-monoliths.

Rh6G Concentration in monoliths/mM	BET specific surface area $(m^2 g^{-1})$	Pore volume $(mL\ g^{-1})$
0.45	322±**7**	0.19
2.2	316±6	0.17
3.6	320±6	0.17

V_ads (cc/g)
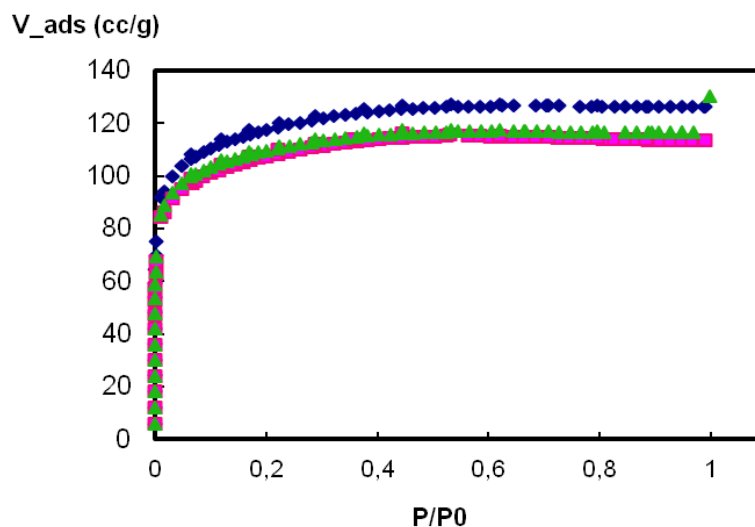
Figure 2.7. N_2 adsorption isotherms of Rhodamine 6G-monoliths: R6G concentration in monoliths 0.45 (blue), 2.2 (pink) and 3.6 (green).

All the adsorption isotherms are of Type I [28], typical of microporous materials, with pore diameters < 2 nm. The pore size distribution is more than 90 % distributed in this range for the three studied monoliths. This pore diameter almost fits the molecular dimensions of Rhodamine dyes, crucial to avoid dye aggregation. The BET (Brunauer-Emmet-Teller) specific surface area was calculated in the range 316-320 m^2 g^{-1}. This specific surface area is quite high and indicative of a porous material. Both specific surface area and pore distribution of the silica monoliths did not change significantly with the dye concentration (Table 2.2).

The photophysical properties of monoliths with the different embedded Rhodamines were studied at the lowest 0.45 mM dye concentration. Once again, the absorption bands are blue-shifted respect to solutions (Table 2.3), which is attributed to the silica matrix contribution.

As explained in chapter 1, this type of xanthene dyes usually have high tendency to aggregate. However, there is no evidence of dye aggregation once they are embedded in the monoliths (Figure 2.8 and Table 2.3), since there are no new spectral bands with respect to dye solutions. Moreover, the fluorescence decay curves are perfectly analyzed as mono-exponential, with longer lifetimes than in diluted solution (Table 2.3), suggesting a reduction of the non-radiative deactivation, *i.e*. internal conversion, likely attributed to the rigidity imposed by the silica matrix.

Table 2.3. Photophysical properties of Rhodamines in solution and embedded in silica monoliths; Absorption (λ_{ab}), fluorescence wavelength (λ_{fl}), fluorescence yield (ϕ_{fl}), fluorescence lifetime (τ),

	λ_{abs}	λ_{fl}	τ (ns)	φ_{fl}
Rh110 monoliths	496	521	4.73	35
*Rh110 solution	501	521	3.78	99
Rh123 Monoliths	509	533	4.74	54
*Rh123 solution	511	529	3.94	81
Rh6G monoliths	522	550	4.02	71
*Rh6G solution	530	555	3.99	77
Rh3B monoliths	554	583	1.37 (16); 4.24 (84)	70
Rh3B solution	556	580	2.27	71

* Rhodamines in diluted ethanol solution (10^{-6} M)
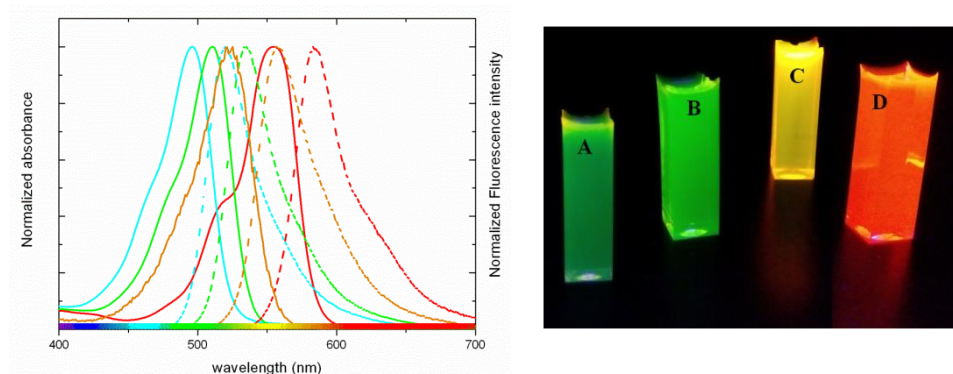
Figure 2.8 Left) absorption (solid-line) and emission (dotted-line) spectra of the different rhodamines embedded in the monoliths; (cyan) Rhodamine 110, (green) Rhodamine 123, (orange) Rhodamine 6G and (red) rodamine 3B.; Right) Fluorescence picture of Rhodamines embedded in silica monoliths: (A) RhD110-monolith, (B) RhD123-monoliths, (C) RhD6G-monoliths and (D) RhD3B-monoliths.

Importantly, for the Rhodamines Rh6G and Rh3B at 0.45 mM in the monoliths, the fluorescence quantum yields (determined by an integrating sphere, see experimental chapter 4) are similar to those in diluted ethanol solutions (Table 2.3). Note here that

the fluorescence efficiency of dyes in solution at such high concentration (0.1 mM range) is usually quenched due to dye aggregation process[29]. However, in the case of Rh110 and Rh123, the fluorescence quantum yields in the monoliths are lower than those in solution. This result can tentatively be attributed to specific interactions between dyes and the silica matrix. Indeed, while the amino groups in Rh6G and Rh3B dyes are respectively secondary or tertiary with bulky ethyl substituents, Rh110 and Rh123 are primary without any alkyl substitution (see molecular structure in Figure 2.3). These primary amino groups might interact more specifically with the acidic silanol OH groups of the silica matrix (isoelectric point of silica around 2) and/or water molecules adsorbed in the pores, reducing the fluorescence capacity of the dyes. Nevertheless, the fluorescence quantum yields of all these Rhodamines-monoliths at relative high dye concentrations (0.45 mM) might be suitable for future applications as laser materials. Besides, these Rhodamines-monoliths still are stable after 1 year.

2.2.2. Laser Efficiency

In order to test these silica monoliths doped with Rhodamine dyes as suitable solid state dye laser (SSDL), laser experiments (energy conversion efficiency and peak wavelength of the laser emission) were carried out by Prof. Inmaculada Garcia-Moreno (Instituto de Química Física Rocasolano, CSIC, Madrid). The laser measurements were performed on the Rh6G-monoliths at different dye concentrations (Figure 2.9, Table 2.4). The monoliths were transversely pumped at 532 nm with 5 mJ, 6-ns pulses from a frequency-doubled Q-switched Nd:YAG laser (spectron SL282G) at a repetition rate of 10 Hz, through the longer optical path.
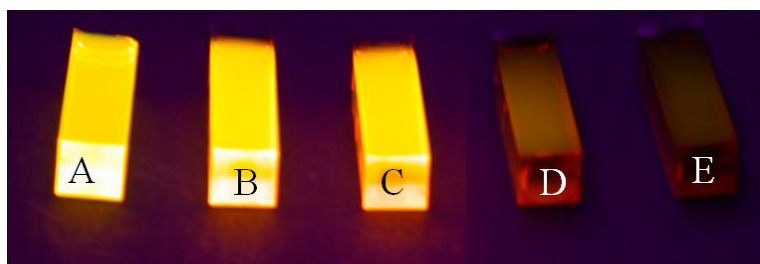
Figure 2.9. Fluorescence pictures of Rhodamines6G-monoliths: (A) 0.45 mM (B) 2.2 mM (C) 3.6 mM (D) 22 mM and (E) 36 mM.

Table 2.4. Lasing properties of Rhodamine6G-monoliths: percent lasing efficiency (Eff), and λ_L maximum lasing wavelength.

Monoliths	[Dye] /mM	Eff (%)	λ_L/ nm
Rh-6G (A)	0.45	31	563
Rh-6G (B)	2.2	18	570
Rh-6G (C)	3.6	9	585
Rh-6G (D)	22	LIF	592
Rh-6G (E)	36	LIF	597

The highest laser efficiency is obtained in the most diluted monoliths (0.45 mM). Then, as dye concentration increases, the laser efficiency decreases and is also red-shifted in a dye concentration range between $0.45 < [\text{dye}] \leq 3.6$ mM. However, at high dye concentration, ≥ 22 mM, instead of the Amplified Spontaneous Emission (ASE) only Laser Induced Fluorescence (LIF) with a broad emission band around 590 nm is detected.

According to previous studies on Rhodamine 6G embedded in different materials, the laser efficiencies substantially depend on the matrices. Therefore, several values from 2% for Rh6G in alumina films[30],16% in silica xerogels[31], 25% in aluminosilicate xerogels[32] to 30% in Rh6G/ORMOSIL[33] ("Organic Modified Silica") are found in the literature. Thus, the laser efficiencies obtained for Rh6G-monoliths (table 2.4) make these materials promising as suitable solid-state dye lasers (SSDL).

The better laser efficiency at the lowest Rh6G concentration may be attributed to two effects. The first is that dye aggregation at higher concentrations will reduce the fluorescence quantum yield by self-quenching. The second is that the higher concentrations introduce optical artifacts similar to well-known inner filter effects in absorption spectroscopy.

Monoliths containing the other laser dyes did not exhibit laser emission. Besides physical stability (dye migration in the sample), a further concern is photostability. Photobleaching experiments conducted at the surface of the monoliths with a confocal microscope revealed a significant difference between Rhodamines and the other dyes (Figure 2.10).
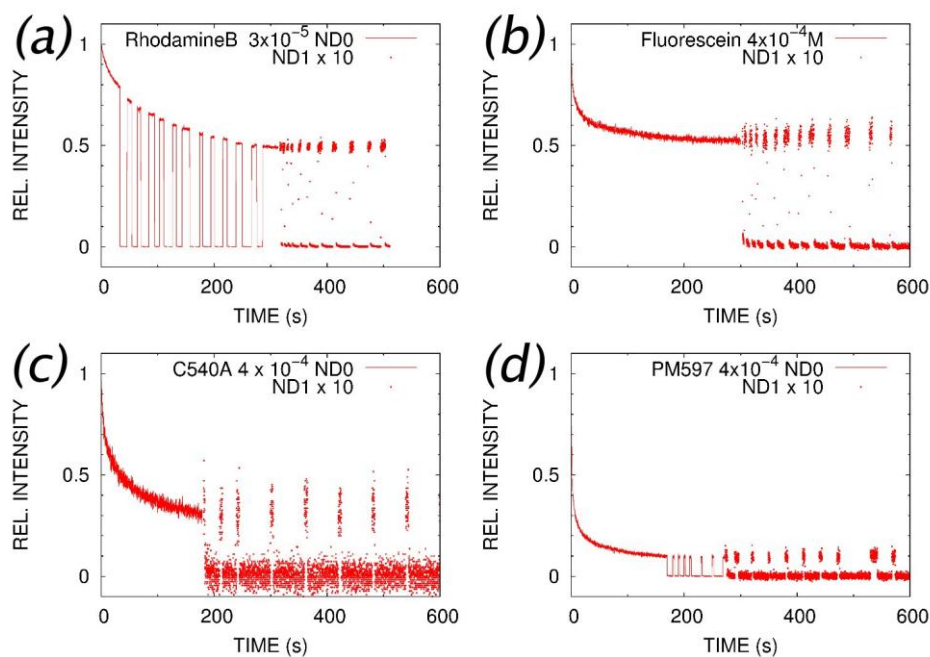
Figure 2.10. Comparison of photobleaching in monoliths of xanthene dyes a) RhB ($3 \ 10^{-5}$ M) and b): fluorescein ($4 \ 10^{-4}$ M), and two other common laser dyes c) Coumarin 540A ($4 \ 10^{-4}$ M) and d) BDP-597 ($4 \ 10^{-4}$ M). After initial period of photobleaching (about 200 s), the laser intensity is reduced tenfold and photorecovery is probed periodically (not observed).

Figure 2.10 suggests that photostability may indeed be an issue with the other dyes. For example, BDP-597 emission bleaches out in seconds whereas RhB emission drops only 50 % in 200 seconds bleaching at full power under the confocal microscope. The rate of bleaching obviously must depend on the extinction coefficient at the chosen wavelength. However, that is comparable to the conditions in the laser tests in Madrid. The relative photostability of the Rhodamine (and to the similar dye, fluorescein) seems to be distinguishing feature. No clear signs of recovery were detected for any of the monoliths, on the timescale explored here. In ancillary tests, bleaching was found proportional to the radiation dose (time x power), *i.e*. a linear process.

Indeed, several issues were raised by the laser efficiency measurements due to the meniscus, mainly present at the top face of the monoliths (Figures 2.4 and 2.9) and resulting from solvent evaporation during the ageing process. This meniscus induces high divergences of the light and does not allow the amplification of emitted photons since the radiation beam cannot successively go through the long axis of the monoliths (feedback). On the other hand, owing to the evaporation process occurring mainly at

the top face of the cuvettes (liquid–vapor interface), the dye concentration close to the meniscus is higher than in the lower part of the monoliths volume (Figure 2.4), inducing also losses in the laser efficiency. As a possible solution, the cut or polishing of the top part of the monoliths was considered, but these processes induced cracks in the monoliths and they finally broke into pieces.

At this point, transversely pumping through the shorter optical path was also tried, but the well-polished faces were not totally parallel since the shrinkage was not homogenous during the ageing process, and this lack of alignment induces losses in the cavity.

As an alternative to the parallelepiped monoliths, cylindrical monoliths (diameter 7.5 mm, length 43 mm) were synthesized with the aim of *i*) reducing the meniscus and *ii*) increasing the laser efficiency by increasing the optical path length (Figure 2.11). The laser measurements are currently carried out on this type of cylindrical monoliths.
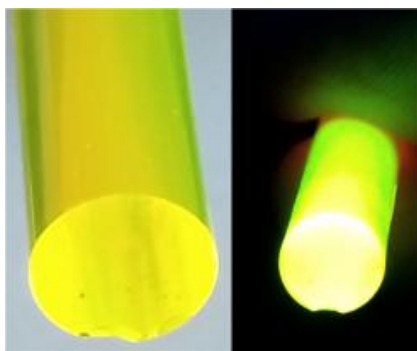
Figure 2.11. Cylindrical monoliths image

As a brief conclusion, these latter monoliths with Rhodamines embedded in their pores may be used as suitable solid state dye laser (SSDL) once the irregularities resulting from the shrinkage during the drying process could be corrected.

2.3. Conclusions

New hybrid solid state materials based on the encapsulation of different laser dyes into silica monoliths were synthesized with the aim of developing solid state dye laser (SSDL). Large parallelepiped silica monoliths (0.5 cm x 0.5 cm x 1.5 cm) with different dye concentrations were analyzed.

First, commercial BDP laser dyes (BODIPY597 and BODIPY605) were encapsulated into the silica network of the monoliths because of their versatility and their good properties as laser dyes in solution. However, the monoliths became dark with time (several weeks), possibly due to the very polar environment typical of silica inducing slow dye agglomeration.

Second, several Rhodamines with absorption and emission bands in different range of the Vis spectra (Rhodamines 110, 123, 6G and 3B) were embedded into the silica monoliths. Contrary to the previous ones, these monoliths, particularly for Rh6G and Rh3B dyes with concentrations in 0.45 mM range, show high fluorescence quantum yields and appear stable after 1 year. The best fluorescence quantum yields of these highly polar cationic dyes embedded in silica monoliths were obtained with two of them, characterized by the presence of secondary or tertiary amino groups. Indeed, a laser efficiency of 31% was demonstrated for the Rh6G silica monolith at a 0.45 mM dye concentration, which is noticeably higher than the efficiencies already probed for this dye in different inorganic host such as alumina films (2%), silica xerogels (16%) or aluminosilicate xerogels (25%). Conversely, the presence of meniscuses and other irregularities in the parallelepiped monoliths faces, as a consequence of the high and inhomogeneous shrinkage occurring during the ageing process, induces important losses in the resonant cavity. As an alternative, a new R110-cylindrical monolith was synthesized as a potential solid-state dye laser (SSDL), in order to limit the meniscus formation and to improve the light feedback through the monoliths optical path.

2.4. Bibliography

1.   Schäfer, F. P. *Principles of Laser Dyes*. (Springer-Verlag, 1990).

2.   Duarte, F. J. & Hilman, L. W. *Dye Laser Principles with Applications*. (1990).

3.   http://www.britannica.com/technology/stimulated-emission.

4.   Sorokin, P. P. IBM J. Res. Develop. *IBM J. Res. Dev.* **10,** 162–163 (1966).

5.   Schäfer, F. P., Schmidt, W. & Volze, J. Organic dye solution laser. *Appl. Phys. Lett.* **9,** 306–309 (1966).

6.   Costela, A., García-Moreno, I. & Sastre, R. Polymeric solid-state dye lasers: Recent developments. *Phys. Chem. Chem. Phys.* **5,** 4745 (2003).

7.   Vietze, U., Krauß, O. & Laeri, F. Zeolite-Dye Microlasers. *Phys. Rev. Lett.* **81,** 4628–4631 (1998).

8.   Yariv, E., Schultheiss, S., Saraidarov, T. & Reisfeld, R. Effciency and photostability of dye-doped solid-state lasers in different hosts. *Opt. Mater. (Amst).* **16,** 29–38 (2001).

9.   Nikogosian, D. N. *Properties of Optical and Laser Related Materials: a Handbook*. (Willey, 1997).

10.   Chénais, S. & Forget, S. Recent advances in solid-state organic lasers. *Polym. Int.* **61,** 390–406 (2012).

11.   Pavlopoulos, T. G. Scaling of dye lasers with improved laser dyes. *Prog. Quantum Electron.* **26,** 193–224 (2002).

12.   López Arbeloa, F., Ruiz Ojeda, P. & López Arbeloa, I. The fluorescence quenching mechanisms of Rhodamine 6G in concentrated ethanolic solution. *J. Photochem. Photobiol. A Chem.* **45,** 313–323 (1988).

13.   Demas, J. N. & Crosby, G. A. The Measurement of Photoluminescence Quantum Yields. A Review. *J. Phys. Chem.* **75,** 991–1024 (1971).

14.   Lavis, L. D. & Raines, R. T. Bright Ideas for Chemical Biology. *ACS Chem. Biol.* **3,** 142–155 (2007).

15.   Shankarling, G. S. & Jarag, K. J. Laser Dyes. *Resonance* 804–818 (2010).

16.   Cao, G. *Nanostructures and Nanomaterials: Synthesis, Properties and Applications*. (World Scientific, 2004).

17.   Klein, L. C. *Sol-Gel Optics processing and Applications*. (1994).

18.   Brinker, J. C. & Scherer, G. W. *Sol Gel Science The physics and chemistry of sol-gel processing*. (1990).

19.   Cantau, C., Pigot, T., Manoj, N., Oliveros, E. & Lacombe, S. Singlet oxygen in microporous silica xerogel: Quantum yield and oxidation at the gas-solid interface. *ChemPhysChem* **8,** 2344–2353 (2007).

20. Arzoumanian, E. *et al.* Transparent organosilica photocatalysts activated by visible light: Photophysical and oxidative properties at the gas-solid interface. *ACS Appl. Mater. Interfaces* **6,** 275–288 (2014).

21. Mackey, M. S. & Sisk, W. N. Photostability of pyrromethene 567 laser dye solutions via photoluminescence measurements. *Dye. Pigment.* **51,** 79–85 (2001).

22. Ahmad, M., King, T. A., Ko, D. K., Heon Cha, B. & Lee, J. Photostability of lasers based on pyrromethene 567 in liquid and solid-state host media. *Opt. Commun.* **203,** 327–334 (2002).

23. Maeda, M. *Laser dyes, Properties of organic compounds for dye Laser.* (1984).

24. López Arbeloa, F., Bañuelos, J., Martínez, V., Arbeloa, T. & López Arbeloa, I. Structural, photophysical and lasing properties of pyrromethene dyes. *Int. Rev. Phys. Chem.* **24,** 339–374 (2005).

25. Bañuelos Prieto, J., Lòpez Arbeloa, F., Martínez Martínez, V., Arbeloa López, T. & López Arbeloa, I. Structural and spectroscopic characteristics of Pyrromethene 567 laser dye. A theoretical approach. *Phys. Chem. Chem. Phys.* **6,** 4247 (2004).

26. Bañuelos, J. *et al.* Difluoro-boron-triaza-anthracene: a laser dye in the blue region. Theoretical simulation of alternative difluoro-boron-diaza-aromatic systems. *Phys. Chem. Chem. Phys.* **13,** 3437–3445 (2011).

27. Joseph R. Lakowicz. *Principles of Fluorescence Spectroscopy.* (Springer).

28. Sing, K. S. W. *et al.* Reporting Physisorption data for Gas/Solid Systems with Special Reference to the Determination of Surface Area and Porosity. *Pure Appl. Chem.* **57,** 603–619 (1985).

29. Valdes-Aguiler, O., & Neckers, D. C. Aggregation Phenomena in Xanthene dyes. *Accounts Chem. Res.* **22,** 171–177 (1989).

30. Kobayashi, Y., Kurokawa, Y., Imai, Y. & Muto, S. A transparent alumina film doped with laser dye and its emission properties. *J. Non. Cryst. Solids* **105,** 198–200 (1988).

31. Charlton, A., McKinnie, I. T., Meneses-Nava, M. A. & King, T. A. A tunable visible solid state laser. *J. Mod. Opt.* **39,** 1517–1523 (1992).

32. Gregg, B., Fox, M. & Bard, A. Photovoltaic effect in symmetrical cells of a liquid crystal porphyrin. *J. Phys. Chem.* **94,** 1586–1598 (1990).

33. Altman, J. C., Stone, R. E., Dunn, B. & Nishida, F. Solid-state laser using a rhodamine-doped silica gel compound. *IEEE Photonics Technol. Lett.* **3,** 189–190 (1991).

3

**MESOPOROUS SILICA NANOPARTICLE FOR BIOIMAGING AND PHOTODYNAMIC THERAPY APPLICATIONS**

3.1. Introduction

Photodynamic therapy (PDT) is a minimally invasive procedure that offers many advantages over traditional cancer treatments. PDT has proved to be able to kill microbial cells, including bacteria, fungi and viruses. PDT is used in clinically treating of a wide range of medical conditions such as acne and malignant cells[1]. PDT applications involve three components: a photosensitizer, a light source and oxygen. When the PS is exposed to suitable wavelengths of light, it can be activated and undergo energy transfer through its triplet excited state to generate cytotoxic reactive oxygen species (ROS) and mainly singlet oxygen ($^1O_2$), to kill the tumor cell by apoptosis or necrosis (Figure 3.1).
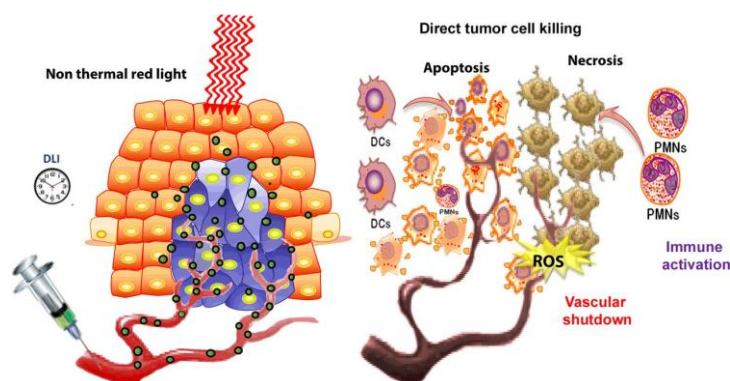
Figure 3.1. Illustrative scheme of Photodynamic Therapy[2]

The advantage of PDT is the possibility of the PS confinement in the tumor region and the localization of light irradiation over the tumor cell. Therefore, the tumor cell can be destroyed while the effects on healthy tissues are limited.

In order to improve the solubility of the PSs for its delivery and targeting in PDT, different kinds of drug-carriers are being studied such as quantum dots, gold, silica and polymeric nanoparticles, to control the PSs transport and their selective localization on tumor tissues.[3,4] In this sense, the application of nanoparticles in cancer therapy and diagnosis has shown several advantages, including overcoming multi-drug resistance, prevention of enzymatic degradation of drugs, and an improvement of tumor selectivity[5].

Among them, silica nanoparticles (NPs) provide an opportunity to introduce different types of compounds with various properties, either grafted on the NP surface (shell) or embedded inside pores (core). Indeed, since several years, an increasing number of researchers have been considering the possibility of using silica nanoparticles for numerous medical applications,[6,7] such as platforms for PDT[8].

Indeed, as previously described in chapter 2, the silica matrix provides a stable environment from a chemical and mechanical point of view when a fluorophore is encapsulated protecting it from external perturbations[9]. This fact has an especial interest in bioimaging[10], where NPs can be monitored by optical techniques both *in vitro* and *in vivo*. Fluorescent molecules encapsulated inside silica NPs are an alternative to "quantum dots" (QDs) fluorescent nanoparticles. The QDs are formed by elements from II-VI or III-V groups such as PbS or CdSe. With these materials, the most interesting point is the modulation of the nanoparticle size during the synthesis from 2 nm to 50 nm: their color, and therefore their excitation wavelength, changes with the exciton Bohr radius. However, the QDs are hydrophobic, which implies the addition of hydrophilic polymeric or inorganic coatings at the external surface. Besides, these kinds of materials bear toxic metallic atoms such as Pb^{2+} or Cd^{2+} [11]. That is why silica/dye hybrid systems are an attractive alternative for biomedical applications[11].

Therefore, in this work the use of silica nanoparticles is combined into two selected applications: bioimaging by embedding fluorescent dyes and photodynamic therapy (PDT) by grafting of singlet oxygen producing photosensitizers (PS).

3.1.1. Mesoporous silica nanoparticles (NP)

Among all of the available nanomaterials, numerous studies have investigated porous silica nanoparticles (NPs) due to their unique properties, such as a large specific surface area and pore volume, controllable particle and pore size and good biocompatibility. Compared with other porous nanocarriers, mesoporous silica nanoparticles with a pore size ranging from 2 nm to 50 nm are excellent candidates for drug delivery and biomedical applications.[6] Many of the methods developed for the synthesis of nanosized mesoporous silica spherical particles are based on the Stöber method, with an additional reactant added to the system, namely a surfactant [12].

In 1968, Stöber and Fink developed one system in which they were able to control the non-porous silica nanoparticle growth, initiating the so-called Stöber method [13].

The Stöber methodology is based on the Sol-Gel process, starting from an alkoxide such as TEOS (tetraethoxysilicate), TMOS (tetramethoxysilicate), etc, in a water/alcohol mixture and using an ammonium hydroxide as a catalyst. In this way monodisperse and electronically stabilized silica nanoparticles are obtained (Figure 3.2).
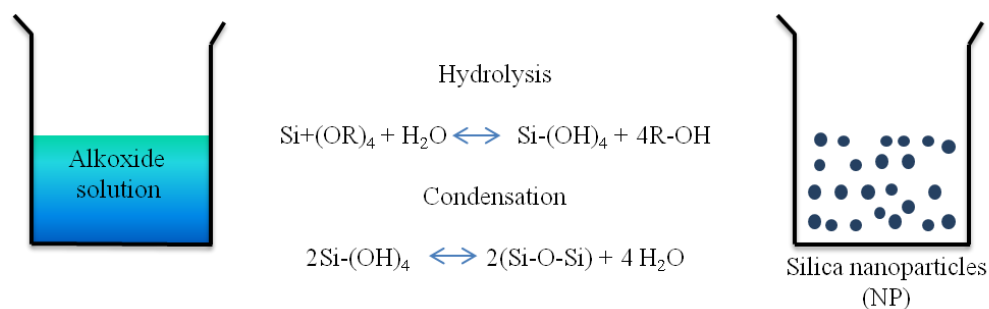
Figure 3.2. Scheme of Stöber method: Hydrolysis and condensation reactions.

In the bibliography there are different studies on the effect of synthesis conditions on the nanoparticles size or morphology[14]. In particular five parameters are the most important in the determination of NP size and size distribution: *i*) the nature and the concentration of the alkoxide, *ii*) the alcoholic solvent, *iii*) the catalyst, *iv*) the water concentration and *v*) the reaction temperature.[15] The variation of these conditions can induce the variation of the NP size from 25 nm to 2 μm. Thus, the following synthesis conditions have to be taken into account:

i) The reactivity of the used alkoxide, which governs the different sizes of the obtained nanoparticles. Tetramethylorthosilicate provides nanoparticles with a smaller size than tetrapentoxysilicate, maybe due to less steric effect during the nucleophilic attack by water.

ii) The alcoholic solvent: by increasing the alcoholic carbonyl chain, the nanoparticle size and the width distribution are larger. Therefore, in order to obtain smaller and more uniform nanoparticles, it is convenient to use methanol or ethanol as solvent[16].

iii) The influence of water/ammonia mixture: on synthesis without ammonia, the obtained nanoparticles are irregular and not spherical. However, in the presence of ammonia, the nanoparticles are spherical and larger. For that reason, the importance of the pH is crucial during the NP synthesis because a low pH values inhibits the

hydrolysis and condensation of TEOS and therefore the reaction time becomes very slow modifying the NP morphology and size [16,17].
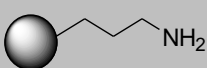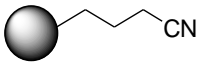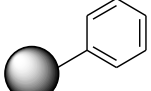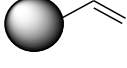
iv) The introduction of surfactant to the system results in complex interactions between the surfactant micelles and the silica oligomers formed during condensation. Particle morphologies are richer compared to the uniform nonporous Stöber silica spheres, and the particle size distributions were often broader.

v) The influence of temperature: previous studies have confirmed that by increasing the reaction temperature the NP size decreases[16].

Therefore, the particle size and particle size distributions are dependent on the alkaline medium, sodium hydroxide/ammonia concentration, surfactant type/concentration, presence of cosolvent, reaction temperature, and amount of TEOS added[12,18].

In this work, silica core-shell nanoparticles were synthesized (experimental chapter: the synthesis of silica NP, section 4.1.3) by a templated sol-gel process in order to control the particle size (around 50 nm), shape (spherical) and porosity[12]. They would be ideal carriers for drugs, especially for photosensitizers [19]. Moreover, silica surfaces are nontoxic, chemically inert, optically transparent, and easily functionalized[20]. In Table 3.1 different possibilities of silica NP functionalization are shown.

Table 3.1. Different possibilities of Silica NP functionalization

| Organoalkoxysilane	Functionalized NP structure
EtO$\diagdown$Si$\diagup$OEt $\diagup\diagdown\diagup$NH$_2$, EtO$\diagup$ OEt aminopropyltriethoxysilane (APTMS)	$\bigcirc\diagup\diagdown\diagup$NH$_2$
EtO$\diagdown$Si$\diagup$OEt $\diagup\diagdown\diagup$CN, EtO$\diagup$ OEt cyanopropyltriethoxysilane (CPTES)	$\bigcirc\diagup\diagdown\diagup$CN
EtO$\diagdown$Si EtO$\diagup$ OEt phenyltriethoxysilane (PTES)	$\bigcirc$
EtO$\diagdown$Si$\diagup\diagdown$ EtO$\diagup$ OEt vinyltriethoxysilane (VTES)	$\bigcirc\diagup\diagdown$

In order to introduce a PS by covalent grafting on the silica NP surface, its surface functionalization can be modulated. Two methods were used in this work:

➢ Direct polymerisation of a PS containing a triethoxysilyl group on the surface hydroxyls (or silanols) of silica, as for instance NP-RB2 or NP-BDP2 in the following.

➢ Conventional peptide coupling reaction between a NH_2-modifed silica and a PS containing a carboxylic group, as for instance NP-RB1, NP-BDP1 in the following.

3.1.2. Bioimaging with Rhodamine dyes

For biomedical applications, it would be interesting to use fluorescent dyes that absorb and emit in the red or Near-IR region, because these wavelengths are not invasive and the light penetration through the skin would be maximum.

In this work Rhodamine 6G and 640 were chosen (Figure 3.3) for embedding inside NPs core. The Rhodamines are xanthene derivatives characterized by their excellent photophysical properties such as high photostability, high molar absorption coefficients, and high fluorescence quantum yield. On the one hand, the probably most used laser dye, R6G, is characterized by its high absorption and emission in the visible region (530 nm and 550 nm respectively). On the other hand, Rhodamine 640 is characterized by its absorption and emission in the red region (575 nm and 595 nm respectively).
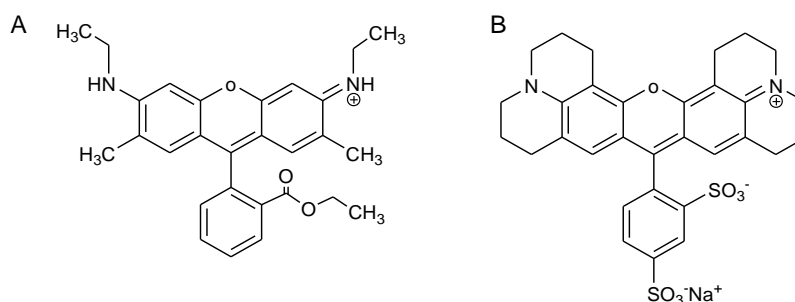
Figure 3.3. Molecular structure of Rhodamines A) Rhodamine 6G and B) Rhodamine 640.

The photophysics of Rhodamines strongly depends on the delocalization of the positive charge of the ammonium group through the electronic π-system of the xanthene ring. Besides, as previously described in Chapter 2, embedding Rhodamines in nanostructured systems could improve their lasing properties and enhance their photo- and thermo-stability. All this things make the use of Rhodamines as laser dyes or fluorescent markers as a good option for bioimaging[21].

3.1.3. Singlet oxygen production for PDT

Photosensitizers for PDT should fulfill several criteria: low toxicity in the absence of light, selective accumulation in cancer tissues, limited in-vivo stability to favor removal from tissues, high absorption in the red region (λ_{abs}> 620 nm, $\varepsilon \geq 50\,000$ M^{-1} cm^{-1}) to maximize light penetration depth in skin (Figure 3.4) and high quantum yield of singlet oxygen production[3]. PSs should also be water soluble, possessing at the same time a hydrophobic moiety to facilitate their penetration in membranes[22].
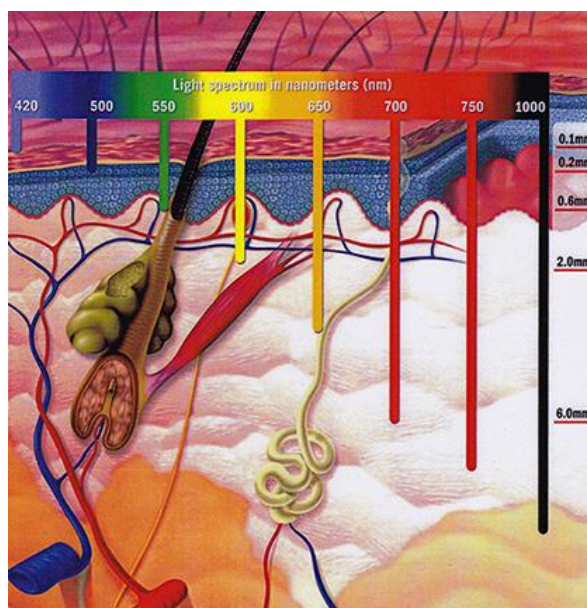
Figure 3.4. Light penetration depth in skin.

3.1.3.1. Singlet oxygen production by photosensitization

Photosensitized reactions are defined as the absorption of a radiation by a photosensitizer (PS), which induces the modification of another molecular species[23]. When the PS absorbs a photon (hυ), the singlet state S_n of the PS is populated. The S_n state is most often deactivated by non-radiative vibrational relaxation to the first singlet excited state (S_1), which can be also deactivated by different ways as shown Figure 3.5.
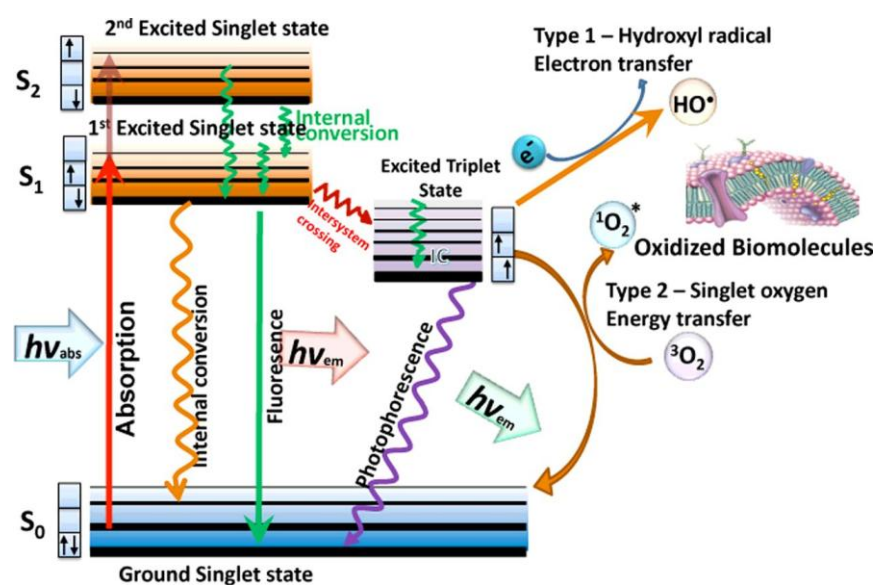
Figure 3.5. Jablonski diagram[2]

When considering now *only photosensitized oxidation processes*, two types of mechanisms are generally possible: i) the type I mechanism by electron transfer leading to radical species and ii) the type II mechanism by energy transfer leading to singlet oxygen production. In the following, we will only focus on Type II oxidation reactions through singlet oxygen production, since it is the main cytotoxic species in PDT [3,24–26].
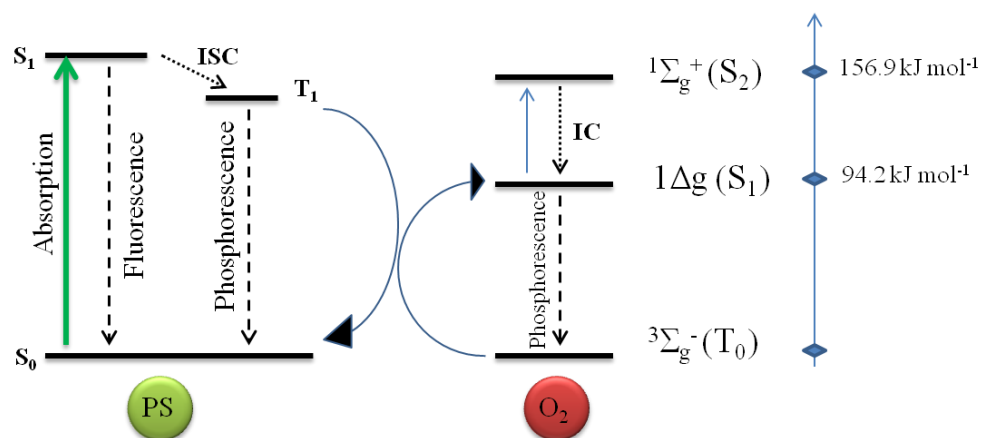
Figure 3.6. Types II reactions in Jablonski diagram with the representation of energetic levels of different ground and excited states of molecular oxygen.

Generally, in order to produce singlet oxygen efficiently, the PS after absorbing a photon undergoes intersystem crossing (ISC) to its triplet-excited state (T_n). Since ISC is a spin-forbidden transition, it becomes more probable when spin-orbit coupling is non-negligible (Figure 3.6). The spin-orbit coupling corresponds to the interaction of the electron spin magnetic moment with the magnetic moment due to the orbital motion of electrons. One consequence of spin-orbit coupling is the mixing of zero-order states of different multiplicity (S_1 and T_n in this case). The states are then partially mixed: the triplet state takes on some singlet state character and *vice versa*. Mechanistically, spin-orbit coupling enhancement is produced by heavy-atom effect, which corresponds to the enhancement of the rate of a spin-forbidden process by the presence of an atom of high-atomic number that is either part of, or external to, the excited molecular entity. Owing to this quantum mixing, the forbidden singlet-triplet transition, ISC, can take place and the triplet-excited state (T_n) of the PS can be populated. As for the $S_n \rightarrow S_1$ transition, by vibrational relaxation the first triplet excited state (T_1) is formed [23,27,28].

For efficient singlet oxygen production by energy transfer, the following conditions have to be fulfilled by the PS: high absorption coefficient in the spectral region of the excitation light, high ISC (intersystem crossing) quantum yield, long triplet lifetimes and triplet energy higher than the energy gap between the ground and a$^1\Delta_g$ states of O_2 (94.2 kJ mol^{-1}). The singlet oxygen-generating ability of a photosensitizer is measured by its quantum yield Φ_Δ (Equation 3.1).

$$\Phi_\Delta = \frac{n^0\text{mols (molecules) singlet oxygen produced}}{n^0\text{einstein (photons) absorbed}} \qquad \textbf{Equation 3.1}$$

Photosensitizers that can produce singlet oxygen only from their excited triplet state due to highly efficient intersystem crossing ($\Phi_{ISC} \approx 1$) and concomitant spin-allowed energy transfer from $^3PS^*$ to ground-state (triplet) molecular oxygen can have a maximum Φ_Δ value of 1 (e.g., 1H-phenalen-1-one or phenalenone in the following).

Once singlet oxygen is formed, several pathways can deactivate it: *i*) luminescence emission (phosphorescence at approx. 1270 nm), *ii*) chemical reaction with a substrate, *iii*) physical quenching (*e.g.* collisions with solvent and/or quencher molecules). It should be recalled here that singlet oxygen lifetimes τ_Δ (=$1/k_d$ with k_d rate constant of $^1O_2$ quenching by the solvent) is most often in the µs range and strongly dependent on the solvent: 3.3-7 µs in water, 54-85 µs in acetonitrile, 160-265 µs in chloroform[28].

3.1.3.2. Photosensitizers for PDT

Several classes of PS dedicated to the production of singlet oxygen and other reactive oxygen species (ROS) such as, xanthene dyes, anthracene, porphyrines, anthraquinone derivates, benzophenone derivates, fullerenes, are found in the literature[3].

Among photosensitizer from the xanthene-like dyes, rose bengal (Figure 3.7) is used as a popular reference in polar solvents such as in ACN or MeOH with Φ_Δ 0.5-0.8 in the Vis region (λ_{abs} 550 nm)[3]. On the other hand, Phenalenone is another common used reference under UV light (λ_{abs} 360 nm), due to its solubility in both polar and non-polar solvents with singlet oxygen quantum yield close to 1 mostly independent from the solvent[29].
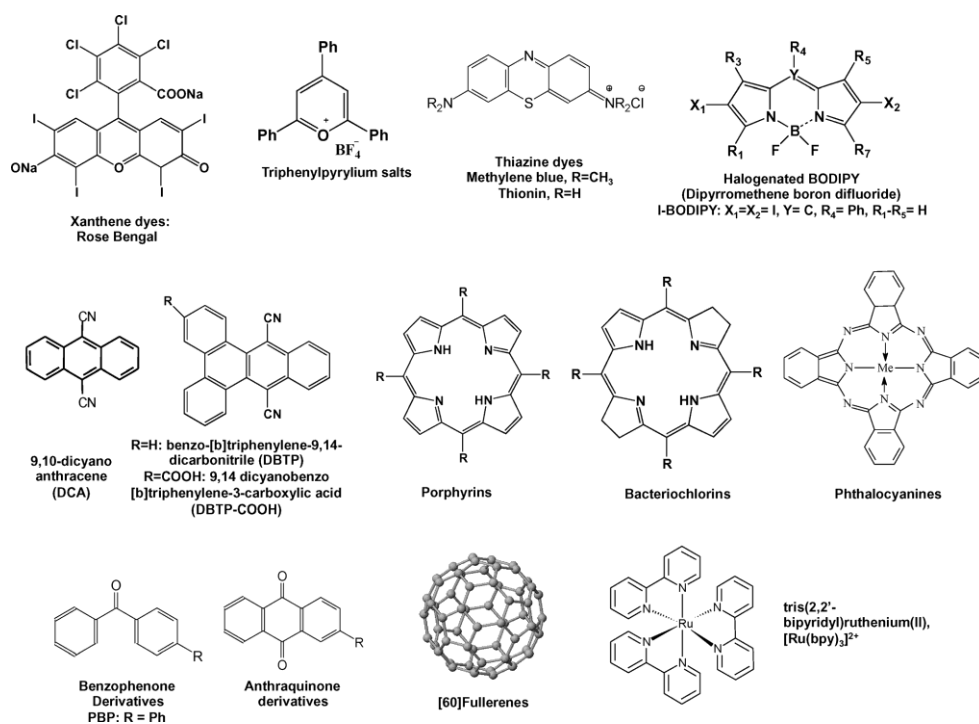
Figure 3.7. Molecular structure of different photosensitizers (PSs)[30]

The extension of photodynamic activity to cancer was initiated by the observation of porphyrins in tumors by Polycard in 1924 and various generations of PSs for PDT were developed over the 20th century (Figure 3.8).
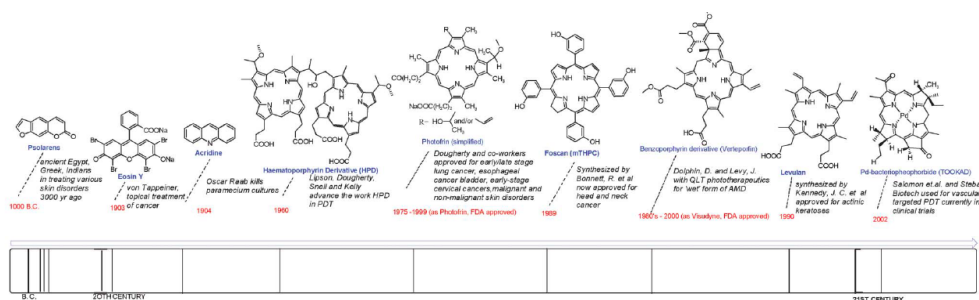
Figure 3.8. Milestones of photosensitizers in PDT from ref [25].

Actually, photosensitizers such as porphyrins have attracted much attention for biological singlet oxygen generation (Figure 3.8). However, they show several disadvantages such as chemical complexity, low molar extinction coefficients in the red-part of the Visible spectra, poor or low specific accumulation in tumour tissue, which considerably increases the doses requirement and the time between administration of drug and irradiation. Moreover, their extremely long clearance from the body may produce high cutaneous photosensitivity post-treatment[31,32] and other side effects[25,32,33]. For instance, one of the clinical PDT agents is porfimer sodium (Photofri®), a purified hematoporphyrin derivative, which has a low absorbance at 630 nm and needs extended irradiation from high-energy source. Moreover, its high photobleaching rates decrease the PDT efficiency.

The development of efficient PSs for PDT led to the second-generation PSs to overcome these problems of Photofri, opening the door to new generation of non-porphyrinic photosensitizers for oncological applications[25,32]. They focus on high molar extinction coefficients within clinic window (650-800 nm) for maximum light penetration, high singlet oxygen quantum yield, but also high selectivity for malignant tissue, rapid excretion, short drug–light intervals and minimal dark toxicity to minimize side effects. Moreover, the compounds should be relatively inexpensive to make them commercially available for extensive utilization.

Recently, a new type of chromophores, 4,4-difluoro-4-bora-3a,4a-diaza-s-indacene, also known as BODIPY (or BDP in the following) have attracted considerable attention, because of their very favorable chemical-physical features, including high extinction coefficients in the visible region and resistance to photobleaching[34]. Moreover, their synthesis versatility allows an exhaustive and selective structural modification/functionalization around the core structure of the chromophore, in order to modulate their properties and to enhance their therapeutic efficiency.

Although BDP dyes usually exhibit negligible efficiency of triplet (T_1) formation due to their high fluorescence quantum yields, heavy atoms (mainly iodine and bromine atoms) are incorporated directly to the BDP core to enhance the spin–orbit coupling, thereby favoring intersystem crossing to the triplet state[32,34,35]. However, the presence of heavy atoms in their structures to promote the required triplet state population would involve an intrinsic dark toxicity. As an alternative, the team of Flamigni recently discovered halogen-free photosensitizers based on orthogonal BODIPY dimers[36,37]. Such an orthogonal disposition of both chromophores has been

pointed out in the bibliography as an elegant way to attain singlet oxygen generation, avoiding the use of heavy halogen or metal atoms and their inherent toxicity[38–42].

3.1.4. Objectives of this work

According to the previous introduction, chapter 3 will contain two main sections:

The first one (3.2.1) is devoted to the photophysical study of new BODIPYs dyes designed for singlet oxygen production. Therefore, before immobilizing on NPs the most efficient and graftable BDPs derivatives, the quantum yields of singlet oxygen production of some of these newly prepared compounds such as halogenated BDPs and BDPs dimers (Figure 3.9, Figure 3.10) were first compared in solution.

Thus, the first section 3.2.1 is focused on the photophysical properties, modeling and the singlet oxygen generation of a series of new BDPs in various solvents. First, halogenated-BPD with different substitution patterns are studied (section 3.2.1.1). Next (section 3.2.1.2), several orthogonal BDP dimers with different substitution are analyzed taking into account also dissymmetric dimers with π-extended functionalization with the aim of shifting the absorption band to the red-part of the Visible spectra (section 3.2.1.2.4.). Finally, a rationally designed multichromophoric system based on BDP chromophores is detailed as a low-toxic agent with dual functionality (imaging and therapy) and panthochromatic action (Section 3.2.1.2.5.).

Halogenated BDP
(Dipyrromethene boron difluoride)
X= I, Br, Cl

BDP dimers
(Dipyrromethene boron difluoride)
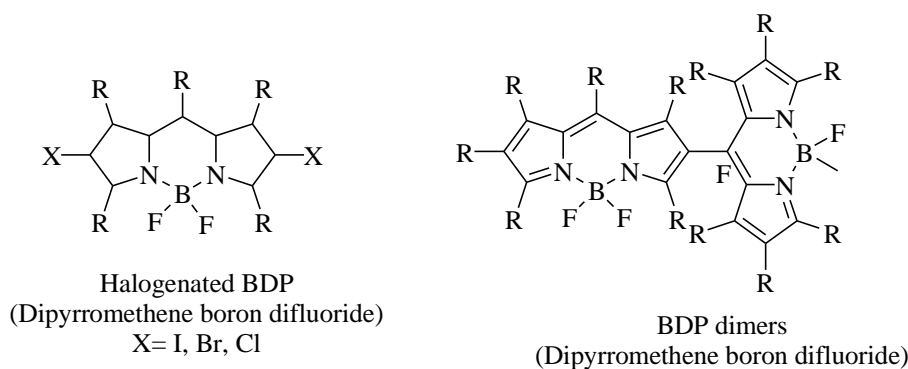
Figure 3.9. New halogenated BDP and BDP dimers molecular structure.

The second part of Chapter 3 (section 3.2.2) is devoted to nanoparticles for bioimaging and PDT. In this work, first different fluorescent dyes have been

encapsulated inside NP core for bioimaging application. To optimize the photophysical properties of the embedded dye molecule, the amount of dye was optimized during the silica NPs synthesis. Then, the immobilization of the most efficient PSs on the external surface of silica nanoparticles was performed, in order to implement them in Photodynamic Therapy (PDT) application. In particular, the PS used were the commercial xanthene dye (Rose Bengal or RB) and two lab-made BODIPY derivatives, BDP2 bearing a triethoxysilane group and BDP1 bearing a carboxylate group, grafted on NP surface (Figure 3.10). Finally, both applications have been combined, bioimaging by the fluorescent dye molecules encapsulation and PDT by grafting new PS on NP surface with dual behavior for a future application in theragnosis.

BODIPY-Si(OEt)$_3$ (BDP2)   Rose Bengal (RB)   BODIPY-Ph-COOH (BDP1)
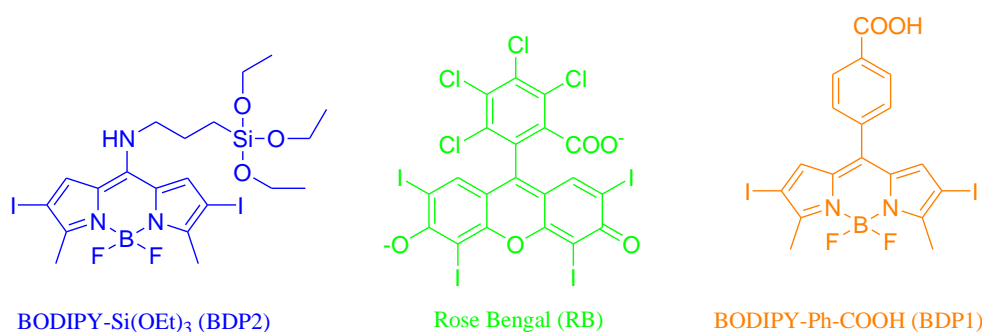
Figure 3.10. The molecular structure of PSs grafted on NPs in the following work.

3.2. Results and Discussion

3.2.1. New photosensitizers for singlet oxygen generation

Photosensitization is one of the most suitable routes for singlet oxygen ($^1O_2$) generation due to the mild condition of the process (visible-light irradiation, room temperature, and molecular oxygen as the only reagent). Many organic commercial photosensitizers (PS's) such as Phenalenone, Rose Bengale or Methylene Blue are well known to generate singlet oxygen. Nowadays, halogenated Boron DiPyrromethenes (BDPs) have attracted considerable attention, because of their favorable chemico-physical features, such as intense absorption bands in the visible region, and high photostability.
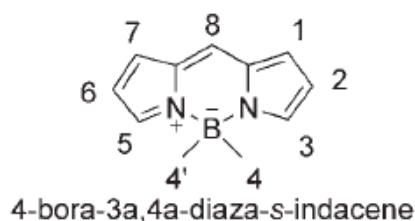
Figure 3.11: Numbering of atoms in BDPs series.

Their properties are practically unaffected by environmental conditions (solvent polarity or pH). Although BDPs usually exhibit negligible efficiency of T_1 formation due to their high fluorescence quantum yields, there are different tactics to enhance the intersystem crossing to the triplet state such as the incorporation of heavy atoms (such as Br, I) directly to the BDP core thereby favoring spin–orbit coupling.

On the other hand, a photosensitizer that does not contain heavy atoms will be more environmentally friendly and much safer for biological applications. For that purpose, the direct link of two BDP-based units through their 8 (*meso*) and 2 positions increases the effectiveness of the spin orbit coupling. Actually as confirmed in the following, the orthogonal disposition of both chromophores avoids any resonance interactions between their electronic clouds. This conformation favors singlet oxygen generation, avoiding the use of heavy halogen or metal atoms and their inherent toxicity[38,41].

3.2.1.1. New Halogenated-BDPs

In this section new halogenated-BPD with different substitution patterns at their meso position are studied. Particularly, several halogenated BDP with different halide atoms (Br or I) at 2,6 positions and different substitutions patterns at *meso* (or atom number 8) position such as substituted R-phenyl groups and heteroatoms such as methylthio (MeS) and amino groups (NR$_2$) are considered. In this sense, depending on the substituted heteroatom at the 8-position, the absorption and emission can be hypsochromically or bathochromically shifted, as previously described for non-halogenated BDP[43]. Since similar photophysical signatures in terms of absorption and fluorescence wavelengths are expected in the halogenated BDP series with the same substitution patterns at *meso* position, this work in mainly focused on the influence of different substitution patterns in several halogenated BDP on the singlet oxygen production, see Figure 3.12.
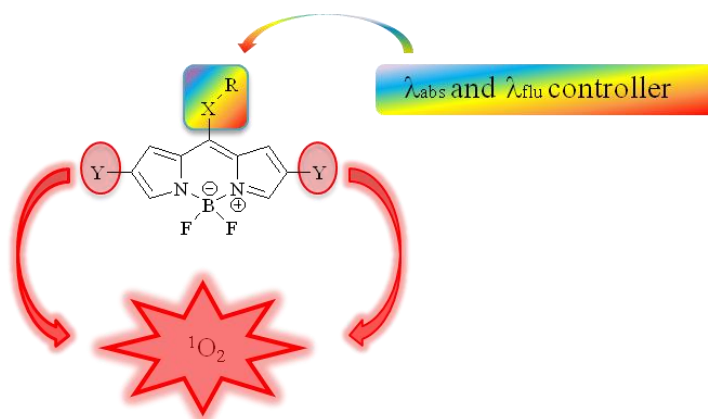
Figure 3.12. Illustrative scheme about the halogenated-BDP photophysical properties with different substituents at *meso* position.

3.2.1.1.1. 8-Phenyl-BDP

In this section, the photophysical properties and singlet oxygen quantum yields of several BDPs with halogenated atoms at 2,6 position and different aryl groups at *meso* (or 8) position are studied in ACN solvent. The results are compared with 2,6-Bromo-BDP without any substitution at its *meso* position (BDP1-2Br), considered as the reference compound (Figure 3.13).
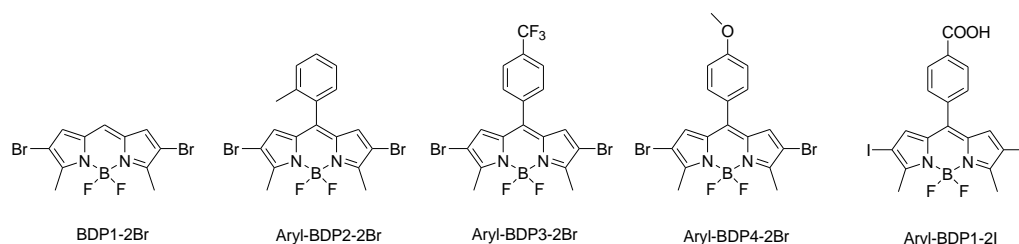
Figure 3.13. The molecular structure of 1) BDP1-2Br (the reference 2,6-dibromo-BDP), 2) aryl-BDP2-2Br (with *ortho*-methyl-phenyl group at *meso*), 3) aryl-BDP3-2Br (with *para*- CF$_3$-phenyl group at *meso*) 4) aryl-BDP4-2Br (with *para*-MeO-phenyl group at *meso*) and 5) aryl-BDP1-2I (with *para*-carboxyl-phenyl group) also denoted BDP1 in section 3.2.2.3.

The photophysical behaviour and more particularly the singlet oxygen quantum yields of the reference compound, 2,6-dibromo-BDP and of its homologous aryl-BDP2-2Br with an *ortho*-methyl-phenyl group substituted at the *meso* position are very similar (Table 3.2).

Table 3.2. Photophysical parameters and singlet oxygen quantum yields of the phenyl-BDP derivatives in ACN solvent. λ_{abs} (absorption maxima), ε_{max} (molar absorption coefficient), λ_{flu} (fluorescence maxima), Φ_{flu} (fluorescence quantum yield), Φ_{Δ} (singlet oxygen quantum yield).

Aryl-BDP	λ_{abs} [nm]	ε_{max} [10^4 M cm^{-1}]	λ_{flu} [nm]	Φ_{flu}	Φ_{Δ}^{1}
BDP1-2Br	538	2.5	552	0.40	0.50
aryl-BDP2-2Br	538	7.5	554	0.33	0.57
aryl-BDP3-2Br	542	5.1	568	0.20	0.33
aryl-BDP4-2Br	534	8.5	554	0.3	0.41
*aryl-BDP1-2I	550	7.3	578	0.03	0.66

[1]References RB in ACN with Φ_{Δ} = 0.53 measured in our laboratory with phenalenone as reference (Φ_{Δ} =1 in ACN)[29]
*This aryl-BDP1-2I is noted as BDP1 in section 3.2.2.3 and was grafted on the external NP surface.

It has been previously demonstrated that non-halogenated 8-aryl-BPD usually presents a very low fluorescence quantum yield, attributed to the deactivation by internal conversion due to the free rotational motion of the pendant 8-phenyl group that can also distort the indacene planarity[44–49]. However, the internal conversion is

drastically reduced by the substitution in *ortho* position of the phenyl group (here by a methyl group) because it hampers the free rotation due to sterical hindrance and the aryl group is blocked practically in perpendicular disposition (Figure 3.14). That means that the substituted aryl group does not take part in the electron delocalization because of its perpendicular disposition relative to the BODIPY core and consequently does not practically affect the photophysical properties and the singlet oxygen generation with respect to the unsubstituted 8-position. It is important to note here, that both 2,6-dibromo-BDPs, BDP1-2Br and aryl-BDP2-2Br, show interesting properties according to their dual behaviour, since fluorescence emission and singlet oxygen generation can be simultaneously recorded. They could thus act as theranostic platforms suitable for imaging (fluorescence) and treatment (photodynamic therapy, PDT).

Conversely, in the aryl-BDP3-2Br and aryl-BDP4-2Br derivatives, the aryl groups at meso position can freely rotate[50,51] and the internal conversion processes increases to the detriment of the radiative emission from the singlet state and the intersystem crossing to the triplet state, consequently decreasing both fluorescence and singlet oxygen production.
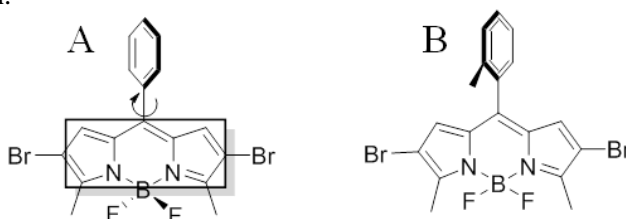
Figure 3.14. Aryl-BDPs rotamers (A) the phenyl group is free rotating and (B) the methyl substitution in *ortho* position reduces the phenyl free rotation.

On the other hand, the position of absorption and emission bands slightly depends on the electronegativity of the different groups attached at the phenyl in *para* position (Table 3.2 and Figure 3.15). Generally, with an electron donor substitution at *meso* position of the BDP such as in the case of 8-*para*-methoxy-phenyl compound (aryl-BDP4-2Br), the LUMO state is destabilized and the energy gap between both states increases, producing a blue shift in their respective spectral bands (Figure 3.15). However, if the substituent is an electron withdrawing group such as in 8-*para*-trifluoromethyl-phenyl (aryl-BDP3-2Br), the LUMO state is more stabilized and the energy gap between both states is lower, giving a red-shift of the bands relative to the un-substituted BDP at *meso* position (Figure 3.15)[52].
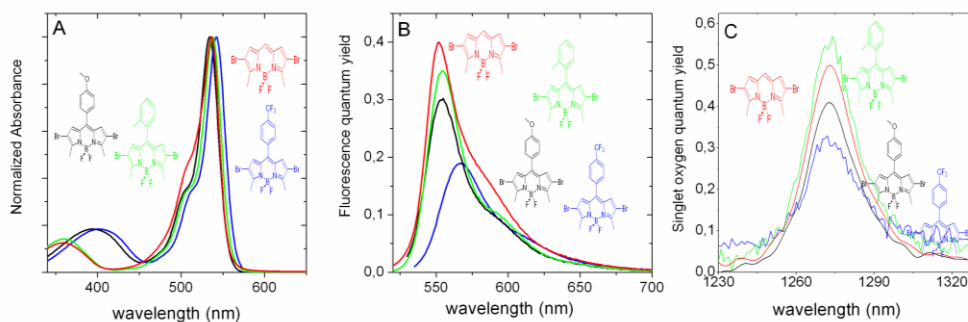
Figure 3.15. Aryl-BDPs (A) Normalized absorbance spectra, (B) Fluorescence quantum yield spectra (C) Singlet oxygen quantum yield spectra.

More importantly, the nature of the group substituted at *meso* position, i.e. methoxy-phenyl *vs* trifluoromethyl-phenyl, has a significant impact on the fluorescence emission and singlet oxygen generation. Indeed, taking BDP1-2Br as the reference, the aryl-BDP4-2Br with the electron donor MeO group shows a lower decrease in the efficiency of both processes relative to the aryl-BDP3-2Br with the electro withdrawing CF$_3$ group. This effect could be related to the activation of a weakly or non-emissive intra charge-transfer (ICT) process between the BDP core and the substituent group at the *meso* position, process already described in similar compounds[53,54]. Accordingly, the more activated is the ICT state, the less favoured will the radiative deactivation by fluorescence from the locally excited (LE) and the intersystem crossing to the triplet state (Figure 3.16).
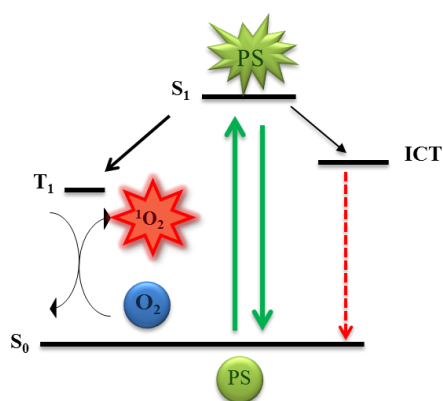
Figure 3.16. Photophysical processes in competition for meso substituted BDPs.

In fact, according to the Hammett parameters, 0.54 and -0.27[55], for trifluoromethyl and methoxy groups, respectively, the electron withdrawing character of CF_3 is relatively higher that the electron donor ability of the MeO groups. Consequently, the CF_3 substituted derivative would activate in a higher extent the ICT process from the BODIPY core to the aryl substituent than the MeO substituted compound where the ICT process is activated from the aryl to the BPD core. Nevertheless, the effect of the ICT on the singlet oxygen production will be more clearly seen below in the 8-Amino-BODIPY derivatives (section 3.2.1.1.3), in which amines with different electro-donor abilities are substituted at the meso-position of the BODIPY.

From these results it can be concluded that the bromination of the BDP core at 2 and 6 positions leads to a balanced contribution of fluorescence emission and singlet oxygen generation. Consequently, they could be used as theranostic platforms for both imaging (fluorescence) and treatment (photodynamic therapy, PDT). The substitution of the aryl group at *meso* position with no restricted rotation significantly decreases both fluorescence emission and singlet oxygen production due to the increase of internal conversion processes. Depending on the electron donor or electron withdrawing capacity of the groups substituted at *meso* position, the efficiency of both processes can also be disturbed (Φ_{fl} and Φ_{Δ}) by the competitive activation of an ICT process.

On the other hand, with respect to the brominated aryl-BDP, the iodination at 2,6 positions of the BDP (aryl-BDP1-2I, also further named BDP1 in the next section 3.2.2.3) induces a higher red shift in the absorption and fluorescence spectral bands and also a higher singlet oxygen generation ($\Phi_{\Delta} = 0.66$). This is due to a greater heavy atom effect, and accordingly a more efficient intersystem crossing process is reached, resulting in a negligible fluorescence capacity (Table 3.2).

3.2.1.1.2. 8-Methylthio-BDP

In this section, the photophysical properties and the singlet oxygen generation of BDPs with a methylthio substituted at *meso* position but with different halogenated atoms, such as Br or I, at 2- and 6- position are studied in ACN solvent and compared with the reference compound BDP1-2Br (Figure 3.17).

Figure 3.17. Methylthio-BDP molecular structure (1) the reference 2,6-dibromo-BDP, BDP1-2Br (2) methylthio-BDP2-2Br, (3) methylthio-BDP3-Br and (4) methylthio-BDP4-2I.

As previously described for non-halogenated BODIPYs[52], the methylthio substitution at meso position modifies both the absorption and emission wavelengths. The methylthio-BPD2 compound shows an apparent blue shift of the absorption band relative to BDP1-2Br (Figure 3.19), ascribed to the stabilization of new resonance form, where the methylthio is delocalized though the BDP core (resonance form B in Figure 3.18). This resonance form is favoured in polar media, such as ACN solvent, and is responsible of the blue-shift in the absorption spectra[56]. Additionally, the shoulder at lower energies observed in the absorption spectra (Figure 3.19) is attributed to the contribution of normal cyanine-like resonance form with a more delocalized π-system (resonance form A in Figure 3.18). However, the fluorescence band for methylthio-BPD2 is red-shifted with respect to the reference compound BPD1-2Br (Table 3.3 and Figure 3.19), since the cyanine-like resonance form (form A) is the only responsible species of the emission. As already published[52], the contribution of the non-emissive resonance form B (methylthio electronically coupled with the BPD core) induces a lower fluorescence quantum yield in methylthio-BPD2-2Br with respect to BPD1-2Br.

**Figure 3.18.** Resonance structures of the BODIPY core upon electronic coupling with methylthio group at position 8.

Table 3.3. Photophysical parameters and singlet oxygen production of the methylthio-BDP derivatives in ACN solvent. λ_{abs} (absorption maxima), ε_{max} (molar absorption coefficient), λ_{flu} (fluorescence maxima), Φ_{flu} (fluorescence quantum yield), Φ_{Δ} (singlet oxygen quantum yield), k_t^{PS} (rate constant of singlet oxygen total quenching by the PS).

Methylthio-BDP	λ_{abs} [nm]	ε_{max} $(10^4\,M\,cm^{-1})$	λ_{flu} [nm]	Φ_{flu}	Φ_{1O2}	k_t^{PS} $[M^{-1}\,s^{-1}]$
BDP1-2Br	538	2.5	552	0.4	0.50^2	$\leqq 1.1\,10^8$
Methylthio-BDP2-2Br	527	4.2	576	0.33	0.62^1 0.61^2	$5.4\,10^8$
Methylthio-BDP3-Br	515	4.3	555	0.51	0.42^2	$\leqq 2.6\,10^7$
Methylthio-BDP4-2I	533	4.3	588	0.04	0.82^1 0.85^2	$\leqq 4.6\,10^7$

[1] Reference PN in ACN (Φ_{Δ} = 1)
[2] Reference RB in ACN (Φ_{Δ} = 0.53)

Halogenation also strongly influences the position of the absorption and emission bands (Table 3.3 and Figure 3.19). In fact, previous studies have confirmed that successive halogenation of the BDP core gave rise to a progressive bathochromic shift of the spectral bands[50]. This is also confirmed for the aryl-BPDs described above with different halogen substitutions (Table 3.2). More importantly, the type and extent of halogenation on the BDP core will have an important impact on the fluorescence capacity and the singlet oxygen generation due to the heavy atom effect. Thus, the methylthio-BPD4-2I with two iodine atom substituted at 2,6- position is characterized by a very low fluorescence quantum yield (φ_{fl} = 0.04) as a consequence of a strong enhancement of the intersystem crossing relative to methylthio-BPD2-2Br with two bromide atoms (Φ_{fl} = 0.33) or to the mono-brominated methylthio-BPD3-Br (Φ_{fl} = 0.51) (Figure 3.19 and Table 3.3).
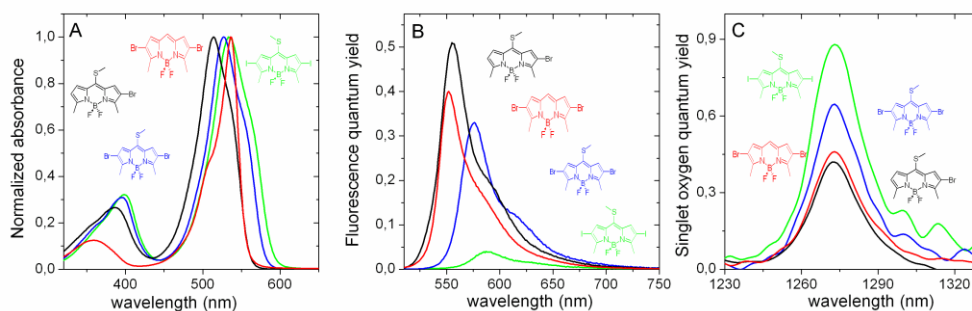
Figure 3.19. Methylthio-BDP (A) Normalized absorbance spectra, (B) Fluorescence quantum yield spectra (C) Singlet oxygen quantum yield spectra.

In this regard, the effect of the type and extent of halogenation of the methylthio-BDP on the singlet oxygen quantum yield is deeply analysed. In the case of methylthio-BDP compounds, the singlet oxygen quantum was determined both by direct method (Figure 3.19C) using as references the commercial Rose Bengal (RB) and/or Phenalenone (PN) in acetonitrile (Table 3.3). Moreover, to get extra information, the indirect method was also applied to the methylthio-BDP4-2I compound using 9,10-dimethylanthracene (DMA) as a chemical probe.

As expected, methylthio-BDP4-2I shows the highest singlet oxygen generation, Φ_Δ = 0.82-0.85, (Table 3.3) since the spin-orbit coupling depends on the fourth power of the atoms orbital quantum number. The substitution by two iodine atoms will thus induce a more efficient ISC relative to the substitution by two bromine atoms, (methylthio-BDP2-2Br: Φ_Δ = 0.61-0.62), or even with respect to the compound with only one bromine atom attached to the BDP core (methylthio-BDP3-Br: Φ_Δ =0.42).

The more relevant aspect in these methylthio-BODIPY compounds, is that owing to their relatively intense S_0-S_2 absorption band around 400 nm ($\varepsilon \sim 1.3 \times 10^4$ M cm^{-1}, Figure 3.19), the determination of the singlet oxygen quantum yield is possible by the direct method exciting either in the UV (with Phenalenone as reference) or in the green-yellow Visible range (using Rose Bengal as standard, Table 3.4). Actually, similar singlet oxygen quantum yields were obtained in ACN for these methylthio-BODIPYs with either reference. This result in turn also validates the singlet oxygen quantum yield determined for RB in ACN (Φ_Δ = 0.53), for which very scattered values (Φ_Δ = 0.42-0.83) may be found in the literature [23,57–59].

In the following, the analysis of singlet oxygen quantum yields of methylthio-BDP4-2I in several solvents of various polarities was addressed. Importantly, the singlet oxygen quantum yield of methylthio-BDP4-2I in ACN, THF, dichloromethane (DCM) or chloroform are very similar ($\Phi_{\Delta(PN)}$ = 0.79-0.82, Table 3.4) when phenalenone (PN) is used as reference. However, when RB in ACN is used as standard, greater discrepancies are observed using eq. 4.7 (experimental section), with an over estimation of the singlet oxygen quantum yields ($\Phi_{\Delta(RB)}$ = 1.15-1.31), particularly in chlorinated solvents, while consistent values with the previous ones are obtained in ACN or THF ($\Phi_{\Delta(RB)}$ = 0.82-0.85). Although Equation 4.7 (experimental section) may properly correct the differences in the lifetime of $^1O_2$ of each solvent (*i.e.* ACN *vs* THF solvents, Table 3.4), it does not take into account other those factors such as the different refractive index or luminescence collection efficiencies of the

solvents (see experimental section equation 4.8 and 4.9)[23,60]. The reason is that the solvent polarity is not the only factor governing singlet oxygen quenching and lifetimes and other parameters dealing with the formation and stability of the collision between a solvent molecule S and oxygen (complex S-O_2), out of the scope of this work, have to be considered.

In other words, since RB is poorly soluble in DCM or $CHCl_3$ and accordingly cannot be used as a reference in such solvents, it is highly possible that the values measured using RB in ACN as standard are poorly reliable. This could account for quantum yields higher than 1 in chlorinated solvent. However the lifetime correction is sufficient in THF (Table 3.4).

Table 3.4. Methylthio-BDP4-2I singlet oxygen quantum yield and lifetime of $^1O_2$ in different solvents. $E_T(30)$ is the Reichardt parameter that indicates the polarity of the solvents.

Solvent	$E_T(30)$	Φ_{PN}[1]	Φ_{RB}[2]	τ_Δ
ACN	45.6	0.82	0.85	81
THF	37.4	0.81	0.82	23
DCM	40.7	0.79	1.15	97
CHCl3	39.1	0.80	1.31	201

[1] PN as reference in each solvent assuming $\Phi_{PN} = 1$
[2] RB as reference in ACN ($\Phi_{RB} = 0.53$)

Moreover, the rate constants of the total quenching of singlet oxygen by the PS itself in ACN, k_t^{PS} (M^{-1} s^{-1}) were determined for these methylthio-BDPs, by varying the PS concentration relative to the reference R (rose bengal) according to Equation 4.5, see experimental section.

The independence of the $(S_e^R/ S_e^{Ps})(\alpha^{Ps}/\alpha^R)$ with respect to the concentration for compounds BDP1-2Br, methylthio-BDP4-2I and methythio-BDP3-Br (Figure 3.20 stars, triangles and squares) indicates that the quenching of $^1O_2$ by these BDPs was negligible (Table 3.3), with respect to the quenching by the solvent [k_t^{PS}[Ps] $<<$ 0.1 k_d]. On the other hand, a much more significant $k_t^{PS} = 5.4 \cdot 10^8$ $M^{-1}s^{-1}$ is obtained for the methythio-BDP2-2Br (Figure 3.20 rhombus, Table 3.3).
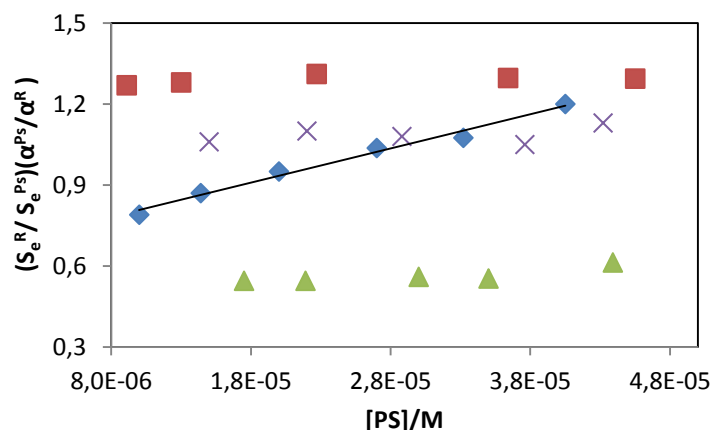
**Figure 3.20.** Variation of the ratio of the $^1O_2$ emission signal for the reference and PS as a function of the PS concentration in ACN at room temperature: BDP1-2Br (stars), methylthio-BDP3-Br (squares), methylthio-BDP4-2I (triangles) and methylthio-BDP2-2Br (rhombus). Errors: approx 10%.

In order to confirm these results, the $^1O_2$ specific chemical probe, 9,10-dimethylanthracene (DMA, Figure 3.21), is added to the photosensitizer solution in ACN. In this case, the singlet oxygen generation can be followed photometrically since the characteristic absorption bands in the 300-400 nm range of DMA will gradually disappear due to the formation of the endoperoxide as the reaction product (without any absorption bands in the UV-Vis region due to the lack of π-conjugations[61]) (Figure 3.21). To carry out such an analysis, the main absorption band of the photosensitizer should not overlap the absorption bands of the chemical probe.

First, the intensity of the absorption band of methylthio-BDP4-2I is constant during the reaction time (Figure 3.22), confirming its stability against photobleaching on the timescale of the experiment. A relatively fast decrease of the absorption bands of DMA with time is observed and the singlet oxygen quantum yield calculated by this approach (Equations 4.11-4.13 in experimental section using $k_t^Q = 8.8 \times 10^7$ M^{-1} s^{-1} and $k_r = 5.3 \times 10^7$ M^{-1} s^{-1} values for DMA in ACN found in the literature)[62,63] is around $\Phi_\Delta \sim 0.75$. This value is in good agreement with the quantum yield determined by the direct method given the possible errors on the kinetic rate constants from the literature
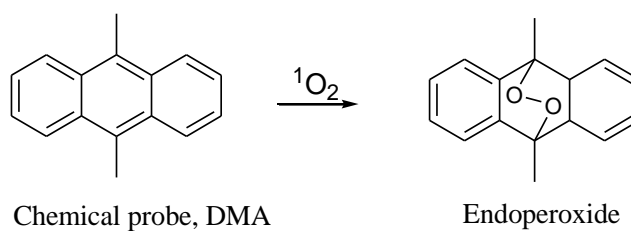
Figure 3.21. The reaction of DMA with singlet oxygen.
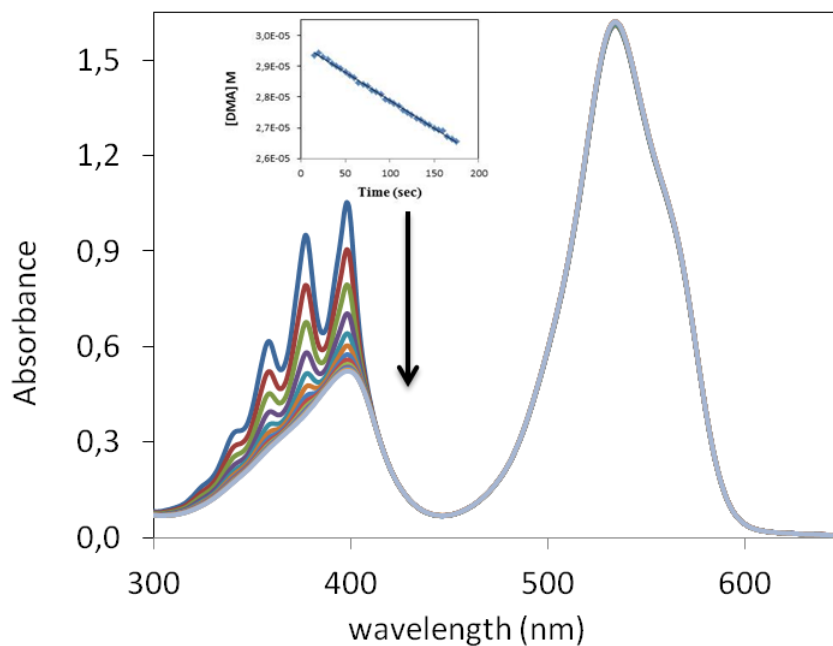
Figure 3.22. A) Evolution of the absorption spectra of a solution containing the methylthio-BDP4-2I and DMA with time upon 547 nm excitation (Inset: the kinetic of DMA recorded every 5s by excitation of methylthio-BDP4-2I at 547 nm).

From all these results, it appears that methylthio-BDP4-2I could be further analysed as a suitable solvent-independent standard for the UV and green-yellow region of the Vis spectra, instead of the usual RB standard, with a possible use in chlorinated solvents such as CH_2Cl_2 or $CHCl_3$ where RB is not soluble. Thus, this BDP will be used as a reference for the other halogen-free BDPs studied in the next sections 3.2.1.2 and 3.2.2.2.

3.2.1.1.3. 8-Amino-BDP

In this section, the photophysical properties and the singlet oxygen generation of BDPs with two iodine atoms at 2,6 position and different amino groups with various substitution patterns at *meso* position are analysed (Figure 3.23).
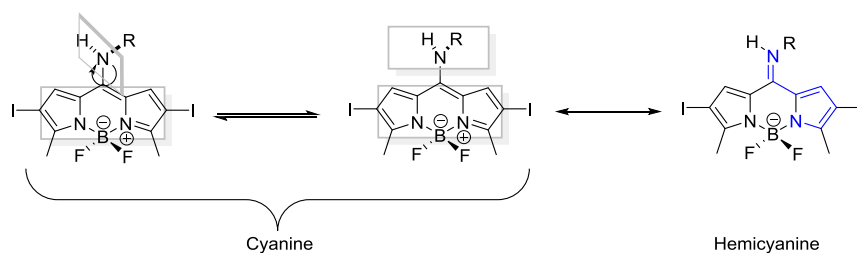

amino-BDP1-2I   amino-BDP2-2I   amino-BDP3-2I
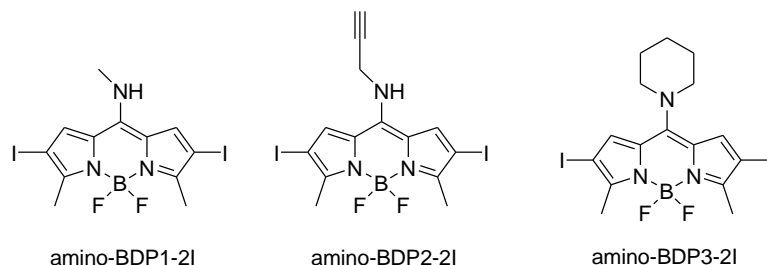
Figure 3.23. The 8-amino-BDP molecular structure (1) amino-BDP1-2I, (2) amino-BDP2-2I and (3) amino-BDP3-2I.

As commented above, the position of the spectral bands markedly depends of the heteroatom attached at the *meso* position of the BDP and more particularly on the electronegativity of that heteroatom. That is, the larger electron donor capacity of the group at *meso* position, the higher will be the hypsochromic shift because the hemicyanine resonance structure (Figure 3.24) is more favoured[43,52,56,64].

Cyanine   Hemicyanine

Figure 3.24. 8-amino BDP1-2I rotamers.

Indeed, the BDP with a NHMe substitution at *meso* position (amino-BDP1-2I) gives a very pronounced blue-shift, more than 100 nm (Table 3.5, Figure 3.25), with respect to the BDP with methylthio groups at *meso* position and the same halogenation pattern (λ_{max} 533 nm for methylthio-BDP4-2I, Table 3.3 in section 3.2.1.1.2), in agreement with their respective Hammett parameters (σ_p^+ = -1.81 for NHMe and σ_p^+ = -0.60 for SMe)[55].
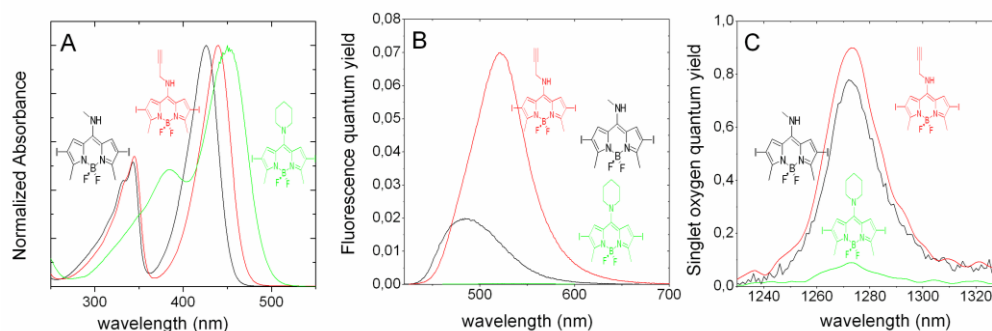
Figure 3.25. The amino-BDP (A) normalized absorbance spectra and (B) the fluorescence quantum yield spectra (C) the singlet oxygen quantum yield spectra.

Table 3.5. Photophysical parameters and singlet oxygen production of amino-BDP derivatives in ACN solvent. λ_{abs} (absorption maxima), ε_{max} (molar absorption coefficient), λ_{flu} (fluorescence maxima), Φ_{flu} (fluorescence quantum yield), Φ_{Δ} (singlet oxygen quantum yield), k_t^{PS} (rate constant of singlet oxygen total quenching by the PS).

8-amino-BDP	λ_{abs} [nm]	ε_{max} [10^4 M cm^{-1}]	λ_{flu} [nm]	Φ_{flu}	Φ_{1O2}[1]	k_t^{PS} [M^{-1} s^{-1}]
*8-amino-BDP1-2I	426	3.9	484	0.02	0.78	$\leqq 1.2 \; 10^7$
8-amino-BDP2-2I	440	3.8	521	0.05	0.96	$\leqq 3.9 \; 10^7$
8-amino-BDP3-2I	450	3.4	535	<0.01	0.09	ND

[1] Reference PN in ACN ($\Phi_{\Delta} = 1$)

*due to the similarity between amino-BDP1-2I with BDP-Si(OEt)$_3$ used in section 3.2.2.3 (denoted as BDP2) for the grafting on NP (Figure 3.10), the same value of singlet oxygen quantum yield is assumed.

ND not determined

The fluorescence spectra of these amino substituted iodo-BPDs show a very poor emission band ($\Phi_{fl} \leq 0.05$) with respect to the analogous compounds without any heavy atom ($\Phi_{fl} \sim 0.8$ in ethanol[52]). This is attributed to the presence of halogen atoms, which enhances the intersystem crossing (ISC) process to the triplet state. However, in these halogenated BODIPY, the competitive formation of an ICT state, which strongly depends on the amine-group substitution pattern at the *meso* position, has a higher impact on the singlet oxygen production than on their fluorescence. Indeed, the replacement of the methyl group ($\sigma_p^+ = -0.31$) in amino-BDP1-2I by a propargyl group

in amino-BDP2-2I (lower electron-donor strength, $\sigma_p^+ = +0.18$), disfavours the activation of ICT and consequently increases the singlet oxygen production ($\Phi_\Delta = 0.96$, Table 3.5) with respect to compound amino-BDP1-2I ($\Phi_\Delta = 0.78$). Note here that the lower electron donor capacity of the amine in amino-BDP2-2I is also in agreement with the lower blue shift recorded with respect to amino-BDP2-2I (Table 3.5).

As a result, both amino-BDP1 and -BDP2 represent an interesting alternative as photosensitisers for singlet oxygen production with high quantum yields upon blue Visible light and UV excitation. Moreover, the $^1O_2$ production by those amino-BODIPY is independent of their concentration (Figure 3.26), indicating a negligible self-quenching of singlet oxygen ($k_t^{PS}[PS] << 0.1k_d$, Table 3.5).
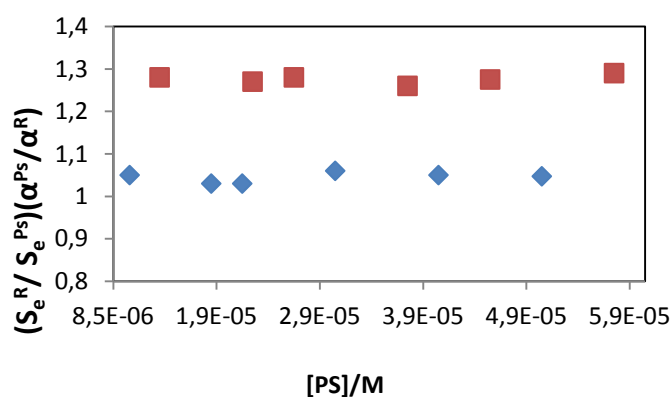
Figure 3.26. Variation of the ratio of the $^1O_2$ emission signal for the reference and PS as a function of the PS concentration in ACN at room temperature: amino-BDP1-2I (squares) and amino-BDP2-2I (rhombus). Errors: approx 10%.

On the other hand, although the tertiary amines have higher electron-donating character, the hypsochromic shift of amino-BDP3-2I is smaller than that observed for secondary amines BDP (amino-BDP1-2I and amino-BDP2-2I). In this particular case, the cyclic amine is not in a coplanar arrangement with BDP due to steric hindrance, reducing the probability of the formation of the hemicyanine, and consequently the shift of the spectral bands to the blue (Figure 3.25). Moreover, this accounts for the negligible singlet oxygen generation by amino-BDP3-2I, that due to the fee rotation of the amine group (Figure 3.27), enhances the internal conversion process at the expense of intersystem crossing to the triplet state and consequently of singlet oxygen generation, as previously commented in section 3.2.1.1.1 for the aryl-BDP

compounds. In fact, as a consequence of these motions, a twisted intramolecular charge transfer state (TICT) may also be favoured, which will also compete with the radiative emission from the singlet state (fluorescence) and intersystem process to the triplet state (singlet oxygen production). Therefore, the substitution of piperidine group at the *meso* position in not recommended.
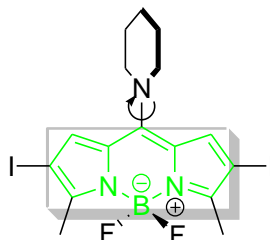
Figure. 3.27 The amino-BDP3-2I free rotation scheme**.**

In the following, due to the similarity in the molecular structure between BDP2 (BODIPY-Si(OEt)$_3$) used in section 3.2.2.3.2.2 for the grafting on NP (Figure 3.10) and 8-amino-BDP1-2I, the same value of singlet oxygen quantum yield were assumed for both compounds (measured for 8-amino-BDP1-2I).

3.2.1.1.4. Conclusions of new halogenated BDPS

First, the type and extent of halogenation on the BDP core have a significant impact on the fluorescence capacity and the singlet oxygen generation due to the heavy atom effect. Thus, by bromination of the BDP core (at 2-position or both 2,6 positions), the chromophores exhibit a dual functionality since they maintain both a high enough fluorescence emission ($\phi_{fl} \sim 0.40\text{-}0.30$) suitable for bioimaging together with a high enough triplet state population to promote singlet oxygen generation ($\Phi_\Delta \sim 0.50\text{-}0.60$) for PDT. A balanced efficiency is thus achieved, which could be important for theranosis application. On the other hand, by the iodination of the BPD at 2,6 positions, the spin orbit coupling is enhanced and very high singlet oxygen quantum yield are obtained ($\Phi_\Delta \sim 0.8\text{-}0.9$) at the expense of the fluorescence efficiency ($\phi_{fl} < 0.1$).

On the other hand, the substitution patterns at the *meso* position of the BPD plays also an important role in the radiative deactivation of the first singlet excited state, owing to possible competitive internal conversion and internal charge transfer processes. Thus, the substitution of groups with free rotational motions (such as phenyl and piperidine groups) deactivates both fluorescence and singlet oxygen generation due to the increase of internal conversion processes. Moreover, the electron-donor strength of the substituent at the meso position (especially when including heteroatoms) not only modifies the position of the spectral bands but also strongly affects the fluorescence and singlet oxygen quantum yields. In this regard, substituents with relatively high electron-donor strength such as NHMe, will activate an ICT state reducing the efficiency of the fluorescence and the singlet oxygen generation.

Importantly, a new standard for singlet oxygen quantum yield determination based on an iodo-BODIPY with a methylthio at its meso position is proposed. This compound shows intense bands in the Visible (λ_{abs} = 533 nm, $\varepsilon_{max} > 40\ 000\ M^{-1}\ cm^{-1)}$) and in the UV range ($\lambda_{abs}$ = 400 nm, $\varepsilon_{max} > 10\ 000\ M^{-1}\ cm^{-1}$), together with high singlet oxygen quantum yields ($\Phi_\Delta \sim 0.8$), practically solvent-independent in a broad polarity range. Moreover, no noticeable quenching of $^1O_2$ by this PS was observed ($kt^{PS}[PS] << k_d$). Other favorable chemico-physical features already demonstrated for BODIPY-dyes (i.e. low photobleaching and high lipophilicity) make this particular BODIPY a possible alternative as a standard photosensitizer for UV and Visible range, in a large variety of solvents, including chlorinated ones, even if further work is needed to firmly establish it as a universal reference[65–67].

3.2.1.2. Halogen-free BDP

Although the halogenated-BDP, previously described in section 3.2.1.1, have shown a relatively high oxygen production, particularly the iodinated-BDP, the presence of heavy atoms in their structures, to promote the required triplet state population, will involve an intrinsic dark toxicity. Alternative new halogen-free orthogonal BDP dimers with significant singlet oxygen production have been recently reported [38–41].

Indeed, different studies have been carried out to elucidate the mechanism of the singlet oxygen production in these orthogonal BDP dimers. On the one hand, experimental and computational studies conducted by Akkaya *et al*., assigned the high ISC quantum yield in these bis(BDP)s to the generation of degenerate HOMOs and LUMOs as a consequence of the orthogonal arrangement of similar subunits in which the π-mixing is avoided. They therefore retained undisturbed monomeric orbital energies. Accordingly, the singlet oxygen production decreased significantly if orthogonality between the two parts of the dimer is distorted or if the dimer is formed by dissymmetric BDP units [38,41,42].

On the other hand, other plausible alternative is that the triplet state population takes place from intramolecular charge transfer states (ICT states) generated by charge recombination (ICT transition) in the singlet excited states [68–70]. Generally, it has been proposed that in totally orthogonal dyads, intramolecular charge transfer transitions occur upon excitation, usually implying a change in the angular momentum, which should be compensated by a fast spin-flip to conserve the overall system angular momentum. Indeed, previous studies performed on orthogonal donor-acceptor dyads with a fixed dihedral angle θ = 90º between the donor and acceptor π systems demonstrated an efficient intersystem crossing via a *spin-orbit charge-transfer intersystem crossing mechanism* denoted as (SOCT-ISC)[71–73]. Particularly, it was demonstrated that orthogonal BDP dimers showed singlet oxygen generation in nonpolar solvents but not in the polar ones, due to the competition between the intramolecular charge transfer (ICT) more favored in polar solvents and intersystem crossing to the triplet state (ISC)[74].

In this section, 3.2.1.2., the photophysical characterization, modeling, and singlet oxygen production is studied for a series of halogen-free BDPs based on covalently tethered BDP in orthogonal disposition with the aim of understanding the mechanism of the singlet oxygen production in orthogonal BDP dimers.

First, the photophysical properties and singlet oxygen production of dimers constituted by two identical BDP 546 units joined in (2,8'), was studied in solvents of different polarity (Figure 3.28). Then, other orthogonal BDP dimers with different donor/acceptor substitution patterns were analyzed to reveal the mechanism of singlet oxygen production in such compounds. Next, with the aim of shifting the absorption band to the red part of the Visible spectra, dissymmetric dimers with π-extended functionalization are discussed and influence of asymmetric substitution in terms of singlet oxygen generation is studied. Finally, a rationally designed multichromophoric molecular dye based only on BDP chromophores is detailed as a low-toxic agent with dual functionality (imaging and therapy) and panthochromatic action.

3.2.1.2.1. BDP DIM 546 as reference dimer.

Photophysical characterization, modeling, and the determination of the quantum yield of singlet oxygen production were performed in a series of multiple covalently tethered BDP, synthesized by the organic group of Prof. Mª Jose Ortiz at Universidad Complutense (Madrid).

The first compound, with two identical BODIPY 546 units bonded in (2,8') positions, denoted as **BDP DIM 546** (commercially known as pyrromethene 546, Figure 3.28), considered as a reference for comparison with the other compounds, is studied in several solvents with different polarity.
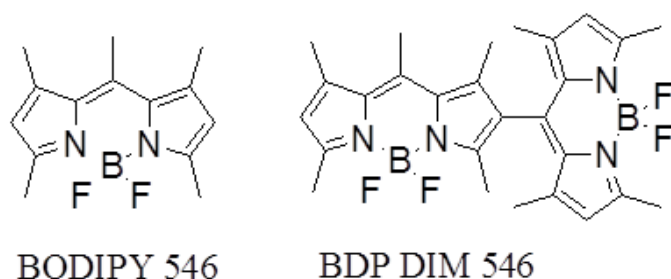
Figure 3.28. Commercial BODIPY 546 and the orthogonal dimer denoted as BDP DIM 546 composed by two identical BODIPY 546 units bonded in (2,8') positions.

The very narrow and intense absorption band (Figure 3.29A, Table 3.6 indicates that there is not any π - mixing between the two monomeric electronically decoupled units as a result of orthogonal condition between the chromophores[36,42]. Therefore, the absorption band of **BDP DIM 546** shows an oscillator strength two times higher than one BDP units ($\varepsilon = 15\text{-}18 \times 10^5$ M^{-1} cm^{-1}, Table 3.6) due to combination of two locally excited states.

Although the absorption band is nearly independent with the nature of the solvent, the fluorescence properties are significantly different (Table 3.6, Figure 3.29A). In the less polar solvents such as toluene, THF and CHCl$_3$, a sole narrow emission band around 530 nm is obtained (Table 3.6), and is assigned to the emission from the S$_1$ of the dimer. The fluorescence capacity in an apolar solvent, *i.e.* toluene, is relatively high with an efficiency around 75% that greatly decreased as the polarity of the solvent increased (modest efficiency around 20% in THF, CHCl$_3$). Indeed, in ACN, solvent with the highest polarity in this series, the fluorescence is practically quenched ($\Phi_{flu} < 0.01$) but two emission bands are discernible, at around 530 nm, previously assigned to the locally excited (LE) emission from the S$_1$ and a broad red-shifted band at around 720 nm, which is characteristic of an ICT ("Intra Charge Transfer") state. In agreement with this tendency, the BDP DIM 546 in CH$_2$Cl$_2$, solvent of intermediate polarity, shows an only slightly red-shifted emission band, centered at 550 nm together with a shoulder at around 530 nm, which can suggest the presence of a less favored ICT state together with LE state, respectively (Figure 3.29, Table 3.6).
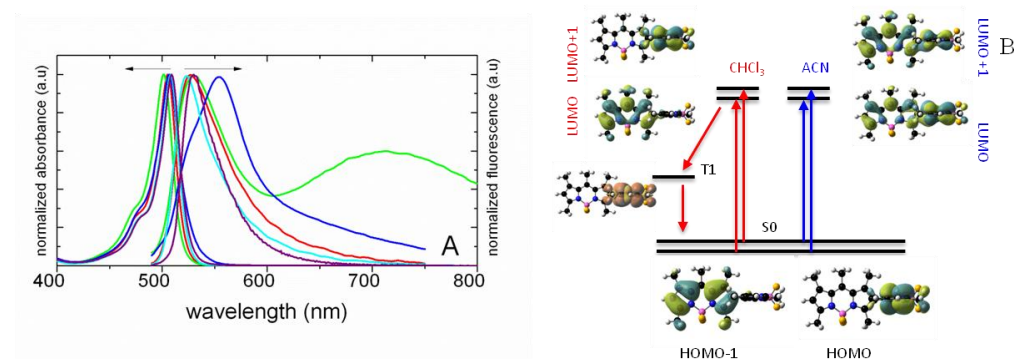
Figure 3.29. (A) Height-normalized absorption and emission spectra and (B) Energy diagram of the electronic levels and the corresponding orbitals involved in the BDP DIM 546 in different solvents, ACN (green), CH$_2$Cl$_2$ (blue), CHCl$_3$ (red), THF (cyan) and Toluene (purple).

Table 3.6 Photophysical properties and singlet oxygen generation of BDP DIM 546 in different solvents: Absorption (λ_{ab}), Full Width at the Medium Height (Δv), molar absorption coefficient (ε) fluorescence wavelength (λ_{fl}), fluorescence yield (Φ_{fl}), fluorescence lifetime (τ), singlet oxygen yield and phosphorescence lifetime of the singlet oxygen (Φ_Δ). E_{T30} is the Reichardt paramerter that indicates the polarity of the solvents

solvent E_{T30}	λ_{abs} (nm)	Δv (cm-1)	ε x10^{-4} (M^{-1}cm^{-1})	λ_{flu} (nm)	Φ_{flu}	τ(%) (ns)	Φ_Δ [1]	τ_Δ (μs)
ACN 45.6	507	924	16.5	530/710	<0.01	-	0.25	81
CH$_2$Cl$_2$ 40.7	507	999	15.0	556	0.03	0.05 (45) 2.1 (39) 4.3 (16)	0.77	97
CHCl$_3$ 39.1	507	831	18.0	527	0.22	0.14 (27) 4.2 (73)	0.75	201
THF 37.4	505	885	18.0	527	0.17	1.2 (56) 4.4(44)	0.86	23
Toluene 33.0	509		18.1	530	0.75	0.80(5) 5.4(95)	0.24	27
BDP 546 [2]	495	803	8.0	506	0.85	5.5	0	-

[1] Methylthio-BDP4-2I used as reference in each corresponding solvent (See Table 3.4, section 3.2.1.1.2)
[2] Photophysical properties in EtOH)[75]

Regarding fluorescence kinetics, the BDP DIM 546 in toluene can be practically analyzed as a monoexponetial decay curve with a fluorescence lifetime of 5.4 ns similar to that obtained in the momomer BDP 546 (Table 3.6). However, two exponentials are required to fit the decay of BDP DIM 546 in most of the other solvents. From these data, a long lifetime, $\tau \sim 4.2 - 4.4$ ns, similar for all the solvents, may be assigned to the fluorescence deactivation of the singlet excited state S_1 of the dimer. A short lifetime, $\tau \leq 1$ ns could tentatively be ascribed to a non-radiative process that quenches the fluorescence of the S_1 state, *i.e.* the intersystem crossing to the triplet. The intermediate lifetime of $\tau \sim 2.1$ ns only observed in CH$_2$Cl$_2$, could be attributed to the radiative deactivation from the ICT state.

Ground state DFT simulations (performed by Dr. H. Manzano from the University of the Basque Country, UPV-EHU) predict a perfectly orthogonal arrangement of the BDP subunits in BDP DIM 546, which is maintained in all the studied derivatives. The CIS-DFT simulations indicate that two nearly degenerated states take part on the electronic transitions of the BDP DIM546. In the less polar solvents (THF and CHCl$_3$ in the simulations), each BDP sub-units are excited independently, from the HOMO-1 $\rightarrow$ LUMO and from the HOMO $\rightarrow$ LUMO+1 (Figure 3.29B). This type of transition

is in agreement with the molar absorption coefficient measured for the BDP DIM546, approximately doubling the value of a single BDP. The simulations predict equally probable transitions for both BDP units, with very similar oscillator strengths, and a wavelengths difference of only 3 nm. After the excitation, a possible intra charge transfer (ICT) process could take place involving both BDP units linked through the "8" and "2" sites that act as the donor and acceptor, respectively.

According to the simulations, BDP DIM 546 in a polar solvent such as ACN shows the same spatial distribution of the HOMO and HOMO-1 orbitals as in $CHCl_3$ or THF. However, the solvent polarity delocalizes the LUMO and LUMO+1 through both BDP sub-units (Figure 3.29B). Furthermore, the more probable excitation transitions involve a different pair of orbitals: HOMO $\rightarrow$ LUMO and HOMO+1 $\rightarrow$ LUMO+1. The delocalization of the LUMO and LUMO+1 is likely triggering the very efficient ICT that can be observed experimentally (Figure 3.29A or Figure 3.30). This result agrees with the study by Thompson and coworkers on symmetrical meso-linked BDP dyad that undergoes symmetry-breaking ICT in the excited state in polar solvents.[71]
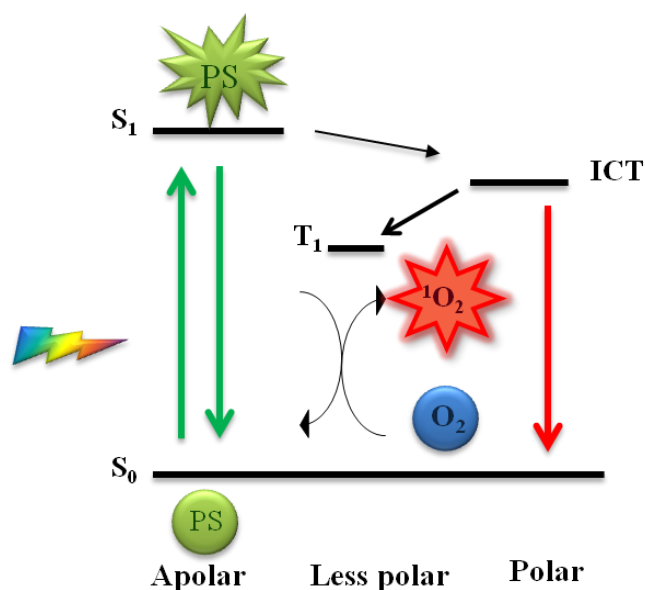

Figure 3.30. Illustrative diagram of the electronic levels involved in the singlet oxygen production of BDP DIM 546 in various solvents.

As already cited above for halogenated-BDP, the formation of very favored ICT states will reduce the singlet to triplet hopping and could be the main reason for the low singlet oxygen production of BDP DIM 546 in polar solvents. Thus, a higher production of singlet oxygen should be expected in the less polar solvents. In fact, BDP DIM 546 in less polar solvent such as CH_2Cl_2, $CHCl_3$ and THF shows singlet oxygen quantum yields ≥ 3 times higher than that obtained in the more polar solvent ACN (Table 3.6). However in toluene, due to the apolar nature of the solvent, BDP DIM 546 preferentially activates the radiative emission from the singlet state rather that the intersystem crossing to the triplet state yielding to a relatively high fluorescence efficiency ($\phi_{fl} = 0.75$), similar to that recorded for the BDP 546 monomer ($\phi_{fl} = 0.85$, Table 3.6)[75] with respect to its singlet oxygen production ($\Phi_\Delta = 0.24$) [23,60,74,76–78].

This dimer was already investigated by Wu, Zhao and coworkers in CH_2Cl_2 solution[41] and although our photophysical properties agree well with these results, the singlet oxygen quantum yield previously reported was different ($\Phi_\Delta = 0.64$ *vs* 0.77 in our case). This discrepancy in the singlet oxygen quantum yields results from the different methodologies applied. In the paper of Wu *et al.*, 1,3-diphenylisobenzofuran was used as a singlet oxygen probe for an indirect determination of singlet oxygen quantum yield in CH_2Cl_2 using Rose Bengal as the reference ($\Phi_\Delta = 0.8$ in MeOH). Obviously, due to the lack of a good standard soluble in CH_2Cl_2 in the visible range (500-600 nm), and to the variation of the quantum yield with the solvent (Rose Bengal, $\Phi_\Delta = 0.53$ in ACN), this result may be questioned. Indeed, it was previously demonstrated that huge variations in the singlet oxygen quantum yield can be obtained depending on the reference[79]. For instance some of our photosensitizers can lead to singlet oxygen productions higher than 100% in chlorinated solvents when RB in ACN is used as reference (Table 3.4 section 3.2.1.1.2. new halogenated BDP). An adequate reference in the same solvent and if possible in the same absorption range is thus absolutely needed to determine accurate singlet oxygen quantum yields. In this regard, methylthio-BDP4-2I compound, previously described in section 3.2.1.1.2. could be a promising reference for new photosensitizers working under Vis in solvents of different polarity, such as these new orthogonal BDP dimers.

On the other hand, chloroform can be considered a good solvent for PS based on BDP chromophores because of the long lifetime τ_Δ of $^1O_2$ in this solvent (201 μs), which gives rise to a more intense luminescence signal for $^1O_2$ with respect to the

typical noisy peaks obtained in other solvent with lower $^1O_2$ lifetime (τ_Δ = 85 µs in ACN, τ_Δ = 23 µs in THF, τ_Δ = 97 µs in CH$_2$Cl$_2$, Figure 3.31). Accordingly, the singlet oxygen quantum yields of BDP dimers will be more accurately determined in CHCl$_3$. Moreover, BDP DIM 546 in this solvent exhibits a high phototoxic power (defined as the product of molar absorption coefficient by the singlet oxygen quantum yield: PP = ε. Φ_Δ = 219 600 cm^{-1} M^{-1}) and also a significant brightness (defined as the product of molar absorption coefficient and the fluorescence quantum yield: BT = ε.$_{flu}$ Φ_{flu} = 39 600 cm^{-1} M^{-1}).
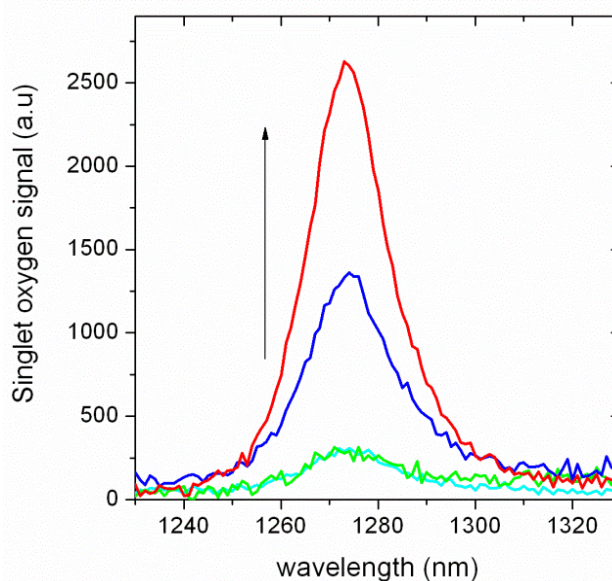
Figure 3.31. BDP DIM 546 singlet oxygen signal in THF (cyan), CHCl$_3$ (red), CH$_2$Cl$_2$ (blue) and ACN (green) under 515 nm excitation wavelength in which BDP DIM 546 shows the same absorbance values in all the solvents.

Note here that oxygen is usually more soluble in these halogenated solvents than in other hydrocarbons[23,60]. Indeed, an increase of about 10% is obtained in oxygen-saturated CHCl$_3$ solution with respect to the air-saturated one (Figure 3.32) yielding a Φ_Δ = 0.82 in oxygen saturated CHCl$_3$. As a direct consequence, the kinetics of the excited states of BDP DIM 546 in oxygen-saturated chloroform solution is faster than that in air-saturated solution (Figure 3.32) decreasing the lifetime assigned to the radiative deactivation of S$_1$ from 4.2 ns (air) to 3.6 ns (oxygen).
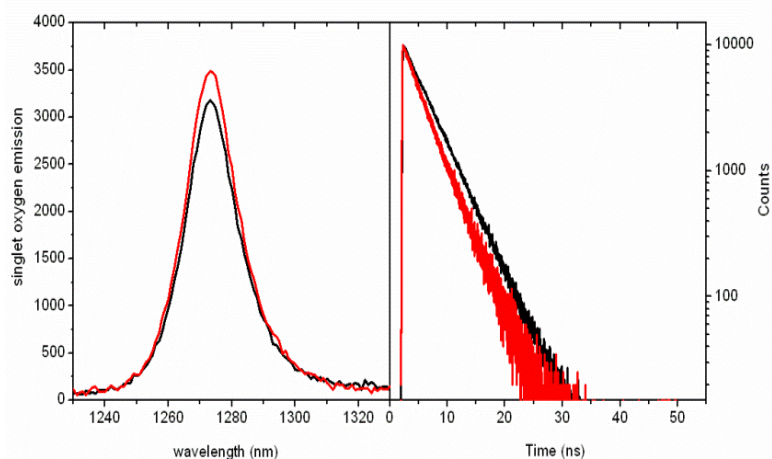
Figure 3.32. Chloroform solution of BDP DIM 546 (A) the singlet oxygen signal recorded in oxygen saturation (red) and in air-saturation (black) and (B) the lifetime in oxygen saturation (red) and in air-saturation (black).

As a brief conclusion, we confirmed that the ability to generate singlet oxygen of these orthogonal BDP-dimers is strongly connected with the intrinsic ICT character[69,72]. The stabilization of ICT states has a double unwanted impact for an efficient singlet oxygen production: 1) it competes with intersystem crossing conversion to the triplet state of the sensitizer and 2) it reduces the probability of the radiative deactivation of the singlet excited state of the dimer decreasing their fluorescence efficiency. Accordingly, the singlet oxygen generation and the fluorescence can be modulated by the proper polarity of the solvent in order to avoid the formation of ICT states.

3.2.1.2.2. Iodinated dimer as maximum reference.

Although the added value of these orthogonal dimers relies on the absence of any halogen atom, an analogous dimer but with iodine atoms substituted at positions 2,6 and 6', BDP DIM 546-3I (Figure 3.33), was analyzed to compare its singlet oxygen production with that of the halogen-free dimers.
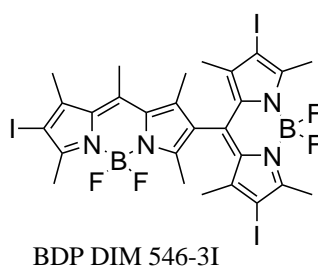
BDP DIM 546-3I

Figure 3.33. Tri-iodo covalently tethered BDP dimer BDP DIM 546-3I.

First, the absorption spectrum of this iodinated compound does not show such a narrow absorption band and the main band at 525 nm is red-shifted relative to BDP DIM 546 (λ_{max} 507 nm). Moreover, this main band also shows a red-shifted shoulder, centered on 545 nm (Figure 3.34, Table 3.7). According to previous studies on halogenated BDPs monomers, the position of these absorption bands agrees well with those recorded for mono-iodo (λ_{max} = 523.5 nm) and di-iodo (λ_{max} = 548.5 nm) BODIPY monomers[50], with bathochromic shifts around 20 nm and 40 nm respectively relative to non-halogenated BDP.
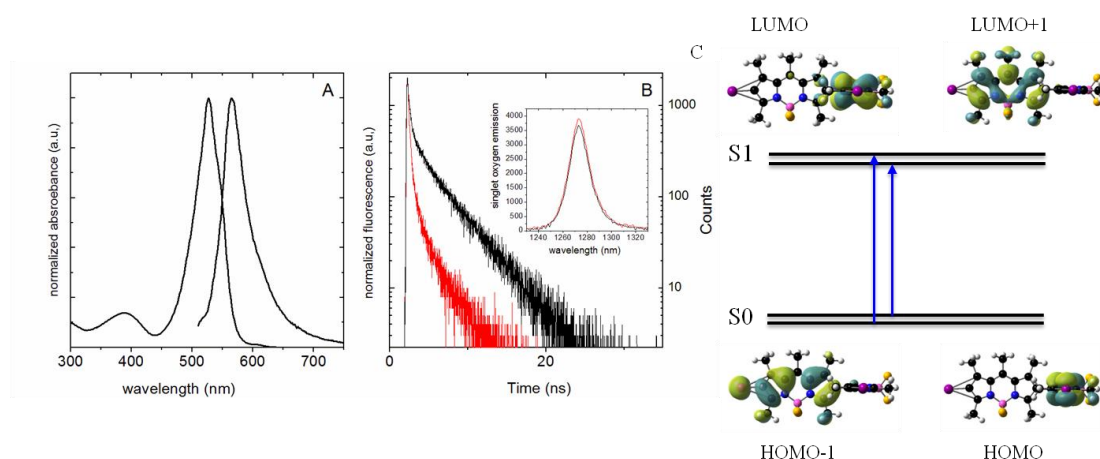
Figure 3.34 A) Absorption and fluorescence spectra; B) Decay curves of BDP DIM 546-3I singlet excited state and in the insert singlet oxygen production in air saturated (black curves) and oxygen-saturated (red curves) CHCl$_3$ solutions of BDP DIM 546-3I. C) Energy diagram of the electronic levels and the corresponding orbitals involved in the BDP DIM 546-3I in CHCl$_3$.

Table 3.7. Photophysical properties and singlet oxygen of a series of dimers: Absorption (λ_{ab}), molar absorption (ε) fluorescence wavelength (λ_{fl}), fluorescence yield (ϕ_{fl}), fluorescence lifetime (τ), singlet oxygen yield (Φ_Δ).

	solvent	λ_{abs} / nm	ε x10^{-4} $M^{-1}cm^{-1}$	λ_{fl} / nm	ϕ_{flu}	τ_{fl} [1]	Φ_Δ [3]
BDP DIM 546-3I	ACN CH$_2$Cl$_2$ CHCl$_3$	520 /~535 526 /~540 526 /~540	6.5 12.0 9.4	549 564 565	<0.01 <0.01 0.03	- - 0.23 (85) 3.7 (15)	0.57 0.93 0.88
BDP PNHDIM	CHCl$_3$	510	8.1	526	0.05	0.05 (77); 3.9 (23)	0.85
BDP PNODIM	CHCl$_3$	513	15.1	532/675	<0.01	-	0.43
P8ENDIM	CHCl$_3$	510	8.2	521	<0.01	-	0.0
BDP DIMTIO	CHCl$_3$	525	10.2	627	0.17	2.86	0.12
BDP DIM 3-Ph	CHCl$_3$	549 /~585	11.0	615	0.24	0.22 (12) 3.6 (88)	0.17
BDP DIMKI	CHCl$_3$	377 509 658	3.2 3.5 5.8	685	0.56 [2]	0.13 (26) 3.9 (74) [2]	< 0.01(PN) 0.11 <0.01(MB)
BDP PNOD3K	CHCl$_3$	346 510 589	1.2 3.1 4.5	613	0.22	0.7 (97) 2.9 (3) [2]	0.08 0.20 0.07

[1] Recorded at the emission maxima

[2] Independent of the excitation wavelength

[3] Methylthio-BDP4-2I used as reference in each corresponding solvent (See Table 3.4, section 3.2.1.1) except when stated.

In agreement with the red-shift of the absorption band with respect to BDP DIM 546, DFT simulations predict a small decrease in the HOMO-LUMO gap of 0.053 eV, equivalent to ~ 8 nm. It is also interesting to note that the location of the orbitals has changed due to the presence of iodine atoms. CIS-DFT simulations indicate that the excitation in BDP DIM 546-3I involves HOMO $\rightarrow$ LUMO and HOMO-1 $\rightarrow$ LUMO+1 transitions (Figure 3.34A), showing the same character of the transition as BDP DIM 546 in polar solvents (ACN).

In ACN, the quantum yield of singlet oxygen production of the iodo-dimer BDP DIM 546-3I increased more than twice (Φ_Δ = 0.57, Table 3.7) relative to the value obtained for BDP DIM 546 (Φ_Δ = 0.25, Table 3.6). This result should be attributed to an effective increase in the intersystem crossing process induced by the presence of iodine atoms directly attached to the BODIPY core (internal heavy atom effect). The singlet oxygen quantum yields of BDP DIM 546-3I in less polar solvents such as

CH_2Cl_2 ($\Phi_\Delta = 0.92$) and $CHCl_3$ ($\Phi_\Delta = 0.88$, Table 3.7) is only slightly larger than that obtained for BDP DIM 546 in the same solvents ($\Phi_\Delta = 0.77$ and 0.75 respectively, Table 3.6). This comparison demonstrates the very efficient intersystem crossing of the halogen free orthogonal BDP DIM 546, likely via a SOCT-ISC mechanism consisting in a fast spin-flip that should occur to compensate the change in the angular momentum of the compound upon excitation since it involves intra-molecular charge transfer transitions.

Besides, this iodinated dimer also showed an increase of the singlet oxygen quantum yield in oxygen-saturated sample with respect to air-saturated solution yielding a singlet oxygen production close to 1 in $CHCl_3$ ($\Phi_\Delta = 0.93$). This increase influenced the kinetics of the excited state (Figure 3.34C), *i.e.*, the lifetime of S_1 state of DIM 546-3I in $CHCl_3$ decreased from 3.9 ns (air saturated) to 1.8 ns (oxygen saturated).

3.2.1.2.3. Donor/acceptor substituent.

Besides the polarity, by introducing donor (EDG) or acceptor (EWG) groups into the BDPs units of orthogonal dimers, it is possible to control their intrinsic CT nature and consequently their capacity of generating singlet oxygen production. Particularly, new BDP dimers, denoted as BDP PNODIM and BDP PNHDIM, with p-nitrophenyl (EWG) and p-aminophenyl (EDG) groups substituted at the *meso* position in one of the BODIPY units (see HOMO-LUMO orbital of BDP DIM 546) were studied in $CHCl_3$ (Figure 3.35).

BDP PNODIM   BDP PNHDIM   BDP P8ENDIM
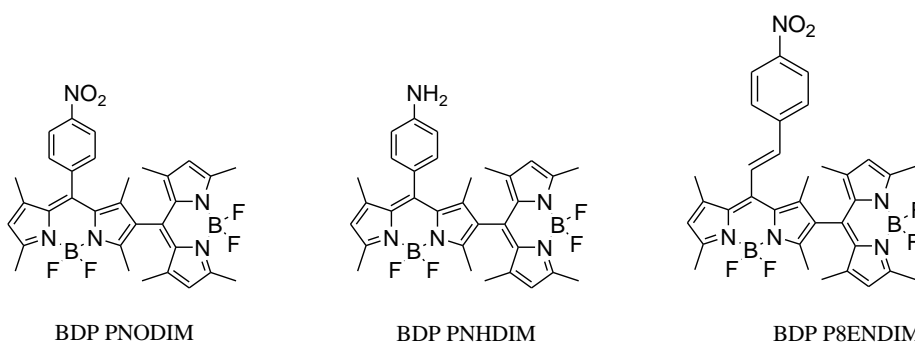
Figure 3.35. Series of multiple covalently tethered BDP with EWG or EDG groups at meso position.

The incorporation of the p-nitrophenyl (EWG) and p-aminophenyl (EDG) groups (see Figure 3.35) did not influence the absorption spectra while significant differences were obtained in their respective fluorescence spectra (Figure 3.36).
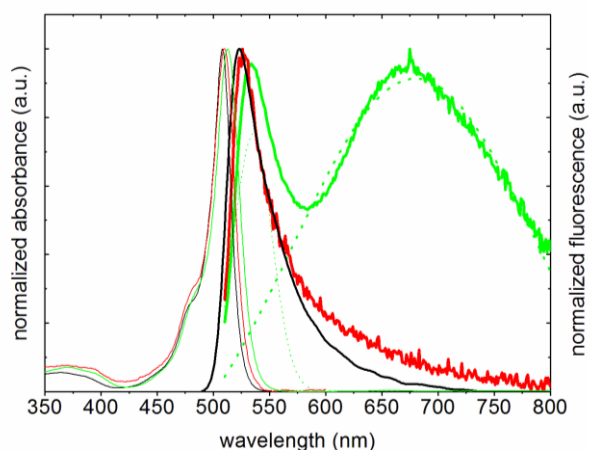
Figure 3.36. Absorption and fluorescence spectra of BDP DIM 546 (black curves), BDP PNHDIM (red curves) and BDP PNODIM (green curves) in CHCl₃.

Thus, BDP PNODIM shows a broad and red-shifted fluorescence band, centered at 680 nm, typical of the ICT emission, together with a narrow fluorescence band at 530 nm ascribed to the radiative emission from S_1. The strong acceptor character of the nitrophenyl substitutent in the BODIPY unit implies a more stabilized ICT character than in BDP DIM 546, which is experimentally detected even in apolar CHCl₃ (Figure 3.36). Indeed in the fluorescence emission spectrum, the ICT contribution is higher than the emission from S_1 (relative area under both curves 11:1, respectively). As already emphasized, favoring the ICT emission decreases the singlet oxygen production due to a non competitive ISC (Figure 3.30). Actually, the quantum yield of singlet oxygen production clearly undergoes a reduction by almost half ($\Phi_\Delta = 0.43$) compared to that of BDP DIM 546 ($\Phi_\Delta = 0.75$, Table 3.6) in chloroform. Note here that for the analogue compound, BDP P8ENDIM, with an extra vinyl group directly tethered at the BDP core, neither singlet oxygen luminescence nor fluorescence could be detected. This is probably due to the free rotation of substituent, effect previously described in section 3.2.1.1.1 which deactivates all the excited states by IC (internal conversion)[80].

However, by inclusion of a *p*-aminophenyl substituent in BDP PNHDIM, only a very weak (Φ_{flu} = 0.05, Table 3.7) reminiscent emission from S_1 at 526 nm compared to BDP DIM 546 in $CHCl_3$ (Φ_{flu} = 0.22,) was detected. The reduction of the fluorescence efficiency with respect to BDP DIM 546 could imply a higher O_2 production. The lifetimes and respective contributions of BDP PNHDIM are in agreement with this assumption, *i.e.* the contribution of the shortest lifetimes of BDP PNHDIM, (τ_1 = 0.05 ns, 77%) previously attributed to quenching of fluorescence of the S_1 of the dimer through the intersystem crossing process (Table 3.7), has a three times higher contribution than that obtained previously for BDP DIM 546 in $CHCl_3$ (τ_1 = 0.14 ns, 27%, Table 3.6), suggesting a more efficient triplet state formation. Accordingly, the longest lifetime of BDP PNHDIM (τ_2 = 3.9 ns), assigned to the radiative deactivation of the S_1 state in the dimer, is slightly shorter than the lifetime in BDP DIM 546 (τ_2 = 4.2 ns), with a much lower contribution (23 % against 73% for BDP DIM 546). Indeed, a slight enhancement in singlet oxygen production (Φ_Δ = 0.85, Table 3.7) with respect the BDP DIM 546 is measured in $CHCl_3$ (Φ_Δ = 0.75, Table 3.6). This result is very promising since by addition of other different electron donating groups, the singlet oxygen quantum yield could be increased practically achieving the maximum singlet oxygen quantum yield obtained in the iodinated BDP DIM 546-3I.

Moreover, DFT simulations indicate that the inclusion of the *p*-aminophenyl group does not modify the spatial location of HOMO and LUMO orbitals (Figure 3.37A). However, the *p*-nitrophenyl substitution has a great impact in the spatial location of the unoccupied orbitals and on the allowed electronic transitions (Figure 3.37B). Due to the strong acceptor character of the nitrophenyl moiety, a new energy level appears between the former LUMO and LUMO+1 level, which is located on this group. From the CIS-DFT simulations the allowed transitions are now on the one hand, the HOMO → LUMO+2, both located on the BDP linked through the *meso* position, and on the other hand the HOMO-1 → LUMO from the BDP with the nitrophenyl group (Figure 3.37B). The inclusion of the nitrophenyl acceptor group and the new LUMO+1 energy level suggest that the ICT process could take place between the BDP linked at 8 position and the nitrophenyl acceptor, acting the second BDP unit linked in position 2 as a mere spacer, as described by Akkaya et al.[73] In this case, the ICT transition involves different orbitals with different symmetry with respect to the BDP DIM 546 that can also induce a lower change in the angular momentum decreasing the spin-

orbit charge-transfer intersystem crossing mechanism (SOCT-ISC) and consequently the singlet oxygen production.
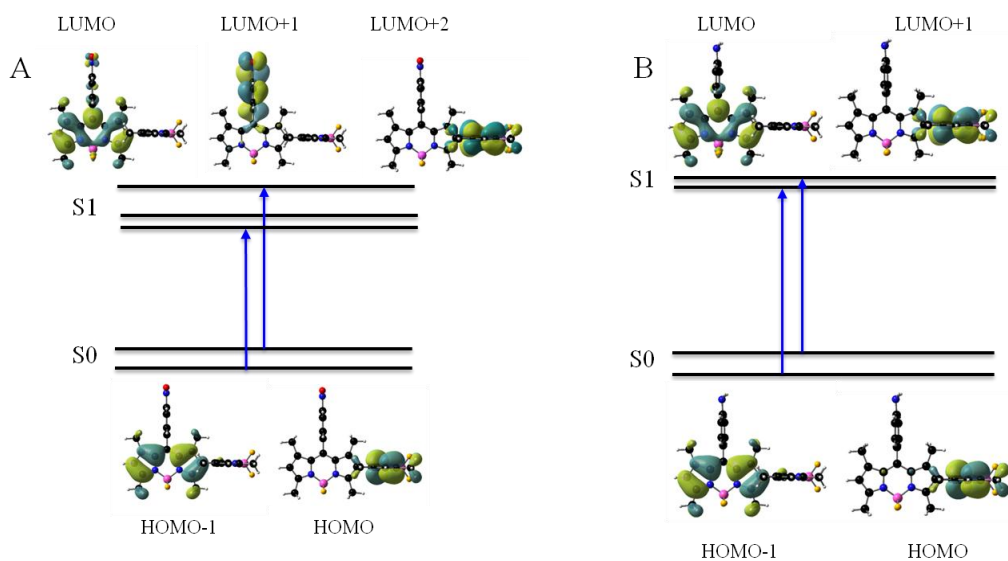
Figure 3.37. Energy diagram of the electronic levels and the corresponding orbitals involved of BDP PNODIM (A) and PNHDIM (B).

3.2.1.2.4. Red shift BDP Dimers.

It will be of a great importance for PDT to develop halogen-free photosensitizers but with absorption band in the red part of the visible spectra into the clinic window (600-800 nm). In this goal, different orthogonal BDP dimers with substituted π-systems are now studied.
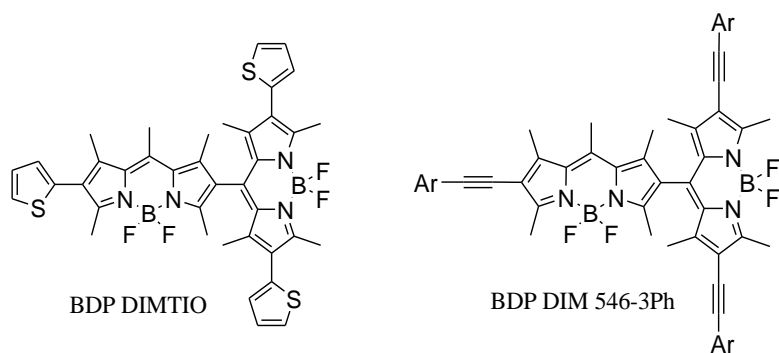
Figure 3.38. Series of multiple covalently tethered BDP with extended π-systems.
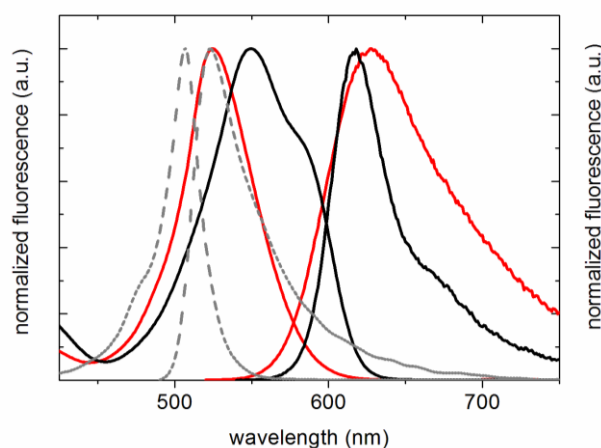
Figure 3.39. Absorption and fluorescence spectra of BDP DIMTIO (red curves), BDP DIM 546-PH (black curves) and BDP DIM 546 (grey curves) in CHCl$_3$.

A first attempt (compound BDP DIMTIO) was the incorporation of thiophene groups in position 2, 6 and 6' (Figure 3.38). Nevertheless, the red shift of the absorption band is less than 20 nm relative to the BDP DIM 546 (Figure 3.29). Conversely, the emission band appears much more red-shifted (627 nm), indicating that the electron delocalization through thiophene groups is more favored in the excited state. Note here that this compound shows modest fluorescence and singlet oxygen quantum yields, around 0.17 and 0.12, respectively (table 3.7).

The HOMO-LUMO gap is 0.15 eV smaller than that of BDP DIM 546, in agreement with the bathochromic shift. Furthermore, the observed strong shift of the emission attributed to the delocalization in the excited state is confirmed by the spatial location of the LUMO and LUMO+1 orbitals (Figure 3.39). As a matter of fact, the delocalization is equal to that of the BDP DIM 546 in polar solvents, which may indicate that a stable ICT takes place, responsible of the reduced singlet oxygen generation.

Another attempt to obtain red absorbing dimers was the substitution of coplanar phenylacetylenes π-system groups in 2,6 and 6' position (Figure 3.38). The absorption band of this system, BDP DIM 546-3Ph, shows a higher red shift than BDP DIMTIO relative to BDP DIM 546. In this case, the absorption spectrum displays a broad band (2637 cm^{-1}) at 549 nm with a shoulder around 580 nm (Figure 3.39), attributed to the contribution of the BDP monomer unit with one and two phenyl-acetylene groups, respectively.[81]

   Regarding its fluorescence, a moderate emission is observed (λ_{fl} = 615 nm and Φ_{fl} = 0.24, Table 3.7). In this case, the narrow emission band indicates that the emission only takes place from the monomeric units with the 2 phenyl-acetylenes substituents either by direct excitation or by excitation energy transfer (EET) from the other excited BDP unit with one phenyl-acetylene group. Note here that, the EET process between monomers should take place by the through-bond energy transfer (TBET) mechanism[82–84] along the single carbon-carbon bond since the totally orthogonal disposition of their transition moments located at their respective longitudinal axis makes the Förster resonance energy transfer (FRET) mechanism practically negligible (orientation factor, κ^2, nearly equal to 0)[85].

   The HOMO-LUMO gap of BDP DIM 546-3Ph is considerably smaller than for the previous compounds (0.38 eV, 65 nm) in agreement with the observed shift in the experimental absorption spectrum. The occupied orbitals are delocalized through the BDP and the linked phenyl-acetylene groups (Figure 3.40), but the empty orbitals are located only on the BDP units. As in the case of iodine and thiophene substitutions in 2,6 and 6'positions, the most probable transitions are those from HOMO $\rightarrow$ LUMO and HOMO-1 $\rightarrow$ LUMO+1, which suggests that substitutions in the 2 and 6 sites induce the same symmetry breaking effect as polar solvents. Nevertheless, the LUMO orbitals are not delocalized, so the ICT state is not favorable.
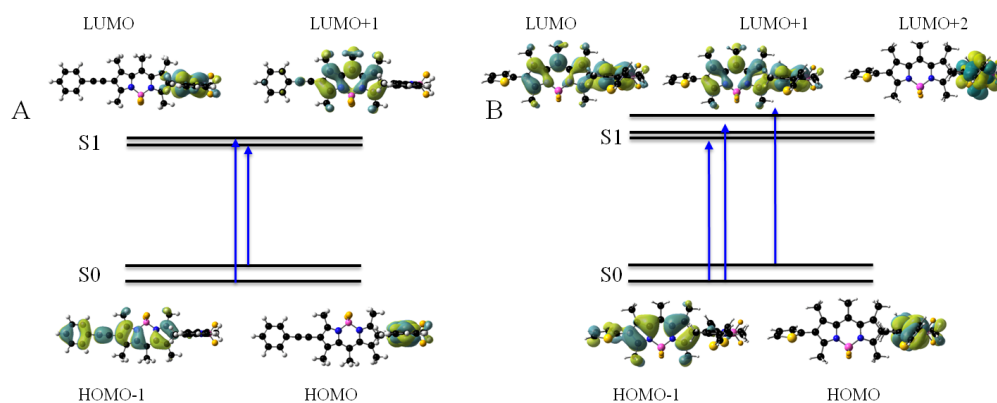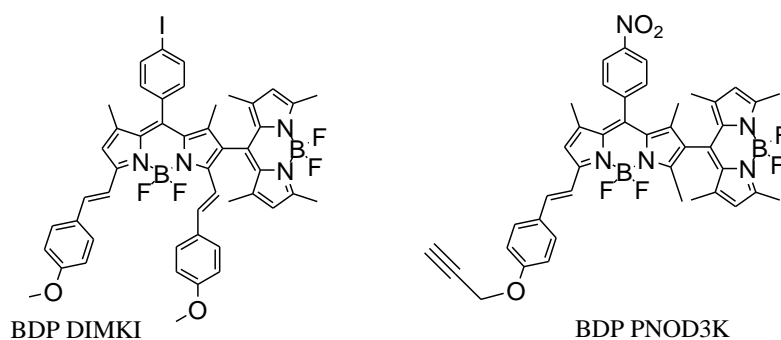

Figure 3.40. Energy diagram of the electronic levels and the corresponding orbitals involved of BDP DIM 546-3PH (A) and BDP DIMTIO (B).

In this sense, the singlet oxygen quantum yield ($\Phi_\Delta = 0.17$, Table 3.7) in $CHCl_3$ is slightly higher than that in BDP DIMTIO, but still quite low with respect to the dimer without π-system substitution BDP DIM 546 ($\Phi_\Delta = 0.75$, Table 3.6). A possible reason could be attributed to the extension of the conjugation by the insertion of two π-system groups, promoting the radiative deactivation over non-radiative processes as previously demonstrated in the photophysical study of the BDP unit with two coplanar phenylacetylenes in position 2,6[81].

Thus, BDP DIM 546-3Ph shows moderate and balanced yields of fluorescence and singlet oxygen production ($\Phi_{fl} = 0.24$ and $\Phi_\Delta = 0.17$, Table 3.7) with relative high extinction coefficients up to 600 nm which could open the possibility of using this compound for theranostic applications.

Next, new molecular designs based on orthogonal-BDP dimers with asymmetric π-substitution in 3 and/or 5 positions in only one of the BDP units were prepared. The aim was a larger shift of the absorption bands into the clinic window (650-700 nm), but also a maximum therapeutic efficiency with minimal toxicity (Figure 3.41). This idea is based on previously published works which indicate that: *i)* the incorporation of π-systems into 3,5 positions of BDP units produce more efficient bathochromic shifts of the absorption bands with respect to π-substitution into 2,6 position[86] and *ii)* the strategy of a symmetric substitution of π-extension in both BDP units does not induce an efficient singlet oxygen generation[39].

BDP DIMKI   BDP PNOD3K

Figure 3.41. Series of multiple covalently tethered BDP substituted in positions 3/5 for red-shifting the absorption bands.
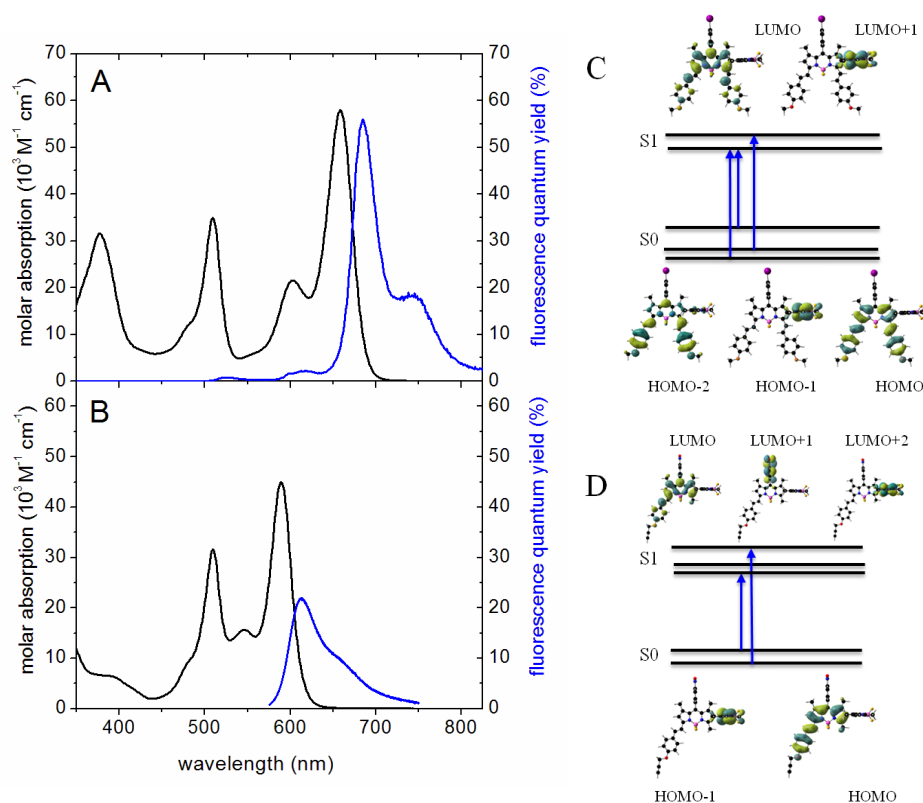
Figure 3.42. Absorption and fluorescence spectra of BDP DIMKI (A) and BDP PNOD3K (B) in CHCl₃. Energy diagram of the electronic levels and the corresponding orbitals involved of BDP DIMKI (C) and BDP PNOD3K (D).

Thus, the first studied example is the compound BDP DIMKI, with two styryl groups at the 3,5-position in one of the BDP monomer. BDP DIMKI shows three clear absorption bands centered at 658 nm (red) at 509 nm (green) and 377 nm (UV), with relative intensity 1/0.9/0.55 respectively (Figure 3.42A). These bands are likely attributed to: *i)* the S_0-S_1 transition of the chromophore with π-extended substitution at 3,5-position, *ii)* the orthogonal dimer core without any π-delocalization and *iii)* the transition S_0-S_2, which becomes more obvious due to the decrease of the relative molar absorption of the main band (ε = 5.8 x 10^4 M^{-1} cm^{-1}) with respect to other dimers ($\varepsilon \geq$ 10 x 10^4 M^{-1} cm^{-1}, Table 3.7). Regarding the emission properties of BDP DIMKI, a relatively intense emission band is recorded in the red part of the visible spectra (λ_{flu} = 685 nm, ϕ_{flu} = 0.56, Table 3.7), independently of the exciting wavelength (λ_{ex} = 350 nm, 500 nm and 600 nm). This latter fact indicates a very efficient energy transfer from the less conjugated moieties to the π-extended BDP unit

in the dimer. In this regard, according to the relative high fluorescence quantum yield, the singlet oxygen production expected should be low. Accordingly, a modest singlet oxygen production ($\Phi_\Delta = 0.11$, Table 3.7) is obtained but only under green light, *i.e.* by direct excitation of the orthogonal BDP core without substitution, whereas no appreciable singlet oxygen is generated under red or UV excitation.

According to the simulations, the styryl groups in the BDP DIMKI molecule induce a breaking of the symmetry in the electronic transitions as previously discussed: the involved energy levels are HOMO $\rightarrow$ LUMO and HOMO-1 $\rightarrow$ LUMO+1 (Figure 3.42C). In addition, the HOMO $\rightarrow$ LUMO transition is now shifted to higher wavelengths due to the π-extended system, giving rise to the two well differentiated bands (658 and 509 nm) in the spectrum. Due to the electronic delocalization, the energy difference between HOMO / HOMO-1 and LUMO+1 / LUMO is the largest of all the studied dyes (more than three times for the occupied levels and more than twice for the unoccupied ones, Figure 3.42C). These energy levels cannot be considered as nearly degenerated anymore. Thus, upon excitation there is no such important change in the angular momentum, mechanism responsible of the intersystem crossing (spin-flip) in these orthogonal compounds.

However, this compound could be used as a multimodal BDP under the adequate irradiation wavelength. That is, it might be possible to activate the therapeutic efficiency under green light and to obtain an improved fluorescence imaging under red excitation reducing the interference from the auto-fluorescence of the cell at these wavelengths.

In order to increase the singlet oxygen production under red light excitation, BDP PNOD3K, with only one styryl group at position 3 of one BDP unit was synthesized. It shows a main absorption band centered at 589 nm together with a less intense band at 510 nm (Figure 3.42B), attributed respectively to the π-extended BDP unit and the core of the BDP dimer without delocalization. On the other hand, it shows a moderate red emission ($\lambda = 613$ nm, $\Phi_{fl} = 0.22$, Table 3.7) independent of the excitation, and a slightly higher singlet oxygen production under green excitation ($\Phi_\Delta = 0.20$, Table 3.7). More importantly, for the first time an orthogonal dimer shows singlet oxygen generation under red light excitation ($\lambda_{ex} = 600$ nm), although with a quite modest quantum yield ($\Phi_\Delta = 0.07$, Table 3.7).

As a result, the design of new halogen-free asymmetric dimers opens the door to potential compounds with dual functionality for theranostic applications

(Photodynamic therapy and imaging) under excitation wavelength into the therapeutic window (600-800 nm).

In BDP PNOD3K, the styryl group is inducing the same effect as in BDP DIMKI, *i.e.,* shifting the HOMO $\rightarrow$ LUMO transition to the red, giving rise to a band splitting (Figure 3.42D). Nevertheless, the presence of the *p*-nitrophenyl group with strong acceptor character in the substituted BDP is inducing the same effect already discussed for BDP PNODIM: it favors a possible CT from the donor BDP to the *p*-nitrophenyl. In addition, the small singlet oxygen production detected upon excitation in the red region could be the consequence of an ICT between the BDP linked at position 6 and the p-nitrophenyl group at meso position.

Because one on the main objective in this work is to implement these types in PDT applications, the most promising candidates such as BDP DIM 546, BDP PNHDIM, BDP DIM546-3PH and PNOD3K should be tested in "in vitro" experiments. Indeed, the phototoxicity study is carried out at this moment by Maria Angeles Villanueva at the Universidad Autónoma de Madrid.

3.2.1.2.5. Multichromophoric BDP dimer with Pantachromic action

In this last section, a halogen-free all-BDP molecular cassette has been rationally designed with a dual functionality, *i.e.* enough fluorescence emission for bioimaging and at the same time high generation of singlet oxygen for photodynamic therapy (PDT). Besides this cassette can work at different wavelengths of the visible spectrum.

The molecular design consists in two asymmetric BDP units directly linked through their *meso* and 2 positions: a fluorescent orange-emitting BDP chromophore (A in orange in Figure 3.43) is orthogonally linked to a dissimilar (green absorbing) BDP chromophore (B in green in Figure 3.43). This geometrical arrangement has been pointed out as an elegant way to attain high $^1O_2$ generation without using toxic heavy halogen or metal atoms, as is previously described above. For widening the absorption spectral window, two additional blue-absorbing 8-amino-BDP chromophores (C in blue in Figure 3.43) were tethered to the central "green" one, by linking together the "blue" amino and the "green" 2 and 6 positions, through a methylene-ethynyl spacer to avoid electronic interaction between them. In addition to its strong blue-absorption, this BODIPY building block exhibits highly efficient and stable emission, which overlaps the absorption of the above dyad prompting efficient EET process.
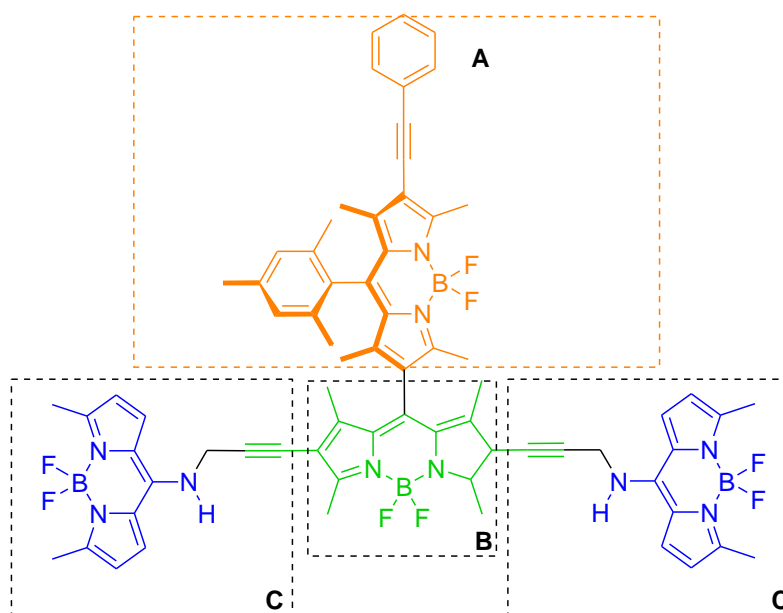
Figure 3.43. Molecular structure of **Tri-BDP** (Key BDP moieties in different colors and spacers in black.

The absorption spectrum is almost the sum of the bands of all the involved individual chromophores (Figure 3.44). Accordingly, three strong absorption bands ($\varepsilon_{max} > 10^5$ M^1 cm^{-1}) at 427, 522, and 554 nm, covering the blue-to-yellow spectral region, were recorded. Thus, the long-wavelength absorption (554 nm) is due to the most π-extended BDP chromophore of Tri-BDP (A orange fragment in Figure 3.43), while the absorption band at 522 nm is attributed to the "green" BDP chromophore (B in Figure 3.43 due to its π-extension with two ethynyl units. Finally, the blue-edge absorption band at 427 nm is assigned to the "blue" 8-amino-BDP chromophores (C in Figure 3.43), owing to the promotion of a hemicyanine π-system by the amine nitrogen[54]. Therefore, the multichromophoric Tri-BDP system should act as an efficient molecular cassette for EET, allowing efficient light-harvesting over the ultraviolet-visible (UV-Vis) spectral region, which is a key factor in the design of efficient solar-induced photosensitizers for topical PDT applied to dermatological diseases, as well as to the treatment of superficial oncologic lesions[87].
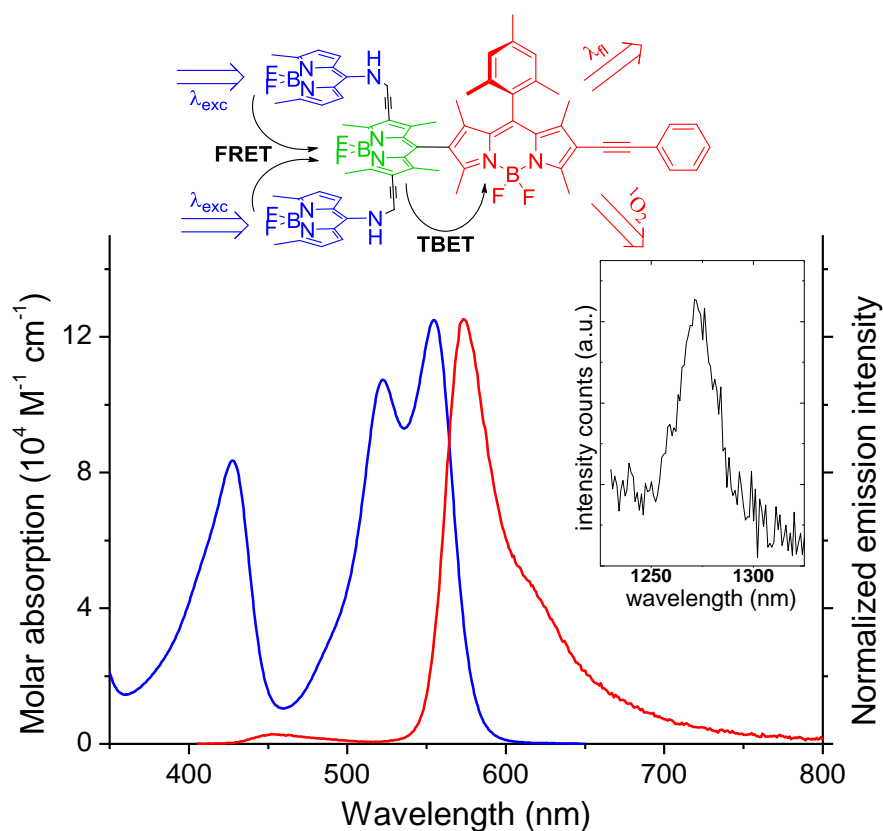
Figure 3.44. Absorption and normalized fluorescence and laser spectra of Tri-BDP in ethyl acetate upon excitation at the blue fragment (400 nm). Inset: singlet oxygen phosphorescence upon the same blue excitation in air-saturated ethyl acetate solution.

Such bands assignments are supported by theoretical simulation of the absorption spectrum (Figure 3.45). The electronic density in each molecular orbital involved in the electronic transition is located at one BDP (mainly in the occupied orbitals). In the 2-8 linked fragments the electronic density is extended to the 2-phenylacetylene and 2,6-ethynyls, respectively, explaining the bathochromic shift and supporting the above assignment of the absorption bands. Thus, the electronic isolation is ensured, at least in the ground state, since each fragment retains its identity in the molecular assembly and consequently can be selectively excited.
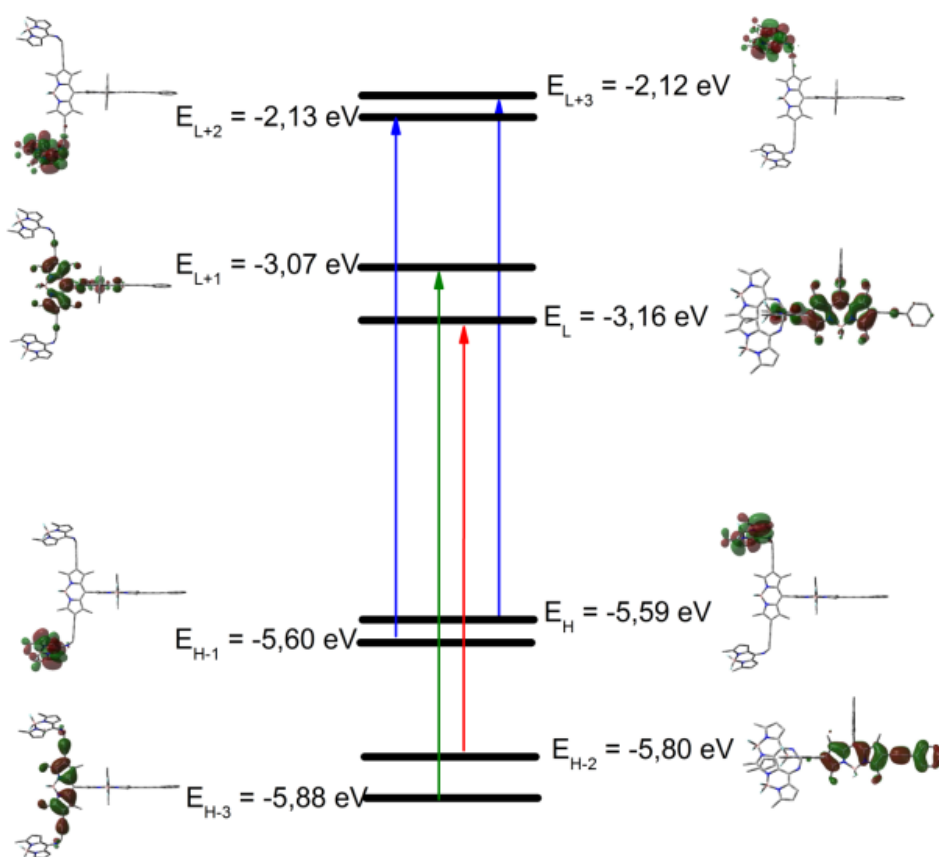
Figure 3.45. Energy diagram of the molecular orbitals involved in the visible electronic transitions of the molecular cassette Tri-BDP.

In fact, regardless of the excitation wavelength (*i.e.,* 400 nm at the blue fragment or at 500 nm at the green fragment) just one fluorescence band is recorded at 573 nm, corresponding to the long-wavelength emitting A orange fragment (Figure 3.44). Therefore, light can be harvested simultaneously over a wide spectral region and transferred from the blue donor moiety to the final acceptor BDP in the orthogonal fragment by successive and efficient EET steps. Indeed, the emission from the blue fragment is drastically quenched albeit it is directly excited (Figure 3.44). The first energy hop from the 8-aminoBDP should take place via Förster mechanism (FRET)[88], due to the high spectral overlap between the fragments. However in the second hop between perpendicular moieties, FRET probability is greatly reduced (the orthogonal disposition of the transition moments, which is located at the longitudinal axis of the indacene core, gives an orientational factor κ^2 nearly equal to 0)[85]. Alternatively, their

direct linkage could enable a through-bond (TBET) mediated EET[82,84,89]. The required electronic exchange seems to be feasible in this case due to the existing orbital overlap upon the 2-8 connection, as shown in the molecular orbitals (see the high electronic density at LUMO and LUMO+1 states at such positions in Figure 3.45).

The photophysical data and the singlet oxygen production of Tri-BDP are listed in Table 3.8. Again, the two different fluorescence lifetimes are ascribed as previously: the longest one (2.41 ns, 84 %) is attributed to the radiative deactivation from the singlet excited state and the shorter and minority lifetime (0.90 ns, 16 %) likely related to the non-radiative relaxation to the triplet state. Such quenching is due to the promotion of the intersystem crossing by the orthogonal arrangement of the final emitting fragment. As explained above, upon excitation ICT transitions usually imply a change in the angular momentum that should be compensated by a fast spin flip to keep constant the overall system angular momentum[69,73]. A closer inspection to the unoccupied molecular orbitals in Figure 3.45 reveals some degree of interaction between the orthogonal fragments upon excitation (see HOMO-2 → LUMO and HOMO-3 → LUMO+1), which suggests that both entities could undergo charge transfer in the excited state.

Regarding the singlet oxygen generation, a significant quantum yield slightly higher than 0.5 (Table 3.8) was recorded upon excitation at the blue-edge band (400 nm) or directly exciting the orange and final emitting moiety (545 nm). The practically equal singlet oxygen yield obtained at different excitation wavelengths also confirmed the very efficient energy transfer from the 8-amino-BDPs moiety to the orthogonal BDP dimer.

Table 3.8. Photophysical and laser properties of Tri-BDP in ethyl acetate. Absorption (λ_{ab}) and fluorescence (λ_{fl}) wavelength, molar absorption (ε_{max}), fluorescence (ϕ_{fl}) and singlet oxygen generation ($\Phi_\Delta(^1O_2)$) quantum yield and fluorescence lifetime (τ).

| λ_{ab} (nm)	ε_{max} ($10^4\,M^{-1}cm^{-1}$)	λ_{fl} (nm)	*Φ_{fl}	*τ (ns)	Φ_Δ
554.5	12.5			2.41 (84%)	0.53[1]
522.5	10.7	573.0	0.19	0.90 (16%)	0.52[2]
427.5	8.4				

*both magnitudes are calculated after excitation at 500 nm
[1] after excitation at 545 nm with Rose Bengal in acetonitrile as reference (Φ_Δ= 0.53)
[2] after excitation at 400 nm with Phenalenone in acetonitrile as reference (Φ_Δ= 1)

Phototoxicity study

On the basis of the properties shown in Table 3.8, the in vitro theranostic activity of panchromatic Tri-BDP (10^{-5} M in DMSO) was studied on living HeLa cells. The intracellular localization of Tri-BDP was analyzed by fluorescence microscopy (Figure 3.46), showing that the developed PDT agent is effectively internalized by HeLa cells. It is clearly visualized under green light excitation as cytoplasmic granules with lysosomal morphology emitting a brilliant red fluorescence. Additionally, a weaker diffuse fluorescence from the entire cytoplasm was detected, whereas almost no fluorescence was found in the nuclear region (Figure 3.46).
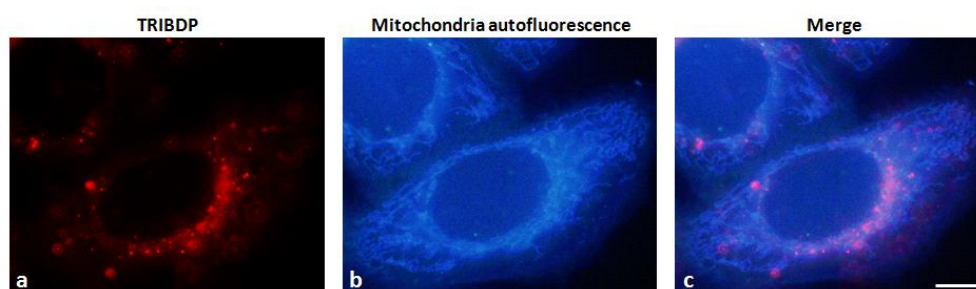
Figure 3.46. Localization of TRIBDP into living HeLa cells after 24 h incubation. (a) Subcellular localization upon irradiation with green light (red fluorescence); (b) mitochondrial autofluorescence upon irradiation with UV light (blue fluorescence); (c) Merge. Scale bar: 5 μm.

In order to test the intrinsic toxicity of Tri-BDP (dark toxicity), HeLa cells were incubated with Tri-BDP (10^{-5} M) for 24 h without irradiation, founding that cell viability did not decrease significantly (Figure 3.47) and, therefore, demonstrating the low toxicity of Tri-BDP under "dark" conditions. The same experiment was repeated under the same conditions, but irradiating the cells with green light (5.7 mW/cm2) for 30 min (total light dose = 10.2 J/cm2) after the conducted incubation. In this case, this incubation+irradiation (photodynamic) treatment has a powerful photo-inactivation effect on HeLa cells, inducing 60% cell death 24 h after treatment (Figure 3.47). On the other hand, images obtained by differential interference contrast (DIC) microscopy (Figure 3.47) showed apoptotic morphologies of HeLa cells after the said photodynamic treatment, while these morphologies were not observed on untreated, control cells.
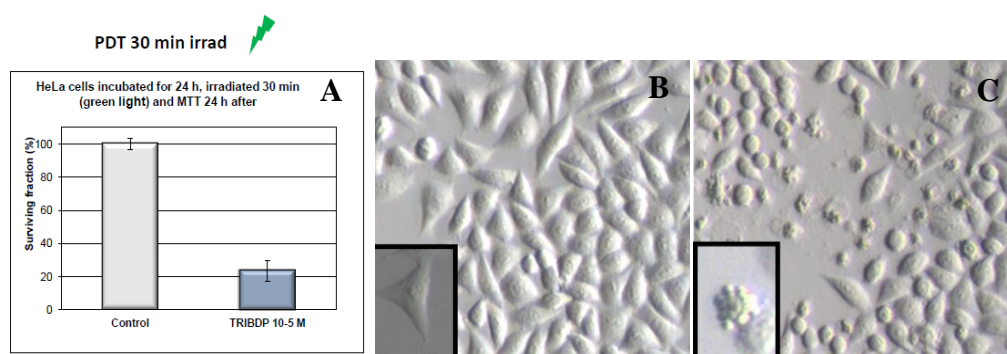
Figure 3.47. A) Light-triggered cytotoxicity of TRIBDP on HeLa cells. Surviving fractions by MTT assay of cells 24 h after of being incubated with TRIBDP (10^{-5} M in DMSO) or without (control experiment). B) Cell morphologies visualized by DIC microscopy before and C) after 2 h of the conducted photodynamic treatment with TRIBDP (inset B and C is signalized normal (control) *vs.* apoptotic morphology). Scale bar: 20 µm

At this moment, those experiments are carried out under radiations of different wavelengths to compare the cytotoxicity effects on the HeLa cells with respect to green light excitation at the same conditions to probe the panthochromic action of this photosensitizer.

3.2.1.3. Conclusions on BDP dimers

A relatively high quantum yield of singlet oxygen production was measured with halogen-free orthogonal-BDP dimers, likely via SOCT-ISC mechanism as a consequence of the orthogonal arrangement. This mechanism consists on the fast spin-flip that occurs to compensate the change in the angular momentum since these compounds involve intramolecular charge transfer transitions after the excitation. Therefore, the ability to generate singlet oxygen is strongly connected with the intrinsic ICT character of the orthogonal dimers. Actually, a very favored ICT state will drastically reduce the generation of the singlet oxygen production because it competes with the intersystem crossing (ISC) conversion to the triplet state of the dye. Accordingly, the singlet oxygen generation can be modulated by the polarity of the environment or by introducing donor/acceptor substituents into the BODIPY units.

A dissymmetric dimer (with the substitution of only one conjugated group and EWG group) has showed a modest singlet oxygen production under red excitation in the therapeutic window (600-800 nm), together with a moderate red fluorescence interesting for potential theranostic applications. Accordingly, the design of new halogen-free asymmetric dimers could open the door to potential compounds with dual functionality (Photodynamic therapy and imaging) under excitation wavelength in the therapeutic window.

Finally, a panchromatic halogen free cassette based on multiple BDP chromophores is described in order to use it for theranostic application with high enough emission for fluorescence microscopy, and high $^1O_2$ generation by excitation at different Vis wavelengths (from blue to yellow). This latter feature is important to gain photostabiliy and bioimaging contrast, as well as PDT activity (*i.e.*, by harvesting solar irradiation in long-time topic treatments or by supporting severe irradiation in short-time internal therapies). The "in vitro" experiments have demonstrated a low toxicity to living cells under dark conditions, but a high toxicity under irradiation, promoting the efficient death of HeLa cells by apoptosis. Moreover, the simple, purely organic molecular structure of orthogonal BDP is efficiently internalized by cells and accumulated in living HeLa cells, probably at the lysosomal compartment.

3.2.2. Mesoporous silica nanoparticles

The main aim of this work is the use of silica nanoparticles for bio-applications such as imaging and photodynamic therapy. Accordingly, core-shell silica nanoparticles were synthetized in order to combine both applications since silica NPs offer the possibility of introducing different types of molecules not only embedded inside NP (Core) but also grafted on NP surface (Shell). In this section, the main results on the mesopororous silica nanoparticles are shown. Their morphology and size distribution was analyzed by Scanning Electron Microscopy (SEM) and Transmission Electron Microscopy (TEM). The dispersity of the nanoparticles in suspension of different solvents is studied by Dynamic Light Scattering (DLS). The surface and more particularly, the presence of photoactive molecules of interest grafted at the surface was studied by to X-Ray photoelectron Spectroscopy (XPS) and Infrared spectroscopy (FTIR-ATR). The photophysical characterization was carried out by absorption and fluorescence (steady-state and time resolved) spectroscopies and the singlet oxygen determination was performed by direct method measuring the singlet oxygen signal at 1270 nm.

3.2.2.1. Silica Nanoparticles characterization

The synthesis of core-shell NP was carried out by the Stöber-modified method, in two steps as previously described in the experimental section. In short words, the core was synthesized through the mixture of TEOS in absolute ethanol and a basic solution in the presence of CTBA as surfactant. By adding APTMS (Table 3.1) in a second step the shell containing amino groups for surface functionalization was formed (Figure 3.48).
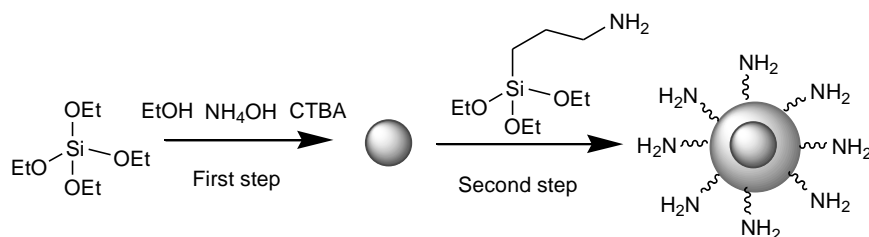

Figure 3.48. Mesoporous silica nanoparticles scheme, modification of the Stöber method.

As previously commented in the introduction, the size, shape and porosity of the silica nanoparticles can be modulated by different synthesis conditions (pH, temperature,…) and gel composition (TEOS, NH_4OH content, ethanol/water ratio, surfactant concentration). Therefore, different syntheses were carried out to obtain silica NP suitable for bio-applications. In this aim, the optimal size is selected around 30-50 nm becuase too big particles will not easily diffuse by the blood stream. Besides this size will be optimal for their elimination[90] since they are able to exit the fenestrated capillaries of the kidney, intestine and some endocrine/exocrine glands.

As an example, with a relative high concentration of NH_4OH of 0.51 M and a temperature of 20ºC during the reaction and 50ºC during aging process, spherical NP with a relative large average particles size (around 150 nm, Figure 3.49A) were obtained. However, by reducing the NH_4OH concentration around 4 times and simultaneously increasing the reaction and aging temperature up to 60ºC, the NP size decreased from ~150 nm to ~50 nm (Figure 3.49B).

To get more insights about the nanoparticles, TEM images were recorded (Figure 3.50). The nanoparticles size distribution was analyzed by Images-J software (Figure 3.50A), which confirmed a homogenous size distribution around 50 nm.

The mesoporous structure of the silica NP is nicely observed Figure 3.51A. Moreover, as previously described, the "shell" of the NP with a thickness of around 10 nm (surface functionalized with amino groups by the addition of APTMS in the second synthetic step) is also clearly seen in Figure 3.51A. In order to estimate the composition and more particularly the amount of amino groups in the shell of the NP, X-ray Photoelectron Spectroscopy (XPS) was used (Table 3.9).
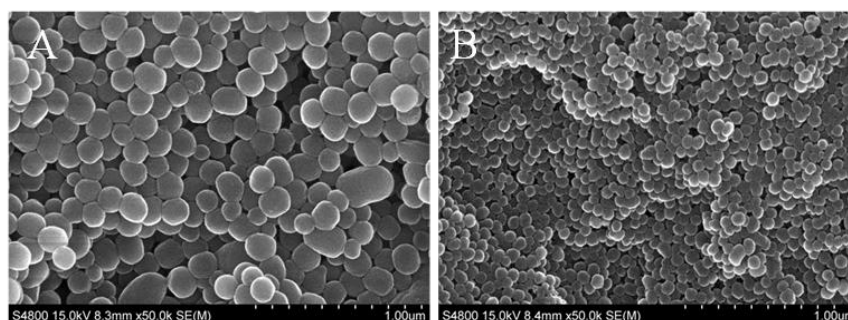
Figure 3.49. SEM images of silica NPs obtained under different synthesis conditions: (A) Silica NP with around 150 nm size; (B) Silica NP with around 50 nm size.
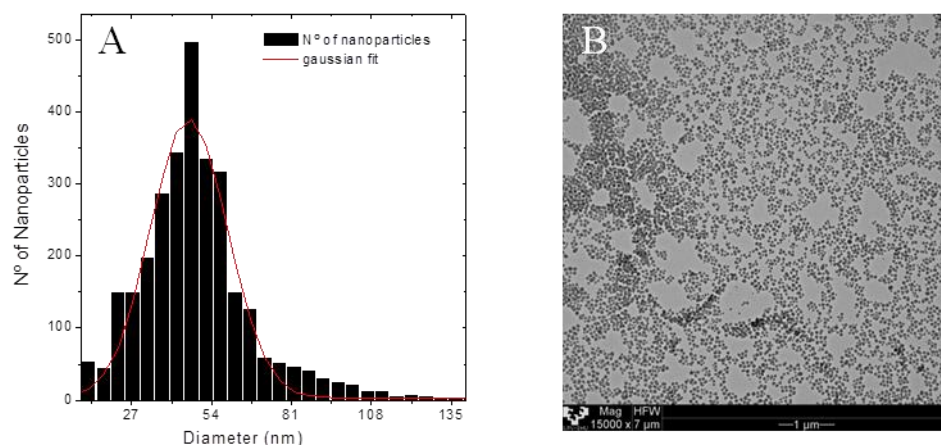
Figure 3.50. (A) NP size distribution and (B) silica NP TEM image.
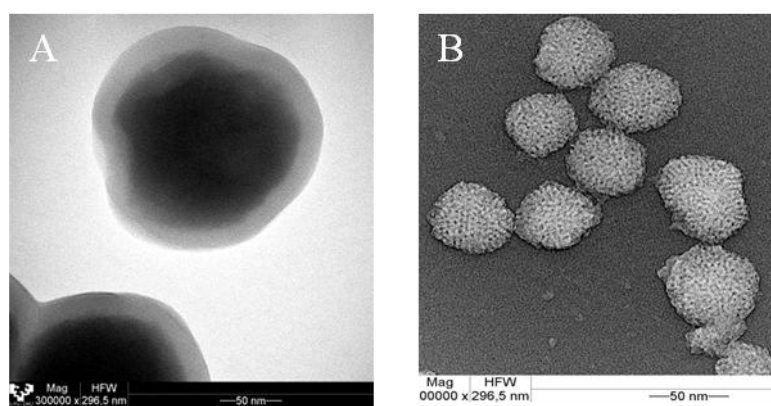
Figure 3.51. (A) Silica NP Core-Shell image and (B) the inverted bright field silica NP TEM image.

According to the XPS results, although the major contribution is due to the presence of SiO_2 (note here the perfect fit of Si/O atom ratio in Table 3.9), the relative atomic ratio of N atoms is 4 %. This amount of amino groups is an adequate proportion to graft photoactive molecules, as described later. The presence of chlorine atoms (2.5 % atomic ratio) is due to the washing of the nanoparticles by a diluted hydrochloric solution at the end of the synthesis, transforming the amino groups in ammonium chloride groups. No comment on carbon content can be drawn from these data, since there is always a significant carbon contamination in these XPS results.

Table 3.9. Silica Nanoparticles XPS results.

Atoms	Relative percentages of atoms
C	15
O	52
N	4
Si	26
Cl	2.5

DLS technique was used to study the dispersity and stability of the nanoparticles in suspension. They were suspended in several solvents with different polarity: water (H_2O), ethanol (EtOH) and acetonitrile (ACN). The DLS measurements were done just after magnetic stirring (t=0) and after one hour (t=1h) without stirring. Figure 3.52 shows the hydrodynamic diameter distribution of the nanoparticles in the different solvents at t=0 (red curve) and setting the sample for one hour, t=1h (green curve). The correlation diagram for the aqueous suspension is also shown (Figure 3.52D). All samples analyzed at t=0 show only one distribution curve. In the case of ethanol (Figure 3.52A) and water (Figure 3.52C), similar hydrodynamic values were obtained (212±13 nm and 257±54 nm respectively, Table 3.10), with a value larger than the size of the NP obtained by TEM images (~50 nm). This result suggests that a slight aggregation of the NPs occurs in these solvents. However, in ACN (Figure 3.52B) the NP size distribution was considerably lower (92±3 nm), indicating a better dispersion of NPs in this solvent. Nevertheless, there are important changes in the hydrodynamic diameter after 1 hour without stirring (Figure 3.52 and Table 3.10). In ethanol higher aggregates (hydrodynamic size around 375 nm) are formed with time. On the other hand, in water and ACN, two different NPs populations were obtained (Figure 3.52B and C) after 1 h, which indicates that the NP in suspension has formed higher aggregates (around 330 nm in both cases) while other proportion of NP remains better dispersed (Table 3.10). The presence of aggregates was verified by correlation diagram (Figure 3.52D). It is important to note that the major contribution of NPs in ACN after 1h comes from the lower hydrodynamic diameter (around 68±7 nm, 60%), which is relatively close to size of the nanoparticles. For all these reasons, ACN is considered as the best solvent to disperse the silica NPs.
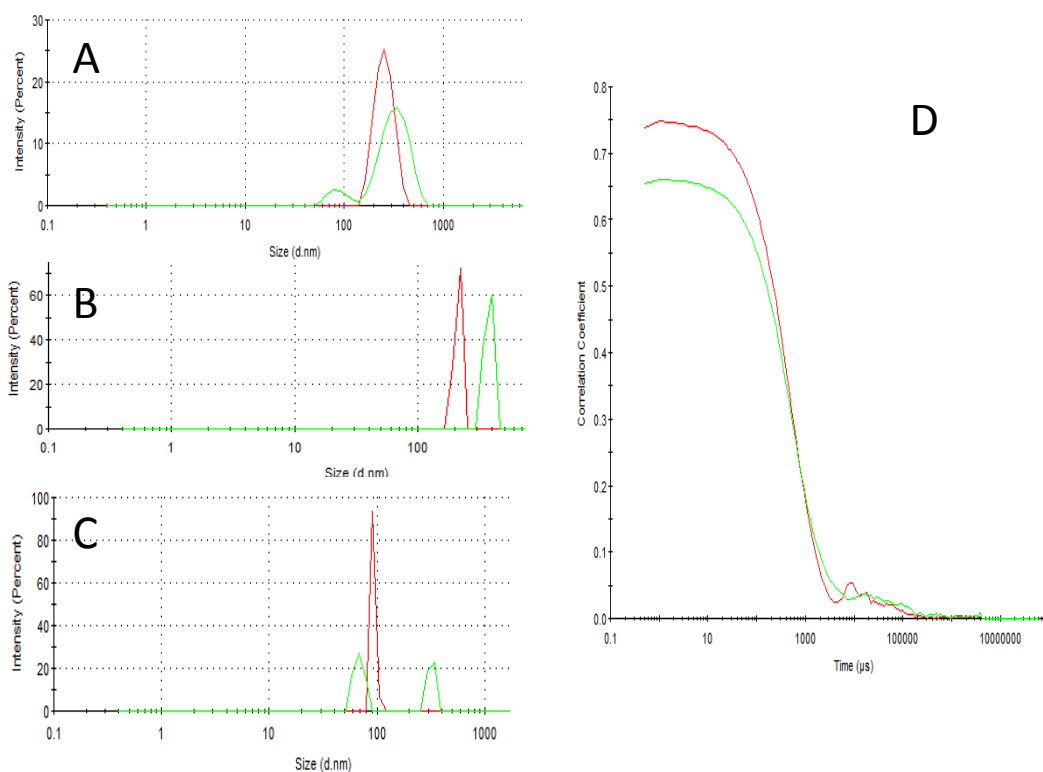
Figure 3.52. Hydrodynamic diameter of silica nanoparticles and intensities distribution previously stirred (t=0, red), after 1 h (green) suspended in ethanol (A), acetonitrile (B), water (C). The correlation curve is shown for water (D).

Table 3.10. Mesoporous Silica Nanoparticles hydrodynamic diameter in different solvents after stirring (t=0s) and after leaving to stand (t=1h).

Solvent	Diameter (nm) (t=0)	Diameter (nm) (t=1h)	
Ethanol	212±13	374±26	
Acetonitrile	92±3	68±7 (60%)	321±23 (40%)
Water	257±54	90±22 (11%)	336±102 (89%)

3.2.2.2. "Working in the Core": Fluorescent nanoparticles by dye Encapsulation for Bio-imaging application

In this section different fluorescent dyes are embedded in the "core" of the silica nanoparticles with the aim of synthesizing fluorescent nanoparticles for potential bio-imaging applications. Two different Rhodamines were chosen: Rhodamine 6G (R6G) and Sulforhodamine 640 (R640).

The encapsulation was done "in situ" by adding the adequate amount of dye into the synthetic gel of the nanoparticles. To get silica nanoparticles with the highest fluorescence properties, the concentration of the dye should be optimized. For this purpose, different R6G dye concentrations were tried in the range of 10^{-2} – $5.0\ 10^{-5}$ M (Table 3.11). Note here that the dye encapsulation did not modify the NP size, morphology and polydispersity (Figure 3.53A).

The amount of dye embedded into the NP "core" was estimated photometrically, by dissolving the silica matrix with KOH 1M (Table 3.11). The number of R6G molecules embedded was estimated through Equations 3.2-3.4.

$$V_{NP} = \left(\frac{4}{3}\right) \cdot \pi r^3 \qquad\qquad\qquad \textbf{Equation 3.2}$$

$$\left(\frac{NP}{g}\right) = V_{NP} \cdot \rho_{SiO_2} \qquad\qquad\qquad \textbf{Equation 3.3}$$

$$\frac{N*mols\ of\ dye\ per\ gram}{number\ of\ NP\ per\ gram} = N * mols\ of\ dye\ per\ gram * V_{NP} * \rho_{SiO2} \qquad \textbf{Equation 3.4}$$

That is, from the volume of the nanoparticles and density of the silica (ρ_{SiO2}=2,2 g cm^{-3}), the number of NP/gr is obtained. Then, equation 3.4 is applied to estimate the total number of dye molecules per NP, where N is the Avogadro constant.
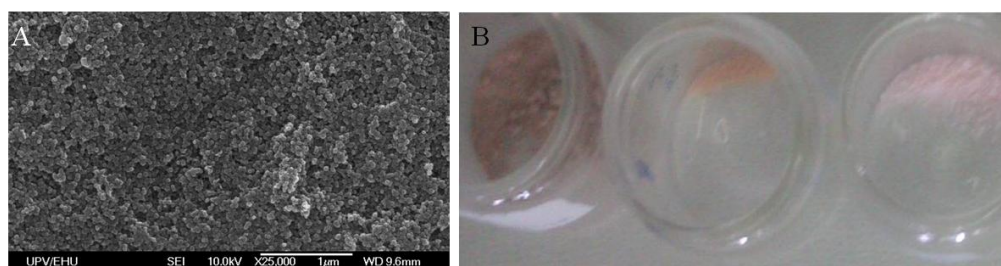
Figure 3.53. (A) SEM image of the nanoparticles with encapsulated R6G; (B) Picture of the NP powder for different encapsulated R6G concentrations (using concentrations in synthesis gel 10^{-2} M (left), 10^{-3} M (middle) and $5\,10^{-4}$ M (right).

Note here that a dye concentration in the sol $\leq 10^{-4}$ M is not enough to ensure the inclusion of enough dye molecules in the NP "core" (Table 3.11). However, the total number of dye molecules included inside the NP increase with dye concentration in the gel from $5\,10^{-4}$ M to 10^{-2} M (Table 3.11). This fact can be clearly seen in the Figure 3.53B, where color tonality of the NP powder is more intense as the dye concentration increases in the gel. It is also confirmed by the absorption spectra of the nanoparticles (Figure 3.54A) measured in an integrating sphere.

Table 3.11. NP/R6G characterization: initial dye concentration in the gel; dye concentration per gr of gel; number of dye molecules inside one NP, absorption (λ_{abs}) and fluorescence ($\lambda_{flu}$) wavelength, NP/R6G fluorescence quantum yield (QY) with excitation wavelength at 495nm and fluorescence lifetimes (τ) and their contribution (%). Lines in dark grey refer to the dyes R6G and R640 in ethanol solution.

Sample	[Dye] in the sol (M)	R6G mol/g xerogel	R6G molecules per NP	λ_{abs} (nm)	λ_{flu} (nm)	ϕ_{flu} $\lambda_{ex=}$495nm	τ (ns)/ (%)
NP-R6G1	$1.0\,10^{-2}$	$1.4\,10^{-5}$	1260	529	566	<1	0,44 (77%) 3,02 (23%)
NP-R6G2	$1.0\,10^{-3}$	$1.1\,10^{-5}$	990	525	553	3	0,76 (80%) 3,11 (20%)
NP- R6G3	$5.0\,10^{-4}$	$6.7\,10^{-7}$	58	529	546	30	3,90
NP- R6G4*	$1.0\,10^{-4}$	$5.6\,10^{-8}$	5	528	543	-	3,90
R6G(EtOH)	-	-	-	530	551	88	3.90
NP-R640	$5.0\,10^{-4}$	$1.0\,10^{-6}$	89	570	590	52	4.42
R640(EtOH)	-	-	-	575	595	86	4.50

* In this case the dye molecules encapsulation is not enough to determinate the fluorescence quantum yield.
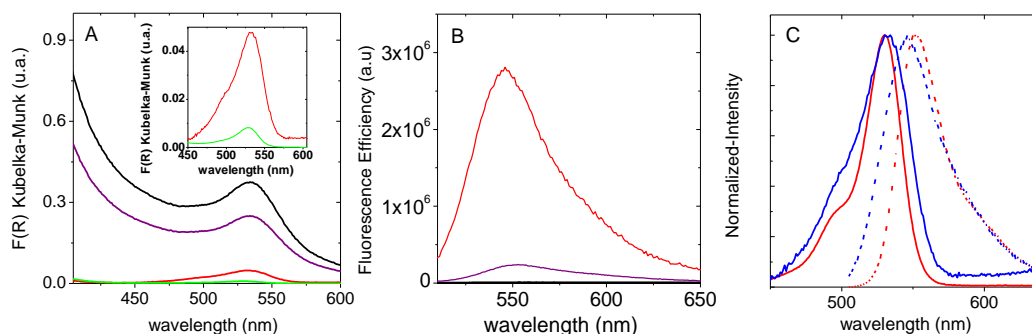
Figure 3.74. (A) Representative Absorption, (B) fluorescence spectra of NP-R6G1 (black), NP-R6G2 (purple), NP-R6G3 (red) and NP-R6G4 (green) and (C) Absorption and fluorescence spectra of R6G solution (red) and powder (blue) samples.

The absorption band for NP-R6G samples is slightly blue-shifted with respect to the dye in ethanol solution (Table 3.11, Figure 3.54C), which could be attributed to the hydrophobic environment of alkane chains of surfactant molecules present in the silica core. Moreover, the spectra of the NP-R6G are wider relative to R6G in solution, which is a typical effect of the dye in adsorbed-state with distorted vibrational states.

However, the opposite influence of R6G concentration is obtained in the fluorescence spectra (Figure 3.54B). The fluorescence efficiency decreases as the number of embedded R6G molecules increases, being practically negligible for the most concentrated NP-R6G sample (NP-R6G1). The decrease of the fluorescence capacity of the nanoparticles with the dye concentration can be attributed to different phenomena. First, one can think that the R6G molecular aggregation inside the nanoparticles would be responsible of the decrease of the fluorescence capacity, which can drastically modify the photophysical properties of the dye, as previously described in chapter 1, for Macroscopically Ordered Systems. However, the absorption and fluorescence spectra do not show any change with the dye concentration, neither in the shape nor in the appearance of new bands (Figure 3.54C). Accordingly, the drop in the fluorescence efficiency in the most concentrated NP-R6G1 sample could more probably be attributed to inner-filter or reabsorption-reemission phenomena. This process occurs when the emitted photons are reabsorbed by dye molecules close to each other. Thus, the global fluorescence efficiency and quantum yield decrease. Therefore, this problem becomes serious when measuring highly concentrated dye. Indeed, the fluorescence band of the most concentrated sample NP-R6G1 shows a

significant red shift (20 nm) with respect to NP-R6G3, confirming that this phenomenon can account for the low fluorescence emission of optically dense nanoparticles.

Regarding the sample NP-R6G3, the fluorescence band at 546 nm is slightly blue shifted with respect to the dye in solution (Table 3.11), in agreement with the absorption spectra of the NP-R6G samples and previously attributed to the presence of the surfactant. More importantly, the quantum yield of this sample NP-R6G3 (around 30%, Table 3.11, is lower than the fluorescence efficiency of the dye in solution (88 %), but should be enough to be detected under conventional fluorescence microscopes and therefore adequate for bio-imaging. In fact, due to the higher photostability of the dye after encapsulation[91] these nanoparticles would offer prolonged times for detection[92]. On the other hand, NP-R6G3 presents a monoexponential behavior with a lifetime around 3.9 ns, identical to that recorded for R6G in diluted solution (Figure 3.55).
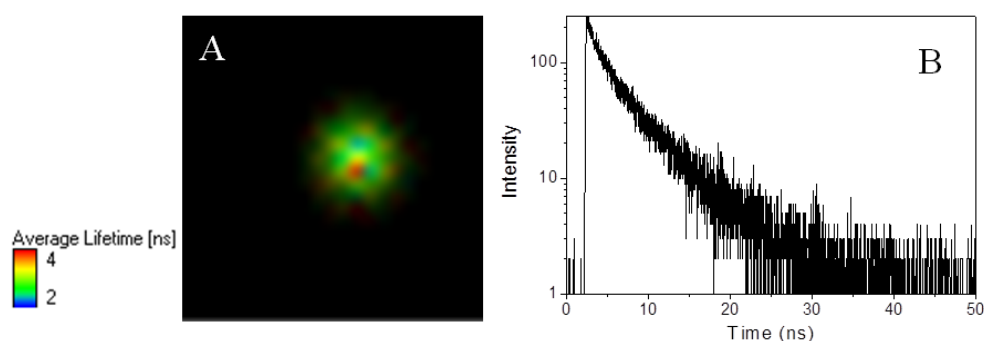
Figure 3.55. The FLIM image for confocal microscopic for an individual nanoparticle for NP-R6G3 sample exciting at 470 nm (A) and its fluorescence lifetime decay (B).

Therefore, an initial dye concentration of $5 \cdot 10^{-4}$ M in the synthesis sol is considered as the optimal concentration to give rise to the best fluorescence properties for NP-R6G samples (NP-R6G3).

Once the dye concentration in the synthesis gel was optimized for R6G dye, a new dye, Rhodamine 640, with absorption and emission bands centered more in the red region of the Vis spectra, is encapsulated by the same procedure, keeping the dye concentration in the gel $5 \cdot 10^{-4}$ M as the best condition.
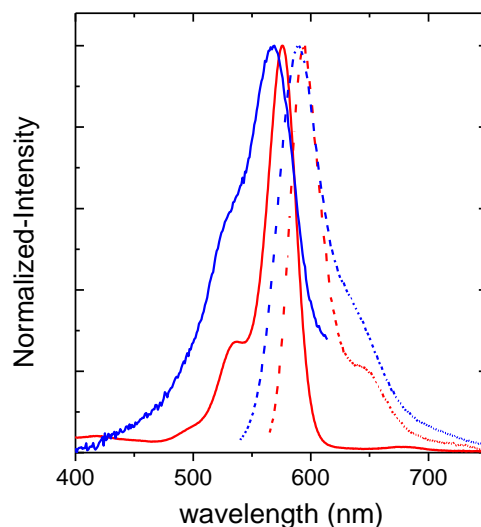
Figure 3.56. Normalized absorption and emission spectra of Rhodamine 640 in ethanol solution (red) and embedded in NPs (blue).

The absorption and emission spectra of R640 embedded in the NPs and in solution is displayed in Figure 3.56. The absorption and emission bands of the physically adsorbed R640 dye, centered at around 570 nm and 590 nm respectively, are again blue shifted respect to solution, likely as a consequence of the interaction with the alkane chains of surfactant molecules co-absorbed in the silica core. As previously described for NP-R6G, both absorption and fluorescence bands are also wider than the respective bands in solution ascribed to the adsorbed-state of the dye. More importantly, NP-R640 sample shows a fluorescence quantum yield of 52%, considerably higher than that obtained for NP-R6G. Moreover, a mono-exponential lifetime is obtained (τ = 4.42 ns), which is similar to R640 in solution (τ = 4.5 ns). Accordingly, these nanoparticles NP-R640 can be of special interest in bio-imaging applications, particularly for their absorption and fluorescence bands more shifted to the red region of the visible spectra than NP with R6G.

In the next section, different dye molecules with photosensitizing properties, will be anchored in the shell of the silica NPs in order to combine the imaging and therapeutic action of the nanoparticles.

3.2.2.3. "Working on the Shell": Nanoparticles for Photodynamic Therapy application by the Grafting of Photosensitizers

As previously recalled, the second important aim of the synthesis of these nanoparticles is to implement them in PDT. For this purpose, different photosensitizers (PS) were covalently linked on the external surfaced of the silica nanoparticles. First attempts were made with a commercial photosensitizer, Rose Bengal (RB), which has demonstrated a relatively high singlet oxygen production[3]. The choice of RB was also guided by the presence of a carboxylate group in its molecular structure (see Figure 3.10) making it an ideal molecule for grafting on the NH_2 groups present on the external surface of the silica nanoparticles (sample denoted as NP-RB1, Figure 3.57A) by conventional peptide coupling reactions (experimental chapter 4, section 4.1.3.2). On the other hand, a triethoxysilyl derivative of RB, was also covalently linked to the OH groups (sample NP-RB2, Figure 3.57B, synthesis described in the experimental chapter 4, section 4.1.3.3) of the silica nanoparticles surface. The singlet oxygen production of these two types of RB-containing NPs will be compared to elucidate which system will have the best performance for PDT.

After the grafting process both on NH_2 and OH groups of the external surface of silica nanoparticles with RB was optimized, new halogenated dipyrromethene boron difluoride (BDP) photosensitizers (see molecular structure in Figure 3.10) with very promising singlet oxygen production described in section 3.2.1.1. were grafted on NH_2 functional groups, denoted as sample NP-BDP1 (Figure 3.57C) and on OH groups of the silica nanoparticles surface, denoted as sample NP-BDP2 and (Figure 3.57D).
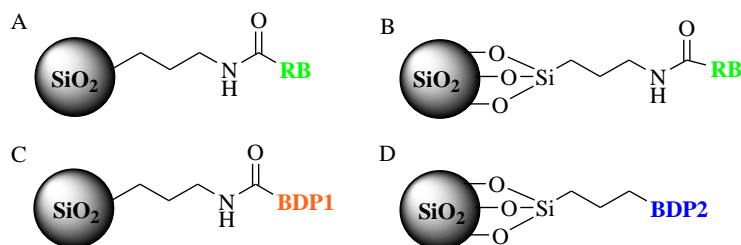
Figure 3.57. Schematic representation of grafted NP: (A) NP-RB1, (B) NP-RB2, (C) NP-BDP1 and (D) NP-BDP2. The BDP derivative used for preparing NP-BDP1 was named aryl-BDP1-2I in section 3.2.1.1.1 (Table 3.2) and will be further simplified as BDP1 in the following. The BDP derivative used for preparing NP-BDP2, named BODIPY-Si(OEt)$_3$ in the experimental chapter 4, Scheme 5 will be named BDP2 in the following and is structurally closed to the 8-amino-BDP1-2I previously studied in section 3.2.1.1.3. See Figure 3.10 for their molecular structure.

3.2.2.3.1. Surface characterization of the PS on silica nanoparticles

Different techniques were employed to confirm the covalent link of the different PS on the external surface of silica nanoparticles.

First, TEM images confirmed that the grafting did not modify the NP morphology and size (Figure 3.58) and shows NP with spherical morphology with particles size around 50 nm, identical to the previous NP before the grafting process on the surface.
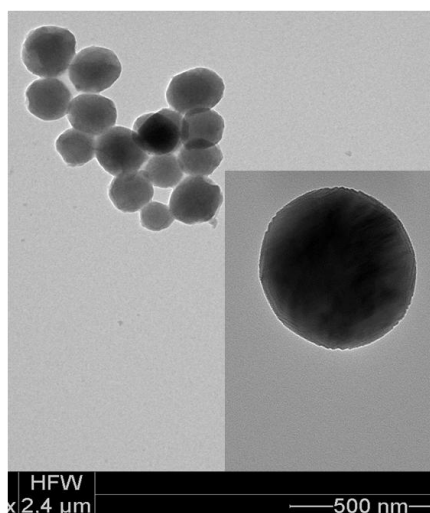
Figure 3.58. TEM representative images of NP-RB1 sample.

Second, the presence of the PS on the NP surface was checked by two different techniques: IR-ATR and XPS.

The grafting of RB and BDP1 on NH_2 and the grafting of the triethoxysilyl derivative of RB on OH groups of the NPs both involves a peptide coupling reaction (see scheme 4.3 and 4.4 in experimental chapter 4): accordingly, NP-RB1, NP-RB2 and NP-BDP1 samples should bring an amide bond. These amide bonds show representative peaks in the IR region: *i*) The amide I, at around 1630 cm^{-1}, which correspond to the C=O stretch and *ii*) the amide II, at around 1550 cm^{-1} which correspond to the C-N stretch and N-H bend[93]. Actually, the analyzed samples NP-RB1, NP-RB2 and NP-BDP1 showed these typical IR peaks, at around 1600 cm^{-1} and 1550 cm^{-1} (Figure 3.59, Table 3.12), confirming the grafting of the PS on the external surface of the silica NP.
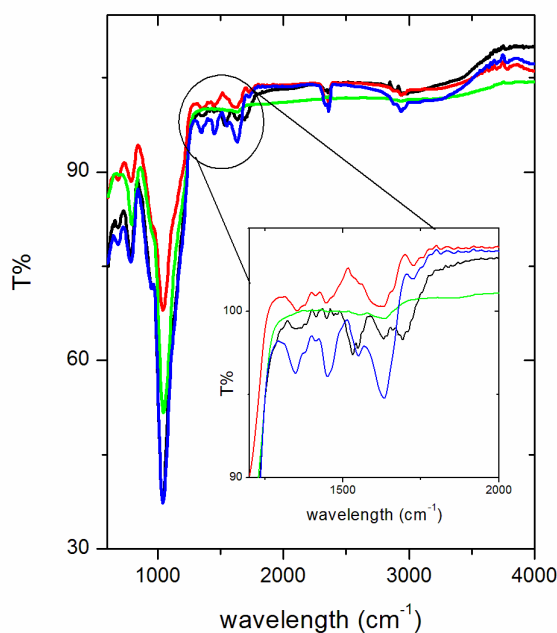
Figure 3.59. FTIR spectra of silica NP (green), NP-RB1 (red), NP-RB2 (blue) and NP-BDP1 (black).

Table 3.12. IR-ATR amide bonds summary.

Sample	Amide I (cm^{-1})	Amide II (cm^{-1})
NP-RB1	1630	1550
NP-RB2	1631	1550
NP-BDP1	1600	

However, in the NP-BDP2 sample, the grafting process was performed by direct polymerization of the triethoxysilyl amino derivative BDP2 on OH groups of the silica surface (see Scheme 4.5 in experimental part). In this case, the only characteristic IR bands are the weak N-H stretching vibrations associated with the amine function between 3500 and 3300 cm^{-1} or the very weak N-H deformation in the 1650-1550 cm^{-1} range. However these bands were only poorly observed in the IR-ATR spectrum of this sample.

Table 3.13. Summary of the grafted NP XPS results.

Sample	% At Concentration						
	C	O	N	Si	Cl	F	I
NP	15	52	4.0	26	2.5	-	-
NP-BDP1	22	44	7	22		2.3	2.2
NP-BPD2	23	42	5.1	24	2.4	2.2	1.6

In order to confirm the presence of BDP2 on the silica surface, XPS was employed as a semi-quantitative technique. According to the XPS results, (Table 3.13) the new presence of the I and F atoms on both samples NP-BDP1 and NP-BDP2, are indicative of the BDP molecular structure, as well as the higher contribution of the C and N atoms with respect to the naked silica nanoparticles. These data indicate that the grafting of BDP1 and BPD2 on the NH_2 and OH groups respectively of the external surface of the silica nanoparticles has successfully taken place. The absence of chlorine in sample NP-BDP1 is due to the use of triethylamine during the grafting step in order to transform the ammonium chloride functions of the NP into amide (graftable) groups. On the other hand, chlorine is still present on NP-BDP2 sample since no base (triethylamine) is used in this case.

On the other hand, in order to estimate the total amount of grafted PS on the NPs, different spectrophotometric approaches were attempted with: A) a solution of previously dissolved silica nanoparticles in tetrabutylammonium fluoride for the cases where the PS was chemically stable and B) the absorbance value of a previously weighted amount of grafted nanoparticles in suspension, assuming the same molar extinction of the PS in the NP and in solution.

The method A, based on the dissolution of the silica matrix, should provide more precise information about the dye quantification, as long as the PS molecules are stable in a fluoride environment: in this case, there is not any approximation on the molar absorption coefficient since the calibration curve is done in the same solvent. Regarding method B, a very stable suspension is required because the aggregation and/or flocculation of the nanoparticles will induce a sub-estimation of the absorbance and consequently in the estimation of the dye concentration. Indeed, this was confirmed by the results obtained with the RB-grafted silica NPS since a lower dye amount is obtained by the method B with respect to method A (Table 3.14). This effect is more significant in the sample NP-RB2 (RB grafted on OH) leading to estimated concentration 6 times lower by method B than by method A.

Table 3.14. Spectrophotometric estimation of the amount of grafted PS on silica NPs.

Sample	method A (mol/gr)	method B (mol/gr)
NP-RB1	8.0×10^{-6}	3.3×10^{-6}
NP-RB2	2.4×10^{-5}	4×10^{-6}
NP-BDP1	-	1.8×10^{-6}
NP-BDP2	-	5.2×10^{-6}

This fact is attributed to the impossibility of getting a well dispersed suspension of NP-RB2 nanoparticles in the different solvents used (more details later in the text, section 3.2.2.3.2.1). On the other hand, the sub-estimation factor on the PS concentration between methods B and A for the sample NP-RB1 (RB grafted on NH_2) was around 2.5 (Table 3.14), due to the better dispersion of the NP-RB1 in suspension (described in more details in section 3.2.2.3.2.1). Moreover Table 3.14 indicates that the amount of RB grafted on the external OH groups (NP-RB2) is larger (3.0 times according to method A) than the RB grafted on the functional NH_2 groups (NP-RB1). This may be simply related to the higher amount of OH groups compared to NH_2 active groups. Accordingly, the NP-RB2 nanoparticle surface is quite hydrophobic and consequently the tendency to agglomerate is higher, making method B inappropriate.

For the case of the BDP-NPs, the estimation of the concentration was only possible by method B, since BDPs were chemically degraded by method A. Although by method B the concentration will be sub-estimated, NP-BDP1 and NP-BDP2 samples give relatively more stable suspensions and the sub-estimation factor on the BDP concentration should not be very high (≤ 2.5). Note here that the amount of BPD grafted on the external OH-groups (NP-BDP2) was also 3 times higher than the amount of BPD covalently linked of the external NH_2 (NP-BDP1).

3.2.2.3.2. Photophysical characterization and singlet oxygen production of PS grafted on NPs

The photophysical characterization and singlet oxygen production of the silica nanoparticles with the different grafted photosensitizers was carried out in suspension by spectroscopic techniques (see experimental section for more details, section 4.3).

a) Grafting of Rose Bengal

In order to study the phototophysical properties and singlet oxygen generation, the RB-grafted NPs were first suspended in ACN. Figure 3.60A shows the absorption spectra of the samples NP-RB1 and NP-RB2 together with that of a diluted solution of RB in ACN (10^{-6} M). Contrary to the Rhodamines embedded in the silica core, the absorption bands of the RB grafted at the external silica surface, centered at 561 nm, are slightly red-shifted with respect to RB in ACN solution (Table 3.15).
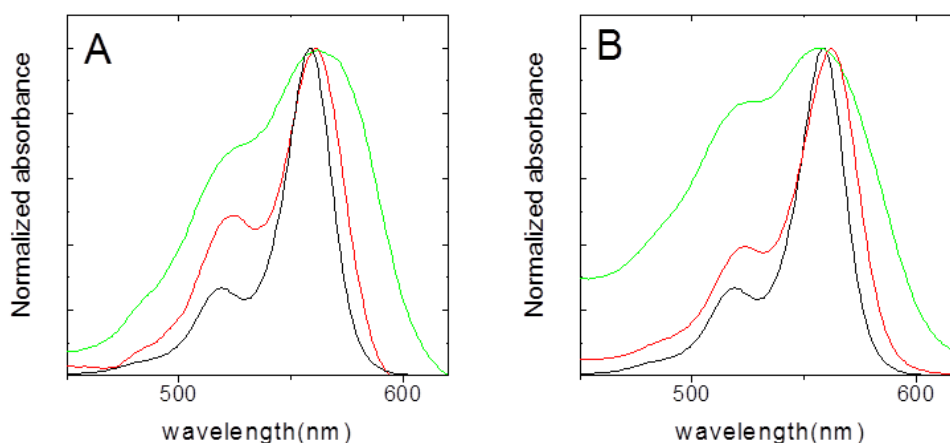
Figure 3.60. (A) Absorption spectra in ACN and (B) in CHCl$_3$ of RB solution (black), NP-RB1 (red) and NP-RB2 (green)

Table 3.15. Photophysical data and quantum yield of singlet oxygen production of NP-RB nanoparticles and RB in ACN solution

	λ_{abs} (nm)	λ_{fl} (nm)	ϕ_{fl}	Φ_{Δ}	
				ACN[1]	CHCl$_3$[2]
RB solution	555	579	0.12	0.53*	--
NP-RB1	561	580	0.08	0.14	0.27
NP-RB2	561	584	0.03	0.10	0.07

*measured in our laboratory by direct method with phenalenone as reference ($\Phi_{\Delta} = 1$ in ACN)[29]
[1] Reference RB in ACN ($\Phi_{\Delta} = 0.53$)
[2] Reference 8-methylthio-BDP4-2I in CHCl3 ($\Phi_{\Delta} = 0.80$)

This fact could be attributed to the interaction between dye molecules themselves and the hydrophilic surrounding of the silica matrix. However, in these samples, the shape of absorption band is quite different with respect to RB in diluted solution. The spectrum of RB-grafted NPs shows a prominent shoulder at around 518 nm, particularly in the sample NP-RB2. These changes could be attributed to RB aggregation, particularly H-type aggregation (discussed previously in chapter 1 on macroscopically ordered systems). Indeed, it is well known that RB as a xanthene-type dye has a high tendency to aggregate in concentrated or rigid media[2,93,94,95].

First, one can think that the dye aggregation could take place intra-particle. To analyze in more detail these results, a rough estimation of the dye molecules distance in the NP surface at the estimated dye concentration was done. Taking into account the total number of NP per gr (equation 3.2 and equation 3.3), the amount of grafted RB estimated before (Table 3.14), and the surface area of a sphere of 50 nm diameter (equation 3.5), a dye intermolecular distance around 20 Å and 33 Å is obtained for NP-RB1 and NP-RB2, respectively.

$$S_{NP} = 4 \cdot \pi r^2 \hspace{4cm} \textbf{Equation 3.5}$$

Those distances are relatively higher than the typical distance between monomers in a dimer, around 2-10 Å.[96] Thus, the self-aggregation of the dye along the surface of one nanoparticle could be considered almost negligible. On the other hand, note here that the external surface of the silica NP has become more hydrophobic relative to naked silica NP because of the presence of RB. Thus, the dye aggregation could be considered to take place inter-particle, due to NP agglomeration especially in polar solvent such ACN. Indeed the higher amount of dye in the sample NP-RB2 (around 3.5 times, RB-grafted on OH groups) with respect to the analogous sample NP-RB1 (RB-grafted on NH_2 groups) will favor this particle agglomeration.

For this reason, a less polar solvent such as chloroform was considered for the suspension of grafted-NPs. Although it is well know that Rose Bengal is not soluble in chloroform,[97] it gives a stable suspension when it is covalently grafted on NP surface (Figure 3.61). Indeed, the absorption band of the sample NP-RB1 in chloroform (Figure 3.60B) shows a much less prominent shoulder at 518 nm, attributed to the dye aggregation, relative to that recorded in ACN (Figure 3.60A). However, for the sample NP-RB2, the aggregation is still noticeable, likely as a consequence of a higher

amount of RB grafted on the active OH of the silica surface (Table 3.15). Unfortunately, for this later sample, no suitable solvent was found to get a stable nanoparticle suspension and some flocculation in chloroform was also clearly visible to the naked eye (Figure 3.61).
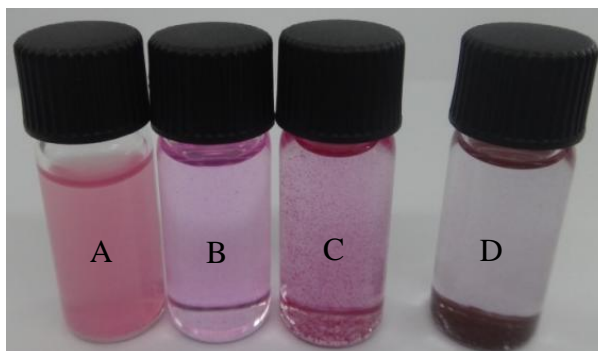
Figure 3.61. (A) NP-RB1milky suspension in ACN, (B) NP-RB1 very transparent suspension in chloroform, (C) NP-RB2 unstable suspension in chloroform (significant NP agglomeration can be seen in the image) and (D) RB dye precipitated in Chloroform.

The singlet oxygen quantum yield for the samples NP-RB1 and NP-RB2 suspended in both solvents, ACN and CHCl$_3$ was measured by direct method using as reference RB in ACN and 8-methylthio-BDP4-2I (described in section 3.2.1.1.2) in CHCl$_3$. It is worth to note here that the dye aggregation not only modifies the absorption spectra but also the singlet oxygen production (Table 3.15). In fact, the particle agglomeration provides negative effect on the RB singlet oxygen generation. According to these results, the highest singlet oxygen quantum yield was obtained for NP-RB1 in CHCl$_3$ suspension (Φ_Δ= 0.27). However, for the sample in ACN, the singlet oxygen production was considerably reduced (Φ_Δ= 0.14) likely as a consequence of the aggregation of RB NPs. In a similar way, the grafting of RB on NPs OH groups in NP-RB2 affects significantly the singlet oxygen quantum yield because of the lack of a good solvent to suspend the silica nanoparticles yielding quite low singlet oxygen generation. These results indicate how important is the control of the aggregation of the photosensitizers since the aggregates will decrease the triplet state population by a direct transfer from the excited singlet state of the monomer to the first singlet excited sate of the aggregate, consequently reducing the singlet oxygen quantum yield of the sample (Figure 3.62).
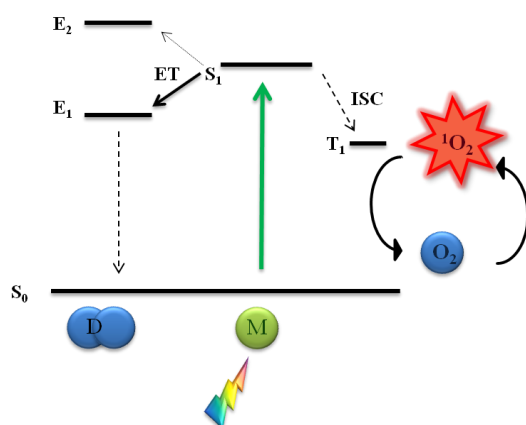
Figure 3.62. Illustrative scheme of the electronic levels involved in the PS aggregates.

For that reason, it is of a crucial importance to get stable nanoparticles suspension to obtain good singlet oxygen production for future implementation in PDT. Therefore, for the particular case of RB, the best option is a controlled grafting on the NH_2 active groups of the silica surface (NP-RB1 sample).

On the other hand, another important aim of this work is to find an efficient new photosensitizer, different from commercial RB, to be grafted on the external surface of silica nanoparticles. As previously described in Section 3.2.1.1., new halogenated BDP, bearing suitable functional groups, such as carboxylic (BDP1) or triethoxysilyl (BDP2) groups, could be possible candidates (Figure 3.10). In that way, these two new halogenated BDPs were grafted on the external surface of silica NPs, either through the NH_2- groups (BDP1) or through the OH- groups (BDP2).

b) Grafting of BDP

First, for new halogenated BDP1 (Figure 3.10), the grafting was performed on active NH_2 groups using an alternative amidation reaction (see Scheme 4.4 of experimental chapter 4) owing to its instability under the conditions of usual peptide coupling (EDC and NHS) previously used for RB. The NP-BDP1 sample was suspended in ACN and $CHCl_3$ to study the singlet oxygen production in both solvents.

In Figure 3.63, the normalized-absorption spectra of the NP-BDP1 in ACN and $CHCl_3$ together with BPD1 in ACN solution are shown. In the same way that RB grafted on NP, the red shift of the absorption band of the sample NP-BDP1 (λ_{abs} = 560 nm, Table 3.16) with respect to the solution is ascribed to the interaction with the

silica matrix. The slight broadening of the band of NP-BDP1 is attributed to the BDP anchored on the silica matrix that could slightly modify the shape of the absorption band. More importantly, in this sample NP-BDP1 there is not clear evidence of dye aggregation in any solvent. The fluorescence quantum yields are quite low ($\phi_{fl} \leq 0.03$) both in solution and in NP-BDP suspensions, in agreement with the presence of the halogen atoms in the molecular structure of the BDP. Indeed, a relative high singlet oxygen quantum yield was previously measured (section 3.2.1.1.1.) for BPD1 in ACN solution ($\Phi_\Delta = 0.66$, Table 3.16), higher than that of RB in ACN solution (0.53, Table 3.15). We thus confirm, as previously described in section 3.2.1, that the use of new photosentizers such as halogenated BDP, may offer a good alternative to the RB commercial photosensitizer, because of their higher photostability and lower tendency to aggregate, together with their good quantum yield of singlet oxygen production.

The quantum yields of singlet oxygen production of NP-BDP1 were quite similar in ACN and CHCl$_3$ suspensions: 0.33 and 0.37 respectively (Table 3.16). Thus, these latter NPs (BPD1 grafted on NH$_2$- active groups) offer stable suspensions in both solvents, avoiding the dye aggregation and therefore improving the range of action of the nanoparticles for singlet oxygen production in solvents with different polarity. These results indicate that the requirement for an optimum dye concentration for singlet oxygen production and stable NPs suspensions was achieved with NP-BDP1 sample.
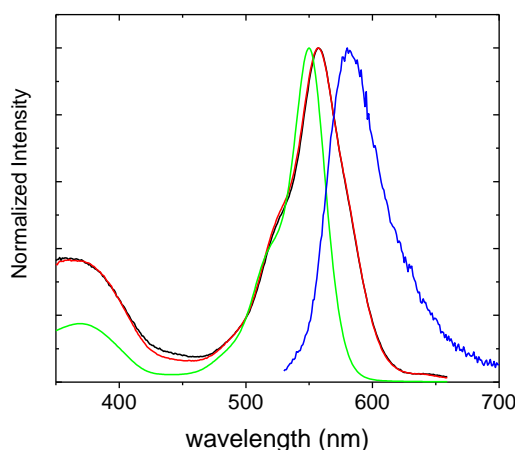
Figure 3.63. Absorbance spectra of BDP1 solution in ACN (green), NP-BDP1 suspension in ACN (red), NP-BDP1suspension in CHCl$_3$ (black) and fluorescence spectra of NP-BDP1 suspension in CHCl$_3$ (blue).

Table 3.16. Photophysical data and quantum yield of singlet oxygen production of NP-BDP1 and NP-BDP2 nanoparticles in ACN and/or CHCl$_3$.

	λ_{abs} (nm)	λ_{fl} (nm)	ϕ_{fl}	Φ_{Δ}	
				ACN	CHCl$_3$
NP-BDP1	560	580	≤0.01	0.33[1]	0.37[3]
BPD1	550	578	0.03	0.66[1]	-
NP-BDP2[2]	430	494	≤0.01	0.36[2]	0.38[3]
BPD2	426	484	0.015	0.78[2]	

[1] Relative to RB in ACN as reference (Φ_{Δ}=0.52) measured in our laboratory with phenalenone as reference (Φ_{Δ} =1 in ACN)

[2] Relative to PN as references in ACN (Φ_{Δ}=1)[29]

[3] Relative to Methylthio-BDP4-2I as reference in CHCl$_3$ (Φ_{Δ}=0.80), table 3.4, section 3.2.1.1.

On the other hand, the grafting of BDP2 on the silica nanoparticles was achieved by polymerization of its triethoxysilyl group (Figure 3.10) on the external OH groups as described in chapter 4, (scheme 4.6 experimental section). The photophysical characterization of NP-BDP2 was performed also in ACN and CHCl$_3$ suspension. The normalized absorption spectra of NP-BDP2 suspensions and of BDP2 in anhydrous THF solution (to avoid self-polymerization) are shown Figure 3.64. Once again the absorption band of NP-BDP2 is wider and red-shifted with respect to BDP2 in solution (Table 3.16) as previously discussed for NP-BDP1.
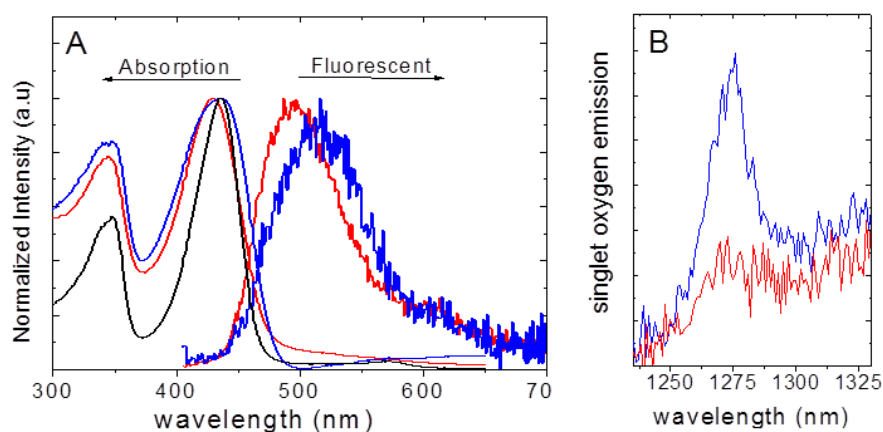
Figure 3.64 (A) Absorbance and fluorescence spectra and (B) the singlet oxygen spectra of NP-BDP2, in ACN (red), in CHCl$_3$ (blue) and of BDP2 in THF solution (black).

Regarding the fluorescence properties of these samples, they show a very poor emission band ($\Phi_{fl} \leq 0.02$) as expected due to the presence of halogenated atoms, which enhances the intersystem crossing (ISC) process to a triplet state.

It should be recalled here that the singlet oxygen quantum yield of BDP2 is assumed to be equal to that obtained for the homologous structure with a 8-methylamino substitution, amino-BDP1-2I ($\Phi_{\Delta} = 0.78$, Table 3.5 in section 3.2.1.1.3.) without the propyl(triethoxysilyl) group. The singlet oxygen quantum yield of the NP-BDP2 in ACN and $CHCl_3$ suspensions was 0.36 and 0.38 respectively. That means that BPD2-grafted on silica NP is not aggregated. As with NP-BDP1, by using BPD2 as graftable photosentitizer, the range of solvent polarities suitable for suspending the grafted nanoparticles is larger than for NP with RB as photosensitizer, with good oxygen quantum yields (although lower than with BDP1 or BDP2 in solution). To summarize, NP-BDP1 and NP-BDP-2 gave the same properties, in term of suspension stability, fluorescence emission and quantum yields of singlet oxygen emission.

3.2.2.4. "Working on Core-Shell"; Combination of Bioimaging and Photodynamic Therapy Applications.

In order to combine the bioimaging and Photodynamic therapy (PDT) applications, a fluorescent dye was embedded in the silica nanoparticle (R6G or R640) and simultaneously a photosensitizer was grafted at the external surface of the nanoparticles (RB, BDP1 or BDP2). In the following, two different strategies were proposed to combine both dyes with complementary photophysical properties:

i) different absorbance range for the fluorescent dye (such as Rhodamine 640) and the photosensitizer (such as BDP1) in order to use different excitation wavelengths for the different actions (i.e. blue light for PDT and orange light for the nanoparticles tracking, sample named as NP/R640-BDP2, Figure 3.65).

ii) similar absorption range for both dyes, such as Rhodamine 6G /Rose Bengal or Rhodamine 640/BDP2 pairs (samples NP/R6G-RB1 and NP/R640-BDP1, respectively) in order to use only one excitation light to trigger both actions (fluorescence and singlet oxygen production, see Figure 3.65).

NP/R640-BDP2   NP/R6G-RB1   NP/R640-BDP1
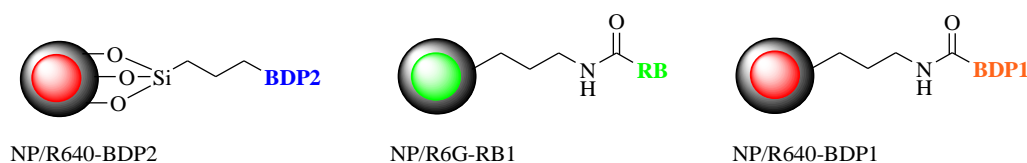
Figure 3.65. The combination of bioimaging and photodynamic therapy.

3.2.2.4.1. Different excitation wavelength for imaging and PDT: NP/R640-BPD2

The silica nanoparticles with BPD2 anchored to the external surface at OH-groups and the Rhodamine 640 physically embedded in the silica core were characterized in chloroform suspension. The absorption spectra (Figure 3.66A) show the characteristic bands of both dyes, at 438 nm ascribed to BPD2 and at 572 assigned to R640 dye. The BPD2 absorption band is around 10 times more intense than that of R640, indicating a higher amount of the photosensitizer on the surface with respect to the fluorescent dye in the core, in agreement with the estimated concentration for each dye detailed above (Table 3.11 and Table 3.14).
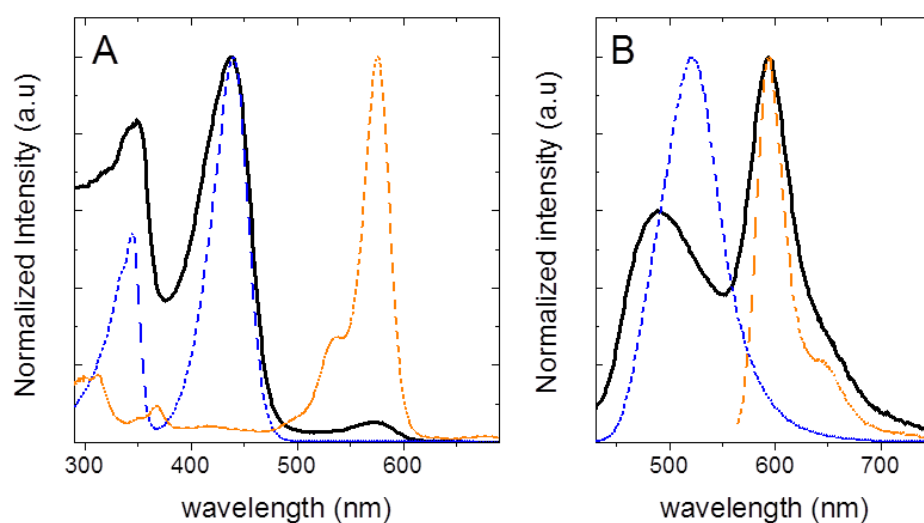
Figure 3.66. (A) Absorption spectra and (B) fluorescence spectra of NP/R640-BDP2 with λ_{exc} 550 or 440 nm (black), BDP2 (blue dotted lines) and R640 (orange dotted lines) in CHCl₃ solution).
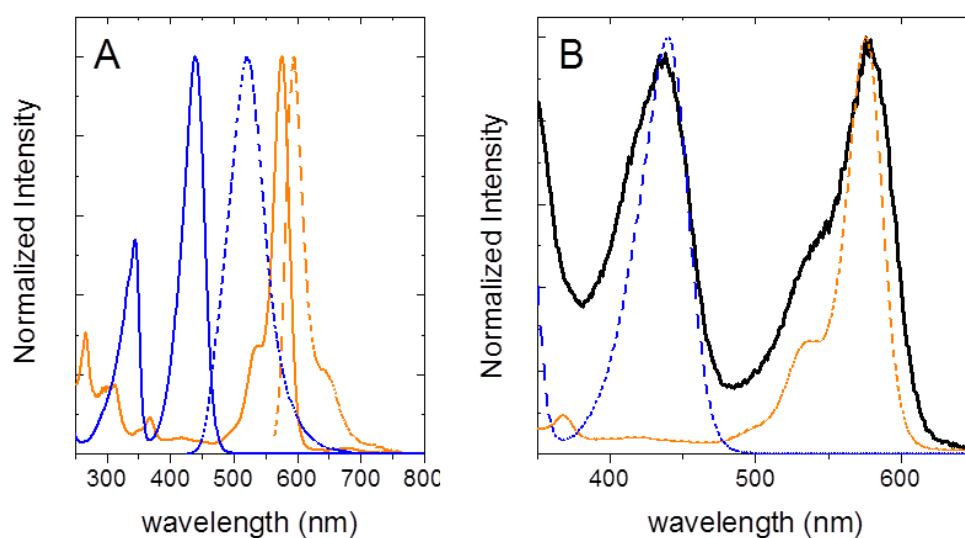
Figure 3.8. (A) Absorbance and fluorescence spectra of BDP2 in THF (blue) and R640 (orange) in EtOH and (B) excitation spectra of NP/R640-BDP2 suspension in CHCl₃ at λ_{em} 575 nm (black), and the absorption spectra of BDP2 in ACN solution (blue dotted line) and R640 in EtOH solution (orange dotted line).

Regarding the fluorescence properties (Figure 3.66B), the emission spectra of R640 at 590 nm is observed after direct excitation of the Rhodamine (λ_{exc} =550 nm) but also upon excitation of BPD2 (λ_{exc} = 440 nm) where the absorbance of the R640 is practically negligible). This indicates a Förster resonance energy transfer process (FRET) from BDP2 to R640. The FRET is a consequence of the overlapping between the fluorescence band of BPD2 (donor) and the absorption band of R640 (acceptor) [85] (Figure 3.66B) and its efficiency depends on the distance between them, which is typically in the range of 1-10 nm. Indeed, the thickness of the shell around 10 nm (previously characterized in section 3.2.2.1) allows FRET process from the BPD2 at the external surface to the fluorescent dye in the core of the silica nanoparticles.

In fact, the contribution of BDP2 is clearly seen in the excitation spectrum (Figure 3.67B) of NP/R640-BDP2 sample at the emission wavelength of R640 (575 nm). This confirms that the excited state of R640 is also populated by an energy process from the excited state of BPD2.

However, a negative consequence of the FRET process between the BPD2 and R640 dyes is that the singlet oxygen quantum yield of NP/R640-BPD2 sample is considerably reduced and a negligible signal was detected since the FRET process from the singlet excited state of the BPD2 to the singlet excited state of the R640 should be more favored than the intersystem crossing process from the singlet excited state of the BPD2 to its triplet state.

3.2.2.4.2. Same excitation wavelength for imaging and PDT: R640-BDP1 and R6G-RB1 samples.

Thus, another approach was to combine the photosensitizer and the fluorescent dye with similar adsorption range such as the Rhodamine 640/BDP1 or R6G/RB pairs, denoted NP/R640-BDP1 and NP/R6G-RB1, respectively.

Note here that due to the high overlapping between the absorption bands of both dyes (the photosensitizer and the fluorescent dye), particularly in R640-BDP1 pair, it will be difficult to distinguish each individual contribution in the absorption spectra. The position of the absorption band of the NP/R640-BDP1 (Figure 3.68A), between the maxima of both dyes (Figure 3.68B and Table 3.17), could be indicative of the contribution of R640 (1.0 10^{-6} mol g^{-1}) and BPD1 (1.8 10^{-6} mol g^{-1}), theoretically in a similar concentration according to the previous characterization (Table 3.11 and Table 3.14).

Table 3.17. Photophysical data and singlet oxygen production of the NP/R60-BDP1 and NP/R6G-RB1 samples suspended in chloroform.

	λ_{abs} (nm)	λ_{fl} (nm)	ϕ_{fl}	Φ_{Δ} [1]
NP/R640-BDP1	564	583	0.10	0.16
NP-BPD1	560	580	≤0.01	0.37
NP-R640	568	590	0.56	-
NP/R6G-RB1	561	580	0.20	0.25
NP-RB1	561	590	0.08	0.27
NP-R6G	530	550	0.30	-

[1] Relative to Methylthio-BDP4-2I as reference in CHCl$_3$ (Φ_{Δ}=0.80), table 3.4, section 3.2.1.1.

On the other hand, for the NP/R6G-RB1 sample, the contribution of the R6G dye in the core of silica NP is observed as a shoulder absorbance with an increased intensity relative to the NP/RB1 sample (Figure 3.68B). According to the estimation of the concentration previously done (Table 3.11 and Table 3.14), R6G amount (6.7 10^{-7} mol g^{-1} taking NP-R6G3 as the optimal NP) could correspond to around 5-10 times less than the RB amount (3.3 10^{-6} or 8.0 10^{-6} mol g^{-1} according to method A or B respectively) grafted on the external surface.
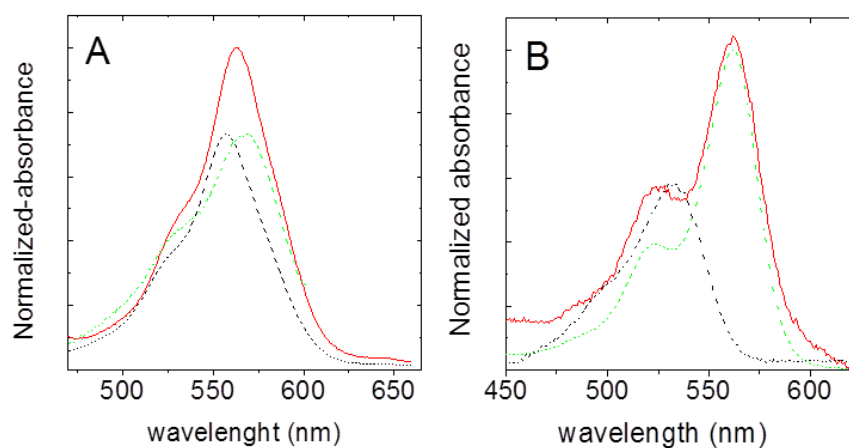
Figure 3.68. Absorption spectra in CHCl$_3$ of; (A) NP/R640-BDP1 (red), NP-BDP1 (black) and NP-R640 (green), and (B) NP/R6G-RB1 (red), NP-R6G (black) and NP-RB1 (green).

But importantly, in these samples, NP/R640-BDP1 and NP/R6G-RB1, the singlet oxygen quantum yield was only slightly reduced in comparison with the NP with only the PS grafted (NP-BPD1 and NP-RB1), to the detriment of an increase of the fluorescence quantum yields (Table 3.17). For instance, the sample NP/R640-BDP1 now has a fluorescence quantum yield around 0.10 (with respect to $\Phi_{fl} = 0.56$ for NP-R640) together with a singlet oxygen quantum yield of 0.16 (with respect to $\Phi_{\Delta} = 0.37$ for NP-BDP1). Even better, the sample NP/R6G-RB1 has a fluorescence quantum yield around 0.2 (with respect to $\Phi_{fl} = 0.3$ for NP-R6G) with a relatively high singlet oxygen quantum yield of 0.25 (with respect to $\Phi_{\Delta} = 0.27$ for NP-RB1). Therefore, the combination of two dyes with complementary actions (high fluorescence *vs* high singlet oxygen production) but with overlapping absorption bands, successfully afforded samples with dual functionality (Table 3.17), which could be interesting for bioimaging and PDT. In any case, phototoxicity experiments are carried out at this moment and will perhaps open the possibilities of implementation of these samples for PDT.

3.2.2.5 Conclusions

Spherical silica NPs with an external surface functionalized by amino groups and with an optimal average size around 50 nm, required for biomedical applications have been successfully synthetized by the Stöber-modified method. Stable suspensions were achieved in ACN solvent.

Fluorescent silica nanoparticles have been elaborated by the encapsulation of different fluorescent Rhodamines in the core, directly added to the synthesis sol at an adequate concentration, resulting in high enough quantum yields ($\Phi_{fl} \geq 0.3$) to be tracked by conventional microscopy techniques. Moreover, the nanoparticles with dyes physically embedded will offer prolonged times for detection due to the increase of photostability of the dye after encapsulation.

By covalently linking different either commercial (Rose Bengal) or new lab-made (halogenated BODIPYs) photosensitizers to the external functional OH- or NH_2-groups of silica, nanoparticles with good singlet oxygen production were also produced. In these samples, the agglomeration of silica nanoparticles is favored due to the presence of the organic photosensitizer on the surface, which depends both on the type of photosensitizer and the graftable groups (OH- and NH_2) used. The aggregation of the particles should be controlled because its negative impact of on the singlet oxygen production. In the case of RB as PS, the nanoparticles aggregation can be reduced by a controlled grafting to the NH_2 groups and by using a less polar solvent than ACN, such as chloroform. However, with the two halogenated BDPs, grafted either to OH groups by direct polymerization or grafted to NH_2 by an amidation reaction, stable suspensions were obtained whatever the solvent, with promising singlet oxygen quantum yields ($\Phi_\Delta \sim 0.35\text{-}0.40$).

Finally, by the combination of two chromophores with overlapping absorption bands and complementary actions, that is a dye with high fluorescence efficiency in the silica "core" and a dye with high singlet oxygen production grafted on the silica "shell", samples with dual functionality were obtained, which could be interesting for bioimaging and PDT.

3.4. General conclusions of chapter 3

In this chapter, we have shown that it was possible to design new nanoparticles platforms with dual functionality, fluorescence and singlet oxygen production, for possible applications in bioimaging and PDT.

Two possible approaches were investigated:

➢ The first one is the selection of suitable sensitizers combining the two properties. Thanks to a complete photophysical study involving the accurate determination of singlet oxygen quantum yields of two new families of photosensitizers based on the BODIPY core, it is now possible to design a PS with either high fluorescence properties or high singlet oxygen quantum yield, or even both but with a reduced efficiency. Significant steps forward was achieved in this field: proposal of a new possible standard photosensitizer for singlet oxygen production soluble in a large range of solvents, proposal of new halogenated BODIPYS or of halogen-free BODIPY dimers with high singlet oxygen quantum yields, proposal of new PSs with a weak but promising singlet oxygen production under NIR excitation, proposal of a multichromophoric BDP dimer for singlet oxygen production. Besides the possible applications in PDT, completed by in vitro phototoxicity study currently undergoing, the understanding of the photophysical processes governing florescence and singlet oxygen formation was carefully analyzed.

➢ The second approach focused on the preparation of silica nanoparticles with defined properties. It was thus possible to design NPs of suitable size, core-shell structure and appropriate photophysical properties by the well-controlled embedding or grafting procedures. The optimization of these two processes with commercial PS or lab-made BODIPYs allowed the complete characterization of NPs with the required dual functionality. The versatility of this approach relies on the possible reasoned use of two different dyes in the same NP, one with fluorescent properties and the other one generating singlet oxygen, with a large range of excitation wavelengths.

3.3.Bibliography

1.	Chem, J. *et al.* New technology for deep light distribution in tissue for phototherapy. *Cancer J.* **8,** 154–63 (2002).

2.	Reports, B. *et al.* Animal models for photodynamic therapy (PDT). *Biosci. Rep.* **35,** 1–14 (2015).

3.	DeRosa, M. C. & Crutchley, R. J. Photosensitized singlet oxygen and its applications. *Coord. Chem. Rev.* **233-234,** 351–371 (2002).

4.	Wang, S., Gao, R., Zhou, F. & Selke, M. Nanomaterials and singlet oxygen photosensitizers: potential applications in photodynamic therapy. *J. Mater. Chem.* **14,** 487 (2004).

5.	Cotí, K. K. *et al.* Mechanised nanoparticles for drug delivery. *Nanoscale* **1,** 16–39 (2009).

6.	Wang, Y. *et al.* Mesoporous silica nanoparticles in drug delivery and biomedical applications. *Nanomedicine Nanotechnology, Biol. Med.* **11,** 313–327 (2015).

7.	Mamaeva, V., Sahlgren, C. & Lindén, M. Mesoporous silica nanoparticles in medicine-Recent advances. *Adv. Drug Deliv. Rev.* **65,** 689–702 (2013).

8.	Zhou, L. *et al.* Encapsulation of hydrophobic anticancer drug in nano-scale porous ceramic materials for photodynamic therapy. *J. Porous Mater.* **18,** 517–522 (2011).

9.	Ow, H. *et al.* Bright and stable core-shell fluorescent silica nanoparticles. *Nano Lett.* **5,** 113–117 (2005).

10.	Luo, S., Zhang, E., Su, Y., Cheng, T. & Shi, C. A review of NIR dyes in cancer targeting and imaging. *Biomaterials* **32,** 7127–7138 (2011).

11.	Erogbogbo, F. *et al.* Biocompatible Luminescent Silicon Quantum Dots for Imaging of cancer Cells. *ACS Nano* **2,** 873–878 (2008).

12.	Valtchev, V. & Tosheva, L. Porous Nanosized Particles: Preparation , Properties , and Applications. *Chem. Rev.* **113,** 6734–6760 (2012).

13.	Stöber, W., Fink, A. & Bohn, E. Controlled growth of monodisperse silica spheres in the micron size range. *J. Colloid Interface Sci.* **26,** 62–69 (1968).

14.	Kim, S., Kim, E., Kim, S. & Kim, W. Surface modification of silica nanoparticles by UV-induced graft polymerization of methyl methacrylate. *J. Colloid Interface Sci.* **292,** 93–98 (2005).

15.	Bogush, G. H. & Zukoski, C. F. Studies of the Kinetics of the Precipitation of Uniform Silica Particles through the Hydrolysis and Condensation of Silicon Alkoxides. *J. Colloid Interface Sci.* **142,** 1–18 (1991).

16.   Lin, Y.-S. & Haynes, C. L. Impacts of Mesoporous Silica Nanoparticle Size, Pore Ordering,and Pore Integrity on Hemolytic Activity. *J Am Chem Soc* **132,** 4834–4842 (2010).

17.   Chiang, Y.-D. *et al.* Controlling Particle Size and Structural Properties of Mesoporous Silica Nanoparticles Using the Taguchi Method. *J. Phys. Chem. C* **115,** 13158–13165 (2013).

18.   Chen, Q., Han, L., Gao, C. & Che, S. Synthesis of monodispersed mesoporous silica spheres (MMSSs) with controlled particle size using gemini surfactant. *Microporous Mesoporous Mater.* **128,** 203–212 (2010).

19.   Lee, J. E., Lee, N., Kim, T., Kim, J. & Hyeon, T. Multifunctional mesoporous silica nanocomposite nanoparticles for theranostic applications. *Acc. Chem. Res.* **44,** 893–902 (2011).

20.   Malvindi, M. A. *et al.* SiO2 nanoparticles biocompatibility and their potential for gene delivery and silencing. *Nanoscale* **4,** 486 (2012).

21.   Kolmakov, K. *et al.* Red-emitting rhodamine dyes for fluorescence microscopy and nanoscopy. *Chem. - A Eur. J.* **16,** 158–166 (2010).

22.   Sobolev, A. S., Jans, D. A. & Rosenkranz, A. A. Targeted intracellular delivery of photosensitizers to enhance photodynamic efficiency. *Prog. Biophys. Mol. Biol.* **73,** 51–90 (2000).

23.   Wilkinson, F., Helman, W. P. & Ross, A. B. Quantum Yield for the Photosensitized formation of the lowest electronically excited singlet state of molecular oxygen in solution. *J phys Chem Ref data* **22,** 113–262 (1993).

24.   Ogilby, P. R. Singlet oxygen: there is indeed something new under the sun. *Chem. Soc. Rev.* **39,** 3181–3209 (2010).

25.   Awuah, S. G. & You, Y. Boron dipyrromethene (BODIPY)-based photosensitizers for photodynamic therapy. *RSC Adv.* **2,** 11169–11183 (2012).

26.   Mehraban, N. & Freeman, H. S. Developments in PDT sensitizers for increased selectivity and singlet oxygen production. *Materials (Open Access).* **8,** 4421–4456 (2015).

27.   Gilbert, A. & Baggott, J. Essential of Molecular Photochemistry Blackwell Scientific. *Angew. Chem. Int. Ed* **11,** 1554–1555 (1991).

28.   Braun, A. M., Maurete, M. T. & Oliveros, E. *Technologie Photochemique: Presses Polytechnique Romandes*. *Photochemical Technology* (1986).

29.   Martinez, C. G. *et al.* Effect of the media on the quantum yield of singlet Oxygen (O-2((1)Delta(g))) production by 9H-fluoren-9-one: Solvents and solvent mixtures. *Helv. Chim. Acta* **86,** 384–397 (2003).

30.   Lacombe, S. & Pigot, T. New materials for sensitized photo-oxygenation.

Photochemistry **38,** 307–329 (2011). and Materials for selective photo-oxygenation vs. photocatalysis: preparation, properties and applications in environmental and health fields, S. Lacombe and T. Pigot, *Catal. Sci. Technol.,* DOI: 10.1039/c5cy01929j (2016).

31.   Lai, Y. C., Su, S. Y. & Chang, C. C. Special reactive oxygen species generation by a highly photostable bodipy-based photosensitizer for selective photodynamic therapy. *ACS Appl. Mater. Interfaces* **5,** 12935–12943 (2013).

32.   Kamkaew, A. *et al.* BODIPY dyes in photodynamic therapy. *Chem. Soc. Rev.* **42,** 77–88 (2012).

33.   O'Connor, A. E., Gallagher, W. M. & Byrne, A. T. Porphyrin and nonporphyrin photosensitizers in oncology: Preclinical and clinical advances in photodynamic therapy. *Photochem. Photobiol.* **85,** 1053–1074 (2009).

34.   Yogo, T., Urano, Y., Ishitsuka, Y., Maniwa, F. & Nagano, T. Highly efficient and photostable photosensitizer based on BODIPY chromophore. *J. Am. Chem. Soc.* **127,** 12162–12163 (2005).

35.   Zhao, J., Wu, W., Sun, J. & Guo, S. Triplet photosensitizers: from molecular design to applications. *Chem. Soc. Rev.* **42,** 5323–51 (2013).

36.   Bröring, M. *et al.* Bis(BF2)-2,2′-bidipyrrins (BisBODIPYs): Highly fluorescent BODIPY dimers with large stokes shifts. *Chem. - A Eur. J.* **14,** 2976–2983 (2008).

37.   Ventura, B., Marconi, G., Bröring, M., Krüger, R. & Flamigni, L. Bis(BF2)-2,2′-bidipyrrins, a class of BODIPY dyes with new spectroscopic and photophysical properties. *New J. Chem.* **33,** 428 (2009).

38.   Cakmak, Y. *et al.* Designing excited states: Theory-guided access to efficient photosensitizers for photodynamic action. *Angew. Chemie - Int. Ed.* **50,** 11937–11941 (2011).

39.   Duman, S., Cakmak, Y., Kolemen, S., Akkaya, E. U. & Dede, Y. Heavy atom free singlet oxygen generation: Doubly substituted configurations dominate S 1 states of bis-BODIPYs. *J. Org. Chem.* **77,** 4516–4527 (2012).

40.   Topel, S. D., Cin, G. T. & Akkaya, E. U. Near IR excitation of heavy atom free Bodipy photosensitizers through the intermediacy of upconverting nanoparticles. *Chem. Commun.* **50,** 8896–8899 (2014).

41.   Wu, W., Cui, X. & Zhao, J. Hetero Bodipy-dimers as heavy atom-free triplet photosensitizers showing a long-lived triplet excited state for triplet-triplet annihilation upconversion. *Chem. Commun. (Camb).* **49,** 9009–11 (2013).

42.   Pang, W. *et al.* Modulating the singlet oxygen generation property of meso–β directly linked BODIPY dimers. *Chem. Commun.* **48,** 5437 (2012).

43.   Esnal, I. *et al.* Reaction of amines with 8-methylthioBODIPY: Dramatic

optical and laser response to amine substitution. *Chem. An Asian J.* **8,** 2691–2700 (2013).

44. Li, F. *et al.* Design, synthesis, and photodynamics of light-harvesting arrays comprised of a porphyrin and one, two, or eight boron-dipyrrin accessory pigments. *J. Am. Chem. Soc.* **120,** 10001–10017 (1998).

45. López Arbeloa, F., Bañuelos, J., Martínez, V., Arbeloa, T. & López Arbeloa, I. Structural, photophysical and lasing properties of pyrromethene dyes. *Int. Rev. Phys. Chem.* **24,** 339–374 (2005).

46. Kee, H. L. *et al.* Structural Control of the Photodynamics of Boron - Dipyrrin Complexes. *J. Phys. Chem. B* **109,** 20433–20443 (2005).

47. Alamiry, M. A. H. *et al.* A molecular rotor based on an unhindered boron dipyrromethane (Bodipy) dye. *Chem. Mater.* **20,** 4024–4032 (2008).

48. Brooker, L. G. S. The Cyanine Dyes and Related Compounds. *J. Am. Chem. Soc.* **87,** 937–938 (1965).

49. Brooker, L. G. S., Craig, A. C., Heseltine, D. W., Jenkins, P. W. & Lincoln, L. L. Color and Constitution. XIII Merocyanines as Solvent Property Indicators. *J. Am. Chem. Soc.* **87,** 2443–2450 (1965).

50. Ortiz, M. J. *et al.* Synthesis and functionalization of new polyhalogenated BODIPY dyes. Study of their photophysical properties and singlet oxygen generation. *Tetrahedron* **68,** 1153–1162 (2012).

51. Bañuelos, J. *et al.* Modulation of the photophysical properties of BODIPY dyes by substitution at their meso position. *RSC Adv.* **1,** 677–684 (2011).

52. Esnal, I. *et al.* Blue-to-orange color-tunable laser emission from tailored boron-dipyrromethene dyes. *ChemPhysChem* **14,** 4134–4142 (2013).

53. Kollmannsberger, M., Rurack, K., Resch-Genger, U. & Daub, J. Ultrafast charge transfer in amino-substituted boron dipyrromethene dyes and its inhibition by cation complexation: A new design concept for highly sensitive fluorescent probes. *J. Phys. Chem. A* **102,** 10211–10220 (1998).

54. Bañuelos, J. *et al.* New 8-Amino-BODIPY derivatives: Surpassing laser dyes at blue-edge wavelengths. *Chem. A Eur. J.* **17,** 7261–7270 (2011).

55. Hansch, C., Leo, a & Taft, R. W. A Survey of Hammett Substituent Constants and Resonance and Field Parameters. *Chem. Rev.* **91,** 165–195 (1991).

56. Bañuelos, J. & López Arbelos, I. Extending the Applications of BODIPY to the whole Visible Spectral Region. *Carbon-Science Technol.* **7,** 1–35 (2015).

57. Schmidt, R. & Afshari, E. Effect of Solvent on the Phosphorescence Rate Constant of Singlet Molecular Oxygen (1Ag). *J phys Chem* **94,** 4377–4378 (1990).

58. Usui, Y., Koike, H. & Kurimura, Y. An Efficient Regeneration of singlet oxygen from 2,5-diphenylfuran Endoperoxide Produced by a Dye-Sensitized Oxygenation. *Bull Chem Soc Japan* **60,** 3373–3378 (1987).

59. Ronzani, F. *et al.* Comparison of the photophysical properties of three phenothiazine derivatives: transient detection and singlet oxygen production. *Photochem. Photobiol. Sci.* **12,** 2160–9 (2013).

60. Schweitzer, C. & Schmidt, R. Physical mechanisms of generation and deactivation of singlet oxygen. *Chem. Rev.* **103,** 1685–1757 (2003).

61. Sels, B. F. *et al.* Molybdate- and Tungstate-Exchanged Layered Double Hydroxides as Catalysts for 1O2 Formation□: Characterization of Reactive Oxygen Species and a Critical Evaluation of 1O2 Detection Methods. *J. Phys. Chem. B* **103,** 11114–11123 (1999).

62. Günther S., G., Lemp M., E. & Zanocco, A. L. in *Boletín de la Sociedad Chilena de Química* 637–644 (2000).

63. Beltrán-García, M. J. *et al.* Singlet molecular oxygen generation by light-activated DHN-melanin of the fungal pathogen Mycosphaerella fijiensis in black sigatoka disease of bananas. *PLoS One* **9,** 1–15 (2014).

64. Osorio-Martínez, C. *et al.* 8-AminoBODIPYs: Cyanines or Hemicyanines? The Effect of the Coplanarity of the Amino Group on Their Optical Properties. *J. Org. Chem.* **77,** 5434–5438 (2012).

65. Schmidt, R., Tanielian, C., Dunsbach, R. & Wolff, C. Phenalenone, a universal reference compound for the determination of quantum yields of singlet oxygen O2(1Δg) sensitization. *J. Photochem. Photobiol. A Chem.* **79,** 11–17 (1994).

66. Martí, C., Jürgens, O., Cuenca, O., Casals, M. & Nonell, S. Aromatic ketones as standards for singlet molecular oxygen photosensitization. Time-resolved photoacoustic and near-IR emission studies. *J. Photochem. Photobiol. A Chem.* **97,** 11–18 (1996).

67. Oliveros, E., Suardi-murasecco, P., Aminian-saghafi, T., Braun, A. M. & Hanseu, H. 1H-Phenalen-1-one:Photophysical Properties and Singlet-Oxygen Production. *Helv. Chim. Acta* **74,** 79–90 (1991).

68. Harriman, A., Mallon, L. J., Ulrich, G. & Ziessel, R. Rapid intersystem crossing in closely-spaced but orthogonal molecular dyads. *ChemPhysChem* **8,** 1207–1214 (2007).

69. Benniston, A. C. *et al.* Effect on charge transfer and charge recombination by insertion of a naphthalene-based bridge in molecular dyads based on borondipyrromethene (Bodipy). *ChemPhysChem* **13,** 3672–3681 (2012).

70. Bandi, V., Gobeze, H. B., Lakshmi, V. & Ravikanth, M. Vectorial Charge Separation and Selective Triplet-State Formation during Charge

Recombination in a Pyrrolyl-Bridged BODIPY − Fullerene Dyad. *J. Phys. Chem. C* **119,** 8095–8102 (2015).

71.   Whited, M. T. *et al.* Symmetry-breaking intramolecular charge transfer in the excited state of meso-linked BODIPY dyads. *Chem. Commun.* **48,** 284–286 (2012).

72.   Dance, Z. E. X. *et al.* Intersystem crossing mediated by photoinduced intramolecular charge transfer: julolidine-anthracene molecules with perpendicular pi systems. *J. Phys. Chem. A* **112,** 4194–4201 (2008).

73.   Kolemen, S. *et al.* Intracellular Modulation of Excited-State Dynamics in a Chromophore Dyad: Differential Enhancement of Photocytotoxicity Targeting Cancer Cells. *Angew. Chemie Int. Ed.* **54,** 1–6 (2015).

74.   Zhang, X. F. & Yang, X. Photosensitizer that selectively generates singlet oxygen in nonpolar environments: Photophysical mechanism and efficiency for a covalent BODIPY dimer. *J. Phys. Chem. B* **117,** 9050–9055 (2013).

75.   Arbeloa, F. L., Arbeloa, T. L. & Arbeloa, I. L. Electronic spectroscopy of pyrromethene 546. *J. Photochem. Photobiol. A Chem.* **121,** 177–182 (1999).

76.   Marianne Kristiansen, Rodger D. Scurlock, Kai-Kong Iu, P. R. O. Charge-Transfer State and Singlet Oxygen Production in Photoexctted Organic Molecule-Molecular Oxygen Complexes. *J. Phys. Chem.* **95,** 5190–5197 (1991).

77.   Yogo, T. *et al.* Selective photoinactivation of protein function through environment-sensitive switching of singlet oxygen generation by photosensitizer. *Proc. Natl. Acad. Sci. U. S. A.* **105,** 28–32 (2008).

78.   Abdel-Shafi, A. a. & Wilkinson, F. Electronic to vibrational energy conversion and charge transfer contributions during quenching by molecular oxygen of electronically excited triplet statesDedicated to Professor Frank Wilkinson on the occasion of his retirement. *Phys. Chem. Chem. Phys.* **4,** 248–254 (2002).

79.   García-Fresnadillo, D. & Lacombe, S. *Reference Photosensitizers for the Production of Singlet Oxygenen Singlet Oxygen in "Singlet Oxygen: Applications in Biosciences and Nanosciences" Volume 1*. 105-143, DOI:10.1039/9781782622208-00105, Eds. S. Nonell & C. Flors (The Royal Society of Chemistry, 2016).

80.   Palao, E. *et al.* 8-Functionalization of Alkyl-Substituted- 3 , 8-Dimethyl BODIPYs by Knoevenagel Condensation. *Org. Lett.* **15,** 4454–4457 (2013).

81.   García-Moreno, I. *et al.* Synthesis and optical and redox properties of symmetric and asymmetric BODIPYs. *Chemphyschem* **13,** 3923–31 (2012).

82.   Speiser, S. Photophysics and Mechanisms of Intramolecular Electronic Energy Transfer in Bichromophoric Molecular Systems: Solution and Supersonic Jet

Studies. *Chem. Rev.* **96,** 1953–1976 (1996).

83. Sykes, D. *et al.* D→f energy transfer in Ir(III)/Eu(III) dyads: Use of a naphthyl spacer as a spatial and energetic 'stepping stone'. *Inorg. Chem.* **52,** 10500–10511 (2013).

84. Ishizaki, A., Calhoun, T. R., Schlau-Cohen, G. S. & Fleming, G. R. Superexchange-mediated electronic energy transfer in a model dyad. *Phys. Chem. Chem. Phys.* **12,** 7378 (2010).

85. Joseph R. Lakowicz. *Principles of Fluorescence Spectroscopy*. (Springer, 1999).

86. Qin, W. *et al.* Boron dipyrromethene analogs with phenyl, styryl, and ethynylphenyl substituents: Synthesis, photophysics, electrochemistry, and quantum-chemical calculations. *J. Phys. Chem. A* **111,** 8588–8597 (2007).

87. Xie, J., Lee, S. & Chen, X. Nanoparticle-based theranostic agents. *Adv. Drug Deliv. Rev.* **62,** 1064–1079 (2010).

88. Förster, Th. Intermolecular Energy Migration and Fluorescence. *Ann. Phys.* **2,** 55–75 (1948).

89. Benniston, A. C. & Harriman, A. Controlling electron exchange in molecular assemblies. *Coord. Chem. Rev.* **252,** 2528–2539 (2008).

90. Xinyue Huang, N. P. Y. and H. E. T. Characterization and Comparison of Mesoporous Silica Particles for Optimized Drug Delivery. *Nanomater. Nanotechnol.* **4,** 1 (2014).

91. Avnir, D. The Nature of the Silica Cage As Reflected by Spectral Changes and Enhanced Photostability of Trapped Rhodamine 6G. *J. Phys. Chem* **88,** 5956–5959 (1984).

92. Sokolov, I. & Naik, S. Novel Fluorescent Silica Nanoparticles: Towards Ultrabright Silica Nanoparticles. *Small* **4,** 934–939 (2008).

93. Martins Estevão, B. *et al.* Rose Bengal incorporated in mesostructured silica nanoparticles: structural characterization, theoretical modeling and singlet oxygen delivery. *Phys. Chem. Chem. Phys.* **17,** 26804–26812 (2015).

94. Uppal, A., Jain, B., Gupta, P. K. & Das, K. Photodynamic action of rose bengal silica nanoparticle complex on breast and oral cancer cell lines. *Photochem. Photobiol.* **87,** 1146–1151 (2011).

95. Gianotti, E. *et al.* An efficient rose bengal based nanoplatform for photodynamic therapy. *Chem.- A Eur. J.* 10921–10925 (2014). doi:10.1002/chem.201404296

96. Rösch, U., Yao, S., Wortmann, R. & Würthner, F. Fluorescent H-Aggregates of Merocyanine Dyes**. *Angew. Chem. Int. Ed* **45,** 7026–7030 (2006).

97.   Magde, D., Rojas ', G. E. & Seybold2, P. G. Solvent Dependence of the Fluorescence Lifetimes of Xanthene Dyes. *Photochem. Photobiol.* **70,** 737–744 (1999).

4

EXPERIMENTAL SECTION

4.1. Hybrid Materials Synthesis

In this chapter 4, the synthesis of the different hybrid materials, such as dye/clays thin films, mesoporous silica monoliths and silica nanoparticles and grafting processes are described. The instrumental and photophysical characterizations are also discussed.

4.1.1. Clay thin films and Dye Intercalation

In this work Smectites, Laponite and Saponite types clay minerals are used to intercalate organic dye molecules into their interlayers. The Laponite (Lap), a synthetic hectorite clay in its sodium form, was supplied by Laporte Industries Ltd and owing to its intrinsic characteristics (particle size <30 nm and high purity)[1,2] did not require any further treatment. Saponite clay (Sap), was supplied by the Clay Minerals Society (Boulder, CO) and the sodium form of the clay with a particle size lower than 0.2 μm was obtained by conventional methods (previously obtained as described elsewhere)[3,4].

The Clay thin films were elaborated by *Spin-Coating*. This technique is based on the distribution of an aqueous clay suspension, previously extended on glass cover slips, by rotating the sample inducing centrifugal forces. The used model is BLE Spinner Delta 10 and the films elaboration scheme is shown in Figure 4.1. The rotating disc speed and time can be controlled. The glass cover slip is held by a vacuum pump coupled to the Spin-coating device.

Figure 4.1. (Left) Spin-Coating equipment BLE Spinner Delta 10 and (Right) the thin film elaboration scheme.

Once the glass cover slip is covered with clay aqueous suspension, the thin film is prepared in two steps: in the first step, the rotation speed is slow to spread the suspended clay particles, and in the second step, the rotation is faster to ensure that the clay layers are parallel over glass cover slip and to remove the suspension solvents through centrifugal forces.

In order to have a suitable clay thin film the most important points to take into account are: i) the clay suspension viscosity, ii) the spin-coating speed conditions[5]. The clay suspension was prepared with 1-2 % of clay by weight in deionised water and the suspension stirred by magnetic stirrers at least for 1 week to obtain well-dispersed and viscous suspensions of clay particles[6]. After preparing the clay suspension, the clay thin film was made by spin-coating first at 500 rpm for 30 seconds and then at 2500 rpm for 60 seconds. The films were then dried at 50ºC in thermostatic vacuum dryer (Vacuo-Temp) for 24h.

In order to intercalate organic dyes into clay minerals layers, the thin films were immersed into staining cuvettes (approx. 40 mL) filled with dye solutions (Figure 4.2). In that step the dye adsorption mainly occurred through cation exchange[5].

Figure 4.2. Clay films immersion inside staining cuvettes.

In this work the used dyes are Styryl 722 (LDS 722, Exciton) and Pyronine-Y (PY, Acro Organics). The Dyes solutions were prepared between 10^{-6} M, 10^{-5} M and 10^{-4} M (microbalance Mettler Toledo model H20T) in ethanol/water mixture v/v 50/50. (Millipore, Milli-Q gradient) and (Merk, grade PA). Dye intercalation was controlled by immersion time, from minutes to hours and by changing the dye solutions concentration. Figure 4.3 shows the clay/dye thin films series after the dye intercalation with different charge of dye.
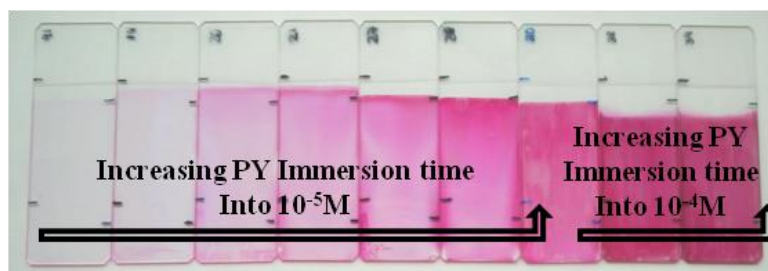
Figure 4.3. Clay/Dye thin films after dye molecule intercalation.

4.1.2. Silica Monoliths with embedded dyes

As previously explained in chapter 2, different fluorescence dyes were embedded into silica monoliths for lasing applications.

The synthesis of silica monoliths was performed by the hydrolysis and condensation of TMOS (tetramethyl orthosilicate, Sigma Aldrich) with methanol and water as solvents and without any additional reactant. In order to embed the commercial laser dye (coumarines, BODIPYs and Rhodamines) inside silica monoliths, laser dyes were dissolved in methanol used for the sol preparation (Merk, Spectroscopic grade) in appropriate concentration from 10^{-5} M to 10^{-3} M. In order to obtain transparent monoliths, a molar ratio *alkoxide/alcohol/water 1/5/4* is used. Changing this molar ratio influences the monolith specific area, porosity and transparency[7,8].

For 5 silica monoliths, TMOS (7.34 mL) was first dissolved in the reaction solvents (10 mL of Methanol containing the required dye concentration, Merck) and the sol was stirred with vigorous agitation for 2 minutes. Immediately water (3.6 mL, miliQ) was added and stirred again with vigorous agitation for other 2 minutes. After that the sol was poured into Plastibrand UV-cuvettes (12.5 x 12.5 x 45 mm, 3.5 mL in each cuvettes). Finally, the cuvettes were tightly closed (parafilm was used to tightly fit the cork on the cuvette) and left in the oven for 3 weeks at 55ºC. Afterwards, the cuvettes were opened and stored in the oven for 3 weeks at 30ºC[7]. Finally, the monoliths were kept in the dark (Scheme 4.1).
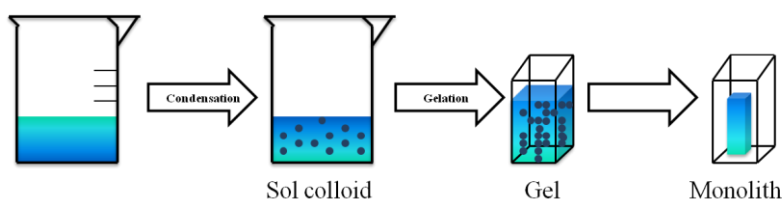

Scheme 4.1. Sol-gel process scheme.

4.1.3. Silica Nanoparticles (NP) and grafting of the photosensitizer

4.1.3.1. Synthesis of Mesoporous silica NP

The synthesis of mesoporous nanoparticles were carried out with TEOS (Tetraethoxysilane, Sigma Aldrich), NH_4OH (Ammonium Hydroxide solution, Sigma Aldrich) as a basic catalyst, CTBA (Hexadecyl-trimethylammoniumbromide, Sigma Aldrich) as a surfactant and APTMS (3-aminopropyl trimerhoxy-silane, Sigma Aldrich) to obtain amino functionalities in the external surface of the NP (Scheme 4.2)[9,10].

The NP synthesis followed a sol-gel process. First, 0.1 g of CTBA was dissolved in 50 mL of NH_4OH at 60ºC. When CTBA was dissolved, 0.8 mL TEOS (0.2 M in EtOH) was added with a vigorous stirring. During this step the NP core is formed. After 5 hours with vigorous stirring at 60ºC, 0.8 mL of TEOS (1M in EtOH, 0.8 mmol) and 0.8 mL of an APTMS solution (12% v/v in EtOH, 0.007 mmol) were added and left under vigorous stirring for 24 h more at 60ºC.
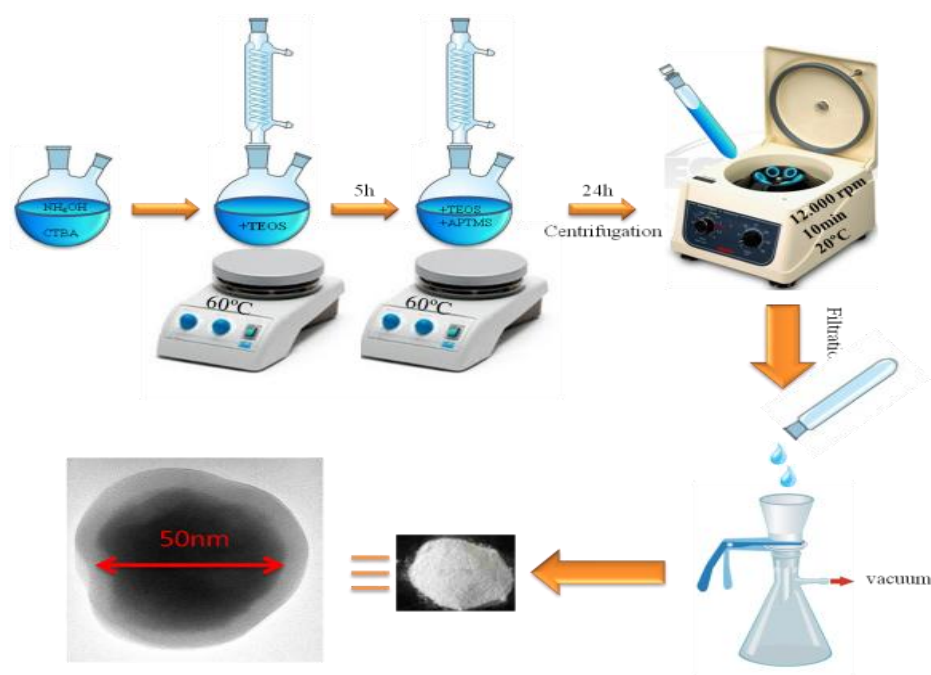
Scheme 4.2. Silica Nanoparticles synthesis scheme.

During this second step, the NP shell is formed and due to the APTMS addition it is functionalized with amine groups. After 24 hours, the temperature was decreased to 20ºC and the mixture was left with a vigorous stirring for 12 hours more. The NPs were collected by centrifugation of the NP suspension at 12000 rpm at room temperature for 10 min. The collected solid was washed three times by mixture of miliQ water/EtOH and a fourth time with EtOH only. The surfactant was removed by stirring the NPs with concentrated HCl (0.2 g of HCl in EtOH) for 12 h. The NPs were collected by filtration. Depending on the reaction, the amount of collected NPs was different (from 15 mg to 40 mg). See in Figure 4.4 the schematic representation of silica NP.
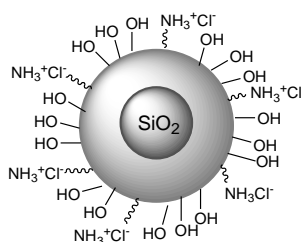

Figure 4.4. Scheme of functionalized silica nanoparticles.

4.1.3.2. PS grafting on NP surface through NH$_2$ groups: NP-RB1 and NP-BDP1.

Owing to the presence of both OH and NH$_2$ groups on NPs surface, there are two different options to graft the PS.

In order to graft the PS on NH$_2$ groups the common peptide coupling reaction was followed. For this grafting synthesis the PS has to bear a carboxylic group (Scheme 4.3). Rose Bengal (NP-RB1, $3x10^{-2}$ mmol Sigma Aldrich) and BODIPY-Ph-COOH (NP-BDP1, $3.5x10^{-2}$ mmol supplied by Eduardo Peña from University of Guanajuato, Mexico) were used. The grafting was performed under argon. First the photosensizer was dissolved in dry THF (20 mL, Sigma Aldrich) and then, N-Hydroxysuccimide or NHS (0.49 mmol, Sigma Aldrich) and N-(3-(dimehylaminopropyl)-N'-ethylcarboiimide or EDC (Sigma Aldrich, 0.46 mmol) was added to activate the carboxylic groups of the PS[9,11]. After 1 hour stirring under argon, dry NP (40 mg) and TEA (triethyl amine, Sigma Aldrich, $3.6x10^{-2}$ mol) were added and the reactants were stirred for 3 h. Next, NPs already grafted were washed with THF and collected by filtration[11].
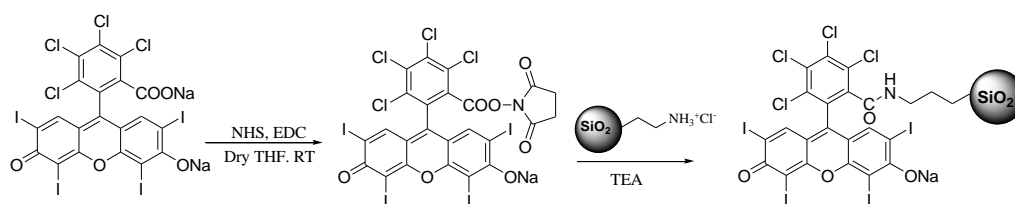
Scheme 4.3. Synthesis of NP-RB1 on NP NH$_2$ groups.

However, BDP1 was decomposed under these conditions (the mixture became dark during the reaction time). As an alternative, a new synthesis was performed using as reactant ethyl chloroformate (Acros) and Triethylamine (TEA, sigma Aldrich). First the PS was dissolved in dry THF and when the PS was completely dissolved, ethyl chloroformate and TEA were added drop by drop. The reaction was carried out under argon at 0ºC for 30 minutes. Then, the NPs were added and the reaction mixture was stirred at room temperature for 30 minutes[12]. The NPs were washed with THF until the supernatant was completely clean and collected by filtration (Scheme 4.4).
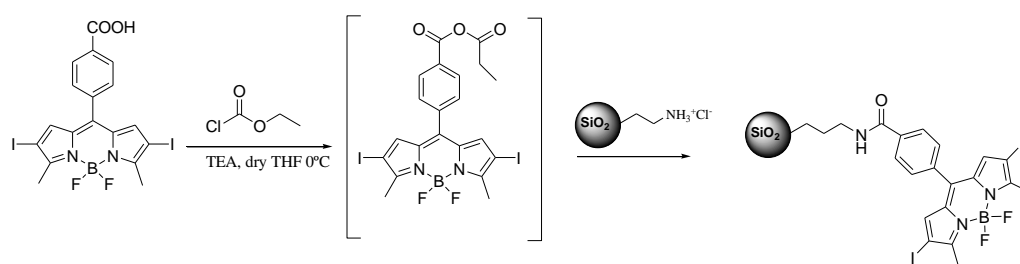
Scheme 4.4. Alternative grafting synthesis of NP-BDP1.

4.1.3.3. PS grafting on NP surface OH groups.

The Rose Bengal (NP-RB2) grafting on OH was performed as previously explained by peptide coupling reaction under Argon. In this case, APTMS was first reacted with the PS: the photosensizer ($6x10^{-3}$ mmol) was dissolved in dry THF (20 mL) and then NHS (0.14 mmol) and EDC (0.1 mmol) were added to activate the PS carboxylic groups. After 1 h stirring under argon, APTMS ($2.8x10^{-2}$ mmol) was added to get a triethoxysilyl-RB, which is formed very quickly (30 minutes). Immediately the NPs

(15 mg) were added and the reaction mixture was stirred for 3 h (Scheme 4.5). The grafted NPs were washed with THF until the surpernatant was completely clean and they were collected by filtration.
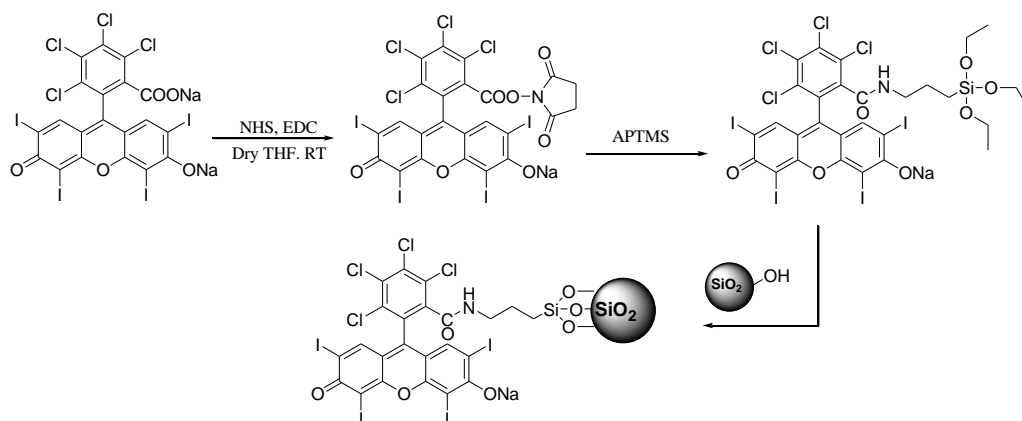
Scheme 4.5. Grafting of a triethoxysilyl-RB on OH groups of NPs.

The BODIPY-Si(OEt)$_3$ (supplied by Mari Jose Ortiz from Universidad Complutense de Madrid, Spain) was grafted directly to the external OH groups of the NP. The BODIPY-Si(OEt)$_3$ (NP-BDP2, 5.1×10^{-2} mmol) was dissolved in dry THF (20 mL) under argon. Then, NPs (28 mg) were added and the reaction mixture was stirred for 3 h (Scheme 4.6). Immediately, the NPs were washed with THF until the surpernatant was completely clean and collected by filtration[11].

Scheme 4.6. NP-BDP2 grafting synthesis on NP OH groups

4.2. Hybrid Materials Structural Characterization

Several techniques were used to characterize the different hybrid materials. Structural properties were studied by X-ray diffraction (XRD), profilometry, nitrogen adsorption isotherms (BET), scanning electron microscopy (SEM) and transmission electron microscopy (TEM). Their chemical composition was estimated by thermogravimetry (TGA), elemental analysis, and X-ray Photoelectron spectroscopy (XPS).

4.2.1. X-Ray Diffraction (XRD)

In clay minerals, the most significant change appears in the modification of basal space between the layers when the dye is intercalated. The swelling of the interlayer space was determined by *X-ray diffraction* diagrams using a Philips model PW 1710 (SGIKER, University of the Basque country). Moreover, by this technique, we can also get information about the clay layer stacking and its order. The XRD was performed with angles in the range 2-20º at 40 kV current and with 1º/min as the scanning speed.

4.2.2. Profilometry

Additionally, the Clay film thickness was determined at the centre of the thin film by *profilometry* (Alpha-step D100, measured at University of the Basque country, UPV-EHU, Physics department). As a result, the film thickness was around 400 nm for Lap films and around 100 nm for Sap films in the centre. In both cases, the films are easily reproducible using the same Spin-Coating conditions.

4.2.3. BET

The structure of porous materials is characterized by *BET* (Brunauer–Emmett–Teller) technique. This technique is an important method for the measurement of the specific surface area of materials. The B.E.T. analyses were carried out employing an ASAP 2010 Micropore Micromeritics (UPPA). The samples were first dried under a vacuum (approx. 1.3×10^{-5} bar) at 150 °C for 24 hours. Once the pressure was constant (samples completely "degassed") the N_2 adsorption-desorption isotherm was recorded at 77 K and the data was analysed and fitted by the Micromeritics software.

4.2.4. Scanning Electron Microscopy (SEM) and Transmission Electron Microscopy (TEM)

The size and morphology of the silica nanoparticles are characterized by electronic microscopies, SEM and TEM. SEM analyses were carried out by JEOL JSM-6400 (SGIKER, University of the Basque Country). TEM analysis were performed by Philips SuperTwin CM200 (SGIKER, University of the Basque Country) at 200 kV.

4.2.5. Elemental Analysis

Elemental analysis (Euro EA 3000 series Elemental analyzer by SGIKER, University of the Basque Country) was used to quantify the amount of intercalated dye into clay minerals.

The Elemental Analysis provides the quantitative content of the C, H, N measured in percentages of the total weight of organic matter. The relative dye-clay concentration is expressed by the percentages of the interchanged dye molecules over the total of cations exchange capacity of clay (Laponite CEC, 76.3 meq/100 g and Saponite CEC, 56.8 meq/100 g). The cationic exchange capacity (% CEC) is the best parameter to quantify the relative amount of intercalated cationic dye.

4.2.6. Thermogravimetric Analysis (TGA)

By *Thermogravimetric analysis* (Mettler Toledo TGA/SDTA 851E, by Laboratorio de Química Macromolecular, LABQUIMAC, University of the Basque Country), the variation of material mass versus temperature under controlled atmosphere (air, O_2, or N_2) is recorded. From TGA the water content and the dye-clay thermostability is obtained. The temperature was increased from 30ºC to 900ºC at constant speed 10ºC/min and under O_2 atmosphere (50 mL min^{-1}).

4.2.7. X-ray Photoelectron Spectroscopy (XPS)

In order to analyse the elements at the sub-surface of the mesoporous silica nanoparticles, *XPS* (the SPECS equipment, measured SGIKER, University of the Basque country) was used. The XPS is a non-destructive technique that gets information about elements present on the NP surface (around 5 nm), on its oxidation state and/or environmental situations (coordination). The measurements were carried out by wide scan: step energy 0.1 eV, dwell time 0.1 s, pass energy 30 eV with 90º of electron exit angle.

4.2.8. IR-ATR spectroscopy

IR-ATR spectra of the silica nanoparticles were collected on IRAffinity-1S Shimadzu spectrometer in a 4000-400 cm^{-1} range. The IR Affinity-1S has the high S/N ratio (30,000:1, 1-minute accumulation, neighborhood of 2,100 cm^{-1}, peak-to-peak), a maximum resolution of 0.5 cm-^{1}, and compact dimensions. By IR-ATR technique, the amide bonds formation in the PS grafting processes is analyzed.

4.2.9. Dynamic light scattering (DLS)

The dynamic light scattering measurements were recorded by Malvem Zetasizer Nano ZS, which has Helio-Neon (λ= 633 nm) laser, available in Inorganic Chemistry Laboratory of University of the Basque Country. By DLS technique the hydrodynamic diameter of the silica nanoparticles can be calculated. Through DLS technique, the estimation of the NP size in suspension was done. In fact, the obtained NP size value is the average of the whole NP suspension. If the distribution is narrow, the suspension is homogeneous, while by obtaining different peaks there are different distribution of NP sizes in the suspension[13].

In this case, the NP size distribution was studied in different solvents; water, ethanol and acetronitile. For DLS measurements, a suspension around 0.1mg/mL of NP was prepared for each solvents and it was left under stirring for 2 days. The DLS measurements were done just after stirring (t=0s) and after let it to stand for 1h to evaluate the NP suspension stability (t=1h).

4.3. Hybrid Materials Photophysical Characterization

The spectroscopic properties of the prepared materials were performed by spectrophotometry (UV-Vis) and by spectrofluorimetry (steady-state and time-correlated).

4.3.1. UV-Vis spectroscopy with linearly polarized light

Absorption spectra of clay minerals, monoliths and new BODIPYs were recorded with a double beam *UV-Vis spectrophotometer* (Varian, model Cary 4E). The spectrophotometer has two emission lamps: halogen lamp (for Vis region) and deuterium lamp (for UV region), which are exchanged at 360 nm. The Cary 4E has a double monochromator with 1200 lines/mm with $\pm$ 0.1 nm resolution diffraction net and a Hamamatsu R928 photomultiplier as a detector (Figure 4.5).

The absorption spectra were recorded in transmittance from 250 nm to 800 nm at 60 nm min^{-1} and slits width of 1 nm. The signal was corrected for clay film (without dye), for monoliths with a blank monolith and for new BODIPYs with solvent in the reference beam. Sometimes this correction is not enough and an extra correction is necessary (the addition or subtraction of clay signal with nothing in the reference beam).
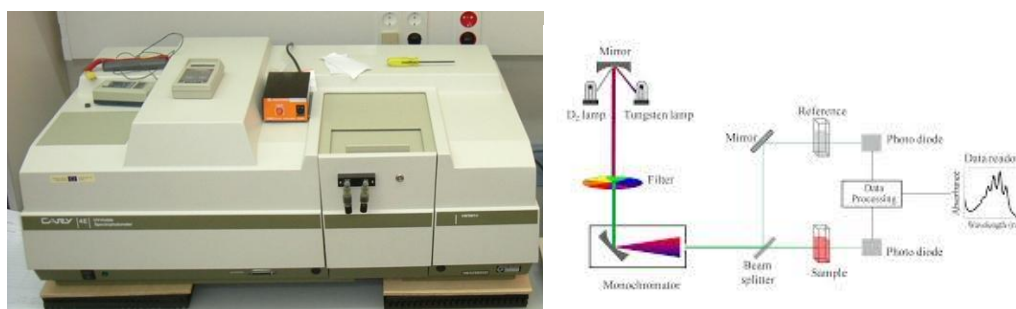
Figure 4.5. Double beam UV-vis spectrophotometer (Cary 4E)

For clay minerals, the dye orientation inside the clay interlayer was characterized by the anisotropic response of the dye/clay films in the absorption spectra to linearly polarized light using a Glam-Thompson (Harrick, model PGT-S1V) polarizer in the incident (absorption) beam. Polarized light is a suitable technique to evaluate the preferential orientation of adsorbed molecules in ordered assemblies[5]. The absorption

probability will depend on the relative orientation between the electric field of the electromagnetic radiation ( ), oscillating in a given plane for a linearly polarized light, and the transition moment of the chromophores ( ).

Figure 4.6 illustrates the experimental set-up used to evaluate the preferential orientation angle of the dye molecules adsorbed in clay films with linearly polarized absorption.
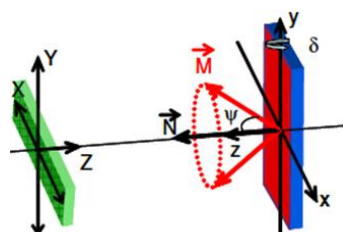
Figure 4.6. Three dimensional scheme for the experimental setup to record the absorption spectra with linearly polarized light. The samples twisting angle δ respect to the incident beam.

The anisotropy study was performed by recording the absorption spectra for horizontal (X axis, A_X) and vertical (Y axis, A_Y) polarized light beam (Z axis) for different orientation of the sample with respect to the incident light by twisting the thin film around its Y axis at different δ angles, as described in ref [14]. The dichroic ratio ($D_{X,Y}$), obtained from the relation between both spectra ($D_{H,V} = A_H/A_V$) was evaluated for δ angles from 0 up to 80°, see equation 4.1.

$$D_{H,V} = \frac{A_H}{A_v} = 1 + \frac{2 - 3 sen^2 \psi}{sen^2 \psi} sen^2 \delta \qquad \textbf{Equation 4.1}$$

being ψ the angle between the dipole moment of the dye respect to the normal to the clay film. Thus, by linear representation of $D_{H,V}$ *vs* $sen^2\delta$, we can determine the angle of inclination ψ of the dye molecules adsorbed relative to the normal to the clay sheets.

Finally, the intrinsic responses of the optical components of the spectrophotometer were corrected by recording the dichroic response of the instrument using an isotropic sample (10^{-5}M of dye solution in 1 mm path length cuvette) at all the covered δ angles.

4.3.2.   UV-Vis-NIR integrating sphere for NPs suspension

The spectra of the mesoporous silica nanoparticles suspension were recorded by *UV-Vis-NIR Spectroscopy* (Cary 7000) equipped with an integrating sphere (Internal DRA 900).

Figure 4.7. UV-Vis-NIR Spectrophotometer (Cary 7000).

The spectrophotometer has two lamps (halogen lamp for Vis-IR region and deuterium lamp for UV region), a double monochromator (Littrow) and double diffraction grating of 1200 lines/mm (Figure 4.7).

4.3.3.   Fluorescence Emission

Two different *spectrofluorimeters* were used for the hybrid materials fluorescence characterization.

In order to record the dye-clay fluorescence spectra, a SPEX model Fluorolog was used. This fluorimeter has a Xenon lamp (450 W), double monochromators in the excitation and emission with 0.2 nm resolution and a Hamamatsu R928-P detector. The detector is cooled by a Peltier in order to reduce the spectra noise and to improve the signal/noise ratio.
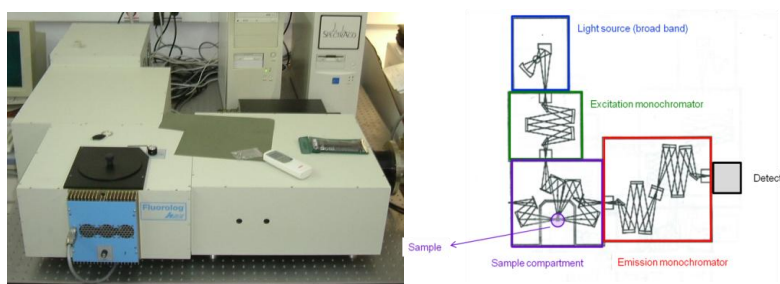
Figure 4.8. Spectrofluorimeter SPEX, Fluorolog model.

The fluorescence spectra of LDS 722-clay films were collected from 520 to 840 nm after excitation at 470 nm and with 5 and 3 nm excitation and emission slits respectively. The emission spectra of PY/clay films were recorded from 550 nm to 800 nm after excitation at 530 nm for monomer and at 470 nm for aggregate. For both dye-clay films, the emission spectra were recorded in the front face configuration where the emitted light is detected at 22.5º by respect to the incident beam (Figure 4.8).

4.3.4. Fluorescence quantum yield and lifetimes

Monoliths fluorescence and lifetime determination were carried out with a *Spectrofluorimeter Edinburgh* Instruments (FLSP920 model, Figure 4.9)

The *Spectrofluorimeter Edinburgh* has a xenon flash lamp 450 W as the excitation source. The fluorescence spectra were corrected from the wavelength dependence of the detector sensibility. Radiative decay curves were recorded with time-correlated single-photon counting technique (Edinburgh Instruments, model FL920) using a microchannel plate detector (Hamamatsu C4878) with picoseconds time resolution (~20 ps).

The BODIPYs fluorescence quantum yields were obtained using several references such as the commercial BODIPY 546, 597 and 605, (ϕ^{r}_{flu} = 0.85, 0.43 and 0.66 in ethanol) and coumarine 152 (ϕ^{r}_{flu} = 0.18 in ethanol). On the other hand, the fluorescence quantum yields of monoliths were measured in an integrated sphere coupled to this spectrofluorimeter using as reference a blank silica monolith.

Figure 4.9. Spectrofluorimeter Edinburgh (FLSP920 model).

Fluorescence decay curves were monitored at the maximum emission wavelength after excitation by means of a fianium laser with 150 ps FWHM pulses (Figure 4.9). Fluorescence lifetimes (τ) were obtained from the slope after the deconvolution of the instrumental response signal from the recorded decay curves by means of an iterative method by the FAST software (Fluorescent Analysis Software Technology). The goodness of the exponential fit was controlled by statistical parameters (chi-square, Durbin-Watson and the analysis of the residuals).

4.3.5. Singlet oxygen emission by direct measurements.

The production of singlet oxygen was determined on the same Spectrofluorimeter Edinburgh (FLSP920 model) by direct measurement of the luminescence at 1270 nm with a NIR detector integrated in the spectrofluorimeter (InGaAs detector, Hamamatsu G8605-23).

The singlet oxygen signal was recorded in front face configuration, 40° and 50° to the excitation and emission beams, respectively and leaned 30° to the plane formed by the direction of incidence and registration in cuvettes of 1 cm. The signal is filtered by a low cut-off of 850 nm. At least 5 solutions of different concentrations between 10^{-6} M and 10^{-5} M have been analysed.

The analysis and quantification of $^1O_2$ by recording its phosphorescence emission signal[15,16] upon continuous monochromatic excitation of the photosensitizer provided quantum yields of $^1O_2$ production (Φ_Δ) and the rate constants of $^1O_2$ total quenching by the PS[17–19]. Under continuous irradiation of a PS, the quantum yield of $^1O_2$ emission is given by:

$$\Phi_e = \frac{P_e}{P_a} = \frac{CS_e}{P_0 \alpha}$$

Equation 4.2

where C is a proportionality factor depending on the detection system and on specific parameters of the medium (refractive index, NIR absorbance), S_e is the $^1O_2$ signal intensity at 1276 nm, P_0 and P_a are the incident photon flux and the photon flux absorbed by the PS ($P_a = P_0\alpha$), P_e is the photon flux emitted by singlet oxygen. α is the absorption factor given by:

$$\alpha = 1 - 10^{-A}$$ **Equation 4.3**

with A, the absorbance of the PS at the wavelength of excitation.

Φ_e maybe also expressed as:

$$\Phi_e = \Phi_\Delta \, k_e \, \tau_\Delta$$ **Equation 4.4**

where k_e (s^{-1}) is the rate constant of $^1O_2$ emission (negligible relative to the rate constant of quenching by the solvent in most solvents, $k_d \gg k_e$),[20,21] and τ_Δ (s) is the singlet oxygen lifetime in the absence of a quencher, $\sigma_\Delta = 1/k_d$.

If the $^1O_2$ phosphorescence signals are recorded in the same solvent for the PS investigated and for a standard sensitizer of know $\Phi_\Delta{}^R$, the following relation is obtained by combining equations 4.2 and 4.4 to equation 4.5 (provided that singlet oxygen quenching by the reference sensitizer is negligible compared to singlet oxygen quenching by the solvent):

$$\frac{S_e^R P_0^{PS} \alpha^{PS}}{S_e^{PS} P_0^R \alpha^R} = \frac{\Phi_\Delta^R}{\Phi_\Delta^{PS}} \left(1 + \tau_\Delta k_t^{PS} [PS] \right)$$ **Equation 4.5**

It should be noted that α^{PS} and α^r (equation 4.2) should not differ significantly, otherwise the geometry of the system and thus the factor C would be modified and the above relation (equation 4.5) would not hold.

The plot of $(S_e^R/S_e^{Ps})(P_a^{PS}/P_a^R) = f([PS])$ should be linear and values of k_t^{Ps} and $\Phi_\Delta^R/\Phi_\Delta^{Ps}$ may be obtained from the slope and the intercept of this plot if the value of τ_Δ in the solvent used is known.

In the cases where $k_t^{Ps}[PS] \ll k_d$ (negligible $^1O_2$ quenching by the PS in the range of concentrations used), the quantum yield of singlet oxygen production of a PS in a given medium does not depend on the PS concentration (equation 4.6).

$$\Phi_\Delta^{PS} = \Phi_\Delta^R \frac{S_e^{PS} P_a^R}{S_e^R P_a^{PS}}$$ **Equation 4.6**

The following reference sensitizers were used: phenalenone (PN) for PS with absorption band in the blue region with $\Phi_\Delta = 1$ [22] in ACN , Rose Bengal (RB) for PS with absorption band in the green region with $\Phi_\Delta = 0.53$ in ACN (measured in our laboratory relative to phenalenone in ACN with $\Phi_\Delta = 1$) and Methylene Blue (MB) for PS with absorption band in the red region with $\Phi_\Delta = 0.57$ in dichloromethane[23].

Note here that relative measurements in the same solvent are directly proportional to Φ_Δ, but if luminescence intensities are compared from different solvents, the measured intensity must be corrected. Indeed, different solvents acetonitrile (ACN), dichloromethane (DCM), chloroform, tetrahydrofurane (THF), ethylacetate and toluene have been used. Accordingly, the differences in the lifetime of $^1O_2$ of each solvent (τ) are corrected in equation 4.7[24]:

$$\phi_\Delta = \phi_\Delta(R) \cdot \left(\frac{\alpha_R}{\alpha_{Ps}}\right) \cdot \left(\frac{Se_{Ps}}{Se_R}\right) \cdot \left(\frac{\tau_R}{\tau_{Ps}}\right) \qquad \textbf{Equation 4.7}$$

The lifetimes of singlet oxygen phosphorescence in different solvents were measured with the same spectrofluorometer, exciting with a pulsed flash lamp 60 microseconds W (µF920) with 5000 counts in the peak emission channel and 100 Hz. Phosphorescence lifetimes (τ_Δ) were obtained from the slope after a tail fit by means of an iterative method by the FAST software (Fluorescent Analysis Software Technology). The goodness of the exponential fit was controlled by statistical parameters (chi-square, Durbin-Watson and the analysis of the residuals).

Note here that although Equation 4.7 may properly correct the differences in the lifetime of $^1O_2$ of each solvent (*i.e.* ACN *vs* THF solvents, Table 3.4, chapter 3), it does not take into account other factors such as the different refractive index or luminescence collection efficiencies of the solvents[25]. That is because the quantum yield of phosphorescence of $^1O_2$, Φ_p^Δ, is related to Φ_Δ as follows (Equation 4.8):

$$\Phi_P^\Delta = \frac{\Phi_\Delta \tau_\Delta}{\tau_P^\Delta} \qquad \textbf{Equation 4.8}$$

with τ_p^Δ, the radiative lifetime. Since the radiative process $^1\Delta_g \leftarrow {}^3\Sigma_g^-$ for the symmetrical molecule O_2 is highly forbidden, τ_P^Δ is highly solvent dependent. Thus, if

luminescence intensities are compared from different solvents, the measured intensity must be corrected for differences in relative probabilities by multiplying by τ_P^Δ and for differences in luminescence collection efficiencies, which often depend on n^2 where n is the refractive index. Thus, corrected values Se_Δ^c of the luminescence signal Se have to be used with (Equation 4.9)[25].

$$Se_\Delta^c = Se \, n^2 \tau_P^\Delta$$

   **Equation 4.9**

However, the estimation of Φ_P^Δ and τ_P^Δ in the literature even by the same authors are often widely different, making this correction almost impossible to be applied.

4.3.6.   Singlet Oxygen probes for indirect determination of Φ_Δ

Alternatively, as a complementary technique, an indirect method was also used to validate the singlet oxygen quantum yields. In this case, a PS solution is irradiated in the presence of a chemical probe, highly selective for singlet oxygen, such as 9,10-dimethylanthracene (DMA, Sigma Aldrich). The decrease of the probe signal is recorded with irradiation time.

The sample holder is a spectroscopy quartz cell irradiated directly in the sample compartment of the UV-Vis spectrometer (Perkin Elmer double beam, double monochromator Lambda850) by a 200 W Xe-Hg light source equipped with a monochromator (Apex Monochromator Illuminator with an off-axis F/4 corrected mirror). A Cornerston 260 motorized 1/4m monochromator with a USB communication interface was used to select the irradiation wavelength. Between the light source and the monochromator a CGA-375nm filter and an IR filter were fixed. An LH1 M4 lens was put between the monochromator and the analytical apparatus to collect and concentrate the light beam. The irradiation and the analysis are thus carried out simultaneously (irradiation is perpendicular to the analysis beam). All optical elements were purchased from Newport (Figure 4.10).

A quartz fluorescence cuvette was filled with mixture of a photosensitizer and 9,10-dimethylanthracene (DMA) in acetonitrile. The PS was excited by the proper excitation wavelength from the monochromator (irradiation wavelength chosen to excite the PSs near its absorption maxima avoiding any absorption of light by DMA). The kinetics decay of the probe DMA during irradiation was quantified by comparing the spectra (absorbance at 378 nm) during irradiation.
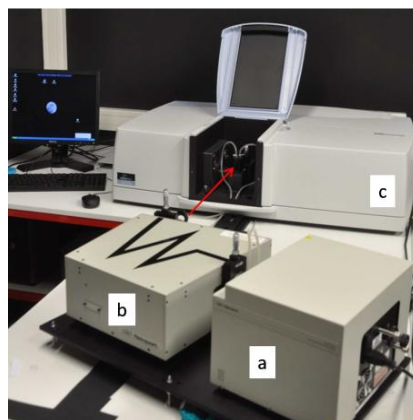
Figure 4.11. Set-up for singlet oxygen indirect measurements (UPPA). (a) Xe-Hg light source (b) the irradiation monochromator (c) spectrophotometer.

By the indirect method, the rate of disappearance of a probe Q (quencher) when reacted with singlet oxygen is given by Equation 4.10[25].

$$-\frac{d[Q]}{dt} = k_t\left[{}^1O_2\right][Q]$$

Equation 4.10

Where the $[{}^1O_2]$ is given by equation 4.11 if it is produced by photosensitization:

$$\left[{}^1O_2\right] = P_a\Phi_\Delta \frac{1}{k_d + k_t^{Ps}[PS] + k_t^Q[Q]}$$

Equation 4.11

P_a (Eisteins L-1 s-1) is the photon flux absorbed by the PS, and Φ_Δ is the singlet oxygen quantum yield. k_d is the rate constant of ${}^1O_2$ quenching by the solvent, k_t^{Ps} is the rate constant of the total quenching of singlet oxygen by the PS itself and k_t^Q is the rate constant of the total quenching of singlet oxygen by the probe (Q). [PS] and [Q] are the respective photosensitizer and probe concentrations. If there is not interference by the reaction products (at the very beginning of the reaction), it is possible to combine Equation 4.10 and Equation 4.11 to Equation 4.12.

$$-\frac{d[Q]}{dt} = P_a\Phi_\Delta \frac{k_r[Q]}{k_d + k_t^{Ps}[PS] + k_t^Q[Q]}$$

Equation 4.12

This is the equation used for the calculation of singlet oxygen quantum yield of the PS using the indirect method. k_t^{Ps} is determined by luminescence (direct method), according to the equation 4.5 (using same solvent for the reference and the PS). If singlet oxygen total quenching by the sensitizer and probe are negligible (k_t^{Ps} [PS] << k_d and k_t^Q [Q] << k_d) the kinetic analysis is simplified to first order model (Equation 4.13)[25,26].

$$\ln\left([Q]/[Q]_0\right) = -P_a \Phi_\Delta \left(k_r/k_d\right)t$$

Equation 4.13

4.3.7. Photostability Measurements

For monoliths photostability measurements, laser scanning confocal setup (Ti-Eclipse,with the NIkon C1 Si-ready scan head) was used. The laser (470nm, run CW, PicoQuant) was connected to the scan head by a single mode fibre. A 470nm razor edge filter (Semrock) in the scan head and a 500nm long pass filter (Chroma) on the detector were used to block back scattered laser light. The signal exiting the scan head was connected to a SPAD based TCSPC system (PicoQuant), *via* a multimode fibre. Results were presented here with 100ms signal averaging.

The monolith was placed on a clean cover-slip and the surface was brought into focus, using the x60 NA 1.45 immersion objective. The air gap between the glass and the monolith was a few 10's of μm thick. The laser was not scanned, but stationary, focused on a point on the surface.

During the bleaching, the signal was recorded for 5 min with the laser on at full power (ND0 filter). Sometimes we had to prevent photon counting overflow in the TCSPC system by dumping the signal to the alternative output port of the scan head (causing dips in the signal up to t=300s).

Then, the power was reduced by a factor 10, using the ND1 filter on the laser, and do the opposite, to monitor recovery: The laser was 'off' most of the time, actually blocked with a shutter, since the power takes ~3s to stabilize after switching on. At regular intervals the shutter (a hand-held piece of black cardboard) was opened for a few seconds to test for recovery of the bleached region. Tests of recovery were not pursued beyond t=10min because of doubts on drift of the microscope stage.

4.4. Bibliography

1. Mering, J. J. *Smectites*. (Springer-Verlag, 1975).

2. Auerbach, S. M., Carrado, K. a. & Dutta, P. K. *Handbook of Layered Materials*. (2004). doi:ISBN: 0-8247-5349-6

3. Tapia Estevez, M. J., Lopez Arbeloa, F., Lopez Arbeloa, T. & Lopez Arbeloa, I. Absorption and fluorescence properties of Rhodamine 6G adsorbed on aqueous suspensions of Wyoming montmorillonite. *Langmuir* **9,** 3629–3634 (1993).

4. Martínez Martínez, V., López Arbeloa, F., Bañuelos Prieto, J. & López Arbeloa, I. Characterization of rhodamine 6G aggregates intercalated in solid thin films of laponite clay. 2 fluorescence spectroscopy. *J. Phys. Chem. B* **109,** 7443–7450 (2005).

5. López Arbeloa, F., Martínez Martínez, V., Arbeloa, T. & López Arbeloa, I. Photoresponse and anisotropy of rhodamine dye intercalated in ordered clay layered films. *J. Photochem. Photobiol. C Photochem. Rev.* **8,** 85–108 (2007).

6. Martínez, V. M., Arbeloa, F. L., Prieto, J. B., López, T. A. & Arbeloa, I. L. Characterization of supported solid thin films of Laponite clay. Intercalation of Rhodamine 6G laser dye. *Langmuir* **20,** 5709–5717 (2004).

7. Arzoumanian, E. *et al.* Transparent Organosilica Photocatalysts Activated by Visible Light: Photophysical and Oxidative Properties at the Gas − Solid Interface. *Appl Mater Interfaces* **6,** 275–288 (2014).

8. Cantau, C., Pigot, T., Manoj, N., Oliveros, E. & Lacombe, S. Singlet oxygen in microporous silica xerogel: Quantum yield and oxidation at the gas-solid interface. *ChemPhysChem* **8,** 2344–2353 (2007).

9. Cheng, S.-H. *et al.* Mesoporous silica nanoparticles functionalized with an oxygen-sensing probe for cell photodynamic therapy: potential cancer theranostics. *J. Mater. Chem.* **19,** 1252 (2009).

10. Lin, Y.-S. & Haynes, C. L. Impacts of Mesoporous Silica Nanoparticle Size, Pore Ordering,and Pore Integrity on Hemolytic Activity. *J Am Chem Soc* **132,** 4834–4842 (2010).

11. Ronzani, F. *et al.* Visible-light photosensitized oxidation of α-terpinene using novel silica-supported sensitizers: Photooxygenation vs. photodehydrogenation. *J. Catal.* **303,** 164–174 (2013).

12. Reaction obtained by private communication. in

13. Llinàs, M. C. & Sánchez-garcía, D. Nanoparticulas de sílice y aplicaciones en biomedicina. *Afinidad LXX!* **565,** 20–31 (2014).

14. Martınez Martinez, V., López Arbeloa, F., Banuelos Prieto, J. & López Arbeloa, I. Orientation of Adsorbed Dyes in the Interlayer Space of Clays. 1.

Anisotropy of Rhodamine 6G in Laponite Films by Vis-Absorption with Polarized Light. *Chem. Mater.* **17,** 4134–4141 (2005).

15. Martí, C., Jürgens, O., Cuenca, O., Casals, M. & Nonell, S. Aromatic ketones as standards for singlet molecular oxygen photosensitization. Time-resolved photoacoustic and near-IR emission studies. *J. Photochem. Photobiol. A Chem.* **97,** 11–18 (1996).

16. Braun, A. M. & Oliveros, E. Applications of singlet oxygen reactions: mechanistic and kinetic investigations. *Pure Appl. Chem.* **62,** 1467–1476 (1990).

17. Aminian-Saghafi, T., Nasini, G., Caronna, T., Braun, A. M. & Oliveros, E. Quantum Yields of Singlet-Oxygen Production by Some Natural Quinoid Fungal Metabolites and Derivatives. *Helv. Chim. Acta* **75,** 531–538 (1992).

18. Thomas, A. H. *et al.* Singlet oxygen (1[capital Delta]g) production by pterin derivatives in aqueous solutions. *Photochem. Photobiol. Sci.* **2,** 245–250 (2003).

19. Cabrerizo, F. M. *et al.* Reactivity of Conjugated and Unconjugated Pterins with Singlet Oxygen (O2(1Δg)): Physical Quenching and Chemical Reaction†. *Photochem. Photobiol.* **83,** 526–534 (2007).

20. Scurlock, R. D., Nonell, S., Braslavsky, S. E. & Ogilby, P. R. Effect of Solvent on the Radiative Decay of Singlet Molecular Oxygen (a1.DELTA.g). *J. Phys. Chem.* **99,** 3521–3526 (1995).

21. Martinez, L. a. *et al.* Nonradiative and radiative deactivation of singlet molecular oxygen (O2(a1Δg)) in micellar media and microemulsions. *J. Photochem. Photobiol. B Biol.* **58,** 94–107 (2000).

22. Schmidt, R., Tanielian, C., Dunsbach, R. & Wolff, C. Phenalenone, a universal reference compound for the determination of quantum yields of singlet oxygen O2(1Δg) sensitization. *J. Photochem. Photobiol. A Chem.* **79,** 11–17 (1994).

23. Usui, Y. Determination of Quatum Yield Of Singlet Oxygen Formation by Photosensitization. *Chem. Lett.* **7,** 743–744 (1973).

24. Mathai, S., Smith, T. a & Ghiggino, K. P. Singlet oxygen quantum yields of potential porphyrin-based photosensitisers for photodynamic therapy. *Photochem. Photobiol. Sci.* **6,** 995–1002 (2007).

25. Wilkinson, F., Helman, W. P. & Ross, A. B. Quantum Yield for the Photosensitized formation of the lowest electronically excited singlet state of molecular oxygen in solution. *J phys Chem Ref data* **22,** 113–262 (1993).

26. Arzoumanian, E. *et al.* Transparent organosilica photocatalysts activated by visible light: Photophysical and oxidative properties at the gas-solid interface. *ACS Appl. Mater. Interfaces* **6,** 275–288 (2014).

GENERAL CONCLUSIONS

Along this memory different hybrid materials have been synthesized and characterized for different purposes: from optical to therapeutic applications.

➢ In chapter 1, hybrid dye-clay films were elaborated by the intercalation of different dyes into the interlayer space of smectite clay–type 2D-host. These systems show a response to linearly polarized light due to the preferential orientation of the dye molecules with respect to the normal to the clay films, offering promising properties for the development of non-linear optical devices. However, owing to its swelling capacity, the interlayer space of clay does not impose rigid enough environments to flexible dyes to avoid non-radiant deactivation (by vibrational motions). On the other hand, xanthene-type dyes tend to aggregate due to low dye-clay interactions. In both cases, the result is the deactivation of fluorescence efficiency. This later phenomenon is hampered by the co-absorption of surfactant molecules in the interlayer space, improving the photophysical properties of films.

➢ In chapter 2, new hybrid solid state materials based on the encapsulation of different laser dyes into large silica monoliths are synthesized via sol-gel chemistry with the aim of developing solid state dye laser (SSDL). Relatively high laser efficiency together with good photo- and chemical stabilities are demonstrated for the rhodamine 6G/silica monoliths. However, owing to irregularities in the parallelepiped monoliths faces, important losses in the laser efficiency are induced. Future work in this direction will be carried out, using strategies to overcome the irregularities resulting from the shrinkage during the drying process.

➢   In chapter 3, firstly an extensive investigation of photophysiscal properties
and singlet oxygen quantum yield determination of new BODIPYs photosensitizers
were carried out. The aim was the development of alternatives to porphyrins
compounds with improved properties such as low toxicity, high molar absorption
coefficient, specific accumulation in tumour tissue and resistance to photobleaching,
for their implementation in medical issues. Among them, a halogenated BODIPY is
proposed as a suitable reference for singlet oxygen determination, since it exhibits a
high singlet oxygen quantum yield, practically constant in different solvents of a wide
polarity range. Secondly, hybrid dye/silica nanoparticles with suitable size (50 nm),
were obtained via sol-gel chemistry. After well-controlled embedding and grafting
procedures of dyes with various functions, the resultant hybrid (nano)materials could
be suitable for bioimaging and Photo Dynamic Therapy (PDT) applications.

This work is the result of a co-advised grant between UPV-EHU and UPPA and of
fruitful collaborations with other research groups that carried out the synthesis of the
new BODIPY photosensitizer (Prof. Mª Jose Ortiz, Univ. Complutense in Madrid and
Prof. Eduardo Peña, Univ. Guagajuato in Mexico), the phototoxicity measurements
(Prof. Angeles Villanueva, Univ Autónoma in Madrid), the laser efficiency (Prof.
Inmaculada Garcia-Moreno, CSIC, Madrid) together with the molecular simulations
of BODIPY structures (Dr. Hegoi Manzano, UPV-EHU).

The high added value of these successful exchanges allowed me to acquire various
skills such as the elaboration through sol-gel chemistry of new materials at various
scales ranging from nanoparticles to several mm large monoliths, or the controlled
grafting/embedding of organic functional dyes. After the preparation of a large range
of dyes and materials (films, monoliths, nanoparticles), I also gained experience in
their extensive structural and photo-physical characterization. Moreover the accurate
determination of quantum yields of singlet oxygen production of new dyes in solution
implied the tuning of a new state-of-the art detection system in the laboratory and its
adaptation to nanoparticles suspensions.

List of publications

Published

➢ Esnal, I.; Uras-Benavides, A.; Gomez-Durán, C.F.A.; Osorio-Martínez, C. A; García-Moreno, I.; Costela, A.; Bañuelos, J.; Epelde, N.; López Arbeloa, I; Hu, R.; Zhong Tang, B.; Peña-Cabrera, E. Reaction of Amines with 8-MethylthioBODIPY: Dramatic Optical and Laser Response to Amine Substitution. *Chem. Asian. J.* **2013,** *8,* 2691-2700.

➢ Duque-Redondo, E.; Manzano, H.; Epelde-Elezcano, N.; Martínez-Martínez, V.; López-Arbeloa, I. Molecular Forces Governing Shear and Tensile Failure in Clay-Dye Hybrid Materials. *Chem.Mater.* **2014***, 26,* 4338-4345

➢ Epelde-Elezcano, N.; Duque-Redondo, E.; Martínez-Martínez, V.; Manzano, H.; López-Arbeloa, I. Preparation, Photophysical Characterization, and Modeling of LDS722/Laponite 2D-Ordered Hybrid Films, *Langmuir,* **2014**, *30,* 10112-10117.

➢ Epelde-Elezcano, N.; Duque-Redondo, E.; Martínez-Martínez, V.; Temino, Ines.; Manzano, H.; López-Arbeloa, I. Strategies for Modulation the Luminescent Properties of Pyronin Y Dye-Clay Films: Experimental and Theoretical Study, *Physical Chemistry Chemical Physics,* **2016**, DOI: 10.1039/C6CP00382F

Submitted

➢ Durán-Sampedro, G.; Epelde-Elezcano, N.; Martínez-Martínez , V.; Esnal, I.; Bañuelos, J.; García-Moreno, I.; Agarrabeitia, A. R.; De la Moya, S.; Tabero, A.; Lazaro-Carrillo, A.; Villanueva, A.; Ortiz, M.J; and López-Arbeloa, I. A Fluorescent-PDT Organic Molecule as All-in-One Platform for White-Light Triggered Theranosis

➢ Epelde-Elezcano, N.; Martínez-Martínez, V.; Peña-Cabrera, E.; Gómez-Durán, C.F.A.; López Arbeloa, I.; Lacombe, S. Modulation of singlet oxygen generation in halogenated BODIPY dyes by substitution at their meso position: towards a solvent-independent standard in the Vis region

In preparation

➢ Singlet oxygen modulation by rational design of orthogonal BODIPY dimers
➢ New BODIPY trimers for Photodynamic therapy applications
➢ Silica Nanoparticles for Bio-imaging and Photodynamic Therapy applications